

Measurement of the electromechanical uterine activity in the non-pregnant human uterus

Citation for published version (APA):

Sammali, F. (2019). *Measurement of the electromechanical uterine activity in the non-pregnant human uterus*. [Phd Thesis 1 (Research TU/e / Graduation TU/e), Electrical Engineering]. Technische Universiteit Eindhoven.

Document status and date:

Published: 04/11/2019

Document Version:

Publisher's PDF, also known as Version of Record (includes final page, issue and volume numbers)

Please check the document version of this publication:

- A submitted manuscript is the version of the article upon submission and before peer-review. There can be important differences between the submitted version and the official published version of record. People interested in the research are advised to contact the author for the final version of the publication, or visit the DOI to the publisher's website.
- The final author version and the galley proof are versions of the publication after peer review.
- The final published version features the final layout of the paper including the volume, issue and page numbers.

[Link to publication](#)

General rights

Copyright and moral rights for the publications made accessible in the public portal are retained by the authors and/or other copyright owners and it is a condition of accessing publications that users recognise and abide by the legal requirements associated with these rights.

- Users may download and print one copy of any publication from the public portal for the purpose of private study or research.
- You may not further distribute the material or use it for any profit-making activity or commercial gain
- You may freely distribute the URL identifying the publication in the public portal.

If the publication is distributed under the terms of Article 25fa of the Dutch Copyright Act, indicated by the "Taverne" license above, please follow below link for the End User Agreement:

www.tue.nl/taverne

Take down policy

If you believe that this document breaches copyright please contact us at:

openaccess@tue.nl

providing details and we will investigate your claim.

MEASUREMENT *of the* ELECTROMECHANICAL
UTERINE ACTIVITY *in the* NON-PREGNANT
HUMAN UTERUS



Federica Sammali

Measurement of the electromechanical uterine activity in the non-pregnant human uterus

The research presented in this thesis was financially supported by the Dutch Technology Foundation NOW TTW research grant 13901 and unconditional Veni grant 12472 along with the financial contribution from Ferring, Samsung, and Twente Medical Systems International (TMSI) companies as well as from 2 academic hospitals, Chatarina Ziekenhuis and Universitair Ziekenhuis Gent.

Cover designed by Agostina Sciotti Manta. Printed by Proefschriftmaken.

Copyright 2019, ©Federica Sammali.

All rights reserved. No part of this publication may be reproduced, stored in a retrieval system, or transmitted, in any form or by means, electronic, mechanical, photocopying, recording or otherwise, without the prior written permission from the copyright owner.

A catalogue record is available from the Eindhoven University of Technology Library.

ISBN: 978-90-386-4863-7

Measurement of the electromechanical uterine activity in the non-pregnant human uterus

PROEFSCHRIFT

ter verkrijging van de graad van doctor aan de Technische Universiteit Eindhoven, op gezag
van de rector magnificus prof.dr.ir. F.P.T. Baaijens,
voor een commissie aangewezen door het College voor Promoties, in het openbaar te
verdedigen op maandag 4 november 2019 om 16:00 uur

door

Federica Sammali

geboren te Genova, Italië

Dit proefschrift is goedgekeurd door de promotoren en de samenstelling van de promotiecommissie is als volgt:

Voorzitter:	prof.dr.ir. A. P.M. Pemen
1 ^e promotor:	prof.dr.ir. J. W. M. Bergmans
2 ^e promotor:	prof.dr. B.C. Schoot (UZ Gent)
Co-promotor:	dr.ir. C. Rabotti
Leden:	dr. ir. J. G. Casado (Universitat Politecnica de Valencia) prof. dr. J. Huirne (Vrije Universiteit Medical Center Amsterdam) prof. dr. ir. C. L. de Korte (Radboud University Nijmegen) prof. dr. Ir. E. Cantatore
Adviseur:	prof. dr. ir. Z. Del Prete (University of Rome 'La Sapienza')

Het onderzoek of ontwerp dat in dit proefschrift wordt beschreven is uitgevoerd in overeenstemming met de TU/e Gedragscode Wetenschapsbeoefening

*To Massimo, who completes me, wonderful father, source of inspiration and daily support,
example of humility, loyalty and dedication.*

To Michael and Mara, to your most beautiful smile, to your purity and genuineness.

To Maya, my little angel. A cruel destiny has taken you away from me, but not from my heart.

SUMMARY

Because of the trend to postpone childbirth, the rate of couples dealing with infertility is rapidly increasing and is approaching 20%. It is estimated that in-vitro fertilization (IVF) represents the only reproduction option for over 2.5 million couples in Europe. In spite of major efforts to improve IVF, the failure rate remains over 70%. As a result, too many couples undergo repeated IVF treatments with the hope of a successful fertilization. There is clear consensus on a major involvement of uterine contractions in IVF failure, especially during and after embryo transfer (ET). In fact, uterine contractions represent an important factor influencing uterine receptivity, both in IVF and in natural menstrual cycles.

It is established that uterine receptivity is crucial during the so-called implantation window, a short period of maximal endometrial receptivity during which the embryo approaches the endometrium in order to implant. This embryo-maternal dialogue is essential for the establishment of a healthy pregnancy. The uterine receptivity is therefore of key importance to the success of IVF.

Specific and precise pharmacological intervention on uterine contractions is feasible and has potential to improve embryo implantation success after ET. Unfortunately, the role of uterine contractions in affecting uterine receptivity for successful embryo implantation is not yet understood, both in IVF and in natural menstrual cycles. The lack of quantitative measurement tools represents the major obstacle for a complete and continuous characterization of the uterine activity outside pregnancy. Availability of such tools would enable an essential step towards improved IVF success rates by better understanding the role of uterine contractions in IVF, possibly leading to new strategies for tailoring specific IVF protocols and pharmacological treatments.

In order to improve the success rate of IVF, in this thesis we introduce new methods to quantitatively and non-invasively measure the electromechanical activity in natural and stimulated cycles, especially in relation to ET. To this end, transabdominal electrohysterography (EHG) and trans-vaginal ultrasound (TVUS) motion analysis are used.

These measurements are complicated by several technical and clinical challenges, such as poor EHG signal-to-noise ratio due to the small size of the non-pregnant human uterus, complex and irregular contraction patterns, complex multilayer uterine structure, and limited and slow uterine motion compared to neighboring organs. To deal with these challenges, we propose an approach that relies on the design of methods that are based on knowledge of the uterine structure, physiology, and electromechanical behavior outside pregnancy. It involves dedicated EHG and TVUS acquisition setups, signal validation, and, finally, probabilistic classification of the uterine activity as either favorable or adverse to ET.

In the first part of the thesis - *on electrohysterography in the non-pregnant human uterus* - it is shown how *ex-vivo* EHG measurements represent a feasible option to investigate the uterine electrical activity and its propagation in resected human uteri. EHG measurements are further used *in-vivo* to characterize the uterine electrical activity in healthy women throughout the natural menstrual cycle.

The second part of the thesis - *on quantitative sonography in the non-pregnant human uterus* - elaborates on the measurement of mechanical uterine activity based on 2D TV-US motion

analysis by speckle tracking. To deal with the challenges mentioned above, a dedicated speckle tracking approach integrating several novel aspects is proposed for the in-vivo quantification of uterine motion. The approach is then translated to in-vivo patient data analysis.

The obtained promising results demonstrate the feasibility of the proposed methods for the quantification and characterization of the electromechanical activity outside pregnancy, and motivated us to assess their clinical value in the context of IVF. To this end, in the third part of the thesis – *on assessment of uterine activity for predicting successful embryo implantation* – probabilistic classification of the uterine activity, as either favorable or adverse to ET, is investigated using machine learning.

In conclusion, this thesis presents for the first time quantitative and noninvasive methods for measuring the electromechanical activity in the non-pregnant human uterus. These methods allow for the characterization of uterine activity in terms of frequency, amplitude, and energy. Our classification results show that a multi-parametric strategy, which combines the estimated parameters, is feasible and establishes a basis for prediction of ET success. This will help doctors to improve clinical decision-making, and possibly opt for specific and precise intervention on uterine contractions to improve the success rate of IVF treatment. Further extensive validation is required to optimize the methods with a larger dataset, as well as to assess their clinical value in the context of fertilization procedures.

TABLE OF CONTENTS

Summary	vi
List of Abbreviations	x
Chapter 1 Background and motivation	1
PART I: Electrohysterography in the non-pregnant human uterus	19
Chapter 2 Propagation of spontaneous electrical activity in the ex-vivo human uterus Submitted to <i>Nature Scientific Reports</i>	21
Chapter 3 Feasibility of transabdominal electrohysterography for analysis of uterine activity in non-pregnant uterus Published in <i>Reproductive Science</i> , 2018, vol 25(7), pp. 1124-1133	43
PART II: Quantitative sonography in the non-pregnant human uterus	59
Chapter 4 Experimental set-up for objective evaluation of uterine motion analysis by ultrasound speckle tracking Published in <i>Biomedical Physics & Engineering Express</i> , 2018, vol 4(3)	61
Chapter 5 Dedicated ultrasound speckle tracking for quantitative analysis of uterine motion outside pregnancy Published in <i>IEEE Transaction on Ultrasonics, Ferroelectrics, and Frequency Control</i> , 2019, vol 66(3)	77
Chapter 6 Blind Source Separation for Clutter and Noise Suppression in Ultrasound Imaging: Critical Review for Different Applications Submitted to <i>IEEE Transaction on Ultrasonics, Ferroelectrics, and Frequency Control</i> , 2019	97
PART III: Assessment of uterine activity for predicting successful embryo implantation	125
Chapter 7 Quantitative ultrasound imaging for assessment of uterine contractility during in-vitro fertilization Submitted to <i>Fertility and Sterility Journal</i>	127

Chapter 8	Multi-modal uterine-activity measurements for prediction of embryo implantation by machine learning Submitted to <i>IEEE Journal of Biomedical and Health Informatics</i> , 2019	141
EPILOGUE		163
Chapter 9	Discussion, conclusions and future perspectives	165
Acknowledgments		187
Curriculum vitae		193
List of publications		195

LIST OF ABBREVIATIONS

2D, 3D	Two-, Three-Dimensional
ADP	Adenosine diphosphate
AIC	Akaike's information criterion
ART	Assisted reproductive technology
ATP	Adenosine triphosphate
AVI	Audio Video Interleave
BSS	Blind source separation
Ca ²⁺	Calcium
CaM	Calmodulin
CF	Cervix to fundus (in terms of contraction direction)
Cl-	Chloride
CNR	Contrast-to-noise ratio
CV	Cross validation
DFT	Discrete Fourier Transformation
DS	Diamond search
DL	Distance signal along the longitudinal direction
DT	Distance signal along the transversal direction
EF	Early follicular (phase of the menstrual cycle)
EHG	Electrohysterography
EL	Early luteal (phase of the menstrual cycle)
ER	Energy ratio
ET	Embryo transfer
ET1	1 hour before ET (phase of the IVF treatment)

ET5-7	Five to seven days after ET (phase of the IVF treatment)
FC	Fundus to cervix (in terms of contraction direction)
<i>fc</i>	Contraction frequency
FFT	Fast Fourier transform
FGS	Full grid search
FS	Follicle stimulation (phase of the IVF treatment)
FSig	Filtered signal
FSH	Follicle stimulating hormone
GMM	Gaussian mixture model
GnRH-a	Gonadotropin-releasing hormone agonist
hCG	Human chorionic gonadotropin
H_d	Hausdorff distance
HSSG	Hysterosalpingoscintigraphy
HW	Healthy women
ICA	Independent component analysis
ICCs	Interstitial cells of Cajal
ICLC	Interstitial Cajal-like cells
ICSI	Intracytoplasmatic sperm injection
IQ	Interquartile
IQR	Interquartile range
IUP	Intra-uterine pressure
IUPC	Intra-uterine pressure catheter
IVF	In-vitro fertilization
K^+	Potassium
KNN	K-nearest neighbour

LD	Longitudinal direction
LDRW	Local density random walk
LDSP	Large diamond search pattern
LF	Late follicular (phase of the menstrual cycle)
LH	Luteinizing hormone
LL	Late luteal (phase of the menstrual cycle)
LV	Left ventricle
MDF	Median frequency
MDL	Minimum description length
MF	Mean frequency
MLCK	Myosin light chain kinase
MLCP	Myosin light chain phosphatase
MRI	Magnetic resonance imaging
MSE	Mean squared error
NFM	Nonnegative matrix factorization
Na ⁺	Sodium
OI	Ongoing implantation
OF	Optical flow
OP	Ongoing pregnancy
PCA	Principal component analysis
PVC	Polyvinyl chloride
r	Correlation coefficient
rbf	Radial based function
RF	Radio frequency
RMS	Root mean squared

ROC-AUC	Area under the Receiver Operating Characteristics curve
SAD	Sum of absolute differences
SD	Standard deviation
SDSP	Small diamond search pattern
SNR	Signal-to-noise ratio
SL	Strain signal along the longitudinal direction
SR	Sarcoplasmatic Reticulum
ST	Strain signal along the transversal direction
SVD	Singular value decomposition
SVM	Support vector machine
TD	Transversal direction
TDE	Thickness of endometrial layer
TE	Teager energy
TIC	Time-intensity curve
TVUS	Transvaginal ultrasound
UC	Uterine contraction
UCAs	Ultrasound contrast agents
UFM	Unnormalized first statistical moment
ULM	Ultrasound localisation microscopy
UP	Uterine peristalsis
US	Ultrasound
WIT	Wash-in-time
WHO	World Health Organization

1

BACKGROUND AND MOTIVATION

This first chapter introduces the reader to the global burden of infertility with emphasis on iv-vitro fertilization (IVF) treatment as well as to currently available technologies for uterine activity assessment and clinical practice. The motivation for the research conducted in this thesis is finally highlighted.

1.1 THE GLOBAL BURDEN OF INFERTILITY

Childbirth and raising of children are deeply ingrained in human nature, leading to completeness, happiness and family integration. According to recent studies carried on by the World Health Organization (WHO), around 8-10% of couples experience infertility problems. Globally, this finding indicates that at least 50 million couples worldwide confronted with infertility problems¹.

Infertility refers to a disease of the reproductive system defined by the failure to achieve a clinical pregnancy after twelve months or more of regular unprotected sexual intercourse². A number of factors including genetics, environmental exposures, and infectious diseases have been associated with infertility risk³. While infertility can affect both men and women, most research on this topic focuses on women.

There are two types of infertility: primary and secondary infertility. Primary infertility refers to couples who have not conceived after at least one year of sex without using birth control methods; secondary infertility refers to couples who have conceived at least once and are unable to conceive again.

According to Mascarenhas et al. ¹, in 2010 roughly 2% of women worldwide experienced primary infertility and approximately 10.5% experienced secondary infertility. Figures 1.1 and 1.2 show the global prevalence of primary and secondary infertility in 2010. The prevalence of secondary infertility, in particular, varies widely by region and country, ranging from less than 6% to greater than 16% of women. The majority of researchers agree that dysfunction of the fallopian tubes contributes largely to infertility⁴⁻⁶.

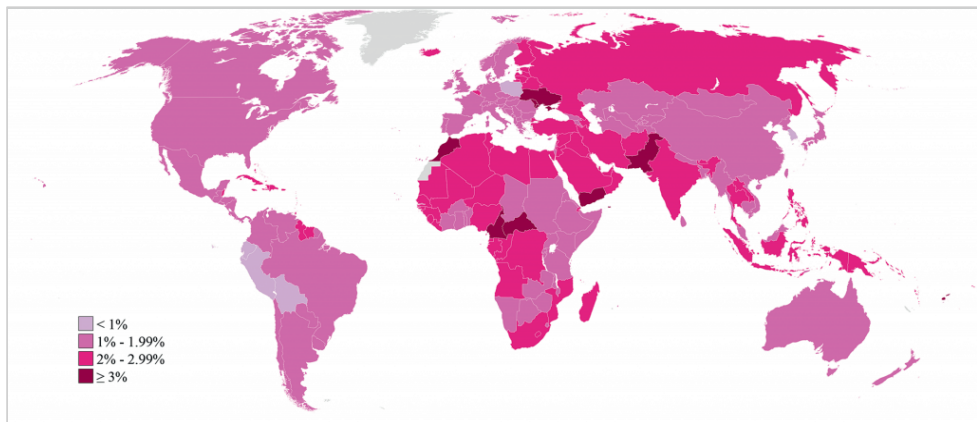


Figure 1.1: Prevalence of worldwide primary infertility in 2010. Taken from [1].

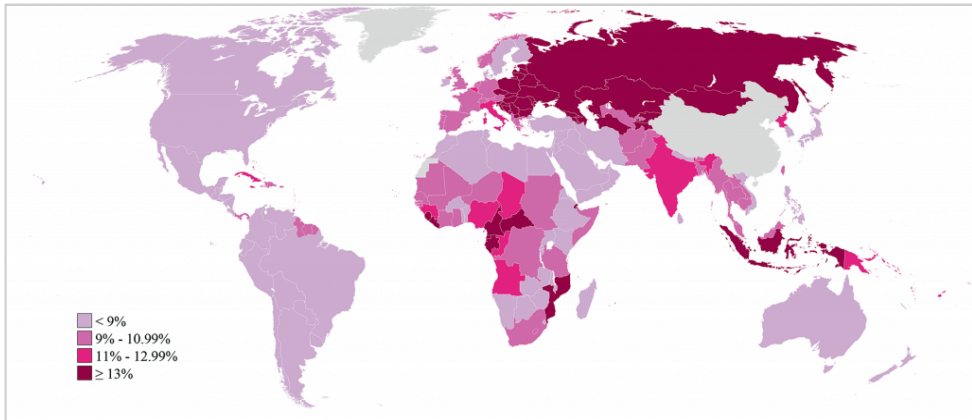


Figure 1.2: Prevalence of worldwide secondary infertility in 2010. Taken from [1].

Declining birth rates over the past 50 years indicate that Europe is producing only 1.5 children per woman. It has been estimated that Europe is the continent with the lowest total fertility rate⁷. This problem is progressively worsening and couples reporting infertility problems are increasing by 8-9% annually⁸. The main reason is ascribed to age-related infertility that is becoming more common because of the trend to postpone childbirth⁹. In fact, fertility declines as a women age due e.g. to the normal decrease in the number of eggs that are produced^{10,11}. Figure 1.3 shows how the likelihood of getting pregnant decreases as women age, developing the chance of becoming infertile.

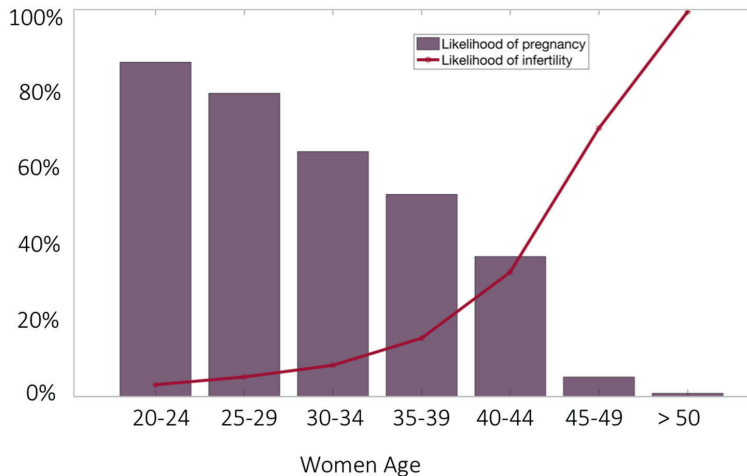


Figure 1.3: Fertility by age: Likelihood of getting pregnant within one year decreases as women age increases leading to an increase in likelihood of infertility. Data taken from [12].

1.2 IN-VITRO FERTILIZATION

Nowadays, infertility represents a serious widespread problem that touches deeply the soul of many infertile couples. Over the past 20 years¹³, medical science has developed novel approaches to infertility problems by Assisted Reproductive Technology (ART). Nowadays, the most advanced ART consists of in-vitro fertilization (IVF). It is estimated that in Europe IVF represents the only option for over 2.5 million couples¹⁴. The direct cost of a single IVF treatment is up to 5,000 euro in Europe¹⁵ and 9,961\$ in the United States¹⁶.

In spite of major efforts to improve IVF, the overall effectiveness remains below 30% per treatment cycle¹⁷ (Figure 1.4). Most IVF failures remain unexplained. As a result, infertile couples often undergo a series of IVF treatments, maintaining just a blind hope of, finally, a successful conception. The emotional, societal, and economical implications of a series of repeated IVF failures are devastating^{18, 19}.

Generally, IVF is offered as a primary treatment for infertility in women over age 40 as well as for certain health conditions such as fallopian tube damage or blockage, ovulation disorders, premature ovarian failure, endometriosis, uterine fibroids, previous tubal sterilization or removal, impaired sperm production or function, unexplained infertility, genetic disorders, and fertility preservation for cancer or health conditions²⁰.

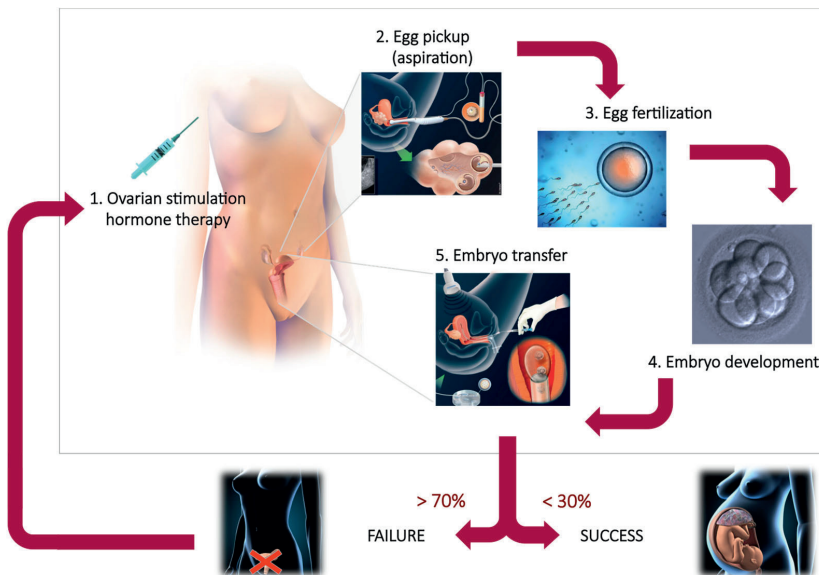


Figure 1.4: IVF repeated treatment cycle (duration = 1 month).

Briefly, IVF treatment consists of the steps²¹ shown in Figure 1.4. First, the woman is prepared by hormone injection to hyperstimulate the egg production (Fig.1.4-1); a transvaginal ultrasound is used repeatedly during the cycle to monitor number and size of follicles, and blood test samples are taken to check hormones levels. Eggs are then retrieved through a hollow needle inserted into the pelvic cavity (Figure 1.4-2). The sperm sample and eggs are

mixed together and stored in a laboratory dish to encourage fertilization during the so called insemination process (Figure 1.4-3). The latter is monitored to confirm that fertilization and cell division are occurring and embryos are developing (Figure 1.4-4). Alternately to conventional IVF, a single sperm is picked up with a fine glass needle and is injected directly into each egg; this procedure refers to Intracytoplasmic sperm injection (ICSI) technique. Finally, based on Alpha/ESHRE guidelines^{22, 23}, one or more embryos are selected and transferred into the pelvic cavity through a catheter three to five days after egg fertilization (Figure 1.4-5). If the procedure is successful, embryo implantation typically occurs after six to ten days following egg retrieval. In case of failure, the woman undergoes repeated IVF treatment cycles.

Each of these steps is highly critical for successful IVF. However, while until embryo development there can be an immediate feedback on the outcome of the undertaken steps, from the moment the embryos are transferred into the pelvic cavity there is no control on the procedure and no intervention is possible.

It is established that uterine receptivity is crucial during the so-called implantation window, a short period of maximal endometrial receptivity during which the embryo approaches the endometrium in order to implant. This embryo-maternal dialogue is essential for the establishment of a healthy pregnancy³⁷. The uterine receptivity is therefore of key importance to the success of IVF. Uterine contractions (UCs) represent an important factor influencing uterine receptivity. In fact, there is a strong evidence of a major involvement of UCs in IVF failure, especially during and after embryo transfer/implantation²⁴⁻³⁰, when the embryo may be expelled^{28, 31-33}. The use of pharmacological treatments to reduce UCs in women with threatened preterm delivery is a routine practice during pregnancy and preliminary studies during embryo implantation suggest that proper use of similar treatments can favor conception³⁴⁻³⁶.

Unfortunately, the role of UCs in IVF failure is not yet understood and the value of pharmacological treatments acting on contractions within IVF treatment remains to be established. The main reason is that, currently, there is no method for a noninvasive, quantitative, and complete characterization of the uterine activity outside pregnancy. It is therefore evident that the possibility of assessing objectively and noninvasively UC characteristics represents an essential step to improve IVF success rate; understanding the impact of UCs on IVF failure is in fact a necessary prerequisite for tailoring specific treatment³⁵.

1.3 UTERINE CONTRACTION IN THE NON-PREGNANT UTERUS

1.3.1 Uterine anatomy

The uterus is a pear-shaped, hollow, muscular organ that is responsible for several functions, such as menstruation, gestation (pregnancy), labor, and delivery. In adults, the uterus is about 7.6-cm (3.0 in) long, 4.5-cm (1.8 in) wide (side to side), and 3.0-cm (1.2 in) thick^{38, 39}. The uterus is located in the female pelvis immediately behind the bladder and in front of the rectum. The anatomical structure of the non-pregnant human uterus is depicted in Figure 1.5.

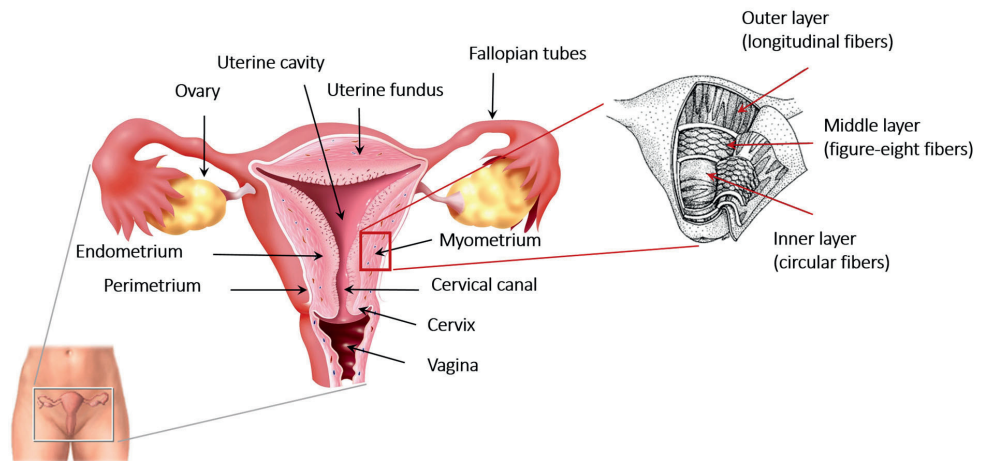


Figure 1.5: Anatomical structure of the non-pregnant human uterus and the myometrial wall fiber organization.

Anatomically, the uterus can be divided into four regions: the cervix or “neck of the uterus” is the lowermost extremity of the uterus protruding into the vagina and it is mostly made up of connective tissue; the cervical canal is the passageway from inside the uterus to the vagina; the corpus (body) is the main body of the uterus including the uterine cavity, it is very muscular and can stretch during pregnancy to accommodate a developing fetus; the fundus is the uppermost rounded extremity of the uterus above the openings of the fallopian tubes.

As indicated in Figure 1.5, the uterus comprises three layers forming together the uterine wall. From the outermost to the innermost, these layers are the perimetrium, myometrium, and endometrium⁴⁰. Perimetrium is the thin outer serosa layer of the uterus covering its outer surface; it is composed of epithelial cells.

The myometrium is the muscle layer composed of smooth muscle cells. Its main function is to produce UCs. The muscular myometrial wall comprises three separate layers (Figure 1.5, zoom): the outer longitudinal smooth muscles, the middle crisscrossing (figure-eight fibers) muscle fibers, and the inner circular fibers⁴¹. The inner one-third of the myometrium is called junctional zone or sub-endometrial layer and it is the major contractile tissue during parturition and abortion; it appears to act like a circular muscle layer producing peristaltic and anti-peristaltic activity⁴².

The endometrium is the innermost layer of the uterus and it represents its non-muscle part. The endometrium is the layer in which the embryo implantation takes place. If the implantation does not occur, the functional (outermost) layer of the endometrium is shed and expelled leading to menstruation.

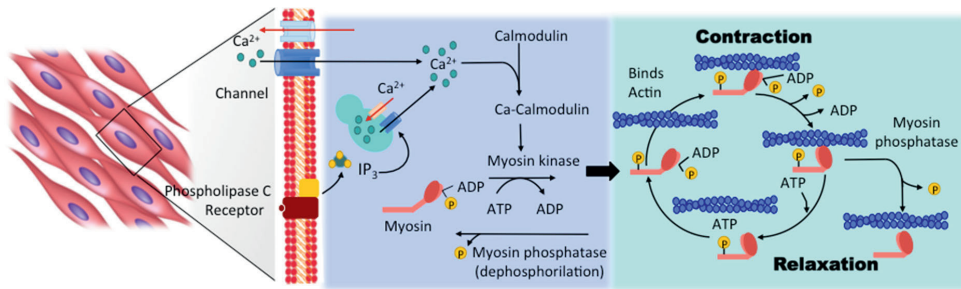


Figure 1.6: Contractile mechanism in a smooth muscle initiating by calcium influx and phosphorylation (left light blue panel) and followed by the cross-bridge formation and contraction cycle (right light green panel).

1.3.2 Contractile mechanism (in non-pregnant uterine muscle)

The uterus belongs to the smooth-muscle group, which contracts spontaneously. This indicates that a piece of isolated, non-pregnant uterus will produce spontaneous contractions without any nervous or hormonal stimulation. Smooth muscles contain both *actin* and *myosin filaments*, having similar chemical characteristics to those of the *actin* and *myosin filaments* in skeletal muscles. Smooth-muscle contraction is initiated by calcium ions (Ca^{2+}) that activate the contractile process leading to the sliding of *actin* and *myosin filaments* over each other through cross-bridges (Figure 1.6). The energy required

to contract is provided by the degradation of Adenosine Triphosphate (ATP) in Adenosine Diphosphate (ADP)⁴³.

Unlike in skeletal muscle cells and neurons, the initiating stimulus for contraction of smooth muscle is due to an increase in intracellular Ca^{2+} rather than sodium ions (Na^{2+})⁴³. The Ca^{2+} ions are the major charge carrier involved in membrane depolarization; therefore, the intracellular calcium concentration ($[\text{Ca}^{2+}]_i$) is a key regulatory factor for UCs^{44, 45} as they are controlled and triggered by a transient increase in $[\text{Ca}^{2+}]_i$, which is initiated and controlled by uterine action potentials (APs). The mechanism involved in the generation of uterine APs and the initiation of muscle contraction is known as excitation-contraction coupling⁴⁴.

Briefly, the initiation of contractions in a smooth muscle mainly depends on two sources of Ca^{2+} : Ca^{2+} sequestered in the Sarcoplasmic Reticulum (SR) of the smooth muscle cell and extracellular Ca^{2+} that can enter the smooth muscle cell via calcium channels present on the membrane of the smooth muscle cell. The release of Ca^{2+} is independently controlled of the entry of Ca^{2+} from extracellular sources and it occurs thanks to the production of a specific signaling molecule named inositol triphosphate (IP_3). The IP_3 opens the calcium channel in the SR releasing Ca^{2+} ⁴⁶.

The entry of extracellular Ca^{2+} in the smooth muscle cell occurs through calcium channels present on the smooth muscle membrane that opens when membrane depolarization occurs; this results in a significant calcium influx into the cell^{43, 46}. The results of this Ca^{2+} influx turns into action potential generation. Once the level of intracellular Ca^{2+} is increased, Ca^{2+} binds a specific protein named Calmodulin (CaM). The formed Calcium-CaM complex then activates the myosin light chain kinase (MLCK), which is an enzyme that phosphorylates the light chain

of myosin (P). Phosphorylated myosin then binds with *actin* filament and initiates cross-bridge formation leading to the uterine muscle contraction cycle.

Uterine muscle relaxation occurs when the light chain of myosin is dephosphorylated by another enzyme located in the fluid of smooth muscle cell named myosin light chain phosphatase (MLCP)¹⁹. At this point, the Ca²⁺ ions move back to the SR or out of the cell by a series of calcium-ATPases and the cross-bridge cycling stops^{43, 46}.

The uterine myocyte is able to contract spontaneously generating a slow wave, simple, or complex AP⁴⁷. How this spontaneous generation of APs is triggered in the myometrium is still not fully understood. In other smooth muscle cells, such as gut, gastrointestinal tract, and bladder, there are specialized interstitial cells of Cajal (ICC) or ICC-like cells (ICLC) that act as pacemakers for producing rhythmical oscillations in the resting membrane potential of the smooth muscle cells⁴⁸⁻⁵⁰. Unlike skeletal and cardiac muscles, the pacemaker cells are not identified and many questions remain as regards to the physiology behind UCs^{42, 50, 51}.

There is evidence of the presence of ICLC in myometrial cells but whether they act as a pacemakers remains unclear^{53, 54}.

1.3.3 Physiological role of uterine contraction (in the non-pregnant uterus)

Uterine contractions are important in many reproductive functions including menstruation, transport of sperms and embryo, pregnancy, and parturition.

The non-pregnant uterus is not a quiescent organ and it can produce contractions. In healthy, non-pregnant, human uteri, previous studies consistently reported specific contractile patterns that evolve throughout the menstrual cycle^{24, 55, 50}. During the menstrual cycle (Figure 1.7), the ovaries and the uterus undergo hormone-dominated physiological changes that, in healthy women, are functional to the establishment of a pregnancy⁵⁵⁻⁵⁸. More specifically, during the follicular phase the ovaries undergo changes aiming at egg production, while the uterus evolves synergistically to a progressively more receptive status towards fertilized embryos. During the follicular phase, the preparatory phase for egg release and the progressive increase in uterine contraction frequency is thought to facilitate sperm transportation toward the Fallopian tubes, where fertilization normally occurs^{24, 55}. Previous studies have shown that, because sperm remains in the uterine cavity within minutes of intercourse, a retrograde uterine contraction pattern (cervico-fundal contractions) is associated with the rapid transport of sperm⁵⁹. After ovulation, the uterus undergoes progressive relaxation that culminates during the early luteal phase; in the transition to the early luteal and late luteal phases, the uterine contraction frequency decreases and the coexistence of opposite UC patterns (cervico-fundal and fundo-cervical contractions) predominates. This relaxation phase may assist proper embryo positioning in the uterine cavity and, thus, facilitate embryo implantation^{57, 61}. During menses (early follicular phase), if no egg has been fertilized to start a pregnancy, an antero-grade UC pattern (fundo-cervical contractions) promotes the forward emptying of the uterine content (menstrual blood). In this phase, the UC pattern is characterized by the so called labor-like contraction because it represents a miniature replica of the expulsive contractions of labor. Differently, during the other phases of the cycle, a sine wave-like (peristaltic) motion dominates⁵⁰.

Abnormal uterine activity may negatively influence these reproductive functions leading to infertility problems. Uterine pathologies, such as endometriosis, adenomyosis, and leiomyomas significantly affect the uterine contractility in the menstrual cycle⁵⁰. Abnormal contractility may cause dysmenorrhea (pelvic pain), infertility, abortion and preterm delivery^{62, 63}. The relationship between uterine pathologies and decreased infertility has been suggested by several studies^{62, 64, 65}. It has been observed that the peristaltic uterine activity is significantly increased in women with endometriosis; this hypercontractility may possibly explain why women with endometriosis show increased incidence of spontaneous abortions⁵⁰. Adenomyosis is a condition when the endometrial tissue infiltrates and disrupts the subendometrial myometrium. As a result, the direct sperm transport is impaired during the ovulatory period causing infertility⁵⁰. Unfortunately, the influence of endometriosis and adenomyosis on uterine contractility remains unclear. These two pathologies often coexist and sometimes one of the two can be diagnosed at a later time; therefore, it is difficult to establish which of the two pathologies has the greatest influence on uterine contractility. According to some studies⁶⁶⁻⁶⁸, abnormal uterine contractility during the mid-luteal phase may lead to infertility problems in women with leiomyomas (fibroid tumor), and these women also presented a decreased success rate in ART.

1.4 ELECTROMECHANICAL UTERINE ACTIVITY ASSESSMENT: AVAILABLE TECHNOLOGIES AND CLINICAL PRACTICE

Understanding the role of uterine activity in influencing uterine receptivity, especially in relation to embryo implantation success, has always been complicated. The lack of quantitative measurement tools has represented the major obstacle for a complete characterization of the uterine activity outside pregnancy. Some research has been carried out in order to evaluate methods/tools for uterine contraction assessment. However, the proposed approaches either lack accuracy, objectiveness or user-friendliness.

Today, UCs can quantitatively be assessed by intrauterine pressure catheter (IUPC) only⁶⁹⁻⁷². IUP is measured by a miniature pressure transducer inserted into the uterine cavity. A single-tip uterine catheter can provide amplitude, frequency, and basal pressure tone of UCs, while multiple-tip catheters can be used to investigate their direction and propagation⁷³. A strong drawback of catheterization lies in the invasive nature of the device, which makes its routine use unpractical and patient unfriendly. IUP may also interfere with the natural contraction characteristics due to irritation and reflex mechanisms⁷⁴. Furthermore, the use of this method is unsuitable in the context of IVF especially during ET, as the catheter might injure the endometrium or the embryo itself.

Hysterosalpingoscintigraphy (HSSG) can be used for indirect assessment of contraction direction by measuring displacements of uterine content⁷⁵. After injection of a radio-labeled suspension in the uterine cavity, the suspension migration is traced as the distribution of radioactivity by a gamma camera^{75, 55, 65}. The main disadvantages of HSSG relate to the time and cost of the procedure as well as to the inability to assess contraction amplitude and frequency. Furthermore, due to the risks associated with radiation exposure, it is not suitable for use immediately after embryo transfer.

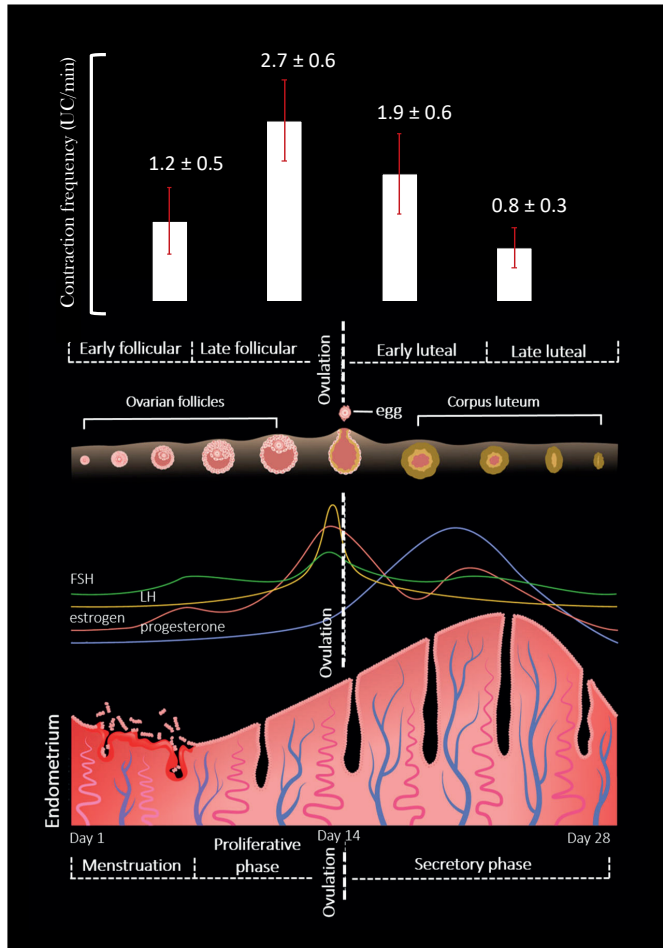


Figure 1.7: Menstrual cycle, hormone-dominated uterine physiological changes, and contraction frequency reported per each phase in terms of mean values and standard deviation⁵⁷. The menstrual cycle can be divided in four main phases named early and late follicular phases and early and late luteal phases. The cycle starts with menstrual flow (3 to 5 days) due to the breakdown of the endometrium (early follicular phase). Menstrual flow occurs only when the egg is not fertilized. During the late follicular phase, the primary follicles mature into the Graafian follicles causing the regeneration of the endometrium. The release of gonadotropins from the pituitary gland (LH and FSH) increases causing follicular growth in the ovaries. During the ovulatory phase (Day 14-middle of the cycle), the Luteinizing hormone (LH) and Follicle Stimulating hormone (FSH) reach their peak causing the rupture of the Graafian follicle (matured follicle) to release one egg. During the early luteal phase, the remains of the mature follicle turns into the corpus luteum which secretes progesterone for maintaining the thickness of the endometrium facilitating implantation. In the absence of fertilization, the corpus luteum degenerates (late luteal phase) causing the disintegration of the endometrium and a new cycle starts⁶⁰.

Reliant on an excellent tissue contrast, magnetic resonance imaging (MRI) allows clear visualization of uterine zonal anatomy and hormone-induced changes clearly undergone by the uterus. It is able to assess uterine contraction frequency; however, amplitude and direction measurements are not possible⁷⁶. In addition, MRI is expensive and time-consuming.

The introduction of a transvaginal high-resolution ultrasound probes offered the possibility to visualize uterine motion throughout the menstrual cycle. Transvaginal ultrasound (TVUS) permits the estimation of contraction frequency and visualization of the contraction direction^{77, 78}. A previous study⁵⁷ demonstrated that measuring the frequency of the uterine activity is as effective as IUPC recordings⁷⁶. However, TVUS imaging cannot provide quantification of uterine contraction amplitude⁵⁷. In principle, TVUS measurements represent a valid, safe alternative to invasive measurement tools, such as IUP and HSSG, for quantitative analysis of the uterus. However, so far only qualitative analysis is available, highlighting the operator-dependency and subjectivity of the results. The accurate interpretation of the resulting image sequences is challenging also for skilled and experienced operators⁷⁵. TVUS images are thus difficult to reproduce for follow-up and comparative studies^{79, 80}. Only one study⁸¹ showed the possibility to use transabdominal US measurements to quantitatively investigate the mechanical changes that the uterus undergoes during pregnancy by speckle tracking techniques. The methods mentioned above are all based on mechanical features of the uterine contraction. Electrophysiological measurements can also be included in automated analysis for assessing the uterine activity.

In a non-pregnant uterus, the electrical activity has so far only been invasively measured *ex-vivo* in animals^{82, 83} and in isolated and perfused human uteri by the use of bipolar silver electrodes⁶³ or needle electrodes⁶⁴. On the contrary, extensive research has been carried out on pregnant uteri with achieving compelling results for the characterization of the electrical activity by abdominal electrohysterography (EHG)⁸⁵⁻⁸⁸, particularly aimed at improving labour monitoring and prediction of preterm delivery⁸⁹⁻⁹⁶. EHG measures the electrical activity that triggers and drives the mechanical contraction of the uterus; it is one of the most promising biophysical markers for the evaluation of UCs and the electrophysiological state of the uterus. These days, commercial products providing EHG measurement are available for hospital monitoring as well as for self-monitoring by patients.

Also for the non-pregnant uterus, EHG potentially allows for a complete characterization of contractions in terms of amplitude, frequency, direction, and velocity, with the additional advantage of being noninvasive, inexpensive, and particularly suitable for long-term measurements. However, EHG it has never been performed in non-pregnant human uteri.

Potential future methods for the assessment of UCs, especially in relation to ET, might include automated quantitative analysis of TVUS and EHG recordings.

1.5 THESIS OBJECTIVE

The role of UCs in affecting uterine receptivity in successful embryo implantation is not yet understood, both in IVF and in natural menstrual cycles. The lack of quantitative measurement tools represents the major obstacle for a complete and continuous characterization of the uterine activity outside pregnancy. Availability of such tools would enable advancing towards improved IVF success rates by better understanding the role of UCs in IVF, possibly leading to new strategies for tailoring specific IVF protocols and pharmacological treatments.

In order to improve the success rate of IVF, in this thesis we introduce new methods to quantitatively and non-invasively measure the electromechanical activity of the uterus in

natural and stimulated cycles, especially in relation to ET. To this end, we propose the use of EHG and TVUS motion analysis being safe, cost-effective, and relatively unobtrusive. These technologies are especially suitable for measuring the uterine activity in the context of IVF.

These measurements are complicated by several technical and clinical challenges, such as poor EHG signal-to-noise ratio due to the small size of the non-pregnant human uterus, complex and irregular contraction patterns, complex multilayer uterine structure, and limited and slow uterine motion compared to neighboring organs. To deal with these challenges, we propose an approach that relies on the design of methods that are based on knowledge of the uterine structure, physiology, and electromechanical behavior outside pregnancy. It involves dedicated EHG and TVUS acquisition setups, signal validation, and, finally, probabilistic classification of the uterine activity as either favorable or adverse to ET.

1.6 THESIS OUTLINE

This thesis, which is based on a collection of journal papers (Chapters), is structured in three main parts (Part I, II, and III).

Part I investigates the use of the EHG in *ex-vivo* resected human uteri showing how EHG represents a feasible option to investigate objectively the uterine electrical activity and its propagation (**Chapter 2**). EHG measurements are further performed *in-vivo* to characterize the uterine electrical activity in the non-pregnant healthy uterus in natural cycles (**Chapter 3**).

Part II elaborates on quantitative sonography in the non-pregnant healthy uterus for the measurement of mechanical uterine activity based on 2D TVUS motion analysis by speckle tracking. The proposed method is first tested and optimized *ex-vivo*, by means of an experimental setup specifically realized to generate controlled and rhythmic uterine motion (**Chapter 4**). Based on this realistic ground truth for uterine motion, a dedicated speckle tracking approach integrating several novel aspects is proposed for the *in-vivo* quantification of uterine motion in healthy women (**Chapter 5**). To validate the proposed technique, we assess its ability to distinguish between different phases of the natural menstrual cycle.

The obtained promising results demonstrate the feasibility of the proposed methods for the quantification and characterization of the electromechanical activity outside pregnancy, suggesting that they can be clinically valuable in the context of IVF. To explore this value, in Part III of the thesis the uterine activity in infertile women undergoing IVF treatment is assessed for prediction of successful embryo implantation (**Chapter 7**); in particular, probabilistic classification of the electromechanical uterine activity, as either favorable or adverse to ET, is investigated using machine learning (**Chapter 8**).

Finally, the epilogue of this thesis provides a final discussion, conclusions as well as future perspectives.

BIBLIOGRAPHY

1. Mascarenhas, M. N., Flaxman, S. R., Boerma, T., Vanderpoel, S., & Stevens, G. A. (2012). National, regional, and global trends in infertility prevalence since 1990: a systematic analysis of 277 health surveys. *PLoS medicine*, *9*(12), e1001356.
2. <https://www.who.int/reproductivehealth/topics/infertility/definitions/en/>.
3. Cates, W., Farley, T. M., & Rowe, P. J. (1985). Worldwide patterns of infertility: is Africa different?. *The Lancet*, *326*(8455), 596-598.
4. Mayaud, P. (2001). Infertility in Africa: the role of reproductive tract infections.
5. Boerma, J. T., & Mgalla, Z. (2001). *Women and infertility in sub-Saharan Africa: a multi-disciplinary perspective*. Royal Tropical Institute, KIT Publishers.
6. Roupa, Z., Polikandrioti, M., Sotiropoulou, P., Faros, E., Koulouri, A., Wozniak, G., & Gourni, M. (2009). Causes of infertility in women at reproductive age. *Health Science Journal*, *3*(2).
7. Update, H. R., & ESHRE Capri Workshop Group. (2010). Europe the continent with the lowest fertility.
8. Kupka, M. S., Ferraretti, A. P., De Mouzon, J., Erb, K., D'Hooghe, T., Castilla, J. A., ... & Kreuz-Kinderwunschzentrum, S. P. G. (2014). Assisted reproductive technology in Europe, 2010: results generated from European registers by ESHRE. *Human reproduction*, *29*(10), 2099-2113.
9. Sobotka, T. (2004). Is lowest-low fertility in Europe explained by the postponement of childbearing?. *Population and development review*, *30*(2), 195-220.
10. Reuss, M. L., Kline, J., Santos, R., Levin, B., & Timor-Tritsch, I. (1996). Age and the ovarian follicle pool assessed with transvaginal ultrasonography. *American journal of obstetrics and gynecology*, *174*(2), 624-627.
11. De Bruin, J. P., Dorland, M., Spek, E. R., Posthuma, G., Van Haaften, M., Looman, C. W. N., & Te Velde, E. R. (2004). Age-related changes in the ultrastructure of the resting follicle pool in human ovaries. *Biology of Reproduction*, *70*(2), 419-424.
12. Rosenthal, M. S. (1995). *The fertility sourcebook: everything you need to know*. Lowell House.
13. Whitman-Elia, G. F., & Baxley, E. G. (2001). A primary care approach to the infertile couple. *J Am Board Fam Pract*, *14*(1), 33-45.
14. A. Andersen *et al.*, "Assisted reproductive technology in europe, 2004: results generated from european registers by eshre," *Human reproduction (Oxford, England)*, vol. 23, no. 4, pp. 756–771, 2008
15. Chambers, G. M., Sullivan, E. A., Ishihara, O., Chapman, M. G., & Adamson, G. D. (2009). The economic impact of assisted reproductive technology: a review of selected developed countries. *Fertility and sterility*, *91*(6), 2281-2294.
16. Connolly, M. P., Hoorens, S., & Chambers, G. M. (2010). The costs and consequences of assisted reproductive technology: an economic perspective. *Human reproduction update*, *16*(6), 603-613.
17. Andersen, A.N., et al., *Assisted reproductive technology in Europe, 2004: results generated from European registers by ESHRE*. Human reproduction (Oxford, England), 2008. **23**(4): p. 756-771.
18. Baram, D., et al., *Psychosocial adjustment following unsuccessful in vitro fertilization*. Journal of Psychosomatic Obstetrics & Gynecology, 1988. **9**(3): p. 181-190.
19. Hynes, G.J., et al., *The psychological well-being of infertile women after a failed IVF attempt: The effects of coping*. British Journal of Medical Psychology, 1992. **65**(3): p. 269-278.
20. <https://www.mayoclinic.org/tests-procedures/in-vitro-fertilization/about/pac-20384716>
21. <https://americanpregnancy.org/infertility/in-vitro-fertilization/>
22. ESHRE Guideline Group on Good Practice in IVF Labs, De los Santos, M. J., Apter, S., Coticchio, G., Debrock, S., Lundin, K., ... & Woodward, B. (2016). Revised guidelines for good practice in IVF laboratories (2015). *Human Reproduction*, *31*(4), 685-686.

23. Restelli, L., Delle Noci, S., Mangiarini, A., Ferrari, S., Somigliana, E., & Paffoni, A. (2015). The impact of Alpha/ESHRE consensus regarding oocytes with aggregates of smooth endoplasmic reticulum (SERa) on in vitro fertilization outcome. *Journal of assisted reproduction and genetics*, 32(11), 1629-1635.
24. Fanchin, R. and J.M. Ayoubi, *Uterine dynamics: impact on the human reproduction process*. Reprod Biomed Online, 2009. **18 Suppl 2**: p. 57-62.
25. Fanchin, R., et al., *Uterine contractility decreases at the time of blastocyst transfers*. Hum Reprod, 2001. **16**(6): p. 1115-9.
26. Fanchin, R., et al., *Uterine contractions at the time of embryo transfer alter pregnancy rates after in-vitro fertilization*. Hum Reprod, 1998. **13**(7): p. 1968-74.
27. Lesny, P., et al., *Junctional zone contractions and embryo transfer: is it safe to use a tenaculum?* Hum Reprod, 1999. **14**(9): p. 2367-70.
28. PUSEY, J., et al., *Myometrial Activity and the Distribution of Blastocysts in the Uterus of the Rat: Interference by Relaxin*. Biology of Reproduction, 1980. **23**(2): p. 394-397.
29. IJland, M.M., et al., *Endometrial wave direction switch and the outcome of in vitro fertilization*. Fertil Steril, 1999. **71**(3): p. 476-81.
30. Lesny, P., et al., *Ultrasound evaluation of the uterine zonal anatomy during in- vitro fertilization and embryo transfer*. Hum Reprod, 1999. **14**(6): p. 1593-8.
31. Mansour, R.T., et al., *Dummy embryo transfer using methylene blue dye*. Hum Reprod, 1994. **9**(7): p. 1257-9.
32. Poindexter, A.N., 3rd, et al., *Residual embryos in failed embryo transfer*. Fertil Steril, 1986. **46**(2): p. 262-7.
33. Rogers, P.A.W., et al., *Effects of relaxin on the intrauterine distribution and antimesometrial positioning and orientation of rat blastocysts before implantation*. Journal of Reproduction and Fertility, 1983. **68**(2): p. 431-435.
34. Pierzynski, P., T.M. Reinheimer, and W. Kuczynski, *Oxytocin antagonists may improve infertility treatment*. Fertil Steril, 2007. **88**(1): p. 213 e19-22.
35. Pierzynski, P., *Oxytocin and vasopressin V(1A) receptors as new therapeutic targets in assisted reproduction*. Reprod Biomed Online, 2011. **22**(1): p. 9-16.
36. Moraloglu, O., et al., *Treatment with oxytocin antagonists before embryo transfer may increase implantation rates after IVF*. Reproductive biomedicine online, 2010. **21**(3): p. 338-343.
37. Heger, A., Sator, M., & Pietrowski, D. (2012). Endometrial receptivity and its predictive value for IVF/ICSI-outcome. *Geburtshilfe und Frauenheilkunde*, 72(08), 710-715.
38. Chakravarti, S. U. D. I. P., & Kushtagi, P. (2015). *Manual of Obstetrics E-book*. Elsevier Health Sciences.
39. D'Amico, D., & Barbarito, C. (2007). *Health & physical assessment in nursing*. Pearson Education.
40. Tortora, G. J., & Derrickson, B. (2017). *Principles of anatomy & physiology*. John Wiley & Sons, Incorporated.
41. Keane, C. B., & Miller, B. F. (1992). *Encyclopedia and dictionary of medicine, nursing, and allied health*. Saunders.
42. Aguilar, H. N., & Mitchell, B. F. (2010). Physiological pathways and molecular mechanisms regulating uterine contractility. *Human reproduction update*, 16(6), 725-744.
43. Hall, J. E. (2010). *Guyton and Hall Textbook of Medical Physiology E-Book: with STUDENT CONSULT Online Access*. Elsevier Health Sciences.
44. Al Otaibi, M. (2014). The physiological mechanism of uterine contraction with emphasis on calcium ion. *Calcium Signaling*, 1(2), 101-119.
45. Word, R. A. (1995, February). Myosin phosphorylation and the control of myometrial contraction/relaxation. In *Seminars in perinatology* (Vol. 19, No. 1, pp. 3-14). WB Saunders.
46. <https://courses.kcumb.edu/physio/smoothmuscle/ecccoupling.htm>
47. Khan, R. N., Matharoo-Ball, B., Arulkumaran, S., & Ashford, M. L. (2001). Potassium channels in the human myometrium. *Experimental physiology*, 86(2), 255-264.

48. Zheng, H., Park, K. S., Koh, S. D., & Sanders, K. M. (2014). Expression and function of a T-type Ca²⁺ conductance in interstitial cells of Cajal of the murine small intestine. *American Journal of Physiology-Cell Physiology*, 306(7), C705-C713.
49. Johnston, L., Woolsey, S., Cunningham, R. M., O'kane, H., Duggan, B., Keane, P., & McCloskey, K. D. (2010). Morphological expression of KIT positive interstitial cells of Cajal in human bladder. *The Journal of urology*, 184(1), 370-377.
50. Kuijsters, N. P. M., Methorst, W. G., Kortenhorst, M. S. Q., Rabotti, C., Mischi, M., & Schoot, B. C. (2017). Uterine peristalsis and fertility: current knowledge and future perspectives: a review and meta-analysis. *Reproductive biomedicine online*, 35(1), 50-71.
51. Young, R. C. (2007). Myocytes, myometrium, and uterine contractions. *Annals of the new york academy of sciences*, 1101(1), 72-84.
52. Sanborn, B. M. (2000). Relationship of ion channel activity to control of myometrial calcium. *Journal of the Society for Gynecologic Investigation*, 7(1), 4-11.
53. Duquette, R. A., Shmygol, A., Vaillant, C., Mobasheri, A., Pope, M., Burdyga, T., & Wray, S. (2005). Vimentin-positive, c-kit-negative interstitial cells in human and rat uterus: a role in pacemaking?. *Biology of reproduction*, 72(2), 276-283.
54. Cretoi, S., Simionescu, A., Caravia, L., Curici, A., Cretoi, D., & Popescu, L. (2011). Complex effects of imatinib on spontaneous and oxytocin-induced contractions in human non-pregnant myometrium. *Acta physiologica Hungarica*, 98(3), 329-338.
55. Kunz, G., Beil, D., Deininger, H., Wildt, L. & Leyendecker, G. The dynamics of rapid sperm transport through the female genital tract: evidence from vaginal sonography of uterine peristalsis and hysterosalpingoscintigraphy. *Hum.Reprod.* **11**, 627–632 (1996).
56. Pusey, J., Kelly, W. A., Bradshaw, J. M. & Porter, D. G. Myometrial activity and the distribution of blastocysts in the uterus of the rat: interference by relaxin. *Biol Reprod* **23**, 394–397 (1980).
57. Bulletti, C. *et al.* Uterine contractility during the menstrual cycle. *Hum.Reprod.* **15 Suppl 1**, 81–89 (2000).
58. Kunz, G., Noe, M., Herberth, M. & Leyendecker, G. Uterine peristalsis during the follicular phase of the menstrual cycle: effects of oestrogen, antioestrogen and oxytocin. *Hum.Reprod.Update.* **4**, 647–654 (1998).
59. Ziegler, D., Bulletti, C., Fanchin, R., Epiney, M., & BRIOSCHI, P. A. (2001). Contractility of the nonpregnant uterus. *Annals of the New York Academy of Sciences*, 943(1), 172-184.
60. <https://medium.com/@bicspuc/menstrual-cycle-an-important-process-of-human-reproduction-e22a4abc2e2>
61. Oike, K., Ishihara, K. & Kikuchi, S. A study on the endometrial movement and serum hormonal level in connection with uterine contraction. *Nihon Sanka Fujinka Gakkai Zasshi* **42**, 86–92 (1990).
62. Bulletti, C., DE ZIEGLER, D. O. M. I. N. I. Q. U. E., Rossi, S., Polli, V., Massoneau, M., Rossi, E., ... & Flamigni, C. (1997). Abnormal uterine contractility in nonpregnant women. *Annals of the New York Academy of Sciences*, 828(1), 223-229.
63. Bulletti, C., Prefetto, R. A., Bazzocchi, G., Romero, R., Mimmi, P., Polli, V., ... & Flamigni, C. (1993). Physiology: Electromechanical activities of human uteri during extra-corporeal perfusion with ovarian steroids. *Human Reproduction*, 8(10), 1558-1563.
64. Campo, S., Campo, V., & Benagiano, G. (2012). Adenomyosis and infertility. *Reproductive biomedicine online*, 24(1), 35-46.
65. Leyendecker, G., Kunz, G., Wildt, L., Beil, D., & Deininger, H. (1996). Uterine hyperperistalsis and dysperistalsis as dysfunctions of the mechanism of rapid sperm transport in patients with endometriosis and infertility. *Human reproduction*, 11(7), 1542-1551.
66. Eldar-Geva, T., Meagher, S., Healy, D. L., MacLachlan, V., Breheny, S., & Wood, C. (1998). Effect of intramural, subserosal, and submucosal uterine fibroids on the outcome of assisted reproductive technology treatment. *Fertility and sterility*, 70(4), 687-691.

67. Healy, D. L. (2000). Impact of uterine fibroids on ART outcome. *Environmental health perspectives*, 845-847.
68. Orisaka, M., Kurokawa, T., Shukunami, K. I., Orisaka, S., Fukuda, M. T., Shinagawa, A., ... & Kotsuji, F. (2007). A comparison of uterine peristalsis in women with normal uteri and uterine leiomyoma by cine magnetic resonance imaging. *European Journal of Obstetrics & Gynecology and Reproductive Biology*, 135(1), 111-115.
69. PUSEY, J., et al., Myometrial Activity and the Distribution of Blastocysts in the Uterus of the Rat: Interference by Relaxin. *Biology of Reproduction*, 1980. 23(2): p. 394-397.
70. IJland, M.M., et al., Endometrial wave direction switch and the outcome of in vitro fertilization. *Fertil Steril*, 1999. 71(3): p. 476-81.
71. Lesny, P., et al., Ultrasound evaluation of the uterine zonal anatomy during in-vitro fertilization and embryo transfer. *Hum Reprod*, 1999. 14(6): p. 1593-8.
72. Mansour, R.T., et al., Dummy embryo transfer using methylene blue dye. *Hum Reprod*, 1994. 9(7): p. 1257-9.
73. Martinez-Gaudio, M., T. Yoshida, and L.P. Bengtsson, Propagated and nonpropagated myometrial contractions in normal menstrual cycles. *Am J Obstet Gynecol*, 1973. 115(1): p. 107-11.
74. Lyons, E.A., et al., Characterization of subendometrial myometrial contractions throughout the menstrual cycle in normal fertile women. *Fertil Steril*, 1991. 55(4): p. 771-4.
75. Bulletti, C. and D. de Ziegler, Uterine contractility and embryo implantation. *Curr Opin Obstet Gynecol*, 2006. 18(4): p. 473-84.
76. Kido, A., & Togashi, K. (2016). Uterine anatomy and function on cine magnetic resonance imaging. *Reproductive medicine and biology*, 15(4), 191-199.
77. IJland, M. M., Hoogland, H. J., Dunselman, G. A., Lo, C. R., & Evers, J. L. (1999). Endometrial wave direction switch and the outcome of in vitro fertilization. *Fertility and sterility*, 71(3), 476-481.
78. IJland, M. M., Evers, J. L., Dunselman, G. A., & Hoogland, H. J. (1996). Subendometrial contractions in the nonpregnant uterus: an ultrasound study. *European Journal of Obstetrics & Gynecology and Reproductive Biology*, 70(1), 23-24.
79. Finberg, H.J., *Whither (Wither?) the Ultrasound Specialist?* *Journal of Ultrasound in Medicine*, 2004. 23(12): p. 1543-1547.
80. Solomon, M.J., et al., *Reliability and validity studies of endoluminal ultrasonography for anorectal disorders*. *Diseases of the Colon & Rectum*, 1994. 37(6): p. 546-551.
81. Rabotti, C., de Lau, H., Haazen, N., Oei, G., & Mischi, M. (2013, July). Ultrasound analysis of the uterine wall movement for improved electrohysterographic measurement and modeling. In *2013 35th Annual International Conference of the IEEE Engineering in Medicine and Biology Society (EMBC)* (pp. 7436-7439). IEEE.
82. Domino, M., Pawlinski, B., & Gajewski, Z. (2016). The linear synchronization measures of uterine EMG signals: Evidence of synchronized action potentials during propagation. *Theriogenology*, 86(8), 1873-1878.
83. Woliński, J., Ziecik, A., Gajewski, Z., Korczyński, W., & Zabielski, R. (2003). A method of recording oviduct and uterine myoelectrical activity in gilts using implantable telemetry. *Journal of Animal and Feed Sciences*, 12(2), 359-368.
84. Tojo, S., Fukunishi, H., Tsuchihashi, T., Shimura, T., Mikami, K., & Kaku, H. (1975). Electrical activity recorded from ovarian tissue in perfused human utero-tubo-ovarian unit. *Reproduction*, 44(3), 587-589.
85. Buhimschi, C., & Garfield, R. E. (1996). Uterine contractility as assessed by abdominal surface recording of electromyographic activity in rats during pregnancy. *American journal of obstetrics and gynecology*, 174(2), 744-753.
86. Kao, C. Y. (1959). Long-term observations of spontaneous electrical activity of the uterine smooth muscle. *American Journal of Physiology-Legacy Content*, 196(2), 343-350.
87. Parkington, H. C., Tonta, M. A., Brennecke, S. P., & Coleman, H. A. (1999). Contractile activity, membrane potential, and cytoplasmic calcium in human uterine smooth muscle in the third

- trimester of pregnancy and during labor. *American journal of obstetrics and gynecology*, 181(6), 1445-1451.
88. Ye-Lin, Y., Alberola-Rubio, J. O. S. É., Prats-boluda, G., Perales, A., Desantes, D., & Garcia-Casado, J. (2015). Feasibility and analysis of bipolar concentric recording of electrohysterogram with flexible active electrode. *Annals of biomedical engineering*, 43(4), 968-976.
 89. de Lau, H., Rabotti, C., Bijloo, R., Rooijackers, M. J., Mischi, M., & Oei, S. (2013). Automated conduction velocity analysis in the electrohysterogram for prediction of imminent delivery: a preliminary study. *Computational and mathematical methods in medicine*, 2013.
 90. de Lau, H., Rabotti, C., Oosterbaan, H. P., Mischi, M., & Oei, G. S. (2014). Study protocol: PoPE- Prediction of preterm delivery by electrohysterography. *BMC pregnancy and childbirth*, 14(1), 192.
 91. Rabotti, C., Mischi, M., Oei, S. G., & Bergmans, J. W. (2010). Noninvasive estimation of the electrohysterographic action-potential conduction velocity. *IEEE Transactions on Biomedical Engineering*, 57(9), 2178-2187.
 92. Lucovnik, M., Maner, W. L., Chambliss, L. R., Blumrick, R., Balducci, J., Novak-Antolic, Z., & Garfield, R. E. (2011). Noninvasive uterine electromyography for prediction of preterm delivery. *American journal of obstetrics and gynecology*, 204(3), 228-e1.
 93. Rabotti, C., Mischi, M., van Laar, J. O., Oei, G. S., & Bergmans, J. W. (2008). Estimation of internal uterine pressure by joint amplitude and frequency analysis of electrohysterographic signals. *Physiological Measurement*, 29(7), 829.
 94. Rabotti, C., & Mischi, M. (2015). Propagation of electrical activity in uterine muscle during pregnancy: a review. *Acta Physiologica*, 213(2), 406-416.
 95. Garcia-Casado, J., Ye-Lin, Y., Prats-Boluda, G., Mas-Cabo, J., Alberola-Rubio, J., & Perales, A. (2018). Electrohysterography in the diagnosis of preterm birth: a review. *Physiological measurement*, 39(2), 02TR01.
 96. Alberola-Rubio, J., Garcia-Casado, J., Prats-Boluda, G., Ye-Lin, Y., Desantes, D., Valero, J., & Perales, A. (2017). Prediction of labor onset type: Spontaneous vs induced; role of electrohysterography?. *Computer methods and programs in biomedicine*, 144, 127-133.

Part I

Electrohysterography in the non-pregnant
human uterus

2

PROPAGATION OF SPONTANEOUS ELECTRICAL ACTIVITY IN THE EX-VIVO HUMAN UTERUS

Abstract: *Contractions of the non-pregnant uterus play a key role in fertility. Yet, the electrophysiology underlying these contractions is poorly understood. In this paper, we investigate the presence of uterine electrical activity and characterize its propagation in five unstimulated ex-vivo human uteri. Multichannel electrohysterographic measurements were performed internally and externally up to 24 hours after hysterectomy and compared to control. Up to 2 hours after hysterectomy, we measured biopotentials in all included uteri, with amplitudes significantly higher than control. The signal amplitude decreased significantly over time and, after 24 hours, was comparable to control. The measured biopotentials propagated following both a plane wave as well as an erratic pattern. No clear pacemaker location nor a preferred propagation direction could be identified. These results show that ex-vivo uteri can spontaneously initiate propagating biopotentials, and provide a fundamental step towards understanding of the electrophysiology of the human non-pregnant uterus.*

From: N. P.M. Kuijsters, **F. Sammali**, X. Ye, C. Blank, L. Xu, M. Mischi, B. C. Schoot, and C. Rabotti, **“Propagation of spontaneous electrical activity in the ex-vivo human uterus”**. Submitted to *Nature Scientific Reports*.

2.1 INTRODUCTION

Similar to other smooth-muscle organs, the uterus is able to spontaneously contract. While the contractile activity of the uterus is mostly known for its role in the expulsion of the foetus during labour at the end of pregnancy, it also contracts throughout the menstrual cycle of women in their fertile age¹. Inspired by ultrasonographic observations, during the menstrual cycle uterine activity is mostly referred to as uterine peristalsis.

There is strong evidence that uterine peristalsis plays a role in fertility, either positive, providing transportation of gametes², or negative, by interfering with proper implantation of the embryo³. The function of uterine peristalsis has therefore been investigated to understand its role in fertility treatments and possibly develop techniques to monitor or even modulate uterine peristalsis³⁻⁶. However, fundamental aspects of the physiology underlying uterine peristalsis remain unclear.

Smooth muscle contractions are invariably initiated by the presence of biopotentials propagating at the cell level. The uterus is provided with sympathetic and parasympathetic innervation. Nevertheless, previous studies demonstrated the ability of the uterus to initiate contractions spontaneously, even when disconnected from the nervous system^{7,8}. This suggests that uterine electrical activity is initiated by an intrinsic source with its own pace-making units. It is hypothesized that specialized cells found in the myometrium of both animals and humans, called Interstitial Cajal-like cells (ICLCs), are involved in this self-initiating mechanism⁹; though, up to now their role remains unsettled. A thorough characterization of the generation and propagation of biopotentials in the non-pregnant uterus may be crucial to advance the basic knowledge of uterine peristalsis and possibly unveil the great potential of contraction management for improving fertility.

In general, studies on the electrical activity of the non-pregnant human uterus are scarce^{8,10}. On the contrary, significant advances have been reported on the characterization of uterine electrical activity in pregnant uteri by abdominal electrohysterography (EHG)¹¹⁻¹⁶. All these studies, aiming at improving labour monitoring and preterm delivery prediction, report patterns of cyclic bursts of biopotentials alternating, in time, with quiescent periods^{17,18}. Spatially, the results of dedicated investigations exclude the existence of a preferred origin and direction of biopotential propagation, and support the validity of both erratic as well as plane-wave propagation patterns¹⁹.

Clearly, a direct translation of the observations derived during pregnancy to the non-pregnant uterus is unfeasible. Moreover, *in-vivo* characterization of the biopotentials of the non-pregnant human uterus by EHG is severely hampered by challenges related, for example, to the small size of the uterus, the distance between the external electrodes and the uterus, and the interference of other organs. These anatomical constraints contribute to a deterioration of the signal-to-noise ratio, complicating the propagation analysis of such unpredictable signals as uterine biopotentials.

Ex-vivo investigations on the intact organ combined with the use of multichannel measurement of the biopotentials are expected to overcome the limitations imposed by *in-vivo*

measurements while substantially advancing current understanding of biopotential propagation in the non-pregnant uterus.

Previous *ex-vivo* studies evaluating contractions on the complete non-pregnant human uterus used extracorporeal perfusion to test the effect of pharmaceuticals on uterine contractility and are mainly based on intra-uterine pressure measurements^{8,10,20,21}. Attempts at measuring biopotentials can be found in two studies^{8,10}, in which observations are limited to a single location in the uterus. Only one study eventually measured biopotentials using a single needle placed at the utero-tubal junction¹⁰, while the other could not measure any electrical activity using 2 bipolar Ag/AgCl electrodes inserted into the uterine wall⁸. No literature is available on the propagation of biopotentials in the non-pregnant human uterus.

In this study, we investigated spontaneous biopotentials in complete non-pregnant human uteri *ex vivo*, using multichannel EHG measurements on five resected uteri from women aged between 35 and 44 years old (Table 2.1). EHG measurements were simultaneously performed externally on the uterine surface using a high-density grid of 64 Ag/AgCl electrodes, and inside the uterine cavity by an array of eight platinum electrodes mounted on a silicon catheter (Figure 2.1). Due to the use of the internal array and a reference electrode for monopolar derivation, only 55 electrodes of the external grid were used. As a control, identical measurements were performed on chicken breast meat (commercial nutrition use) under the assumption that no biopotentials could be measured on this muscle. All uteri were measured directly after surgical removal (*T0*, 30-min duration), one hour after removal (*T1*, 15-min duration) and 2 hours after removal (*T2*, 15-min duration). One patient had an additional measurement 24 hours after removal (*T24*, 15-min duration).

Table 2.1: Patient characteristics and number of propagation events found per patient.

Patient	Age	Pathology found in uterus	Phase of the cycle	Number of propagation events	Erratic propagation events	Plane-wave propagation events
1	44	Leyomyoma Adenomyosis	Day 28, first cycle on progesterone treatment	6	6	0
2	44	Adenomyosis	Day 1, menstruation	18	1	17
3	48	Adenomyosis	Irregular cycle	11	10	1
4	35	Adenomyosis	Day 10, follicular phase	6	6	0
5	38	None	Day 7, follicular phase	10	10	0

In order to detect the presence of spontaneous biopotentials, both externally and internally, we evaluated the root mean squared (RMS) values of the EHG signal of the five uteri as compared to control. Furthermore, we investigated the EHG signal propagation. Under the assumption that propagating biopotentials are recorded as similar, delayed spikes at different locations, coherence was used as similarity measure to detect propagation. Finally, we focused on describing the observed propagation patterns qualitatively and quantitatively by estimating the propagation velocity by a validated maximum likelihood approach²².

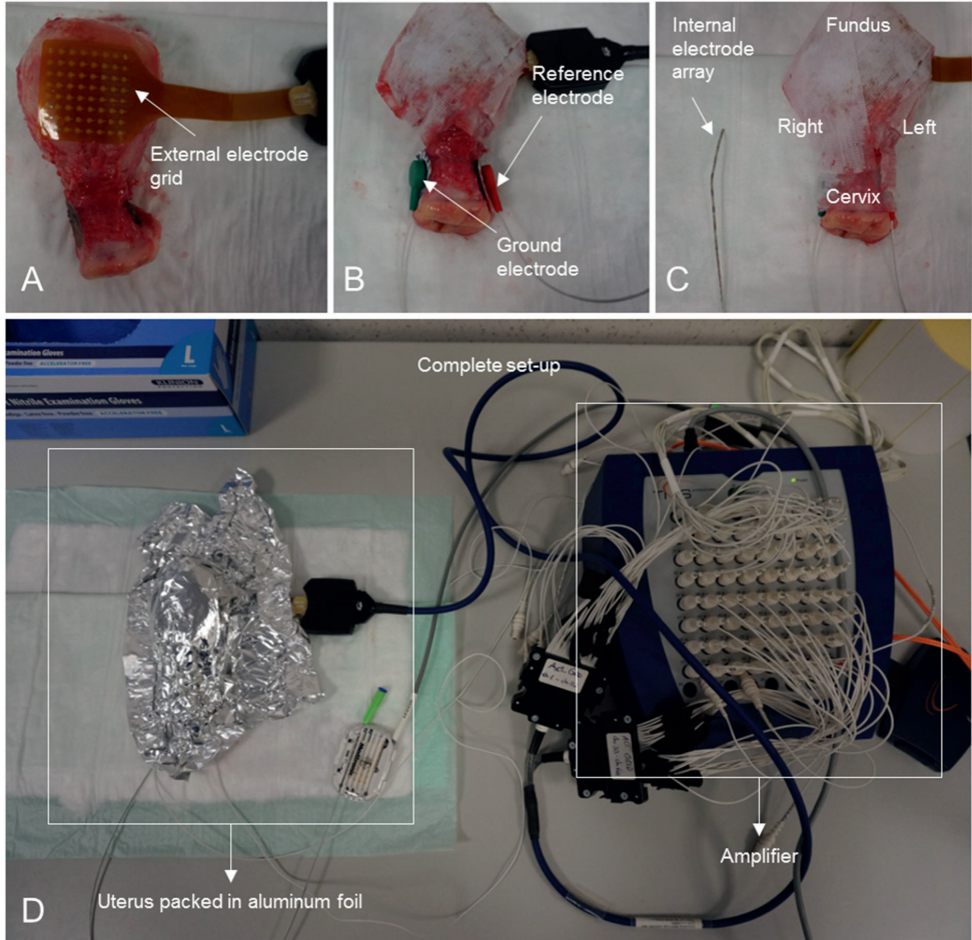


Figure 2.1: Measurement set-up.

A. The external grid is placed directly on the surface of the *ex-vivo* uterus and fixed using paper-based tape. Fifty-five channels of the grid are used for the analysis.

B. Two silver-based surface electrodes, representing the ground and reference electrode, are placed on the left and right side of the uterine cervix and fixed with paper-based tape.

C. The internal array with eight electrodes (shown next to the uterus for scale) is inserted into the uterine cavity.

D. All electrodes are connected to the amplifier for simultaneous recording and the uterus is wrapped in aluminium foil to keep moisture and avoid any deterioration of the electrical contact.

Take note: In order to avoid delays in the measurements, the pictures were taken after the experiment. This explains also the imprint of the silver electrodes which is visible in picture A.

Since a significant decrease in the RMS values of the measured biopotentials can be expected as a consequence of progressive tissue deterioration, the RMS values were also evaluated over time as additional evidence for the presence of electrical activity after resection.

2.2 RESULTS

2.2.1 Detection of biopotentials

The presence of electrical activity was detected by estimating the root mean square (RMS) value as indicator of the signal amplitude of the EHG signal recorded at T_0 by the external grid and the internal array. We calculated a median RMS of the 55 external grid channels for each uterus, after excluding the channels with poor contact (maximum 2 per grid). Medians between 3.95 μV (interquartile (IQ) range 2.41-14.18 μV) and 39.4 μV (IQ range 10.84-105.64 μV) were obtained for the external grid (Figure 2.2). Compared to control (median 1.69 μV , IQ range 1.13-3.11 μV), we found a significant difference in RMS values for all five uteri (p-values <0.05). The internal array showed median RMS values between 2.05 μV (IQ range 1.84-2.60 μV) and 4.83 μV (IQ range 3.62-14.23 μV), which were all significantly different from control (median 1.07 μV , IQ range 0.87-1.37 μV) with p-values <0.05.

Qualitatively, visual inspection of the individual channels revealed isolated spikes of biopotentials rather than clear bursts, with the exception of uterus number two, which showed distinct bursts (Figure 2.3). Propagation was detected in all five uteri (Table 2.1). A median of 10 propagation events (range 6-18) was observed per 30-min measurement.

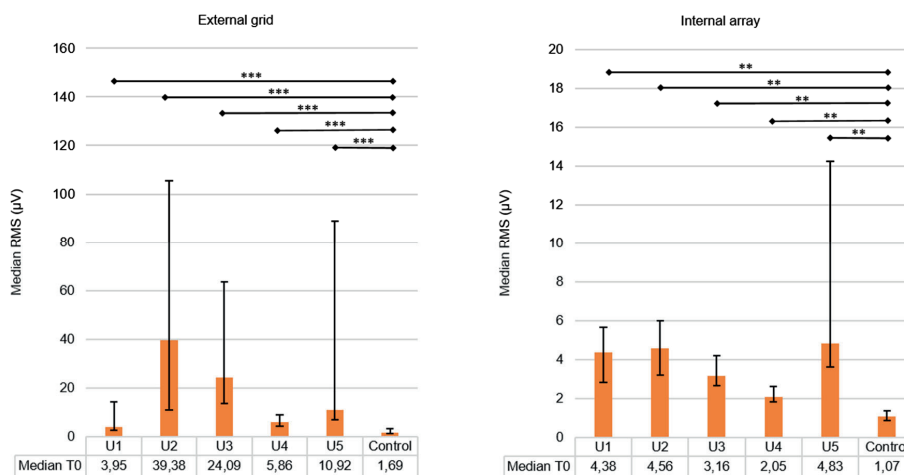


Figure 2.2: RMS values of each uterus (U1, U2, U3, U4, and U5) and the chicken breast meat (control) measured at T_0 . The results are expressed as median RMS of the signals of the external grid (55 signals per uterus) and the internal array (8 signals per uterus). The error bars represent the interquartile range. Significant difference with the control, tested with a Mann-Whitney U test (SPSS Inc., Chicago, IL, USA), are indicated by asterisks: *** p-value <0.001 and **p-value <0.01.

2.2.2 Characterization of biopotential propagation

In line with previous studies in pregnancy¹⁹, visual analysis of the propagating segments revealed the presence of both plane-wave propagation, i.e., wave fronts with a constant direction and velocity, and different events showing spikes with an erratic pattern, characterized by re-entries and circulation²³. Examples of plane-wave and erratic propagation are shown in Figure 2.4. In total, 18 plane-wave

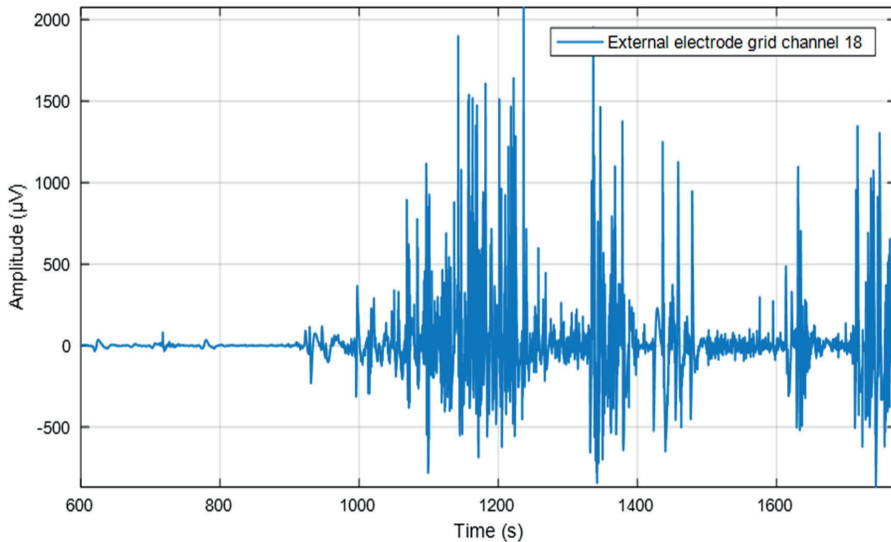


Figure 2.3: Example of a burst recorded from channel 18 of the external grid on uterus number two at T0.

propagation events were detected. Noteworthy, 17 out of 18 were detected in uterus number two and this uterus did not show any erratic propagation. No deviation in age, body-mass index, use of medication or operating time was found in patient number two relative to the other patients in the dataset. The only singularity of patient number two was that she was the only woman in the menses phase at the time of surgery. A total of 33 events of detected propagating spikes did not show plane-wave propagation.

For events showing plane-wave propagation, speed and direction of the conduction velocity vector were estimated using a maximum likelihood approach previously proposed for EHG analysis in pregnancy²². This resulted in a median speed of 3.5 mm/s (range 1.6-8.5 mm/s) in the 17 propagation events detected in uterus number two. Concerning the propagation direction, 58.8% of propagation events occurred from left to right, and 41.2% from fundus to cervix (upper to lower part of the uterus). We measured no event showing propagation right to left or cervix to fundus.

For the events showing erratic propagation, the peak value of every spike was used to estimate the inter-channel delay and define its propagation pattern. In most cases, no clear pattern was found and no delay could be calculated (Figure 2.5). In both plane-wave and erratic propagation events, we could not find a preferred pacemaker region and the location from which spikes originated varied over different events. Of the 18 plane wave propagation events detected externally, 10 also showed propagation on the internal array. An example is shown in Figure 2.6. The speed of the external signals was calculated along the uterine vertical axis and compared with the speed of the internal signals. A median speed equal to 3.4 mm/s was found externally, against a median speed equal to 6.15 mm/s internally. No correlation between the internal and external velocities was found (Pearson's correlation coefficient=0.018, $p=0.96$).

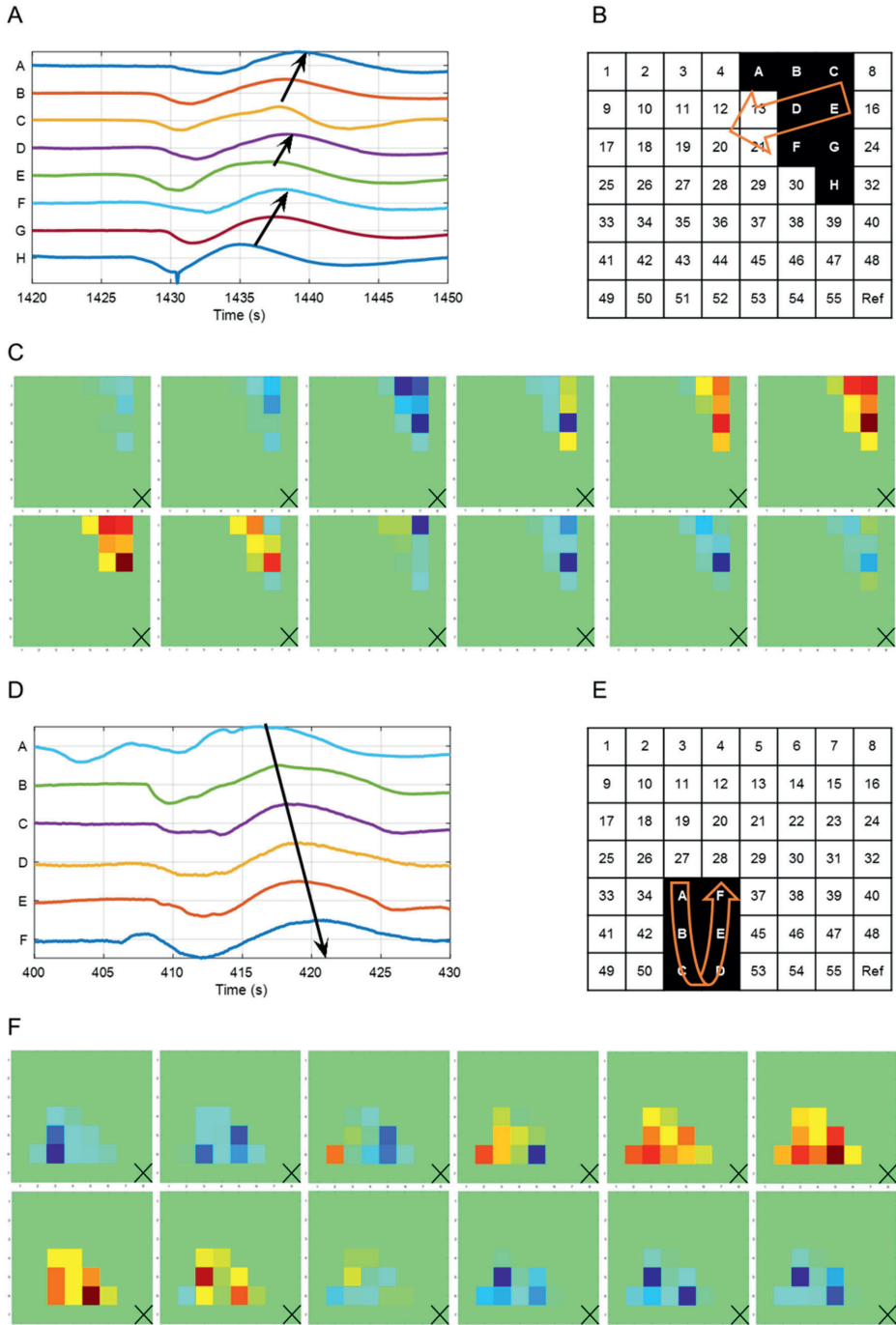


Figure 2.4: Example of plane-wave propagation and erratic propagation.

Figure 2.4 continued:

A: Example of a signal showing plane-wave propagation in uterus number two at T_0 , time interval 1420-1470 s. The signal propagates in time between channels C-B-A, E-D, and H-G-F.

B: Propagation of the signal in A, projected on the external grid. For this example, the propagation speed is 3.4 mm/s and the direction is shown by the orange arrow.

C: Signal shown in panel A, depicted as a colour map in time. Each block represents an electrode position of the external grid and the colours represent the signal amplitude. Red and blue correspond to a positive and negative signal, respectively (range -500 to 500 μV). The channels which do not show any propagation are set to a constant light green colour (0 μV). The selected time interval between each frame in the figure is 2 s (22 s shown in total).

D: Example of recirculation during an erratic propagation in uterus number three at T_0 , time interval 400-450 s. The signal propagates in time from channels A to F.

E: Propagation of the signal in D, projected on the external grid. For this example, the average propagation speed was 2.3 mm/s and the direction is shown by the orange arrow.

F: Signal shown in panel D, depicted as a colour map in time. Same properties as described in C.

1	2	3	4	5	6	7	8
9	10	11	12	13	14	15	16
17	18	19	→ 20	← 21	← 22	23	24
	↑	↓	↓	↓	↓		
25	← 26	→ 27	→ 28	29	30	31	32
	↑	↓	↓	↓	↓		
33	← 34	→ 35	← 36	→ 37	← 38	← 39	40
	↓	↑	↓	↑	↑		
41	42	→ 43	→ 44	← 45	→ 46	47	48
			↑	↓	↑		
49	50	51	52	→ 53	← 54	55	Ref

Figure 2.5: Example of erratic propagation in uterus number three at T_0 , time interval 200-250 s. The arrows show the direction of propagation between adjacent electrodes on the external grid. No clear propagation pattern can be observed.

2.2.3 Decay of biopotentials over time

Over time, the RMS values showed a decrease in most uteri. The median RMS of all external grid measurements at T_0 was 10.92 μV (IQ range 5.35-44.66 μV) and significantly differed from the median at T_1 (10.29 μV , IQ range 2.66-43.30 μV), T_2 (10.37, IQ range 2.37-34.04 μV) and T_{24} (1.27, IQ range 0.86-3.04), with p-values of 0.011, <0.001 and <0.001, respectively (Figure 2.7). T_1 and T_2 also differed significantly from T_{24} (both with p-values <0.001). There was no

significant difference between $T1$ and $T2$ ($p=0.250$). Like at $T0$, the RMS values of all uteri at $T1$ and $T2$ were significantly different ($p<0.05$) from control (median of $1.25 \mu\text{V}$, IQ range $0.91\text{--}2.58 \mu\text{V}$ at $T1$ and $1.14 \mu\text{V}$, IQ range $0.88\text{--}2.57 \mu\text{V}$ at $T2$). At $T24$ the RMS values were not significantly different from control at either $T0$, $T1$ or $T2$ ($p=0.125$, $p=0.837$, $p=0.922$, respectively). For the internal array measurements, the median RMS at $T0$ was 3.73

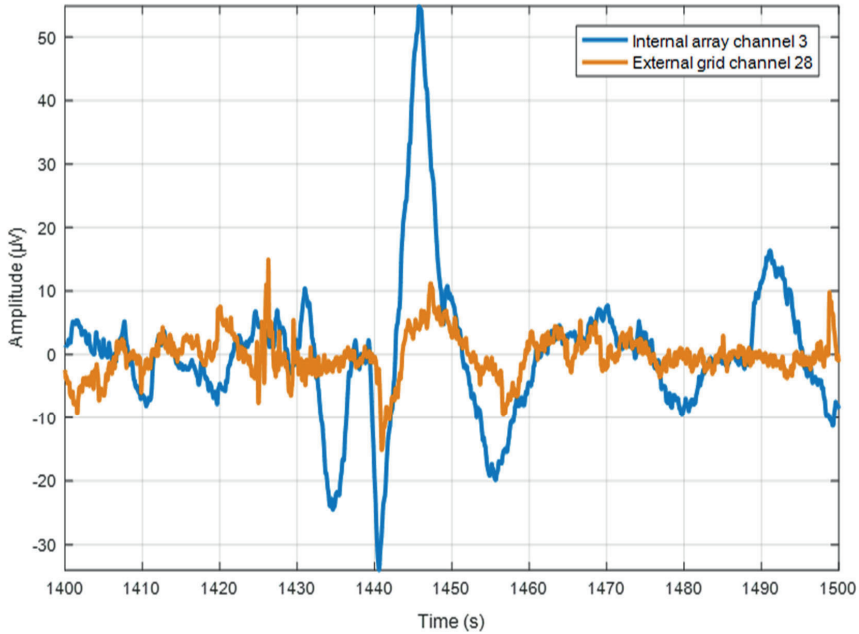


Figure 2.6: Example of simultaneous recordings of the external grid (orange) and internal array (blue) with comparable shapes.

μV (IQ range $2.63\text{--}4.83 \mu\text{V}$), which differed significantly from the median at $T2$ ($2.36 \mu\text{V}$, IQ range $1.96\text{--}3.49 \mu\text{V}$, $p=0.002$) and at $T24$ ($1.90 \mu\text{V}$, IQ range $0.95\text{--}2.77 \mu\text{V}$, $p<0.001$) but not from the median at $T1$ ($2.66 \mu\text{V}$, IQ range $1.93\text{--}4.32 \mu\text{V}$, $p=0.060$). Comparable with the external results, the values of both $T1$ and $T2$ differed significantly from $T24$ ($p=0.005$ and $p=0.041$, respectively). There was no significant difference between $T1$ and $T2$ ($p=0.226$). The RMS values of all uteri at $T1$ and $T2$ were significantly different (p -values <0.05) from control (median $0.65 \mu\text{V}$, IQ range $0.62\text{--}1.90 \mu\text{V}$ at $T1$ and median $0.73 \mu\text{V}$, IQ range $0.67\text{--}1.18 \mu\text{V}$ at $T2$). At $T24$ the RMS values were not significantly different from control at $T0$ and $T1$ ($p=0.165$ and $p=0.064$, respectively), but they were different from control at $T2$ ($p=0.011$).

For the time segments showing plane-wave propagation, we extended the propagation analysis to $T1$ and $T2$. We found that the number of propagation events per minute decreased ($T0=0.57/\text{min}$, $T1=0.33/\text{min}$, $T2=0.20/\text{min}$), but did all show plane-wave patterns, i.e., there was

no switch to erratic propagation. The mean speed ranged from 4.0 mm/s at T_0 to 13.6 mm/s at T_1 and 4.6 mm/s at T_2 .

No preferred direction was found at T_1 and T_2 , while at all events T_0 all propagated either from fundus to cervix (41.2%) or from left to right (58.8%).

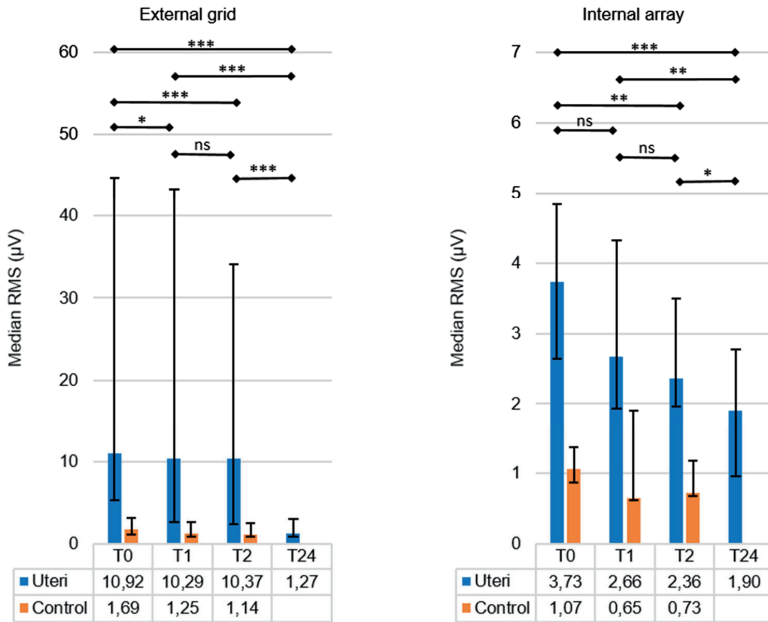


Figure 2.7: RMS values of all 5 uteri measured directly after surgery (T_0) and after one, two and twenty-four hours (T_1 , T_2 , and T_{24} , respectively) and of control (chicken breast meat) measured at T_0 , T_1 and T_2 . The results are expressed as medians of the signals of the external grid (5 uteri times 55 signals) and the internal array (5 uteri times 8 signals). The error bars represent the interquartile range. Statistically significant differences in time were tested using a generalized linear model (SPSS Inc., Chicago, IL, USA): * $p < 0.05$, ** $p < 0.01$, *** $p < 0.001$, ns = no significant difference. Although not depicted in this figure, the values at T_0 , T_1 and T_2 were significant different from the control (orange bars) in both the external grid and the internal array (Mann Whitney U test: p-value at least < 0.05).

2.3 DISCUSSION

To the best of our knowledge, this is the first study investigating the propagation of the biopotentials in *ex-vivo*, non-pregnant human uteri. Based on our results, spontaneous biopotentials can be measured and characterized on an unstimulated *ex-vivo* uterus. This conclusion is supported by two observations: significantly higher average RMS than control showing a decay over time, and the presence of propagation both internally and on the uterine surface.

Propagation events were found in all patients. Plane-wave propagations were almost exclusively and consistently observed in uterus number two. The only factor that distinguished patient number two from the others was the fact that she was menstruating at the time of the surgery. This suggests that the pattern of biopotentials is different in this specific phase of the menstrual cycle. Intra-uterine pressure measurements²⁴ also showed peculiar properties of uterine contractions during menses as opposed to the other phases of the cycle. During menses, contractions are typically described as “labour-like”, with low contraction frequency and high amplitude. In the other phases, “peristalsis-like” activity, with a high contraction frequency and a lower amplitude is mostly reported²⁴. Ultrasound studies suggest the outer two-third of the myometrium to be mostly involved in the contraction during menses²⁵⁻²⁷, while in the other phases contractions are concentrated in the inner third of the myometrium, the junctional zone^{25,28}. From the electrophysiological point of view, the fact that uterus number two was also the only one with a typical burst-like organization of electrical spikes suggests an additional link between menstruation and pregnancy, where slow and cyclic patterns of action potential bursts are typically measured by EHG¹⁹.

A direct comparison of our finding with the literature on non-pregnant uteri is complicated by the fact that previous studies mainly investigated the cine-mechanical properties of the uterus by ultrasound or pressure measurements as opposed to our study that focusses on electrophysiology. While the electrical and mechanical activity of muscles are closely related, a direct relationship for the non-pregnant uterus has not been described yet. Unfortunately, an additional intra-uterine pressure catheter could not be included in our measurement set-up as it would interfere with the internal array. In our preliminary study²⁹, ultrasound measurements using a transvaginal probe on the external surface of the unperfused *ex-vivo* uterus did not show any spontaneous mechanical activity. Based on the literature, even perfused *ex-vivo* uteri need some stimulations to show mechanical activity^{8,21,30}.

Like in the pregnant uterus¹⁹, we could not find any specific pacemaker region in this study. In the human uterus, ICLCs were found that are similar to the Cajal-cells which act as pace making cells in the gastro-intestinal tract³¹. Although histologic studies have shown spontaneous biopotentials in these uterine cells³² and spontaneous contractions in pregnant uterine tissue samples³³, there is no hard evidence that these cells have the same function as the Cajal-cells in the gastro-intestinal tract. The conduction velocities of plane-wave propagation in this study (range 1.6-8.5 mm/s) are in the absolute lower range of what is mentioned in the literature (range 1-520 mm/s)¹⁹ in both humans and animals. However, a direct comparison of speed values with literature is complicated by the fact that the reference figures are based on uteri in the pregnant or even labouring phase. Furthermore, little is known on the effects of organ resection and lack of perfusion on the characteristics of electrical propagation. Only a very weak correlation could be found between the internal and external propagation properties.

A certain level of disagreement was evident also in the amplitude of the internal and external signals. This discordance might be partially explained by the complex architecture of the uterus. The myometrium consists of multiple muscle layers with different fibre orientation (and possibly different function and embryologic origin)³⁴, which could result in different conduction properties of the electrical activity in the inner and outer layers. The effect of the different

geometry, material and type of sensors employed internally and externally may also explain the observed weak correlation.

Over time, we measured a decrease in the global amplitude of the biopotentials; this decrease was significant only between $T0$ and $T1$. This decrease could be associated to progressive deterioration of the organ tissue. Up to two hours after resection, we still found a significantly different RMS value relative to control, which we did not find after 24 hours. Histological studies, focussing on uterine preservation in a transplantation setting, illustrated that the unpreserved uterus shows severe deterioration after twelve hours³⁵ and that warm ischemia of more than four hours already makes the uterus unsuitable for transplantation^{36,37}. This suggests that the five measured uteri were most probably 'electrically dead' and not able to produce any relevant biopotential after 24 hours.

To conclude, this study proves that spontaneous biopotentials can be measured in the non-pregnant human uterus *ex vivo* and that the organ remains electrically active for at least two hours after surgical resection. In this time frame, electrical propagation can be measured and characterized, possibly providing novel insights into the physiology of this organ. In particular, this study supports the theory that the uterus is an organ with autonomic initiation and, in line with qualitative *in-vivo* studies^{24,38}, highlights the peculiarity of the menstrual phase. These results may pave the way for future studies aiming at a better understanding of the complex (electro-)physiology of the non-pregnant uterus, contributing to future diagnostics and treatment involving monitoring and management of uterine contractions, e.g. to improve fecundability.

2.4 METHODS

2.4.1 Subjects

Five human uteri were included in this study. Patients were eligible if they were prescribed to undergo a hysterectomy for benign pathology and were premenopausal (for details see Table 1). Standard laparoscopic hysterectomy procedures were performed on all uteri. Exclusion criteria included any risk of malignancy and pathologies such that the uterus could not be resected in one piece. The day of the menstrual cycle was recorded by anamnestic means.

2.4.2 Ethical statement

This study was approved by the medical ethical committee of the Catharina Hospital Eindhoven (MEC-U approval number NL52466.100.15). The research is part of the WAVES study registered under the Dutch Trial Register number NTR5264. Written informed consent was given by each participant prior to using their uteri for this observational study. The study was conducted according to the WMA Declaration of Helsinki: Ethical Principles for Medical Research Involving Human Subjects³⁹

2.4.3 Measurement set-up

Directly after resection (approximately 20-30 min after eliminating blood supply), the uteri were incorporated into the measurement set-up. Room temperature was kept constant at 21°C. No preservative measures were used for the resected organs.

Two-dimensional electrode grids are needed for a complete characterization of the propagating waves, as the a-priori origin and direction are unknown. We placed a high-density 64-electrode grid (TMSi, Oldenzaal, Netherlands) directly on the external surface of the resected organ. Each of its circular Ag/AgCl electrodes (2-mm diameter) is printed on the flexible grid following a regular, two-dimensional pattern with 4-mm centre to centre inter-electrode distance, covering a total 36x36-mm² area. The grid was positioned in the middle of the uterine body and held in place using medical tape. No adhesive sticker or conductive gel was employed as the uterine natural moisture functioned as a conductive layer. After sensor placement, the uterus was wrapped in aluminium foil to avoid evaporation and deterioration of the electrical contact of the grid with the tissue.

For internal measurements, a platinum octapolar electrode array (Pisces Plus lead model 3877, Medtronic, Minneapolis, MN, USA), normally used for spinal cord stimulation, was positioned inside the uterine cavity. Two circular 24-mm disposable surface EMG/ECG electrodes (Covidien, part of Medtronic, Minneapolis, MN, USA) were secured on the cervix with circular tape (Figure 1) and used as ground and reference, since electrical propagation in the uterus requires unipolar measurements¹⁹. The cervix was chosen as reference because it is assumed to be the most electrically neutral, as it does contain the least smooth muscle tissue⁴⁰.

All biopotentials were simultaneously recorded and digitized at 1024-Hz sampling frequency using a Refa 72 Amplifier (TMSi, Oldenzaal, Netherlands), connected to a laptop with Polybench 5 software (TMSi, Oldenzaal, Netherlands) for real-time visualization of the signals. Signal analysis was performed off-line using Matlab (The Mathworks® Inc., Natick, MA, USA).

2.4.4 Pre-processing

The acquired signals were first made unipolar by subtracting the common reference signal and then down-sampled from 1024 Hz to 32 Hz after proper antialiasing filtering. *In-vivo* EHG studies commonly use a filter range from 0.34 Hz to 1 Hz in order to avoid interference from signals produced by e.g. cardio-respiratory activity^{41,42}. In this study, an upper frequency limit of 5 Hz was chosen, as we expected no interferences and higher-frequency components when measuring directly on the uterus⁴³. For similar reasons, due to the absence of respiration artefacts and the low frequency content of EHG signals, a lower frequency limit of 0.05 Hz was used. The filter was implemented as a cascade of a low-pass and a high-pass 6th order Butterworth filters.

2.4.5 Signal amplitude estimation

Amplitude estimators such as the RMS value have been previously used to derive an estimate of EHG signal amplitude^{44,45}. The RMS value RMS_c of the discrete signal $x_c[n]$ recorded by channel c is calculated as follows:

$$\text{RMS}_c = \sqrt{\frac{1}{N} \sum_{n=1}^N |x_c[n]|^2} \quad (2.1)$$

where $x_c[n]$ is the down-sampled, filtered signal obtained from one single electrode of the grid, and N is the total number of time samples considered.

In this study, the RMS value was used as feature for two different objectives: to evaluate the signal amplitude of the recorded uteri in the first hour after removal as compared to control muscle (chicken meat) and to quantify the signal amplitude decay over time after surgical removal. In both cases, median and interquartile range of the RMS values of the signal in the external grid were used as features.

2.4.6 Propagation detection

At the cell level, uterine biopotentials have been reported to occur in groups (bursts)^{17,18,46}. However, propagation analysis of individual electrical spikes, i.e., the surface signal peaks associated to individual action potentials, has been proven more informative^{13,19}.

Both for the external grid and for the internal catheter, propagation analysis was therefore based on individual spikes selected by 50-s sliding windows (25-s overlap). Preliminary inspection of our data suggested such a time window to be optimal to isolate single spikes.

Based on the segmented signals, the first step aimed at identifying events of propagating spikes on the external grid. We identified propagation with the detection of spikes measured by N_p contiguous channels with a similar shape and a certain delay. In formulas, considering in the current 50-s time interval, the pre-processed discrete signals $x_{C1}(n)$, $x_{C2}(n)$, ..., $x_{CN_p}(n)$ ($n \in [1, 2, \dots, N]$) in the contiguous channels (by row, by column, or diagonally) $C1$, $C2$..., CN_p , respectively, are assumed to propagate when they satisfy the equations:

$$\begin{aligned} x_{C1}(n) &= s(n + \tau_1) + w_1(n) \\ x_{C2}(n) &= s(n + \tau_2) + w_2(n) \\ &\vdots \\ x_{CN_p}(n) &= s(n + \tau_{N_p}) + w_{N_p}(n). \end{aligned} \quad (2.2)$$

In (2.2), the same noise-free shape $s(n)$ is recorded by electrodes $C1, C2, \dots, CN_p$ with delays τ_1, τ_2 and τ_{N_p} after the addition of white Gaussian noise $w_1(n), w_2(n)$, and $w_{N_p}(n)$.

Considering the noise-free biopotential $s(n)$ propagating through a set of electrodes arranged in a grid composed of N_r rows and N_c columns (Figure 2.8), the plane-wave condition is satisfied when the measured signal $x_{rc}(n)$ at the channel (r, c) in the r^{th} row ($r \in [1, 2, \dots, N_r]$) and c^{th} column ($c \in [1, 2, \dots, N_c]$) can be modelled as

$$x_{rc}(n) = s(n - (r - 1)\tau_r - (c - 1)\tau_c) + w_{rc}(n) \quad (2.3)$$

i.e., the delay between adjacent rows and columns of electrodes, τ_r and τ_c , respectively, are constant throughout the electrode set. The noise present in the signal recorded by channel (r, c) , $w_{rc}(n)$, is assumed to be white and Gaussian with variance σ_{rc}^2 .

The aim of this first step was to register both the time segments and the electrode subset CN_p for which the propagation condition described in (2.2) could be considered valid on the external grid. To this end, coherence was chosen as the similarity feature.

Given two signals $x_{c1}(n)$ and $x_{c2}(n)$, the magnitude squared coherence is a real-valued function defined in the frequency domain, f , as

$$C_{x_{c1}x_{c2}}(f) = \frac{|G_{x_{c1}x_{c2}}(f)|^2}{G_{x_{c1}x_{c1}}(f)G_{x_{c2}x_{c2}}(f)}, \quad (2.4)$$

where $G_{x_{c1}x_{c2}}(f)$ is the cross-spectral density between x_{c1} and x_{c2} , and $G_{x_{c1}x_{c1}}(f)$ and $G_{x_{c2}x_{c2}}(f)$ the power spectral densities of x_{c1} and x_{c2} , respectively. The coherence function estimates the extent to which $x_{c2}(n)$ may be predicted from $x_{c1}(n)$ by an optimum linear least squares function. The magnitude squared coherence is not affected by time delays and reflects only the similarity between signal shapes. Values of coherence will always satisfy $0 \leq C_{x_{c1}x_{c2}}(f) \leq 1$.

For each 50-s time window, coherence was calculated among all available combinations of signal couples $x_{c1}(n)$ and $x_{c2}(n)$ using a Hamming window such that each signal was divided into eight overlapping (50%) segments. The maximum value of the coherence function in the frequency range between 0.05 and 5 Hz, which is the frequency band of interest given by the pre-processing filters, was used as similarity feature.

A value of maximum coherence equal to 0.75 was set as threshold to select the signals satisfying the condition in (2.2). Eventually, only time segments in which one or more channels had a high coherence with at least two other channels in different rows or columns were selected as propagating events. In fact, due to the *a-priori* unknown origin and direction of uterine biopotentials, a plane (3 points) is necessary for identification of the EHG two-dimensional

velocity vector. Those selected channels and time segments were then chosen for further analysis of the conduction velocity.

For biopotentials showing plane-wave propagation, i.e. satisfying (2.3), we searched for propagation in the internal array. Also in this case, the maximum of the coherence function and a value equal to 0.75 were chosen as the similarity feature and threshold, respectively. The internal and external velocity vectors identified according to the approach described in the following paragraph were then compared in the direction parallel to the internal array.

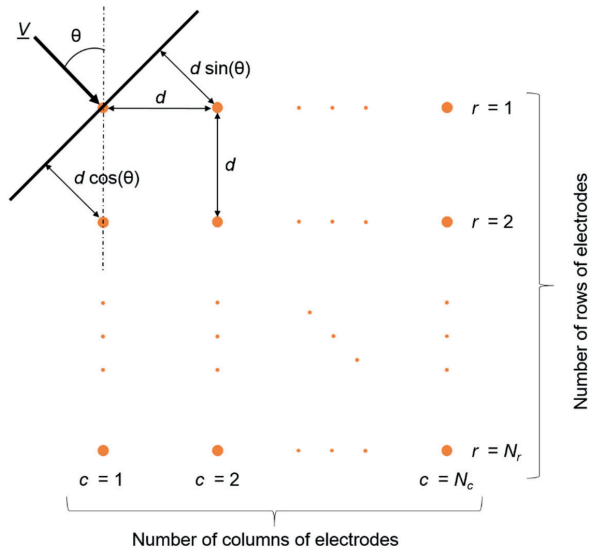


Figure 2.8: Schematic description of plane-wave propagation.

2.4.7 Conduction velocity

Visual analysis of the propagating segments revealed the presence of both events with plane-wave propagation, i.e., a wave front with a constant direction and speed as in (2.3), as well as erratic patterns characterized by re-entries and circulation²³. Characterization of propagation was carried out separately, depending on the validity of the plane-wave propagation conditions. For plane-wave propagation events, speed and direction of the conduction velocity were estimated using a maximum-likelihood approach previously proposed for EHG analysis in pregnancy²².

Based on the plane-wave condition in Equation 3, τ_r and τ_c can be estimated according to a maximum-likelihood approach and therefore by minimizing the cost function⁴⁷:

$$\epsilon^2(\tau_r, \tau_c) = \sum_{r=1}^{N_r} \sum_{c=1}^{N_c} \sum_{n=1}^N [x_{rc}(n) - s(n - (r-1)\tau_r - (c-1)\tau_c)]^2 \quad (2.5)$$

By using Parseval's equality, ϵ^2 can be transformed into the frequency domain, where τ_r and τ_c become continuous multiplicative factors of the phase and can be estimated without resolution limits.

Furthermore, the propagating biopotential, $s(n)$, can be estimated in the frequency domain as the weighted average of all channels, $X_{mp}(f)$ in row m and column p , after alignment. The resulting estimated cost function $\hat{\epsilon}^2(\tau_r, \tau_c)$ is:

$$\hat{\epsilon}^2(\tau_r, \tau_c) = \frac{2}{N} \sum_{r=1}^{N_r} \sum_{c=1}^{N_c} \sum_{f=1}^{N/2} \left[X_{rc}(f) - \frac{1}{N_r N_c} \sum_{m=1}^{N_r} \sum_{p=1}^{N_c} X_{mp}(f) e^{j2\pi f[(m-r)\tau_r + (p-c)\tau_c]} \right]^2 \quad (2.6)$$

where $X_{rc}(f)$ is the Discrete Fourier Transform (DFT) of the signal recorded by the channel in row r and column c . For electrode distance equal to d and temporal-sampling frequency f_s , the speed v and angle θ can be computed by the relations:

$$\tau_r = \frac{f_s d \cos(\theta)}{v} \quad (2.7)$$

$$\tau_c = \frac{f_s d \sin(\theta)}{v} \quad (2.8)$$

2.4.8 Statistical analysis

In order to assess the statistical significance of our findings, SPSS statistics 23 (SPSS Inc., Chicago, IL, USA), was used. The Shapiro Wilk test showed that our RMS data, both from the external grid and the internal array, were not Gaussian distributed. RMS data were presented as the median and the interquartile range. To compare each individual uterus ($n=5$) with control ($n=1$), we used a Mann-Whitney U test for non-Gaussian data. To assess the significance of the RMS decay in time we used a generalized linear model for repeated measures⁴⁸ comparing the RMS total data of all five uteri at each time (T). This model assumes that the input data is Gaussian distributed. By logarithmic transformation of our data, the requirements for a Gaussian

distribution (skewness and kurtosis values between -1 and +1) were met. To evaluate the correlation between the propagation speed obtained by internal and external recordings, Spearman's rank correlation coefficient test was used. The level of statistical significance was set at $p < 0.05$ for all tests used.

2.4.9 Data Availability

The datasets generated and analysed during the current study are available from the corresponding author on reasonable request.

2.5 ACKNOWLEDGEMENTS

We thank Michelle Hendrikx MD and Marinella Maragno MSc. For their assistance during the *ex-vivo* measurements.

BIBLIOGRAPHY

1. Kuijsters, N. P. M. *et al.* Uterine peristalsis and fertility: current knowledge and future perspectives: a review and meta-analysis. *Reprod. Biomed. Online* **35**, 50–71 (2017).
2. Kunz, G., Beil, D., Deininger, H., Wildt, L. & Leyendecker, G. The dynamics of rapid sperm transport through the female genital tract: evidence from vaginal sonography of uterine peristalsis and hysterosalpingoscintigraphy. *Hum.Reprod.* **11**, 627–632 (1996).
3. Fanchin, R. & Ayoubi, J. M. Uterine dynamics: impact on the human reproduction process. *Reprod.Biomed.Online*. **18 Suppl 2**, 57–62 (2009).
4. Fanchin, R. *et al.* Uterine contractions at the time of embryo transfer alter pregnancy rates after in-vitro fertilization. *Hum.Reprod.* **13**, 1968–1974 (1998).
5. IJland, M. M. *et al.* Relation between endometrial wavelike activity and fecundability in spontaneous cycles. *Fertil.Steril.* **67**, 492–496 (1997).
6. Zhu, L., Che, H. S., Xiao, L. & Li, Y. P. Uterine peristalsis before embryo transfer affects the chance of clinical pregnancy in fresh and frozen-thawed embryo transfer cycles. *Hum. Reprod.* **29**, 1238–1243 (2014).
7. Sterling, L., Keunen, J., Wigdor, E., Sermer, M. & Maxwell, C. Pregnancy outcomes in women with spinal cord lesions. *J. Obstet. Gynaecol. Can.* **35**, 39–43 (2013).
8. Bulletti, C. *et al.* Physiology: Electromechanical activities of human uteri during extra-corporeal perfusion with ovarian steroids. *Hum. Reprod.* **8**, 1558–1563 (1993).
9. Duquette, R. A. *et al.* Vimentin-positive, c-kit-negative interstitial cells in human and rat uterus: a role in pacemaking? *Biol.Reprod.* **72**, 276–283 (2005).
10. Tojo, S. *et al.* Electrical activity recorded from ovarian tissue in perfused human utero-tuboovarian unit. *J Reprod Fertil* **44**, 587–589 (1975).
11. de Lau, H. *et al.* Automated Conduction Velocity Analysis in the Electrohysterogram for Prediction of Imminent Delivery: A Preliminary Study. *Comput. Math. Methods Med.* **2013**, 1–7 (2013).
12. de Lau, H., Rabotti, C., Oosterbaan, H. P., Mischi, M. & Oei, G. S. Study protocol: PoPE-Prediction of Preterm delivery by Electrohysterography. *BMC Pregnancy Childbirth* **14**, 192 (2014).
13. Rabotti, C., Mischi, M., Oei, S. G. & Bergmans, J. W. Noninvasive estimation of the electrohysterographic action-potential conduction velocity. *IEEE Trans.Biomed.Eng* **57**, 2178–2187 (2010).
14. Lucovnik, M. *et al.* Noninvasive uterine electromyography for prediction of preterm delivery. in *American Journal of Obstetrics and Gynecology* **204**, 228.e1-228.e10 (2011).
15. Vlemminx, M. W. C. *et al.* Could electrohysterography be the solution for external uterine monitoring in obese women? *Journal of Perinatology* 1–7 (2018). doi:10.1038/s41372-018-0065-3
16. Ye-Lin, Y. *et al.* Non-invasive electrohysterogram recording using flexible concentric ring electrode. in *2014 36th Annual International Conference of the IEEE Engineering in Medicine and Biology Society, EMBC 2014* 4050–4053 (IEEE, 2014). doi:10.1109/EMBC.2014.6944513
17. Rabotti, C., Mischi, M., van Laar, J. O., Oei, G. S. & Bergmans, J. W. Estimation of internal uterine pressure by joint amplitude and frequency analysis of electrohysterographic signals. *Physiol Meas.* **29**, 829–841 (2008).
18. Vinken, M. P., Rabotti, C., Mischi, M. & Oei, S. G. Accuracy of frequency-related parameters of the electrohysterogram for predicting preterm delivery: a review of the literature. *Obstet.Gynecol.Surv.* **64**, 529–541 (2009).
19. Rabotti, C. & Mischi, M. Propagation of electrical activity in uterine muscle during pregnancy: A review. *Acta Physiol.* **213**, 406–416 (2015).
20. Richter, O. *et al.* Extracorporeal perfusion of the human uterus as an experimental model in gynaecology and reproductive medicine. *Hum. Reprod.* **15**, 1235–1240 (2000).

21. Richter, O. N. *et al.* Contractile reactivity of human myometrium in isolated non-pregnant uteri. *Hum.Reprod.* **21**, 36–45 (2006).
22. Rabotti, C. & Mischi, M. Two-dimensional estimation of the electrohysterographic conduction velocity. *Conf.Proc.IEEE Eng Med.Biol.Soc.* **2010**, 4262–4265 (2010).
23. Lammers, W. J. E. P. Circulating excitations and re-entry in the pregnant uterus. *Pflugers Arch. Eur. J. Physiol.* **433**, 287–293 (1997).
24. Bulletti, C. *et al.* The patterns of uterine contractility in normal menstruating women: from physiology to pathology. *Ann.N.Y.Acad.Sci.* **1034**, 64–83 (2004).
25. Bulletti, C. *et al.* Uterine contractility during the menstrual cycle. *Hum.Reprod.* **15 Suppl 1**, 81–89 (2000).
26. Lesny, P. & Killick, S. R. The junctional zone of the uterus and its contractions. *BJOG.* **111**, 1182–1189 (2004).
27. de Ziegler, D., Bulletti, C., Fanchin, R., Epiney, M. & Brioschi, P. A. Contractility of the nonpregnant uterus: the follicular phase. *Ann.N.Y.Acad.Sci.* **943**, 172–184 (2001).
28. de Vries, K., Lyons, E. A., Ballard, G., Levi, C. S. & Lindsay, D. J. Contractions of the inner third of the myometrium. *Am.J.Obstet.Gynecol.* **162**, 679–682 (1990).
29. Sammali, F. *et al.* Experimental setup for objective evaluation of uterine motion analysis by ultrasound speckle tracking. *Biomed. Phys. Eng. Express* **4**, 035012 (2018).
30. Dittrich, R. *et al.* The Extracorporeal Perfusion of Swine Uterus as an Experimental Model: The Effect of Oxytocic Drugs. *Horm. Metab. Res.* **35**, 517–522 (2003).
31. Hutchings, G., Williams, O., Cretoi, D. & Ciontea, S. M. Myometrial interstitial cells and the coordination of myometrial contractility. *J.Cell Mol.Med.* **13**, 4268–4282 (2009).
32. Ciontea, S. M. *et al.* C-kit immunopositive interstitial cells (Cajal-type) in human myometrium. *J.Cell Mol.Med.* **9**, 407–20 (2005).
33. Parkington, H. C., Tonta, M. A., Brennecke, S. P. & Coleman, H. A. Contractile activity, membrane potential, and cytoplasmic calcium in human uterine smooth muscle in the third trimester of pregnancy and during labor. *Am. J. Obstet. Gynecol.* **181**, 1445–1451 (1999).
34. Noe, M., Kunz, G., Herbertz, M., Mall, G. & Leyendecker, G. The cyclic pattern of the immunocytochemical expression of oestrogen and progesterone receptors in human myometrial and endometrial layers: characterization of the endometrial-subendometrial unit. *Hum.Reprod.* **14**, 190–197 (1999).
35. Bulletti, C. *et al.* A 48-hour preservation of an isolated human uterus: endometrial responses to sex steroids. *Fertil. Steril.* **47**, 122–129 (1987).
36. Kisu, I. *et al.* Allowable warm ischemic time and morphological and biochemical changes in uterine ischemia/reperfusion injury in cynomolgus macaque: A basic study for uterus transplantation. *Hum. Reprod.* **32**, 2026–2035 (2017).
37. Díaz-García, C., Akhi, S. N., Martínez-Varea, A. & Brännström, M. The effect of warm ischemia at uterus transplantation in a rat model. *Acta Obstet. Gynecol. Scand.* **92**, 152–159 (2013).
38. IJland, M. M. *et al.* Endometrial wavelike movements during the menstrual cycle. *Fertil.Steril.* **65**, 746–749 (1996).
39. World Medical Association. WMA DECLARATION OF HELSINKI – Ethical Principles for Medical Research Involving Human Subjects. 29–32 (2013). Available at: <file:///Users/willem-paul/Downloads/wma-declaration-of-helsinki-ethical-principles-for-medical-research-involving-human-subjects.pdf>.
40. Vink, J. Y. *et al.* A new paradigm for the role of smooth muscle cells in the human cervix. *Am. J. Obstet. Gynecol.* **215**, 478.e1-478.e11 (2016).
41. Maner, W. L., Garfield, R. E., Maul, H., Olson, G. & Saade, G. Predicting term and preterm delivery with transabdominal uterine electromyography. *Obstet. Gynecol.* **101**, 1254–1260 (2003).
42. Garfield, R. E., Maner, W. L., MacKay, L. B., Schlembach, D. & Saade, G. R. Comparing uterine electromyography activity of antepartum patients versus term labor patients. *Am. J. Obstet. Gynecol.* **193**, 23–29 (2005).

43. Rabotti, C., Mischi, M., Beulen, L., Oei, G. & Bergmans, J. W. M. Modeling and identification of the electrohysterographic volume conductor by high-density electrodes. *IEEE Trans. Biomed. Eng.* **57**, 519–527 (2010).
44. Jezewski, J., Horoba, K., Matonia, A. & Wrobel, J. Quantitative analysis of contraction patterns in electrical activity signal of pregnant uterus as an alternative to mechanical approach. *Physiol. Meas.* **26**, 753–767 (2005).
45. Rooijackers, M. J., Rabotti, C., Oei, S. G., Aarts, R. M. & Mischi, M. Low-complexity intrauterine pressure estimation using the Teager energy operator on electrohysterographic recordings. *Physiol. Meas.* **35**, 1215–1228 (2014).
46. Marshall, J. M. Regulation of activity in uterine smooth muscle. *Physiol. Rev. Suppl.* **5**, 213–227 (1962).
47. Bishop, C. M. & others. *Pattern recognition and machine learning*. (Springer-Verlag New York Inc., 2006). doi:10.1117/1.2819119
48. Chatfield, C., Zidek, J. & Lindsey, J. *An Introduction to Generalized Linear Models*. (Chapman and Hall/CRC, 2002).

3

FEASIBILITY OF TRANSABDOMINAL ELECTROHYSTEROGRAPHY FOR ANALYSIS OF UTERINE ACTIVITY IN NON-PREGNANT WOMEN

Abstract: *Uterine activity plays a key role in reproduction, and altered patterns of uterine contractility have been associated with important physio-pathological conditions, such as subfertility, dysmenorrhea, and endometriosis. However, there is currently no method to objectively quantify uterine contractility outside pregnancy without interfering with the spontaneous contraction pattern. Transabdominal electrohysterography has great potential as a clinical tool to characterize non-invasively uterine activity, but results of this technique in non-pregnant women are poorly documented. The purpose of this study is to investigate the feasibility of transabdominal electrohysterography in non-pregnant women. Longitudinal measurements were performed on 22 healthy women in 4 representative phases of the menstrual cycle. Twelve electrohysterogram-based indicators previously validated in pregnancy have been estimated and compared in the 4 phases of the cycle. Using the Tukey honest significance test, significant differences were defined for P values below 0.05. Results: Half of the selected electrohysterogram-based indicators showed significant differences between menses and at least 1 of the other 3 phases, that is the luteal phase. Our results suggest transabdominal electrohysterography to be feasible for analysis of uterine activity in non-pregnant women. Due to the lack of a golden standard, this feasibility study is indirectly validated based on physiological observations. However, these promising results motivate further research aiming at evaluating electrohysterography as a method to improve understanding and management of dysfunctions (possibly) related to altered uterine contractility, such as infertility, endometriosis, and dysmenorrhea.*

From: **F. Sammali**, N. P.M. Kuijsters, B. C. Schoot, M. Mischi, and C. Rabotti, “**Feasibility of transabdominal electrohysterography for analysis of uterine activity in non-pregnant women**”, *Reproductive Sciences* 2018, vol 25(7), pp. 1124-1133.

3.1 INTRODUCTION

Uterine activity is most evident during pregnancy when it culminates in the expulsion of the foetus at the end of the delivery. However, uterine activity plays a key role in different, possibly related, aspects of reproduction outside pregnancy as well.

Uterine activity is known to affect embryo implantation in animals¹⁻³. In healthy, non-pregnant, human uteri, previous research consistently reported specific contractile patterns that evolve during the menstrual cycle⁴⁻⁶. These evolving patterns are in line with the hypothesis of a functional role of uterine motion in normal menstrual cycles to promote fertilization^{1,5,7,8}. Furthermore, there is evidence that disruption of these natural properties is the cause of a number of dysfunctions, including subfertility, dysmenorrhea, endometriosis, and adenomyosis⁹⁻¹¹. An increasing percentage of couples, currently 20%, have difficulties conceiving^{12,13}. Approximately half of these sub-fertile couples seek medical care services and eventually recur to assisted reproduction^{14,15}. In spite of major efforts to improve assisted reproductive technology over the past 20 years, the overall effectiveness remains below 30% per treatment cycle, even for in vitro fertilization (IVF)¹⁶.

Embryo implantation is the factor with the greatest limitation on IVF¹⁷. Successful establishment of a pregnancy after embryo transfer is governed by complex mechanisms¹⁸, which depend on the quality of the embryo as well as uterine receptivity^{19,20}. While classically, uterine receptivity has been identified with the histological and biochemical readiness of the endometrium to accept an embryo, uterine quiescence has been recently suggested as an additional determinant for the successful establishment of pregnancy after embryo transfer^{4,17,21-24}.

Dysmenorrhea occurs in up to 50% of menstruating females. Dysmenorrhea is characterized by fluctuating, spasmodic pelvic cramps that begin shortly before or at the onset of menses and last 1 to 3 days²⁵. This debilitating pain can lead to a woman's failure to function normally during menstruation, making them unable to perform regular daily activities. Dysmenorrhea is associated to abnormalities in uterine activity, including elevated basal tone and active pressure, increased contraction frequency, and lack of rhythm and coordination²⁶. Yet, the link between the contraction pattern, the degree of dysfunction, and the effectiveness of treatment has never been defined.

Endometriosis is a chronic disease characterized by development of endometrial tissue outside its normal location in the uterus. Its prevalence approaches 10% to 15% of the general female population and is associated with pain, dysmenorrhea, and, in 30% of the women, with infertility²⁷. Unfortunately, the links among these diseases, particularly between endometriosis and infertility, are unclear, even though the association is clinically recognized²⁸. In line with the theory that links retrograde menstruation to migration of viable endometrial cells that attach and implant in the pelvic cavity, altered uterine contractility is hypothesized to play a key role in endometriosis²⁹. Unfortunately, aetiology and pathogenesis of this disorder remain uncertain, hampering any progress for new treatment for disease associated with pain and infertility³⁰.

In fact, the lack of an objective and non-invasive tool for quantifying contractility in non-pregnant women has limited the possibility of investigating the complex and largely unknown mechanisms underlying uterine contractility and to quantify their impact on reproduction and in dysfunctions, such as sub-fertility, dysmenorrhea, and endometriosis^{4,9}.

In non-pregnant humans, uterine activity has been first explored by using invasive intra-uterine pressure catheters^{7,10,31}, magnetic resonance imaging^{5,32,33}, and hysterosalpingoscintigraphy⁵. Unfortunately, these methods are unfeasible for routine use during IVF procedures and check-ups because they are invasive, expensive, or employing ionizing radiations^{4,34}. Visualization of uterine contractility by transvaginal ultrasonography TVUS has been more extensively used due to the availability and non-invasiveness of ultrasound¹⁰. However, this visual approach, based on either unprocessed image sequences^{5,9,11,35-44} or derived anatomical motion-mode images, is operator dependent and thus difficult to reproduce for follow-up and comparative studies^{45,46}.

As an alternative to current diagnostics, transabdominal electrohysterography has been successfully proposed to characterize uterine contractions during pregnancy⁴⁷⁻⁵². The electrohysterogram (EHG) measures the electrical activity that triggers and drives the mechanical contraction of the uterus. The EHG signals can be recorded non-invasively by electrodes placed on the abdominal skin^{53,54}. Being related to the root cause of the uterine muscle contraction, the EHG can potentially allow for a complete characterization of uterine activity also in the non-pregnant uterus. However, descriptions of EHG measurements on non-pregnant humans mainly focus on recordings performed directly on the uterus or on the cervix^{55,56}.

In this article, we evaluate for the first time (to our knowledge) the feasibility of transabdominal electrohysterography for the analysis of uterine contractions in healthy non-pregnant women, aimed at understanding the electrophysiology of uterine contractions during the menstrual cycle by a non-invasive approach.

3.2 MATERIALS AND METHODS

3.2.1 Patients and Study protocol

All measurements were performed at the Gynaecology Department of the Catharina Hospital in Eindhoven (the Netherlands) after approval by the relevant medical ethical committee (protocol NL52466.100.15). After signing an informed consent, 22 women were enrolled in the study. The inclusion criteria were an age between 18 and 40 years and a regular, natural menstrual cycle. Exclusion criteria were ongoing pregnancy, mental disability, significant language barrier, and caesarean delivery in the past. Uterine anomalies (congenital or non-congenital), uterine pathologies (leiomyomas, adenomyosis, and endometriosis), and infertility were additional exclusion criteria.

Women were recorded longitudinally at 4 predefined moments of the menstrual cycle, namely, during menses, which coincides with the early follicular (EF) phase⁵⁷, in the late follicular (LF)

phase, in the early luteal (EL) phase, and in the late luteal (LL) phase. All phases were in the same cycle. Menses dates were based on the last menstrual period. The LF phase, expected between day 11 and day 13 of the cycle, was established based on estimates of the follicle size measured on TVUS images. The EHG measurements for the LF phase were performed only when one of the follicles had a diameter larger than 16 mm. The EL and LL phases were set at 3 and 7 days after ovulation, respectively. Blood tests were performed in order to measure hormone levels and exclude any hormonal unbalance that might contribute to dysfunctional uterine activity⁷. More specifically, concentrations of luteinizing hormone (LH), follicle-stimulating hormone (FSH), oestrogen and progesterone were measured.

During each measurement session, 4-minute data were acquired. Based on the literature, depending on the phase of the cycle, at least 2 contractions can be expected to occur in this time range⁷.



Figure 3.1: Electrode grid on the abdomen. The authors confirm permission from the woman to use this picture.

3.2.2 Electrohysterogram Recording

After skin preparation for contact impedance reduction, the EHG was recorded by a flexible electrode grid placed on the abdomen immediately above the pubic bone (Figure 3.1). The correct placement of the abdominal grid was guided by TVUS in order to maximize alignment with the uterus.

The adopted electrode grid (Figure 2) comprises an 8 x 8 array of electrodes (2 mm diameter, 4 mm distance). Such high-density electrode grids provide the augmented spatial resolution that might be necessary for analysis of EHG propagation properties in future work^{58,59}. In this feasibility study, however, we focus on single-channel analysis for a qualitative evaluation of contraction timing and strength⁶⁰. For this purpose, which does not require high spatial resolution, the signal quality is improved by averaging neighbouring electrodes and simulating larger sensing surfaces^{53,61}. Furthermore, larger inter-electrode distances are more suited than a high-density grid to investigate electrophysiological signals originated deeper as in the case on the non-pregnant uterus^{53,61}. Furthermore, vertical derivations, aligned to the middle line

of the muscle, are expected to be closer to the uterus and, therefore, provide a better signal to noise ratio. Two larger sensing areas, A and B in Figure 3.2, were therefore obtained by averaging the corresponding electrodes. Since bipolar derivations improve the signal quality by reduction of the common mode noise, a single bipolar signal was derived by subtracting the 2 sensing areas A and B^{62,63}. The EHG was then recorded and digitized, after the required antialiasing low-pass filtering, at a sampling frequency of 1024 Hz using a Refa system (TMS International, Enschede, the Netherlands), a multichannel amplifier for electrophysiological signals.

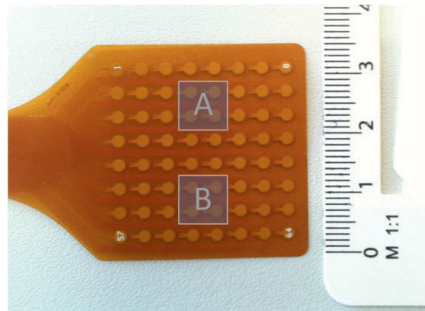


Figure 3.2: High-density electrode grid and schematic of the sensing surfaces A and B.

3.2.3 Feature Extraction

For each recording session, a set of features is extracted from the single-channel EHG signal. Depending on the chosen feature, the acquired signal is first pre-processed by dedicated pre-filtering^{64,65}. Features are then extracted following a 2-step approach: the pre-processed EHG is analysed in step 1 in order to enhance specific properties of the EHG signal related to the contraction strength. Four different approaches, based on previous research on EHG analysis during pregnancy and implemented both in the time and in the frequency domain, are used in step 1 to provide a set of signals, referred to as (time-varying) features. From these features, the (global) indicators are extracted in step 2 and compared among the representative phases of the menstrual cycle for validation. The proposed approach for feature extraction is schematically described in Figure 3 using a recorded EHG signal as an example.

In clinical practice, timing and strength of uterine activity during pregnancy and delivery are assessed by direct or indirect measurement of the intra-uterine pressure variations induced by contractions⁶⁶. In pregnant women, previous research demonstrated an accurate measure of the intra-uterine pressure variations related to uterine contractions by estimating the EHG signal energy⁶⁰. The unnormalized first statistical moment (UFM) and its low-complexity alternative, the Teager energy (TE) operator, have been proposed in the previous literature for intra-uterine pressure estimation^{67,68}. The UFM is obtained as the product between the average signal frequency and the signal energy, both estimated in the time-frequency domain⁶⁰. The TE operator is calculated in the discrete-time domain using a multiband solution for energy tracking^{68,69}. In pregnancy, these frequency-weighted estimates of the signal energy seem, in

fact, to provide a good representation of the hypothesized physiology of uterine muscle force development in response to electrical activity⁶⁰. In this article, both the TE and the UFM are investigated as features and calculated in sliding windows similarly^{60,68}. Signal amplitude estimations obtained by the root mean squared (RMS) and the band-filtered EHG signal (FSig) are considered as 2 additional features (see Figure 3.3)^{63,70,71}. Further details of the feature extraction steps are provided in the subsequent section.

3.2.4 Pre-filtering

The electrical signals originating from the activity of smooth muscles like the uterus are characterized by a low-frequency content⁷². For the uterus, frequencies below 5 Hz are expected, while the frequency band below 0.3 Hz can be seriously affected by movement artifacts related, for example, to respiration^{64,65}. To estimate the intra-uterine pressure increase by EHG analysis in pregnancy, frequency bands below 1 Hz have been previously adopted^{60,68,71,73}. In fact, a better correlation with the invasively recorded intra-uterine pressure was found in this frequency band while rejecting the maternal electrocardiogram. Nevertheless, during pregnancy, the EHG signal energy distribution extends beyond the upper frequency limit of 1 Hz^{70,74–76}. Analysis of our data suggests the EHG signal energy to show similar frequency distribution also outside pregnancy.

Due to the current lack of a reference golden standard, in this feasibility study, all features are derived in the 0.3 and 5 Hz frequency band, where an improved signal quality is expected. Preliminary tests confirmed that the interference due to the electrocardiographic signal, expected at frequencies as low as 1 Hz⁷⁷, could be neglected due to the small inter-electrode distance on the abdomen. For the TE, RMS, and BF, a fourth-order Butterworth filter with cutoff frequencies at 0.3 and 5 Hz is employed prior to calculation of the features. The definition of the UFM in the frequency domain allows estimation in the desired frequency band without prefiltering⁶⁰.

3.2.5 Time-varying Features

The time-varying features have been calculated in 6-second sliding Han windows. The choice of the window type is in line with the previous literature⁶⁸, while the window length is experimentally optimized in agreement with the frequency band of interest. In fact, this band allows to resolve the lowest frequency of interest (0.3 Hz) at a sufficient temporal resolution to enhance possible contractile events.

3.2.6 Indicators

Comparison of the considered phases of the menstrual cycle is then based on indicators subsequently extracted from the 4 chosen features. To this end, the standard deviation (SD), median frequency (MF), and UFM are estimated from each feature to form the set of indicators evaluated in the representative phases. These specific indicators, extracted from each of the above time-varying features (see Figure 3.3), were chosen in order to assess whether their

frequency (represented by the MF), amplitude (as SD), or a combination of both frequency and amplitude (UFM) could be representative of the uterine activity in the considered phase⁷⁰.

3.2.7 Statistical analysis

The indicators extracted in the 4 selected phases of the menstrual cycle, 12 in total, are compared using 1-way analysis of variance with repeated measures. Post hoc analysis is performed using the Tukey honest significance test (Tukey- Kramer method) and a significance level $P = 0.05$ ⁷⁸.

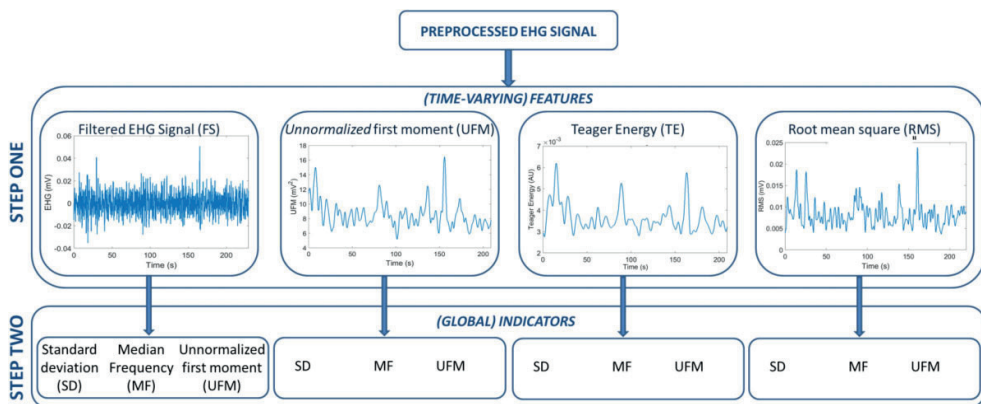


Figure 3.3: Scheme of the proposed approach for feature extraction. The same EHG signal recorded during the LF phase from one of the included women is shown as an example. EHG indicates electrohysterogram; LF, late follicular phase.

3.3 RESULTS

Of the 22 women enrolled in the study, only 11 were eventually retained for the data analysis. Of the 11 women, 6 were excluded due to subfertility issues that emerged during or immediately after the study, 2 withdrew their consent after inclusion, and 3 could not attend the recording sessions, which resulted in an incomplete dataset.

Of the 11 retained participants, 9 had a natural pregnancy shortly before or after the measurement, while 2 of them had no child wish at the moment of recording. At the time of measurement, women had an age between 25 and 39 years (31 years on average) and a cycle length between 24 and 40 days (29 days on average). Tests on the hormone levels did not show any unbalance, and figures were all within the expected ranges for healthy women in the presumed phase of the menstrual cycle. The average values of hormone test results are reported in Table 3.1.

As shown in Table 3.2, significance emerged only when the SD and the UFM were used as indicators. Instead, the use of the RMS as feature did not produce any significance difference among phases, independently from the adopted indicator.

The values of the derived indicators are plotted in Figures 3.4 to 3.6, in terms of average and SD. Normalized values are used to mitigate the impact of interpatient variability for improved visualization. Normalization was performed patient-wise, relatively to the LL phase. When SD and UFM are used as indicators, a decreasing trend along the cycle can be observed, which is absent in the results obtained by the MF indicator.

Table 3.1: Hormone Test Results

Phase	Median Day of Cycle	Mean FSH (IU/L)	Mean LH (IU/L)	Mean Estrogen (nmol/L)	Mean Progesteron (nmol/L)
Early follicular (EF)	2	6,48	4,77	0,13	1,59
Late follicular (LF)	13	5,63	17,81	0,85	1,81
Early luteal (EL)	18	4,46	7,93	0,44	24,82
Late luteal (LL)	22	2,92	5,27	0,61	45,52

FSH = follicle stimulating hormone; LH = luteinizing hormone

Table 3.2: Significance of feature differences for each combination of indicator and feature.

Features	Indicators	Standard Deviation (SD)	Median Frequency (MDF)	Unnormalized First Statistical Moment (UFM)
Filtered signal (FSig)		0,035769*	0,71865	0,032974*
Unnormalized first statistical moment (UFM)		0,040727*	0,822843	0,011567*
Teager energy (TE)		0,020207*	0,625007	0,012538*
Root mean square (RMS)		0,070321	0,655169	0,083205

* $p < 0,05$.

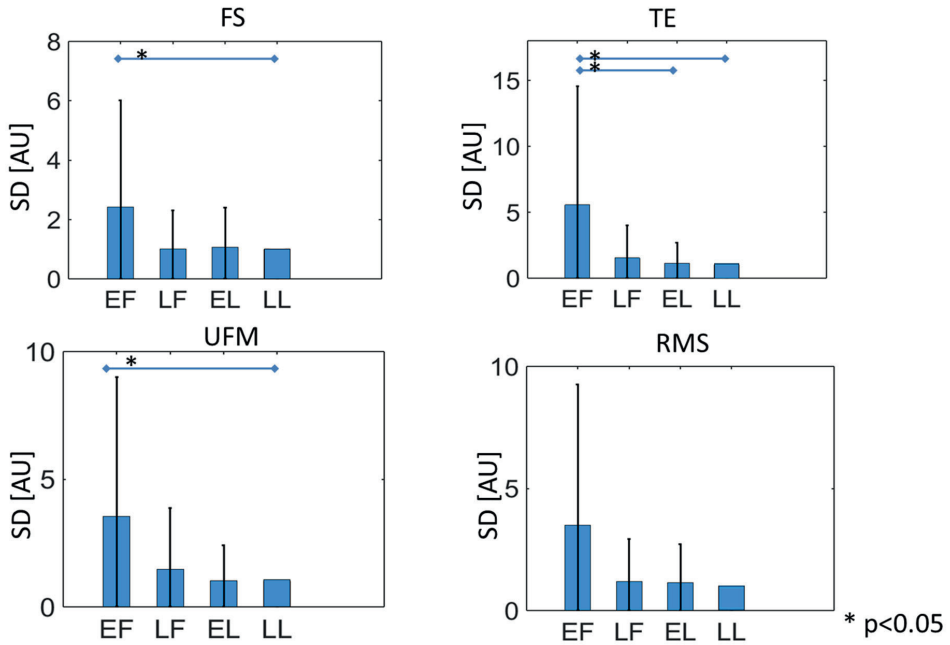


Figure 3.4: Value of the SD indicator (average and standard deviation [SD]) for different features in each of the evaluated cycle phases. Normalized values are used to mitigate the impact of interpatient variability for improved visualization.

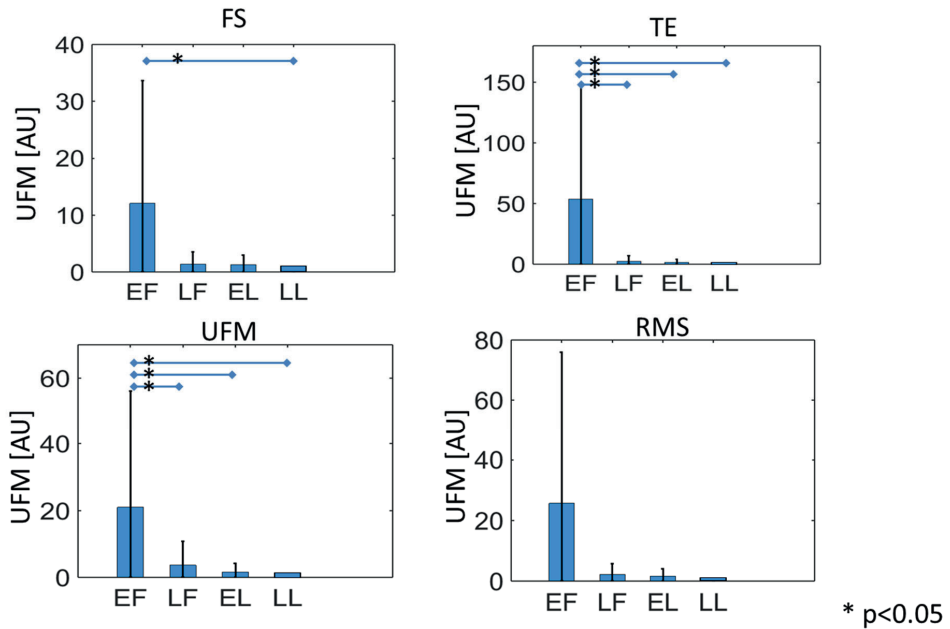


Figure 3.5: Value of the UFM indicator (average and standard deviation) for different features in each of the evaluated cycle phases. Normalized values are used to mitigate the impact of interpatient variability for improved visualization. UFM indicates unnormalized first statistical moment.

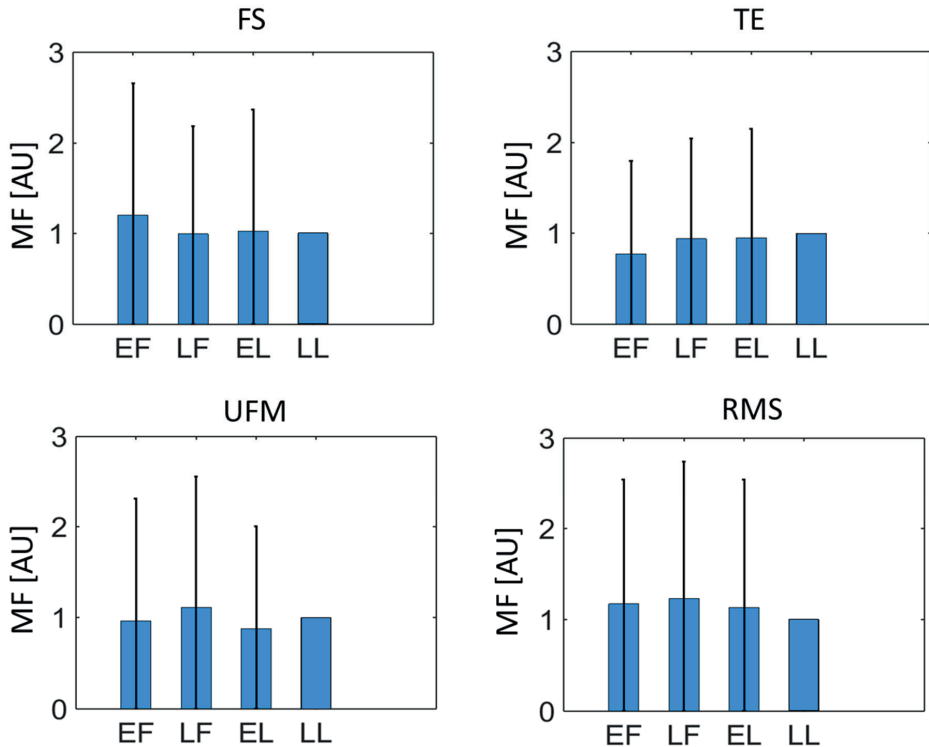


Figure 3.6: Value of the MF indicator (average and standard deviation) for different features in each of the evaluated cycle phases. Normalized values are used to mitigate the impact of interpatient variability for improved visualization. MF indicates median frequency.

3.4 DISCUSSION

Uterine activity plays a key role in natural as well as in assisted reproduction. Furthermore, dysfunctional uterine activity is recognized among the main causes of important medical issues, including subfertility, dysmenorrhea, and endometriosis⁹⁻¹¹. Unfortunately, the lack of an objective method for uterine activity quantification hampers progress in understanding and treatment of these dysfunctions. This article studies for the first time the feasibility of transabdominal EHG in the non-pregnant uterus. EHG measures the biopotential underlying the physiological process of uterine muscle contractions. Due to the lack of a golden standard for uterine contraction assessment outside pregnancy, an indirect validation approach is proposed in this study, which relies on the different motility patterns reported for the uterus at different stages of a physiological menstrual cycle. To this end, non-pregnant healthy women are measured longitudinally, at 4 selected representative phases of the menstrual cycle, namely, the EF, LF, EL, and LL phases.

During the cycle, the ovaries and the uterus undergo hormone-dominated physiological changes that, in healthy women, are functional to the establishment of a pregnancy. More

specifically, the ovaries undergo changes aiming at egg production, while the uterus evolves synergistically to a progressively more receptive status toward fertilized embryos. During the follicular phase, the preparatory phase for egg release, the progressive increase in uterine contraction frequency is thought to facilitate sperm ascension toward the distal end of the fallopian tubes, where fertilization takes place^{4,5}. After ovulation, the uterus undergoes progressive relaxation that culminates during the mid-luteal phase. This relaxation phase, which usually occurs approximately 7 days after ovulation, may assist proper embryo positioning in the uterine cavity and, thus, facilitate embryo implantation^{7,44}. During menses, if no egg has been fertilized to start a pregnancy, labour-like contractions promote shedding the uterine lining and a new cycle begins.

Based on validated approaches previously developed for EHG analysis in pregnancy, in this study, a number of selected features is extracted from the recorded EHG signal at each of the representative phases of the menstrual cycle. Half of the 12 indicators here extracted from the recorded EHG show some significant differences among phases. Consistent, significant differences have been found between the EF phase and the LL phase. Especially with the UFM indicator, the EF phase shows consistent significant difference from all other phases. This phase, which coincides with menses, also shows the highest variability. Both these aspects, namely, its significant difference from the other phases and the indicator variability, can be related to intermittent and cramp-like contractions typical of menses. Previous studies on non-pregnant uteri have in fact reported a wave-like, peristaltic activity of the uterus during most of the menstrual cycle as opposed to menses and parturition, when cramp-like contractions are alternated to quiescent periods of inactivity^{7,37,55,79–81}. Qualitative comparison of the recordings of this study with signals recorded during pregnancy with a similar protocol also indicates a more continuous, peristaltic activity, rather than alternation of contracting and quiescent periods of electrical activity (burst), which are typical of pregnancy and observed more frequently during menses. Noteworthy, as an initial step toward the use of EHG outside pregnancy, our approach is based on previous EHG studies in pregnancy.

Due to the size increase and hormonal changes that the uterus undergoes in pregnancy, some additional challenges should be accounted for when using EHG measurements outside pregnancy. Yet, similarly to pregnancy, pressure increases have also been measured during contractions outside pregnancy^{26,55}, and spontaneous electrical activity has been observed and recorded^{55,82}.

Furthermore, the significance of the features extracted during menses supports the employment of the proposed methods for the investigation of dysfunctions related to menses, such as dysmenorrhea. Future studies, aiming at developing tailored methods for the analysis of the EHG outside pregnancy, may also reveal significance differences between the LF and the luteal phases as well as between different moments within the luteal phase.

All features show decreasing trend in their value along the cycle. This decrease is mostly not significant but may reflect a progressively more quiet state along the cycle that is in line with the uterine function of promoting embryo implantation by increased receptivity.

In contrast, previous TVUS and intra-uterine pressure measurements during the menstrual cycle evidenced a progressive increase in contraction frequency and strength in the follicular phase followed by a decrease in the luteal phase^{34,43,55}, suggesting a role of oestrogens as stimulator and progesterone as inhibitor of uterine contractions^{8,83,84}. In general, a direct comparison between the EHG features evaluated in this work and the uterine contraction properties evidenced by intra-uterine pressure catheters and TVUS should be cautiously evaluated; the fundamental different nature of the measurement approaches used in this study and in the previous literature (electrical vs mechanical) and the specific signal analysis employed in this study should first be jointly evaluated in relation to the underlying physiological mechanisms, which are still largely unknown.

We record the EHG signal transabdominally, using an electrode patch containing 64 channels. Our choice for testing the feasibility of transabdominal recording of the EHG, rather than more invasive methods to evaluate uterine electrical activity, is motivated by the urgent need for a cost-effective, non-invasive, and easy-to-use method for deriving uterine activity in everyday clinical practice. This abdominal approach does not take into consideration the possible role of other organs, such as the bladder or the intestine, that also produce biopotential. Based on our results, we may conclude that the main organ activity extracted by our measurements is from the uterus. Additional evidence that our signals are representative of uterine biopotential alone is being researched. As for the electrodes chosen in this study, in pregnancy, it has been demonstrated that the EHG can potentially quantify amplitude, frequency, and, when arrays of electrodes are used, direction and velocity of contractions. The use of a multichannel grid for the signal acquisition is here meant to demonstrate the feasibility of multichannel EHG recording and possibly open the way to future studies aiming at assessing contraction direction and velocity. Eventually, the optimal inter- electrode distance should be carefully evaluated in relation to the increased depth at which the uterus lies into the pelvic cavity as compared to pregnancy.

3.5 DECLARATION OF CONFLICTING INTERESTS

The author(s) declared no potential conflicts of interest with respect to the research, authorship, and/or publication of this article.

3.6 FUNDING

The author(s) disclosed receipt of the following financial support for the research, authorship, and/or publication of this article: This work was supported by an unconditional Veni grant from the Dutch Technology Foundation STW (project number 12472).

BIBLIOGRAPHY

1. Pusey, J., Kelly, W. A., Bradshaw, J. M. & Porter, D. G. Myometrial activity and the distribution of blastocysts in the uterus of the rat: interference by relaxin. *Biol Reprod* **23**, 394–397 (1980).
2. Rogers, P. A., Murphy, C. R., Squires, K. R. & MacLennan, A. H. Effects of relaxin on the intrauterine distribution and antimesometrial positioning and orientation of rat blastocysts before implantation. *J. Reprod. Fertil.* **68**, 431–5 (1983).
3. McLaren, A. & Mischie, D. The spacing of implantations in the mouse uterus. *Mem Soc Endocrinol* **6**, 65–74 (1959).
4. Fanchin, R. & Ayoubi, J. M. Uterine dynamics: impact on the human reproduction process. *Reprod.Biomed.Online.* **18 Suppl 2**, 57–62 (2009).
5. Kunz, G., Beil, D., Deininger, H., Wildt, L. & Leyendecker, G. The dynamics of rapid sperm transport through the female genital tract: evidence from vaginal sonography of uterine peristalsis and hysterosalpingoscintigraphy. *Hum.Reprod.* **11**, 627–632 (1996).
6. Kuijsters, N. P. M. *et al.* Uterine peristalsis and fertility: current knowledge and future perspectives: a review and meta-analysis. *Reprod. Biomed. Online* **35**, 50–71 (2017).
7. Bulletti, C. *et al.* Uterine contractility during the menstrual cycle. *Hum.Reprod.* **15 Suppl 1**, 81–89 (2000).
8. Kunz, G., Noe, M., Herberth, M. & Leyendecker, G. Uterine peristalsis during the follicular phase of the menstrual cycle: effects of oestrogen, antioestrogen and oxytocin. *Hum.Reprod.Update.* **4**, 647–654 (1998).
9. IJland, M. M., Evers, J. L. & Hoogland, H. J. Velocity of endometrial wavelike activity in spontaneous cycles. *Fertil.Steril.* **68**, 72–75 (1997).
10. Bulletti, C. & de Ziegler, D. Uterine contractility and embryo implantation. *Curr. Opin. Obstet. Gynecol.* **18**, 473–484 (2006).
11. Leyendecker, G., Kunz, G., Wildt, L., Beil, D. & Deininger, H. Uterine hyperperistalsis and dysperistalsis as dysfunctions of the mechanism of rapid sperm transport in patients with endometriosis and infertility. *Hum.Reprod.* **11**, 1542–1551 (1996).
12. Whitman-Elia, G. & Baxley, E. A primary care approach to the infertile couple. *J Am Board Fam Pr.* **14**, 33–45 (2001).
13. De Graaff, A. A., Land, J. A., Kessels, A. G. H. & Evers, J. L. H. Demographic age shift toward later conception results in an increased age in the subfertile population and an increased demand for medical care. *Fertil. Steril.* **95**, 61–63 (2011).
14. Boivin, J., Bunting, L., Collins, J. & Nygren, K. International estimates of infertility prevalence and treatment-seeking: potential need and demand for infertility medical care. *Hum. Reprod.* **22**, 1506–1512 (2007).
15. Moreau, C., Bouyer, J., Ducot, B., Spira, A. & Slama, R. When do involuntarily infertile couples choose to seek medical help? *Fertil. Steril.* **93**, 737–744 (2010).
16. Andersen, A. N., Goossens, V. & Ferraretti, A. Assisted reproductive technology in Europe, 2004. Results generated from European registers by ESHRE. *Hum.Reprod.* **23**, 756–771 (2008).
17. Fanchin, R. *et al.* Uterine contractions at the time of embryo transfer alter pregnancy rates after in-vitro fertilization. *Hum.Reprod.* **13**, 1968–1974 (1998).
18. Tabibzadeh, S. & Babaknia, A. The signals and molecular pathways involved in implantation, a symbiotic interaction between blastocyst and endometrium involving adhesion and tissue invasion. *Mol. Hum. Reprod.* **1**, 179–202 (1995).
19. Yoshinaga, K. Uterine Receptivity for Blastocyst Implantation. *Ann. N. Y. Acad. Sci.* **541**, 424–431 (1988).
20. Paulson, R., Sauer, M. & Lobo, R. Factors affecting embryo implantation after human in vitro fertilization: a hypothesis. *Am.J.Obstet. Gynecol.* **163**, 2020–2023 (1990).
21. Fanchin, R. *et al.* Uterine contractility decreases at the time of blastocyst transfers. *Hum.Reprod.* **16**, 1115–1119 (2001).

22. Knutzen, V. *et al.* Mock embryo transfer in early luteal phase, the cycle before in vitro fertilization and embryo transfer: a descriptive study. *Fertil Steril* **57**, 156–162 (1992).
23. Lesny, P., Killick, S. R., Tetlow, R. L., Robinson, J. & Maguiness, S. D. Embryo transfer--can we learn anything new from the observation of junctional zone contractions? *Hum.Reprod.* **13**, 1540–1546 (1998).
24. Pierzynski, P., Reinheimer, T. M. & Kuczynski, W. Oxytocin antagonists may improve infertility treatment. *Fertil.Steril.* **88**, 213–222 (2007).
25. Durain, D. Primary dysmenorrhea: assessment and management update. *J Midwifery Womens Heal.* **49**, 520–528 (2004).
26. Csapo, A. & Pinto-Dantas, C. The cyclic activity of the nonpregnant human uterus. A new method for recording intrauterine pressure. *Fertil. Steril.* **17**, 34 (1966).
27. Ación, P. & Velasco, I. Endometriosis: A Disease That Remains Enigmatic. *ISRN Obstet. Gynecol.* 1–12 (2013). doi:10.1155/2013/242149
28. Gupta, S. *et al.* Pathogenic mechanisms in endometriosis-associated infertility. *Fertil. Steril.* **90**, 247–257 (2008).
29. Bulletti, C. *et al.* Characteristics of uterine contractility during menses in women with mild to moderate endometriosis. *Fertil.Steril.* **77**, 1156–1161 (2002).
30. de Ziegler, D., Borghese, B. & Chapron, C. Endometriosis and infertility: pathophysiology and management. *Lancet* **376**, 730–738 (2010).
31. Martinez-Gaudio, M., Yoshida, T. & Bengtsson, L. P. Propagated and nonpropagated myometrial contractions in normal menstrual cycles. *Am.J.Obstet.Gynecol.* **115**, 107–111 (1973).
32. Orisaka, M. *et al.* A comparison of uterine peristalsis in women with normal uteri and uterine leiomyoma by cine magnetic resonance imaging. *Eur.J.Obstet.Gynecol.Reprod.Biol.* **135**, 111–115 (2007).
33. Togashi, K. Uterine contractility evaluated on cine magnetic resonance imaging. *Ann. N. Y. Acad. Sci.* **1101**, 62–71 (2007).
34. Lyons, E. A. *et al.* Characterization of subendometrial myometrial contractions throughout the menstrual cycle in normal fertile women. *Fertil. Steril.* **55**, 771–774 (1991).
35. IJland, M. M., Evers, J. L., Dunselman, G. A. & Hoogland, H. J. Endometrial wavelike activity, endometrial thickness, and ultrasound texture in controlled ovarian hyperstimulation cycles. *Fertil.Steril.* **70**, 279–283 (1998).
36. IJland, M. M., Hoogland, H. J., Dunselman, G. A., Lo, C. R. & Evers, J. L. Endometrial wave direction switch and the outcome of in vitro fertilization. *Fertil.Steril.* **71**, 476–481 (1999).
37. van Gestel, I., IJland, M. M., Hoogland, H. J. & Evers, J. L. Endometrial wave-like activity in the non-pregnant uterus. *Hum.Reprod.Update.* **9**, 131–138 (2003).
38. Birnholz, J. C. Ultrasonic visualization of endometrial movements. *Fertil. Steril.* **41**, 157–158 (1984).
39. Abramowicz, J. S. & Archer, D. F. Uterine endometrial peristalsis--a transvaginal ultrasound study. *Fertil.Steril.* **54**, 451–454 (1990).
40. de Vries, K., Lyons, E. A., Ballard, G., Levi, C. S. & Lindsay, D. J. Contractions of the inner third of the myometrium. *Am.J.Obstet.Gynecol.* **162**, 679–682 (1990).
41. Oike, K., Ishihara, K. & Kikuchi, S. A study on the endometrial movement and serum hormonal level in connection with uterine contraction. *Nihon Sanka Fujinka Gakkai Zasshi* **42**, 86–92 (1990).
42. Chalubinski, K., Deutinger, J. & Bernaschek, G. Vaginosonography for recording of cycle-related myometrial contractions. *Fertil. Steril.* **59**, 225–228 (1993).
43. IJland, M. M. *et al.* Endometrial wavelike movements during the menstrual cycle. *Fertil.Steril.* **65**, 746–749 (1996).
44. IJland, M. M. *et al.* Relation between endometrial wavelike activity and fecundability in spontaneous cycles. *Fertil.Steril.* **67**, 492–496 (1997).
45. Finberg, H. J. Whither (with?) the ultrasound specialist? *J.Ultrasound Med.* **23**, 1543–1547 (2004).

46. Solomon, M. J., McLeod, R. S., Cohen, E. K., Simons, M. E. & Wilson, S. Reliability and validity studies of endoluminal ultrasonography for anorectal disorders. *Dis. Colon Rectum* **37**, 546–551 (1994).
47. Lucovnik, M. *et al.* Use of uterine electromyography to diagnose term and preterm labor. *Acta Obstet. Gynecol. Scand.* **90**, 150–157 (2011).
48. Rabotti, C., Mischi, M., Van Laar, J., Oei, G. & Bergmans, J. Electrohysterographic analysis of uterine contraction propagation with labor progression: A preliminary study. in *Annual International Conference of the IEEE Engineering in Medicine and Biology - Proceedings* 4135–4138 (2007). doi:10.1109/IEMBS.2007.4353246
49. Rabotti, C., Oei, S. G., van't Hooft, J. & Mischi, M. Comment to electrohysterographic propagation velocity for preterm delivery prediction. *Am. J. Obstet. Gynecol.* **205**, e9–e10 (2011).
50. Vinken, M. P. G. C., Rabotti, C., Mischi, M., van Laar, J. O. E. H. & Oei, S. G. Nifedipine-Induced Changes in the Electrohysterogram of Preterm Contractions: Feasibility in Clinical Practice. *Obstet. Gynecol. Int.* 1–8 (2010). doi:10.1155/2010/325635
51. van 't Hooft, J., Rabotti, C. & Oei, S. G. Electrohysterographic evaluation of preterm contractions in a patient with a unicornuate uterus. *Acta Obs.* **92**, 730–733 (2013).
52. Mischi, M. *et al.* Dedicated Entropy Measures for Early Assessment of Pregnancy Progression from Single-Channel Electrohysterography. *IEEE Trans. Biomed. Eng.* **65**, 875–884 (2018).
53. Rabotti, C. & Mischi, M. Propagation of electrical activity in uterine muscle during pregnancy: A review. *Acta Physiol.* **213**, 406–416 (2015).
54. Maul, H., Maner, W. L., Saade, G. R. & Garfield, R. E. The physiology of uterine contractions. [Review]. *Clin. Perinatol.* **30**, 665–676 (2003).
55. Bulletti, C. *et al.* Physiology: Electromechanical activities of human uteri during extra-corporeal perfusion with ovarian steroids. *Hum. Reprod.* **8**, 1558–1563 (1993).
56. Shafik, A. Electrohysterogram: study of the electromechanical activity of the uterus in humans. *Eur. J. Obstet. Gynecol. Reprod. Biol.* **73**, 85–89 (1997).
57. Cramer, D. W. Determinants of early follicular phase gonadotrophin and estradiol concentrations in women of late reproductive age. *Hum. Reprod.* **17**, 221–227 (2002).
58. Rabotti, C., Mischi, M., Oei, S. G. & Bergmans, J. W. Noninvasive estimation of the electrohysterographic action-potential conduction velocity. *IEEE Trans. Biomed. Eng.* **57**, 2178–2187 (2010).
59. Xu, L., Rabotti, C. & Mischi, M. Towards Real-Time Estimation of Muscle-Fiber Conduction Velocity Using Delay-Locked Loop. *IEEE Trans. Neural Syst. Rehabil. Eng.* **25**, 1453–1460 (2017).
60. Rabotti, C., Mischi, M., van Laar, J. O., Oei, G. S. & Bergmans, J. W. Estimation of internal uterine pressure by joint amplitude and frequency analysis of electrohysterographic signals. *Physiol Meas.* **29**, 829–841 (2008).
61. Rooijackers, M. J. *et al.* Influence of electrode placement on signal quality for ambulatory pregnancy monitoring. *Comput. Math. Methods Med.* (2014). doi:10.1155/2014/960980
62. Xu, L., Rabotti, C. & Mischi, M. Novel vibration-exercise instrument with dedicated adaptive filtering for electromyographic investigation of neuromuscular activation. *IEEE Trans. Neural Syst. Rehabil. Eng.* **21**, 275–282 (2013).
63. Xu, L., Rabotti, C. & Mischi, M. Analysis of Vibration Exercise at Varying Frequencies by Different Fatigue Estimators. *IEEE Trans. Neural Syst. Rehabil. Eng.* **24**, 1284–1293 (2016).
64. Maner, W. L., Garfield, R. E., Maul, H., Olson, G. & Saade, G. Predicting term and preterm delivery with transabdominal uterine electromyography. *Obstet. Gynecol.* **101**, 1254–1260 (2003).
65. Buhimschi, C., Boyle, M. B. & Garfield, R. E. Electrical activity of the human uterus during pregnancy as recorded from the abdominal surface. *Obstet. Gynecol.* **90**, 102–111 (1997).
66. Garfield, R. E. *et al.* Methods and devices for the management of term and preterm labor. *Ann. N. Y. Acad. Sci.* **943**, 203–224 (2001).
67. Rabotti, C. *et al.* Relationship between electrohysterogram and internal uterine pressure: a preliminary study. *Conf. Proc. IEEE Eng Med Biol. Soc.* **1**, 1661–1664 (2006).
68. Rooijackers, M. J., Rabotti, C., Oei, S. G., Aarts, R. M. & Mischi, M. Low-complexity intrauterine

- pressure estimation using the Teager energy operator on electrohysterographic recordings. *Physiol. Meas.* **35**, 1215–1228 (2014).
69. Evangelopoulos, G. & Maragos, P. Multiband modulation energy tracking for noisy speech detection. *IEEE Trans. Audio, Speech Lang. Process.* **14**, 2024–2038 (2006).
 70. Vinken, M. P., Rabotti, C., Mischi, M. & Oei, S. G. Accuracy of frequency-related parameters of the electrohysterogram for predicting preterm delivery: a review of the literature. *Obstet. Gynecol. Surv.* **64**, 529–541 (2009).
 71. Jezewski, J., Horoba, K., Matonia, A. & Wrobel, J. Quantitative analysis of contraction patterns in electrical activity signal of pregnant uterus as an alternative to mechanical approach. *Physiol. Meas.* **26**, 753–767 (2005).
 72. Devedeux, D., Marque, C., Mansour, S., Germain, G. & Duchene, J. Uterine electromyography: a critical review. *Am. J. Obstet. Gynecol.* **169**, 1636–1653 (1993).
 73. Skowronski, M. D., Harris, J. G., Marossero, D. E., Edwards, R. K. & Euliano, T. Y. Prediction of intrauterine pressure from electrohysterography using optimal linear filtering. *IEEE Trans. Biomed. Eng.* **53**, 1983–1989 (2006).
 74. Marque, C. K., Terrien, J., Rihana, S. & Germain, G. Preterm labour detection by use of a biophysical marker: The uterine electrical activity. *BMC Pregnancy Childbirth* **7**, 1–6 (2007).
 75. Léman, H., Marque, C. & Gondry, J. Use of the electrohysterogram signal for characterization of contractions during pregnancy. *IEEE Trans. Biomed. Eng.* **46**, 1222–1229 (1999).
 76. B., M., M., K., C., M. & M.O., D. Energy distribution analysis of uterine electromyography signals. *J. Med. Biol. Eng.* **30**, 361–366 (2010).
 77. Bailey, J. J. The triangular wave test for electrocardiographic devices: A historical perspective. *J. Electrocardiol.* **37**, 71–73 (2004).
 78. Tukey, J. W. Comparing Individual Means in the Analysis of Variance. *Biometrics* **5**, 99 (1949).
 79. Hendricks, C. H. Inherent motility patterns and response characteristics of the nonpregnant human uterus. *Am. J. Obstet. Gynecol.* **96**, 824–841 (1966).
 80. Hendricks, C. H. A New Technique for the Study of Motility in the Non-Pregnant Human Uterus. *BJOG An Int. J. Obstet. Gynaecol.* **71**, 712–716 (1964).
 81. Moawad, A. H. & Bengtsson, L. P. In vivo studies of the motility patterns of the nonpregnant human uterus. I. The normal menstrual cycle. *Am. J. Obstet. Gynecol.* **98**, 1057–1064 (1967).
 82. Popescu, L. M., Ciontea, S. M. & Cretoiu, D. Interstitial Cajal-like cells in human uterus and fallopian tube. *Ann. N.Y. Acad. Sci.* **1101**, 139–165 (2007).
 83. Graham, J. D. & Clarke, C. L. Physiological action of progesterone in target tissues. *Endocr. Rev.* **18**, 502–519 (1997).
 84. Noe, M., Kunz, G., Herbertz, M., Mall, G. & Leyendecker, G. The cyclic pattern of the immunocytochemical expression of oestrogen and progesterone receptors in human myometrial and endometrial layers: characterization of the endometrial-subendometrial unit. *Hum. Reprod.* **14**, 190–197 (1999).

Part II

Quantitative sonography in the non-pregnant
human uterus

4

EXPERIMENTAL SET-UP FOR OBJECTIVE EVALUATION OF UTERINE MOTION ANALYSIS BY ULTRASOUND SPECKLE TRACKING

Abstract: Recent research suggests that uterine contractions play an important role for the success of conception. Unfortunately, the lack of tools for quantitative analysis limits our understanding of the uterine contractility outside pregnancy. More recently, several methods based on speckle tracking have gained attention for uterine contractility assessment; however, the absence of a ground truth hampers the optimization of any tracking method. Therefore, in this study we present an experimental set-up based on a human ex-vivo uterus able to generate controlled uterine motion aiming at assessing the accuracy of motion tracking techniques and obtaining clear indications on the optimal imaging setting. Uterine motion was obtained by use of an electromagnetic actuator generating a controlled, sinusoidal (0.05 Hz), linear displacement of a syringe piston, injecting 3-mL saline through a balloon catheter inserted into the uterine cavity. This way, controlled, rhythmic uterine motion was generated while maintaining the original speckle characteristics. The use of the proposed set-up was tested for comparison of ultrasound speckle tracking methods. Block matching by sum of absolute differences (SAD) with three different block sizes was employed as a use case for speckle tracking evaluation. Correlation coefficient (r), mean square error (MSE), and Hausdorff distance (H_d), were the adopted objective metrics for evaluating the speckle tracking performance. The two markers, along with the driving signal of the actuator, represented the reference for assessing the speckle tracking accuracy. SAD was optimized and compared for its agreement with the reference signals. The results show the tracking performance of SAD with higher block size (1.724 x 1.724 mm²) to produce the most accurate tracking of the controlled tissue (speckle) motion ($p < 0.05$). To conclude, the realized proposed experimental set-up represents a realistic ground truth for uterine motion, allowing objective evaluation of speckle tracking techniques and aiding with the choice of the optimal imaging settings for quantitative imaging of uterine motion outside pregnancy.

From: F. Sammali, C. Blank, L. Xu, Y. Huang, N. P. M. Kuijsters, B. C. Schoot, and M. Mischi, "Experimental set-up for objective evaluation of uterine motion analysis by ultrasound speckle tracking", *Biomedical Physics & Engineering Express* 2018, vol 4(3), p 035012.

4.1 INTRODUCTION

Ultrasound (US) imaging represents a valid, non-invasive, and safe option for quantitative analysis of the uterus and can be used as an alternative to invasive techniques, such as intra-uterine pressure measurements, and hysterosalpingoscintigraphy, in order to investigate the uterine mechanical function¹. Current knowledge on uterine motion is however limited. Only qualitative evaluation of uterine motion has been performed, evidencing variations of uterine contractile patterns during the menstrual cycle² and the important role of peristaltic movements on infertility treatment outcome³.

Accurate interpretation of the resulting US image sequences is challenging also for skilled and experienced operators⁴. Therefore, the operator-dependency of qualitative ultrasound analysis hampers its adoption for assessment of the uterine function in relation to uterine dysfunctions and infertility.

Motion tracking by US imaging is an active field of scientific research that has already been translated into several applications; in particular, for cardiovascular⁵ and muscular⁶ investigations, and vector Doppler imaging⁷⁻⁹. A general approach, not requiring access to the US scanner hardware and radio frequency (RF) signals, consists of tracking the characteristic speckle pattern of ultrasound grey-level images^{10,11}.

The characterization of the uterine motion outside pregnancy, and in relation to uterine dysfunctions, is not trivial due to several technical and clinical challenges, such as complex and irregular patterns, complex multilayer uterine structure and speckle distribution, limited and slow uterine motion as compared to neighbouring structures, and speckle anisotropy and depth dependency. Against these challenging aspects, a speckle tracking algorithm can be designed and optimized for quantification of uterine motion.

Quantitative analysis by use of motion tracking and strain imaging has so far only been performed either *in-vitro*, by the use of dedicated phantoms producing fluid-driven motion¹² or *ex-vivo*, by applying a freehand palpation to an *ex-vivo* uterus to produce mechanical stimulus for US strain imaging¹³. However, assessing the quality of the developed methods is challenging due to the lack of a reliable reference for the uterine strain and motion.

In this paper, we propose a system for objective evaluation of the speckle tracking performance on three *ex-vivo* uteri, whose controlled rhythmic motion is generated by a dedicated experimental set-up. The resulting speckle pattern reproduces that of a real uterus. The *ex-vivo* uterus was marked with two hypodermic needles to produce clear markers. Objective metrics were employed for speckle tracking evaluation. As a use case to evaluate the utilization of the proposed experimental set-up, this was tested to optimize the block size for speckle tracking by block matching with sum of absolute differences (SAD) cost function. The results confirmed that the realized experimental set-up can support the development of uterine motion and strain imaging methods by providing objective comparison/evaluation of the tracking performance.

4.2 METHODS

4.2.1 Experimental set-up

The realized set-up permits generating a controlled, sinusoidal, and linear displacement of a syringe piston for inducing uterine rhythmic motion. Figure 4.1 shows an overview of the experimental set-up.

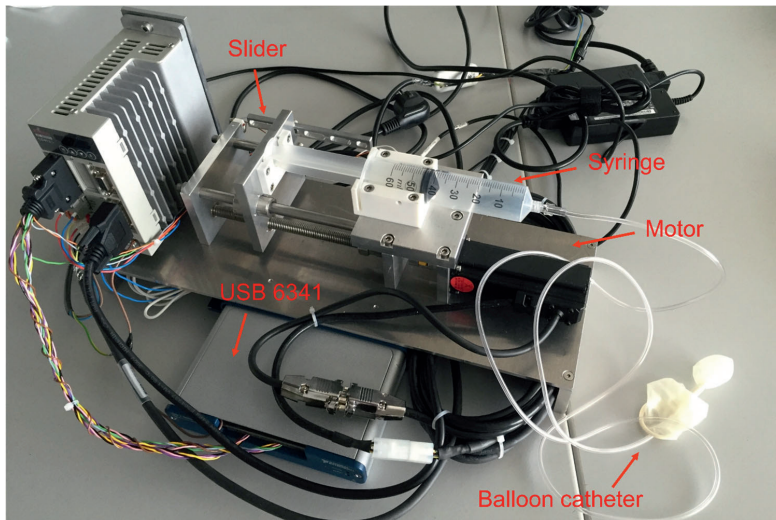


Figure 4.1: The experimental set-up.

Uterine motion is generated by an electromagnetic actuator. The adopted electromagnetic actuator is a servo motor (SMH40S, Kinco, Shenzhen, China) generating rotary motion at its output shaft, as shown in Figure 4.1. The voltage driving the actuator is generated by a National Instrument (NI) Board (USB 6341, National Instruments, Austin, Texas, USA), which is connected to a laptop and controlled by dedicated software implemented in LabView® (National Instruments, Austin, Texas, USA). The driver (IndraDrive HCS02, Bosch Rexroth, Boxtel, The Netherlands), which works in analog voltage mode, receives the driving voltage to control the motor. A screw-slider system with pitch equal to 1.8 mm is connected to the output shaft of the motor in order to convert rotary motion into linear motion at the slider. The motor and the slider are mounted on a metal frame, as shown in Figure 4.1. A syringe is employed for fluid injection into a balloon catheter, which is placed into the uterine cavity of the *ex-vivo* uterus. The barrel of the syringe is fixed to a holder mounted on the metal frame of the screw-slider system, while the plunger of the syringe is connected to the slider such that its motion is facilitated. By moving the slider forward and backward, the plunger of the syringe can slide injecting and withdrawing fluid through the balloon catheter, respectively. This way, repetitive inflation and deflation of the *ex-vivo* uterus is generated, thus simulating the rhythmic uterine motion.

LabView® software is employed to implement the actuator control as well as to realize the system user interface. A sinusoidal motion (injection volume) is adopted to mimic real uterine motion, choosing a period equal to one cycle of the simulated rhythmic uterine motion, as shown in Figure 4.2a. The injection volume is then converted into motion range of the syringe plunger based on the diameter of the adopted syringe. The adopted motion results in a sinusoidal velocity of the plunger as shown in Figure 4.2b. The velocity of the plunger is then converted into rotary velocity of the motor, according to the pitch of the screw equal to 1.8 mm. The injection volume, the inflation and deflation time (period in seconds), and the initial position of the syringe can be independently adjusted by the operator. The core software is implemented in a while loop using a feedback control scheme. Inside each loop, the real time position of the syringe plunger is first measured by the rotary encoder. A state

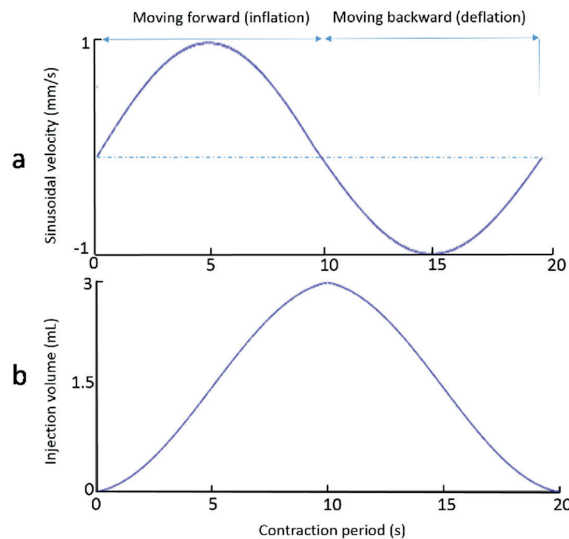


Figure 4.2: Velocity of the syringe (a) and injection volume (b) during inflation and deflation of the ex-vivo uterus for mimicking peristaltic uterine movement.

machine is then adopted to determine the next state of the actuator, i.e., inflating, deflating or no motion, based on the current state and the measured position of the plunger. The instantaneous velocity is first determined according to the next state and position of the plunger and then sent to the NI Board controlling the motor driver. The execution time of one loop is about 10.1 ms, resulting in a sampling frequency of the position/rotary encoder of 90 Hz. The entire program flowchart is shown in Figure 4.3.

US acquisition was performed at the Catharina Hospital Eindhoven (the Netherlands). The surgery for uterus removal was preventive laparoscopic hysterectomy; therefore, the removed uterus presented benign pathology. The patient signed an informed consent prior to the surgery, and all acquired post-surgical imaging was exempt from Regional Ethics Review Board

approval, under the legal requirements for clinical research in the Netherlands. 4-min US recording was performed in saline on the *ex-vivo* uterus, immediately after LH. An US scanner WS80A (Samsung-Medison) equipped with a transvaginal V5-9 probe imaging at 5.6 MHz (central frequency) was employed for the US acquisition. The acquisition frame rate was 30 frames/s, which was amply sufficient to meet Nyquist condition given the limited bandwidth of uterine motion². The acquired grey-level data were then exported in AVI (Audio Video Interleave) format for off-line analysis, implemented in Matlab® (MathWorks, Natick, USA). This implied the use of log-compressed data, as implemented in all US scanners for visualization purpose.

Immediately after laparoscopic hysterectomy, the human *ex-vivo* uterus was first marked with two hypodermic needles, as shown in Figure 4.4, to realize clear markers as a reference for uterine motion tracking. The *ex-vivo* uterus was then submerged in a saline-filled plastic container, and sustained by a polyvinyl chloride (PVC) transparent foil fixed at the two sides of the container.

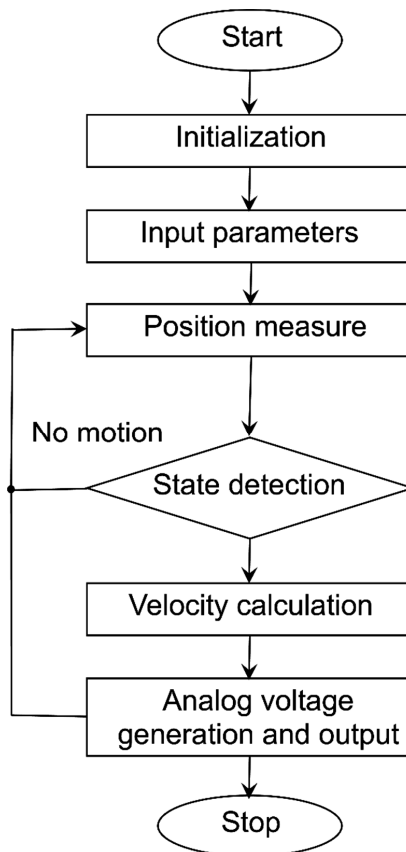


Figure 4.3: Flowchart of the control software implemented in LabView®.

A sterile syringe (BD Plastipak™, Luer-Lok™ Syringe) was employed to inject 3 mL of saline through a balloon catheter (Drip SWAN® I88, Transfusion set). In order to avoid air bubbles into the uterine cavity, the balloon catheter was inserted into the uterine cavity under saline, and sutured, similar to a drain¹⁴, with a surgical knot tied tightly above the cervix of the *ex-vivo* uterus. Motion artefacts were avoided by holding the transvaginal probe with a US probe holder during the acquisition. An acoustic absorber was positioned on the bottom of the container for limiting US reflection and reverberation while imaging the *ex-vivo* uterus.

Rhythmic uterine motion was induced with periodic (sinusoidal) inflation and deflation of the uterine cavity. A period of 20 s (0.05 Hz), corresponding to an average contraction period², was set to generate one cycle of the rhythmic uterine motion. Finally, we operated the experimental set-up with synchronized US B-mode recording. This way, realistic and controlled uterine motion was generated while maintaining the original speckle characteristics of the uterus. Figure 4.5 shows the complete set-up (experimental set-up and *ex-vivo* uterus).

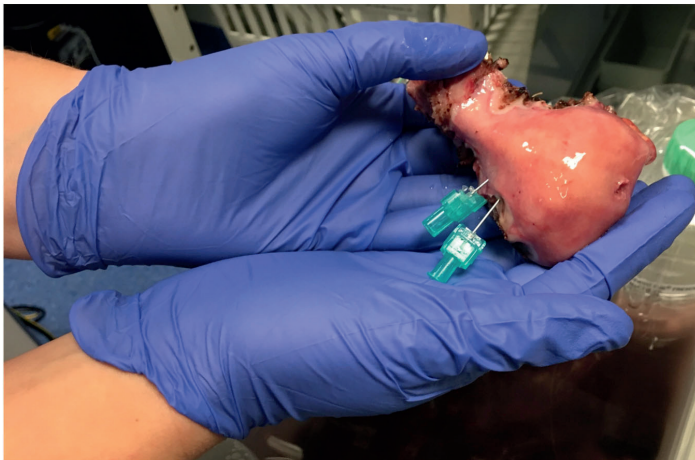


Figure 4.4: Example of one *ex-vivo* uterus marked with two hypodermic needles.

4.2.2 Experimental set-up validation

The motion generated by the experimental set-up was validated using six needle markers inserted in the myometrial wall of three different *ex-vivo* uteri. In particular, two needle markers were inserted in each *ex-vivo* uterus. One of the six needle marker was not visible on the US image providing poor speckle contrast for tracking; therefore, only five needle markers were automatically tracked over time by optical flow (OF) based on Lucas-Kanade algorithm with a neighbourhood size (number of equations) experimentally chosen equal to twice the speckle size ($1.724 \times 1.724 \text{ mm}^2$); this method was proven to be especially suitable for needle tracking¹⁵. The motion of the needle markers was estimated along the lateral and axial direction and the displacement (Euclidean distance) of each needle marker was then computed between subsequent frames, resulting in an absolute motion. The absolute motion of each needle

marker was then compared with the corresponding driving signal to establish the accuracy and reproducibility of the controlled and rhythmic uterine motion generated by the proposed experimental set-up. The adopted objective metrics for the signal agreement are described further on.

4.2.3 Use case of speckle tracking evaluation

The use of the proposed experimental set-up was tested for optimization of 2D US speckle tracking methods. Block matching by SAD cost function was employed in this study as use case for uterine speckle tracking evaluation. Its evaluation and optimization was shown on one human *ex-vivo* uterus by means of the proposed experimental set-up. For each US loop acquired, twelve blocks were positioned around each marker (needles) in a way that shadowing from the needles was avoided (Figure 4.6). The twelve surrounding blocks were simultaneously tracked over time by the 2D speckle tracking method under evaluation. The markers, together with the sinusoidal driving signal of the electromagnetic actuator, represent the reference for assessing the speckle tracking accuracy. Prior to speckle tracking, each image in the acquired loops was first pre-processed to regularize the spatial resolution, here represented by the speckle size. The convexity of the adopted transvaginal probe enhances the anisotropy and depth dependency of the image resolution, complicating the block-matching implementation. Therefore, image regularization was obtained by Wiener deconvolution filtering after performing an *in-vitro* experiment as proposed by Kuenen et al.¹⁶. After regularization, the resulting images presented an isotropic resolution with speckle size of 0.862 mm, calculated as the full-width half-maximum of the autocorrelation function¹⁷. Being the adopted frame rate (30 Hz) relatively high compared to the slow myometrial motion $\leq 2\text{mm s}^{-1}$ ¹⁸, the US images were up-sampled in space (bilinear interpolation) by a factor of two to increase the tracking resolution and to detect subpixel motion.

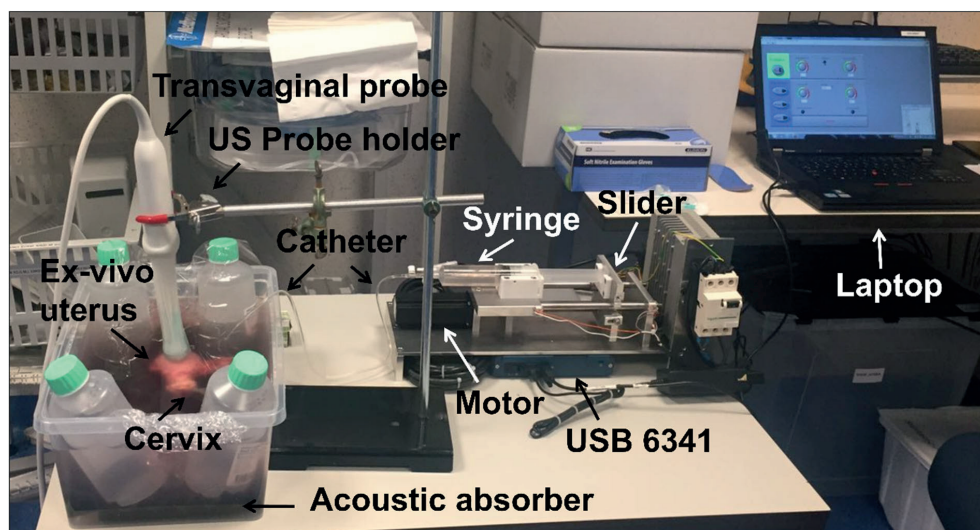


Figure 4.5: The complete set-up (experimental set-up and *ex-vivo* uterus) inducing simulated rhythmic uterine motion for validation of speckle tracking algorithm.

Off-line analysis of the collected grey-level data consisted of performing a block-matching algorithm based on SAD to track the controlled uterine speckle motion. In order to determine the search area needed for block matching analysis, each search area was adjusted to cover the maximum displacement expected between two consecutive frames. The controlled uterine speckle motion estimation was performed across subsequent frames with three different block sizes. In particular, $0.431 \times 0.431 \text{ mm}^2$ (BSize1), $0.862 \times 0.862 \text{ mm}^2$ (BSize2), and $1.724 \times 1.724 \text{ mm}^2$ (BSize3) block sizes were used that correspond to half, once, and twice the speckle size, respectively.

4.2.4 Objective metrics for signal agreement

In order to validate the experimental set-up, the absolute motion of the needle markers was compared with the driving signal. Correlation coefficient (r) and mean square error (MSE) are standard similarity metrics that can be used to evaluate the agreement between two signals.

Here, Hausdorff distance (H_d)¹⁹ is also adopted as an additional distance metric to evaluate the similarity between the absolute motion of the needle markers and the driving signals. In general, given two sets of points $A = a_1, \dots, a_i$ and $B = b_1, \dots, b_j$, H_d can be expressed as

$$H(A, B) = \max(\vec{h}(A, B), \vec{h}(B, A)), \quad (4. 1)$$

with

$$\vec{h}(A, B) = \max_{a \in A} (\min_{b \in B} \|a - b\|) \quad (4. 2)$$

being the directed Hausdorff distance from A to B . The Euclidean distance between each point a_j in A and all points b_j in B is first calculated and then the minimum is chosen. This procedure is repeated for all points a_j in A . $\vec{h}(A, B)$ is then defined as the maximum distance from A to B . The distance $\vec{h}(A, B)$ is not symmetric, therefore, between the two directions, $\vec{h}(A, B)$ and $\vec{h}(B, A)$, the maximum is considered.

H_d is a measure of the spatial distance between two sets of points and it represents the maximum deviation between two compared sets. H_d is a representative index not only of the distance of contours in absolute terms, but also of the shape of a sets. Here, the two sets of points are represented by the motion of the driving signal and the absolute motion of the needle markers.

Mean and standard deviation of the described objective metrics were then considered as an indication of reproducibility of the generated motion and resulting measurements. Good reproducibility is required to consider the generated motion of the needle markers as a reference for assessing the quality of the employed block-matching algorithms.

These objective metrics are also adopted for the use case, in order to assess the performance of the 2D speckle tracking algorithm for its ability to follow the (reference) motion of the two needle markers. The estimated motion of the surrounding blocks was compared with the motion of their respective needle markers. In particular, similarity analysis was performed between the absolute motion of the two needle markers and the one of their surrounding blocks. This way, twenty-four values (twelve for the comparison between marker 1 and its surrounding blocks, and twelve for the comparison between marker 2 and its surrounding blocks) per each similarity measure were obtained. Mean and standard deviation of the 24 MSE, and H_d values were then calculated.

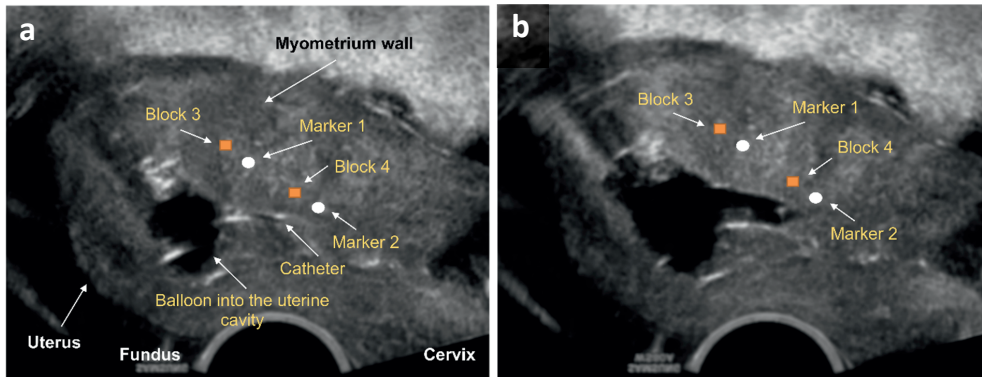


Figure 4.6: Transvaginal ultrasound image of the ex-vivo uterus. Example of blocks' placement in the first frame (a) before volume injection in the uterine cavity: two white blocks are placed on top of the two hypodermic needles (marker 1 and 2) and two of their surrounding (orange) blocks are placed next to the markers. The two markers are tracked over time by optical flow while the two orange blocks are tracked over time by block-matching. In (b) the position of the blocks and markers during speckle tracking is shown after volume injection into the uterine cavity.

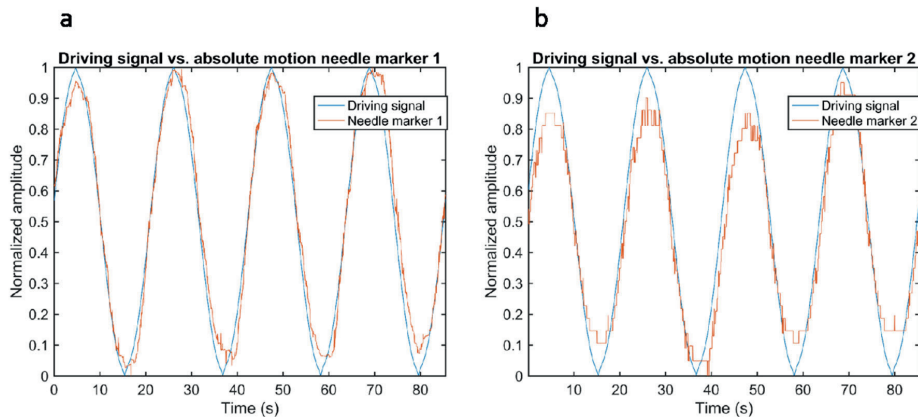


Figure 4.7: Example of comparison between the driving signal and the absolute motion of needle marker 1 and 2, represented in (a) and (b), respectively, during 4 cycles. In both graphs, the blue signal represents the driving signal. The two signals are normalized and aligned in time.

4.2.5 Statistical analysis

Statistical analysis was performed in order to compare the three block sizes adopted in the tested SAD block-matching algorithm. According to Shapiro-Wilk test²⁰, all data were not Gaussian distributed ($p < 0.05$). Therefore, the three adopted block sizes were compared per each adopted similarity measure, r , MSE, and H_d by Kruskal-Wallis test²¹ for establishing the significance level (p value) of the mean values. Wilcoxon signed rank test²² was then performed as multi-comparison test between the three groups. For all the analyses, the confidence level α was set at 0.05.

4.3 RESULTS

4.3.1 Experimental set-up validation

Figure 4.7 shows an example of comparison between the driving signal and the absolute motion provided by the two needle markers inserted in one *ex-vivo* uterus. Table 4.1 reports the similarity results when comparing the absolute motion of the needle markers with the driving signal, for validation of the experimental set-up. The results are reported in terms of mean \pm standard deviation.

4.3.2 Use case

Figure 4.8 shows an example of absolute motion for marker 1 and 2 compared with that estimated by tracking a surrounding block with SAD using BSize3. The values of the adopted similarity measures for assessment of SAD tracking are plotted in Figure 4.9 in terms of mean \pm standard deviation. The values are obtained for the three adopted block sizes (BSize1, Bsize2 and BSize3) when comparing the markers with their surrounding blocks. These results are obtained averaging the 24 values obtained from the similarity analysis between markers and surrounding blocks for each block size.

Our statistical analysis on the MSE results reveal the separation between the three different groups (BSize1 - BSize2, BSize1 - BSize3, and BSize2 - BSize3) to be significant ($p < 0.05$), with BSize3 showing the best performance.

4.4 DISCUSSION

Motion and strain analysis by US speckle tracking has recently gained attention for the assessment of the uterine motion. However, the optimization of this technology is hampered by the lack of a ground truth. The proposed experimental set-up based on a human *ex-vivo* uteri is proven to be able to generate controlled and rhythmic uterine motion. The high agreement reported in Table 4.1 and obtained by comparing the absolute motion of the needle markers with the driving signal, shows the ability of the needle markers to follow the well-controlled and rhythmic uterine motion generated by our experimental set-up. As a results, the

motion of the needle markers can be considered as a reference for assessing the quality of block-matching algorithms. Since we are interested in the evaluation of motion in space, the driving signal alone does not provide sufficient information for validation of speckle tracking methods.

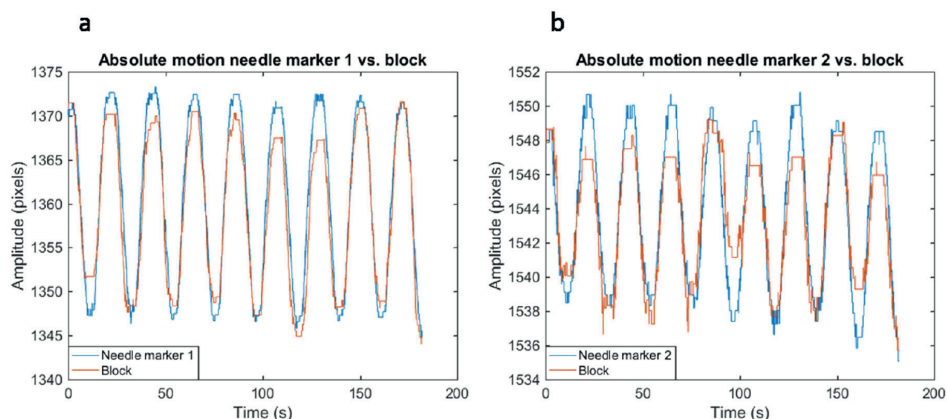


Figure 4.8: Example of comparison between the absolute motion of needle marker 1 and one of its surrounding blocks (a). Example of comparison between the absolute motion of needle marker 2 and one of its surrounding blocks (b). The two signals in both (a) and (b) start from the same position and they refer to the blocks' placement depicted in figure 6. Here, the surrounding blocks are tracked by SAD with BSize3 (twice the speckle size).

The developed experimental set-up leads to motion limitations compared to real uterine peristalsis (UP). UP is known as rhythmic wave-like motion that propagates along the myometrium in different directions for different phases of the natural menstrual cycle²³. Our set-up is not able to generate a propagating wave that mimics such a real condition. However, reproducing real UP goes beyond the objective of this study, which focuses on generating controlled tissue motion maintaining the original uterine speckle characteristics for objective evaluation of speckle tracking performance. For the provided use case, i.e. SAD block matching with different block sizes, significant difference ($p < 0.05$) was revealed by the performed Kruskal-Wallis test only when MSE was employed as a similarity measure. Based on Wilcoxon signed rank test, the performance of SAD tracking with the three adopted block sizes was significantly different, revealing SAD tracking with BSize3 ($1.724 \times 1.724 \text{ mm}^2$) to produce the best performance. Also when a significant difference was not found, our results showed that SAD tracking improved its performance with increased block size at the expense of worse spatial resolution²⁴. A possible explanation may be that SAD metrics are affected by time variations of the signal mean and variance; a larger block contains more samples and those variations are mitigated by the included larger statistics^{25,26}.

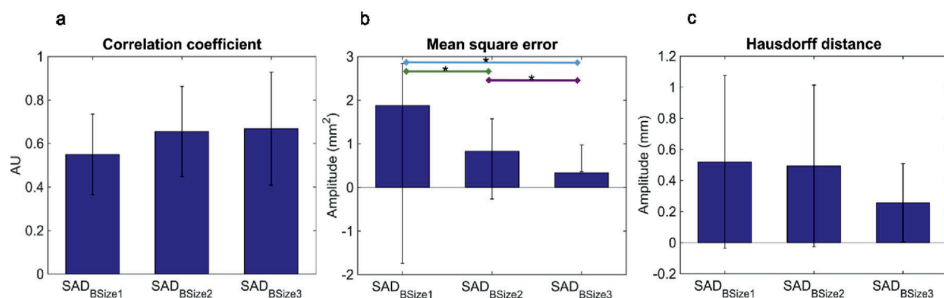


Figure 4.9: Similarity results: (a) Correlation coefficient (r) results for SAD cost function with the three adopted block sizes (BSize1, BSize2 and BSize3). The results are reported in terms of mean \pm standard deviation; (b) MSE results for SAD cost function with the three adopted block sizes (BSize1, BSize2 and BSize3). The results are reported in terms of mean \pm standard deviation. The asterisk (*) indicates a significant difference ($p < 0.05$); (c) H_d results for SAD cost function with the three adopted block sizes (BSize1, BSize2 and BSize3). The results are reported in terms of mean \pm standard deviation.

We only tested block sizes up to twice the speckle size because larger block sizes would be too large compared to the myometrium size and the resulting spatial resolution would hamper the analysis. In this study, our experimental set-up was used and tested for evaluation of speckle tracking techniques with B-mode imaging data; however, performance evaluation on RF data is also possible for more accurate estimate of displacement due to the available phase information.

In this study, a simple sinusoidal wave was employed to approximate uterine motion. To this end, a realistic frequency was selected based on the literature. However, different motion patterns can also be generated with the proposed experimental set-up; different motion can be especially useful for testing and optimizing the tracking in different conditions. Moreover, unhealthy uteri with pathologies such as adenomyosis or myomas could be employed. Pathological uteri may be characterized by different speckle and the tissue motion may differ with respect to healthy uterine tissue; therefore, by marking with needles both the pathological and healthy tissue, it would be possible to assess differences in tissue strain reflecting different mechanical properties of tissue. This way, we could understand the influence of pathological uteri on uterine motion, enabling doctors and physicians to enrich their diagnostic information and improve treatment.

Table 4.1: Similarity results. Comparison between the driving signal and the absolute motion of the five needle markers. These results are reported in terms of mean \pm standard deviation and they refer to the signals normalized in amplitude and aligned in time.

Compared signals	Correlation coefficient (r)	Mean squared error (MSE)	Hausdorff distance (H_d)
Needle marker vs. driving signal	$0,909 \pm 0,054$	$0,010 \pm 0,009$	$0,413 \pm 0,250$

4.5 CONCLUSION

An experimental set-up based on a human *ex-vivo* uterus is proposed for generating controlled and rhythmic uterine tissue motion while maintaining the original speckle characteristics, thus providing a reliable ground truth for objective evaluation of US speckle tracking techniques aimed at quantitative analysis of uterine motion. The recorded US videos can therefore support with the choice of optimal imaging settings for uterine motion and strain quantification in clinical studies. To this end, by means of the developed experimental set-up many other speckle tracking algorithms, such as normalized cross-correlation, mean square differences, and non-normalized correlation, can be tested and compared beyond SAD, employing different block sizes.

4.6 ACKNOWLEDGEMENTS

We acknowledge the help of dr. Cristina Caresio from the "Politecnico di Torino", Italy, with the measurements in the hospital.

4.7 FUNDING

We acknowledge the Dutch TTW HTSM-13901 grant along with the financial contribution from Ferring and Samsung companies.

BIBLIOGRAPHY

1. Birnholz, J. C. Ultrasonic visualization of endometrial movements. *Fertil. Steril.* **41**, 157–158 (1984).
2. Bulletti, C. *et al.* Uterine contractility during the menstrual cycle. *Hum. Reprod.* **15**, 81–89 (2000).
3. IJland, M. M., Hoogland, H. J., Dunselman, G. A. J., Lo, C. R. & Evers, J. L. H. Endometrial wave direction switch and the outcome of in vitro fertilization. *Fertil. Steril.* **71**, 476–481 (1999).
4. Bulletti, C. & de Ziegler, D. Uterine contractility and embryo implantation. *Curr. Opin. Obstet. Gynecol.* **18**, 473–484 (2006).
5. Lopata, R. G. P. *et al.* Dynamic imaging of skeletal muscle contraction in three orthogonal directions. *J. Appl. Physiol.* **109**, 906–915 (2010).
6. Kawagishi, T. Speckle tracking for assessment of cardiac motion and dyssynchrony. *Echocardiography* **25**, 1167–1171 (2008).
7. Bohs, L. N., Geiman, B. J., Anderson, M. E., Gebhart, S. C. & Trahey, G. E. Speckle tracking for multi-dimensional flow estimation. *Ultrasonics* **38**, 369–375 (2000).
8. Udesen, J. *et al.* High frame-rate blood vector velocity imaging using plane waves: Simulations and preliminary experiments. *IEEE Trans. Ultrason. Ferroelectr. Freq. Control* **55**, 1729–1743 (2008).
9. Lenge, M. *et al.* High-frame-rate 2-D vector blood flow imaging in the frequency domain. *IEEE Trans. Ultrason. Ferroelectr. Freq. Control* **61**, 1504–1514 (2014).
10. Wagner, R. F., Insana, M. F. & Brown, D. G. Unified approach to the detection and classification of speckle texture in diagnostic ultrasound. *Opt. Eng.* **25**, 738–742 (1986).
11. Burckhardt, C. B. Speckle in Ultrasound B-Mode Scans. *IEEE Trans. Sonics Ultrason.* **25**, 1–6 (1978).
12. Hobson, M. *et al.* Anthropomorphic Phantoms for Assessment of Strain Imaging Methods Involving Saline-Infused Sonohysterography. *Ultrasound Med. Biol.* **34**, 1622–1637 (2008).
13. Hobson, M. *et al.* In vitro uterine strain imaging: Preliminary results. *J. Ultrasound Med.* **26**, 899–908 (2007).
14. Hormbrey, E., Pandya, A. & Humzah, D. Drain fixation made foolproof. *Ann. R. Coll. Surg. Engl.* **82**, 290–292 (2000).
15. Lee, S. S. M., Lewis, G. S. & Piazza, S. J. An algorithm for automated analysis of ultrasound images to measure tendon excursion in vivo. *J. Appl. Biomech.* **24**, 75–82 (2008).
16. Kuenen, M. P. J. Contrast-ultrasound dispersion imaging for prostate cancer localization. *Ultrasound Med. Biol.* **39**, 4268–4271 (2014).
17. Wagner, R. F., Smith, S. W., Sandrik, J. M. & Lopez, H. Statistics of Speckle in Ultrasound B-Scans. *IEEE Trans. Sonics Ultrason.* **30**, 156–163 (1983).
18. IJland, M. M. *et al.* Relation between endometrial wavelike activity and fecundability in spontaneous cycles. *Fertil. Steril.* **67**, 492–496 (1997).
19. Huttenlocher, D. P., Klanderman, G. A., A., K. G. & Rucklidge, W. J. Comparing Images using the Hausdorff Measure. *IEEE Trans. Pattern Anal. Mach. Intell.* **15**, 850–863 (1993).
20. Shapiro, S. S. & Wilk, M. B. An analysis of variance test for normality (complete samples). *Biometrika* **52**, 591–611 (1965).
21. Breslow, N. A generalized test for comparing of censorship to unequal patterns subject. *Biometrika* **57**, 579–594 (1970).
22. Rosner, B., Glynn, R. J. & Lee, M. L. T. The Wilcoxon signed rank test for paired comparisons of clustered data. *Biometrics* **62**, 185–192 (2006).
23. Kuijsters, N. P. M. *et al.* Uterine peristalsis and fertility: current knowledge and future

- perspectives: a review and meta-analysis. *Reprod. Biomed. Online* **35**, 50–71 (2017).
24. Friemel, B. H., Bohs, L. N. & Trahey, G. E. Relative performance of two-dimensional speckle-tracking techniques: normalized correlation, non-normalized correlation and sum-absolute-difference. *1995 IEEE Ultrason. Symp. Proceedings. An Int. Symp.* **2**, 1481–1484 (1995).
 25. Bohs, L. N. & Trahey, G. E. A Novel Method for Angle Independent Ultrasonic Imaging. *IEEE Trans. Biomed. Eng.* **38**, 280–286 (1991).
 26. Trahey, G. E., Allison, J. W. & Von Ramm, O. T. Angle Independent Ultrasonic Detection of Blood Flow. *IEEE Trans. Biomed. Eng.* **BME-34**, 965–967 (1987).

5

DEDICATED ULTRASOUND SPECKLE TRACKING FOR QUANTITATIVE ANALYSIS OF UTERINE MOTION OUTSIDE PREGNANCY

Abstract: *Fertility problems are nowadays being paralleled by important advances in assisted reproductive technologies. Yet the success rate of these technologies remains low. There is evidence that fertilization outcome is affected by uterine motion, but solutions for quantitative analysis of uterine motion are lacking. This work proposes a dedicated method for uterine-motion quantification by B-mode transvaginal ultrasound. Motion analysis is implemented by speckle tracking based on block matching after speckle-size regularization. Sum of absolute differences is the adopted matching metrics. Prior to the analysis, dedicated Singular Value Decomposition (SVD) filtering is implemented to enhance uterine motion over noise, clutter, and uncorrelated motion induced by neighbouring organs and probe movements. SVD and block matching are first optimized by a dedicated ex-vivo set-up. Robustness to noise and speckle decorrelation is improved by median filtering of the tracking coordinates from surrounding blocks. Speckle tracking is further accelerated by a diamond search. The method feasibility was tested in vivo with a longitudinal study on nine women, aimed at discriminating between four selected phases of the menstrual cycle known to show different uterine behaviour. Each woman was scanned in each phase for four minutes; four sites on the uterine fundus were tracked over time to extract strain and distance signals along the longitudinal and transversal direction of the uterus. Several features were extracted from these signals. Among these features, median frequency and contraction frequency showed significant differences between active and quiet phases. These promising results motivate towards an extended validation in the context of fertilization procedures.*

From: **F. Sammali**, N. P. M. Kuijsters, Y. Huang,, C. Blank, C. Rabotti, B. C. Schoot, and M. Mischi, **“Dedicated ultrasound speckle tracking for quantitative analysis of uterine motion outside pregnancy”**, *IEEE Transactions on Ultrasonics, Ferroelectrics, and Frequency Control* 2018.

5.1 INTRODUCTION

The non-pregnant uterus manifests periodic contractile activity known as uterine peristalsis (UP), which consists of rhythmic contractions of the subendometrial layer of the myometrium (Figure 5.1). UP undergoes cyclic changes that vary throughout the different phases of the menstrual cycle, such as menses (during menstruation) late follicular (LF), early luteal (EL), and late luteal (LL) phases¹⁻³. During menses, UP propagates from the fundus (the upper rounded extremity of the uterus above the orifices of the fallopian tubes) to the cervical end of the uterus (Figure 5.1), contributing to the forward emptying of the uterine contents. As established throughout several studies^{1,4-6}, during the EF phase the UP propagates from cervix to fundus and its frequency increases until the LF phase, just prior to ovulation (pre-ovulatory phase). Here, the UP function is to transport sperm from the vagina to the orifices of the fallopian tubes, where fertilization normally occurs. After ovulation, the frequency of the UP decreases during the transition to the EL and LL phases, when convergent UP predominates. During the LL phase, the uterus is expected to undergo a period of quiescence, facilitating embryo nidation. Based on a possible physiological role of the UP to enhance the reproductive processes, e.g., assistance to sperm transport to the fallopian tubes during follicular phase and support to embryo nidation during luteal phase⁴, there is evidence that dysfunctions of the uterine contractile activity may be involved in infertility problems⁷. Accurate assessment of uterine motion outside pregnancy may therefore open up new possibilities for clinical studies aimed at understanding the link between normal uterine contractility and pathological conditions, such as subfertility and infertility, as well as at improving diagnosis and clinical decision making. To this end, the introduction of a clinical tool for objective assessment of UP, suitable for use in daily practice, would allow identifying patients with normal and abnormal uterine contractility. Transvaginal ultrasound (TVUS) represents a valid, non-invasive, and safe option for the assessment of uterine motion as well as contraction timing, representing a potential tool for assessment and management of couples referred for fertility treatment⁸. At present, only qualitative evaluation of the uterine motion has been performed by visual inspection of ultrasound (US) image sequences⁶. However, accurate interpretation of US image sequences is rather challenging also for skilled and experienced sonographers⁹. The associated operator-dependency hampers the employment of TVUS for clinical studies, where the characterization of uterine motion outside pregnancy is an essential aspect, especially in the field of infertility.

Characterizing the uterine motion is rather complicated due to several technical and clinical challenges, such as complex and irregular patterns, complex multilayer uterine structure and speckle distribution, as well as limited and slow uterine motion compared to neighbouring organs. Against these challenges and to overcome the operator-dependency that hampers the employment of TVUS for clinical studies, in this paper, we present the first dedicated approach for quantification of uterine motion and strain in the non-pregnant, human uterus by US motion tracking. US motion tracking is implemented by speckle tracking after introducing several novelties.

Novel, dedicated Singular Value Decomposition (SVD) filtering is introduced to suppress signals that are uncorrelated with the UP and that affect the speckle tracking performance. For singular value selection, we introduce for the first time an energy ratio (ER) metric.

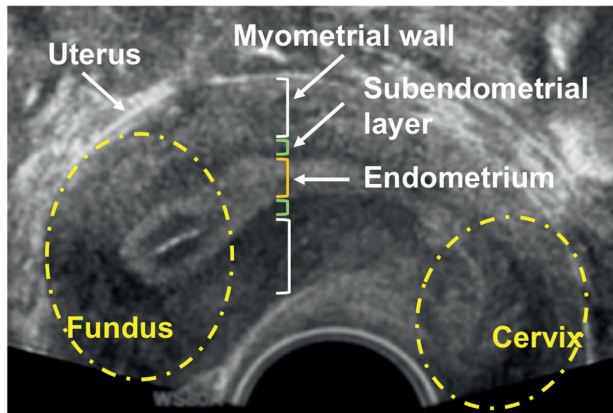


Figure 5.1 Longitudinal view of the uterus during trans-vaginal ultrasound. The white segment indicates the myometrial wall; the green segment indicates the subendometrial layer, also known as junctional zone (inner third of the myometrium); the orange segment indicates the endometrium. The upper rounded extremity on the left of the figure represents the fundus while the extremity on the right represents the cervical end (cervix).

After SVD filtering, speckle tracking is implemented for tracking over time a defined block. The use of the grey-level (demodulated) US loops^{10,11} is adopted to facilitate the clinical translation of the method. The match between corresponding blocks in consecutive frames is determined by similarity measures. Following up on our previous *ex-vivo* work¹², the minimum of sum-of-absolute differences (SAD) is adopted as similarity metrics. The block-matching is accelerated by applying a novel diamond search (DS) strategy instead of the typical full-grid search (FGS) method; similar tracking accuracy is maintained with the benefit of a reduced computational time.

Prior to SAD analysis, homogeneous and isotropic speckle size is obtained by a speckle regularization procedure based on Wiener deconvolution filtering, as proposed by Kuenen et al.¹³. Robustness to noise and speckle decorrelation is improved by applying a novel mean and median filtering on the displacement of neighbouring blocks (matching coordinates).

In this study, the ER metrics and speckle tracking parameters were optimized for improving the speckle tracking accuracy and performance, providing relevant uterine motion quantification for various clinical applications, such as in the context of assisted reproduction technology. The optimization was first carried out *ex vivo*, by means of the experimental set-up proposed in Sammalli et al.¹² (chapter 6 of this thesis). In addition, the DS strategy was tested aiming at reducing the computational time while preserving the tracking accuracy. The proposed method reliability was further optimized and validated *in vivo* by choosing proper filtering for improving the classification performance between the different phases of the menstrual cycle. To this end, the proposed mean and median filtering were validated and compared.

The method feasibility was tested on nine healthy women with a longitudinal study, aimed at discriminating between four selected phases of the menstrual cycle known to show different uterine behaviour. Each woman underwent four US scans during menses, LF, EL, and LL phases, respectively. On the recorded loops, four sites were manually selected on the uterine fundus and tracked over time for the measurement of strain and distance signals along the longitudinal and transversal direction of the uterus. Finally, several frequency and amplitude features were extracted from the measured signals and evaluated for their ability to distinguish between the different phases of the menstrual cycle.

5.2 MATERIALS

5.2.1 Ultrasound data acquisition

This study was approved by the relevant ethical committee and each participant signed an informed consent prior to the measurements. Nine women with no infertility problem were included in this preliminary study. Before inclusion, the participants filled a questionnaire and underwent a hormonal profiling screening to exclude the presence of infertility-related problems. US acquisitions were performed at the gynaecology department at the Catharina Hospital Eindhoven (the Netherlands) both *ex vivo*, as described in ¹², and *in vivo*.

In vivo, during standard recording sessions, 4-min TVUS scans of the uterus were performed while the subject was lying in a supine position and with the operator holding the probe steady. Each woman was scanned four times, during each of the four selected phases of the menstrual cycle: menses, LF, EL, and LL phase, suggested to evidence variations in the uterine contractility pattern¹. An ultrasound scanner WS80A (Samsung-Medison) equipped with a transvaginal V5-9 probe was employed for all the *in-vivo* acquisitions. 2D TVUS acquisitions were performed at 5.6 MHz central frequency and 30 frames/s, amply sufficient to meet Nyquist condition given the limited bandwidth of the uterine movement⁴. The recorded B-mode, grey-level data were then exported in AVI (Audio Video Interleave) format for off-line analysis, implemented in Matlab® (MathWorks, Natick, USA).

5.3 METHODS

5.3.1 Pre-processing

1) *Speckle regularization*: The convexity of the adopted TVUS probe produces evident anisotropy and depth dependency of the speckle size, affecting the block-matching performance. The speckle size was therefore regularized by applying a Wiener deconvolution filter after performing a dedicated *in-vitro* experiment as described by Kuenen et al.¹³. The resulting homogeneous (depth independent) and isotropic resolution was calculated as the full-width half maximum of the autocorrelation function¹⁴. The speckle regularization was performed on both the *ex-vivo* and *in-vivo* US image sequences.

2) *Singular Value Decomposition*: SVD has recently emerged as a method for spatiotemporal filtering in US image analysis¹⁵⁻¹⁷. In general, uterine US image sequences comprise of slow uterine tissue motion along with fast motion elicited by surrounding organs, respiratory motion, and stationary tissue clutter. Signals that are uncorrelated with uterine

motion may affect the block-matching performance, leading to incorrect estimates of uterine motion. To overcome this problem, SVD was here introduced and optimized *ex vivo* prior to its translation *in vivo*. In order to compute SVD, the US image sequences were rearranged into a 2D Casorati matrix representing a new spatiotemporal data representation (Figure 5.2). The 2D Casorati matrix A was then decomposed into a set of spatiotemporal matrices (Figure 5.3) using and adjusting the optimized SVD algorithm proposed by Liu et al.¹⁸, especially dedicated for large matrices. After SVD, a new spatial singular vector basis U and a new temporal singular vector basis V were obtained as

$$A = U\Delta V^T = \sum_i \lambda_i U_i(x, z) \times V_i^T(t) \quad (5.1)$$

where Δ is a diagonal matrix with dimensions $(n_x \times n_z, n_t)$, λ_i are the sorted singular values in Δ , U and V are orthonormal matrices with dimension $(n_x \times n_z, n_x \times n_z)$, and (n_t, n_t) , respectively, U_i and V_i are the i th columns of U and V , and V^T indicates the transposed of V . U_i corresponds to a spatial variation of the singular vectors in A , describing 2D image sequences with dimension (n_x, n_z) , and each column in V_i corresponds to a temporal variation of the singular vectors in A with length n_t . Generally, stationary tissue and clutter are described by the first singular values and vectors, where $U_1(x, z)$ and $V_1(t)$ are the most dominant. On the contrary, high-frequency noise and dynamics are described in the last singular values and vectors^{17,19}. Slow uterine motion is expected to be described by singular values and vectors that are close to the first ones. An image sequence enhancing uterine motion can therefore be reconstructed by selecting a proper range of singular values.

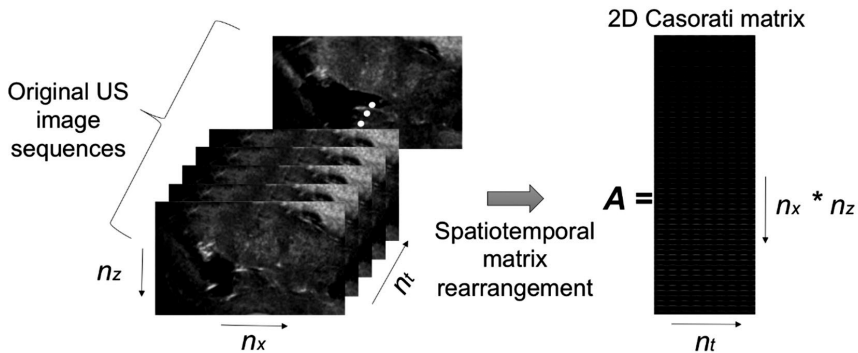


Figure 5.2: The uterine US image sequences are rearranged in one spatiotemporal representation (2D Casorati matrix) where all pixels at each time point are arranged in each column.

3) *SVD filtering:* In the literature, no method has been reported for the automatic selection of singular values resulting in optimal image reconstruction for a given application. Here, we propose an energy metrics to discard undesired singular values while retaining those singular

values related to uterine motion. For each temporal signal $V_i(t)$, two energies were obtained by integration of the power spectrum over the entire frequency band [0-15 Hz] and over the interval $[f_1 - f_2]$. The adopted energy metrics was then based on the following energy ratio (ER),

$$ER_i = \frac{\sum_{f=f_1}^{f_2} |X_i(f)|^2}{\sum_{f=0}^{f_s/2} |X_i(f)|^2} \tag{5.2}$$

where, f_s is the frame rate (sampling frequency), $X_i(f)$ represents the Fast Fourier transform (FFT) of each $V_i(t)$, and i indicates the number of the singular values. The frequency interval $[f_1 - f_2]$ in (5.2) is chosen to reflect the uterine motion bandwidth *ex vivo* and *in vivo*. As a result, the ER represents the amount of uterine dynamics for each singular value compared to the full signal. A range of subsequent singular values, from the first one to the last with ER larger than a defined threshold, was therefore selected to enhance uterine motion in the US video while suppressing undesired components. This range of subsequent singular values was then determined and used for image reconstruction. The value of the ER threshold was optimized *ex vivo*.

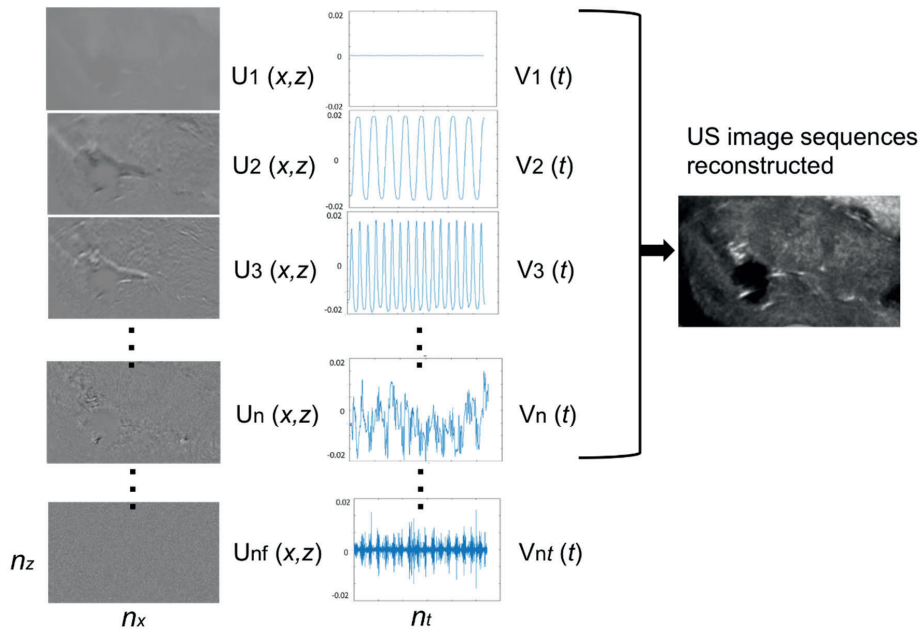


Figure 5.3: Uterine US image sequences are decomposed by SVD into a set of spatio-temporal matrices, U and V .

5.3.2 Ultrasound uterine speckle tracking

Prior to speckle tracking, due to the limited range of uterine motion (expected displacement of 1-2 pixels between consecutive frames), the US image sequences were up-sampled in space (bilinear interpolation) by a factor of 2 to achieve sub-pixel motion estimation. The spatial up-sampling was performed on both the *ex-vivo* and *in-vivo* US image sequences achieving a pixel size of 0.131 mm.

1) *Block matching*: After pre-processing, speckle tracking by block matching was first performed by using a FGS method on the *ex-vivo* US image sequences. In essence, block matching consists of selecting a block in the reference frame and searching for the optimal match in the subsequent frame within a predetermined search area. Following up on our previous work¹², the optimal match was determined by a block similarity measure, here represented by the SAD. The block size was defined equal to twice the speckle size, as this produced the best performance with our *ex-vivo* data¹². Because the SVD reconstruction can influence the speckle size, this was estimated by analysis of the block autocorrelation function on the SVD-filtered image sequence. As a result, different US scans could result in different speckle sizes.

For the FGS method, the search area was adjusted to cover the maximum displacement of the block in the case of maximum uterine tissue velocity (2 mm/s^{20}) which in our case (frame rate = 30 Hz) corresponds to 0.46 mm. The adopted acquisition frame rate (30 Hz) is relatively high compared to the slow myometrial motion 2 mm/s^{20} . Therefore, temporal down-sampling with a frame interval t was also considered and optimized, at the cost of a larger search area.

2) *Diamond search*: Traditional block matching uses the FGS method to find the best matching position, evaluating the block similarity for every pixel inside the search area. Although FGS has the highest accuracy among all the search methods, it also poses the highest computational demand²¹. To overcome this problem while preserving similar tracking quality, a DS strategy was considered for block matching after SVD filtering both *ex vivo* and *in vivo*. Briefly, DS²² is based on predefined search patterns, i.e., large diamond search pattern (LDSP) (Figure 5.4a) and small diamond search pattern (SDSP) (Figure 5.4b). LDSP includes the evaluation among the central pixel and all surrounding pixels with a step size of 2 pixels, while SDSP includes the central pixel and all surrounding pixels with a step size of 1 pixel. The similarity to the block which is centred at the original position in the reference frame is first evaluated for the positions within the LDSP. If the highest similarity is found at the central pixel, SDSP is then applied. On the contrary, the pixel where the highest similarity is found will be treated as the new central pixel. Under this new condition, LDSP is again applied until the highest similarity is found in the centre. Once the search goes to SDSP, only few pixel positions are evaluated and the best match is found at the position with the highest similarity. With its unique search pattern, DS finds the best match evaluating only few pixel positions rather than all pixels in the search area. Following this strategy, the computation effort is greatly reduced. Moreover, the definition of a search area is no longer required.

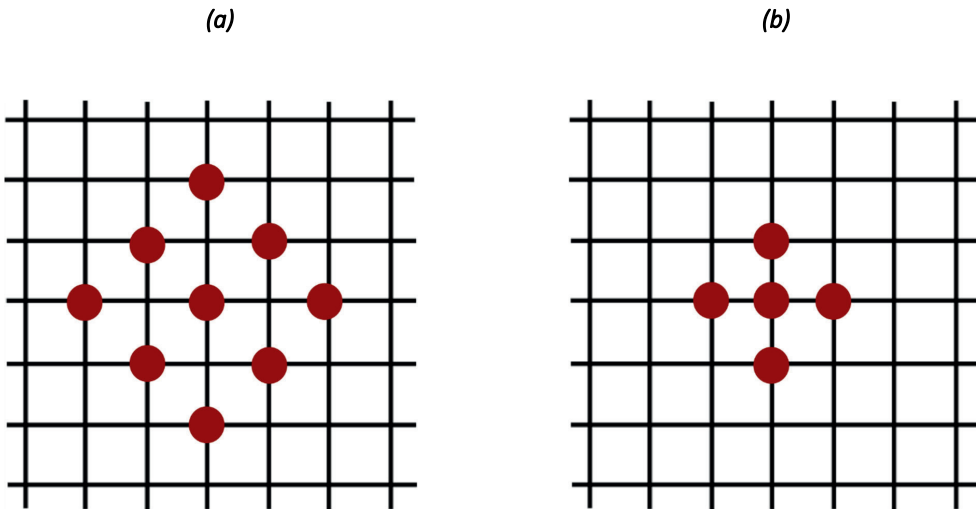


Figure 5.4: (a) Large diamond search pattern. (b) Small diamond search pattern.

3) *Mean and median filter:* Especially *in vivo*, out-of-plane motion and small changes in the interference pattern may cause speckle decorrelation, affecting the tracking accuracy by “peak hopping” in the similarity metrics. Assuming the strain of neighbouring pixels to be comparable, peak hopping can be reduced by shifting the block around the original central position. Here, we introduced a new approach based on the mean and median of the displacements of the neighbouring surrounding blocks; median filtering is in general more robust against outliers, which can be severe when the search is not bound to a predetermined search area such as by DS. Different from previous correlation filtering²³, the proposed filters are suitable to be integrated with a DS strategy.

In vivo, the two filters were integrated in the DS algorithm for finding the best block matching estimated as the mean and median for a number of shifted blocks. Both filters were chosen of size 3 pixels, i.e., only blocks shifted by 1 pixel in all directions (nine blocks in total) were considered for calculating the mean or median displacement. The schematics of the implemented SAD with mean and median filtering is shown in Figure 5.5.

5.4 OPTIMIZATION AND VALIDATION STRATEGY

In this study, several parameters were optimized for improving the speckle tracking accuracy and performance, providing relevant uterine-motion quantification for various clinical applications, such as in the context of assisted reproduction technology. The optimization was carried out through two procedures: *ex vivo*, making use of an *ex-vivo* uterus undergoing controlled movement and establishing a reference to optimize the SVD filter for enhancing the signal generated by the moving uterine structures such that the tracking was closest to the

reference. In particular the ER metrics was optimized for singular value selection. Along with the SVD filter, also the frame interval Δt was optimized to achieve the most accurate tracking. Furthermore, the block matching search by DS was tested aiming at reducing the computational time while preserving the tracking accuracy. The ER metrics and the frame interval Δt were translated *in vivo* and the method reliability was further optimized *in vivo* by choosing proper filtering for improving the classification performance between the different phases of the menstrual cycle. To this end, novel median and mean filters were applied on the displacement of neighbouring blocks to find the best match.

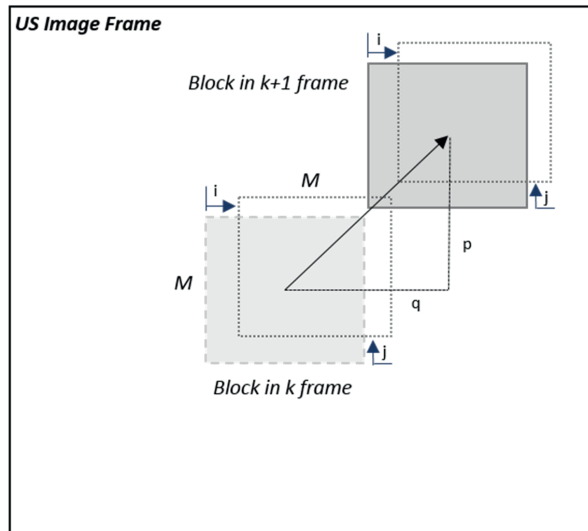


Figure 5.5: Schematics of the implemented SAD with mean and median filter where $M \times M$ represents the size of the block; i and j are the shift in pixels around the centre of the original block in x and y direction, respectively; $(q; p)$ represents the SAD displacement domain between two blocks at subsequent frames.

5.4.1 Ex-vivo optimization

1) *Ex-vivo experimental set-up:* Controlled uterine motion was generated by a dedicated experimental set-up¹². Briefly, an electromagnetic actuator generated a sinusoidal displacement of a syringe piston, injecting saline through a balloon catheter inserted into the uterine cavity of an *ex-vivo* uterus removed by laparoscopic hysterectomy. This way, controlled, rhythmic inflation and deflation of the uterine cavity was generated with a period of 20 s, while maintaining the uterine speckle characteristics. Two needles were inserted in the myometrial wall realizing clear markers as a reference for validation of the uterine motion tracking. Based on 4-min US recording of the moving *ex-vivo* uterus, twelve blocks were positioned around each marker (two needles), following the same measurement protocol as described in chapter 6¹², and tracked over time after SVD filtering. The estimated motion of the total twenty-four blocks was compared with the reference motion of their respective needle markers,

obtained by optical flow tracking on the original video. Two objective metrics, namely the correlation coefficient r and the mean squared error (MSE), were employed to assess the tracking quality in terms of agreement with the reference needle motion. These quality measures were therefore used for optimizing the parameters of the proposed method and evaluating its tracking performance.

2) *Parameter optimization*: The parameters to be optimized were the ER metrics for singular-value selection and the frame interval Δt for speckle tracking. In particular, ER thresholds from 0.4 to 0.8 were tested as well as Δt from 3 to 17 frames with steps of 2 frames. Based on the sinusoidal-motion frequency (0.05 Hz) induced in the *ex-vivo* uterus, a frequency range of 0.05 ± 0.01 was chosen to calculate ER, resulting in a narrow frequency band [$f_1 = 0.04 - f_2 = 0.06$ Hz]. For each parameter setting, the accuracy of the estimated uterine motion after SVD filtering was evaluated with respect to our previous results reported in chapter 6¹².

3) *Full-grid search vs. diamond search*: A comparison between the performance of the two search methods, FGS and DS, was performed on the US image sequences after ER metrics and frame interval Δt optimization. Objective metrics, such as r and MSE, were considered for their comparison. Perfect match would indicate no difference between search algorithms in terms of estimated uterine motion, preserving the same tracking accuracy and substantially improving the time efficiency.

5.4.2 In-vivo validation

The ER metrics and frame interval Δt after optimization *ex vivo* were translated and adjusted *in vivo*. Prior to speckle tracking, the ER metrics was calculated according to Equation 2 in the frequency interval [$f_1 = 0.008 - f_2 = 0.066$ Hz]; based on visual inspection, this frequency band provides a good representation of uterine motion for all the identified phases⁴.

1) *US recording protocol*: Validation in women aimed at testing the proposed speckle tracking method for its ability to discriminate between the four selected phases of the menstrual cycle, i.e. EF, LF, EL, and LL. As described in Section II, two 4-min US loops were acquired in nine healthy women during the four phases. Four sites were manually defined along the myometrial wall in the fundus area which is the most contractile part of the uterus according to the literature¹. In this study we focused on the subendometrial layer of the myometrium (Figure 5.6), being the muscle mostly involved in uterine peristalsis; therefore, two sites were manually defined in the anterior (sites 1 and 2) and two in the posterior wall (sites 3 and 4) of the subendometrial layer as shown in Figure 5.6. The spatial distance between the sites along the longitudinal direction was kept on the order of the block size (twice the speckle size).

The four sites were then tracked over time by the proposed speckle tracking method with the frame interval Δt optimized *ex vivo* and using the optimal image setting based on the *ex-vivo* experiment described in section III-B. The block-matching algorithm was accelerated by the DS and the best match was obtained by applying mean and median filtering on the matching coordinates.

2) *Distance and strain estimation*: The four sites defined on the subendometrial layer were coupled in pairs in order to estimate distance and strain longitudinally and transversally. Longitudinally, sites 1-2 and 3-4 were coupled in pairs P1 and P2, respectively, while transversally, sites 1-3 and 2-4 were coupled in pairs P3 and P4, respectively, as shown in

Figure 5.6. The distance (d) and strain (ϵ) between each pair was then calculated. The distance was defined as the Euclidean distance between each pair of sites in 2D space, resulting in an absolute motion estimate. The strain, ϵ , was defined as the relative variation of the distance between the tracked sites as follows:

$$\epsilon = \frac{d(i) - d(i - 1)}{d(i - 1)} \quad (5.3)$$

with $d(i)$ and $d(i - 1)$ being the distance between the tracked sites at the current frame (i) and the previous frame ($i - 1$), respectively. P1 and P2 measured the contraction in the longitudinal direction of the uterus, P3 and P4 measured the contraction in the transversal direction.

3) *Feature extraction*: Since speckle tracking has never been performed for uterine motion quantification outside pregnancy, there was no reference for the choice of motion features that were able to discriminate between the phases of the uterine menstrual cycle. To this end, our choice was to consider, as a starting point, amplitude- and frequency-related features already used during several studies on electrohysterography in pregnant²⁴ and non-pregnant women²⁵. Therefore, standard deviation (SD), mean frequency (MF), median frequency (MDF), and unnormalized first statistical moment (UFM) were estimated. These specific features were considered in this study in order to obtain a good understanding of the uterine motion in the considered phases in terms of amplitude (described by the SD), frequency (described by the MF and MDF), and energy (described by the UFM). In addition, the contraction frequency, f_c , was also estimated in terms of contractions per minutes.

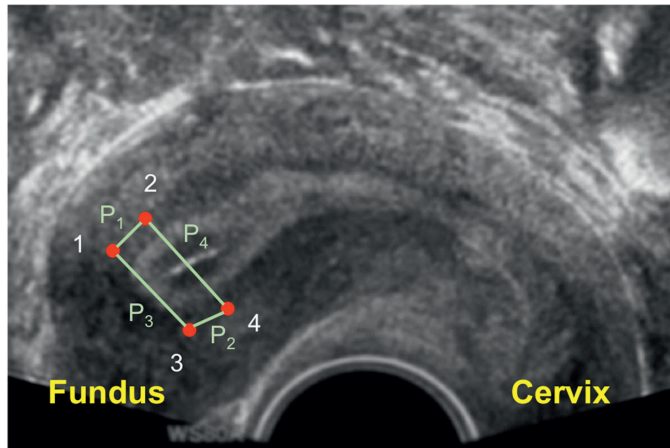


Figure 5.6: US image of the uterus with overlaid markers indicating two couples of sites P1, P2 along the longitudinal direction and two P3, P4 along the transversal direction. The four sites are tracked on the fundus region of the uterus; in particular on the subendometrial layer.

All features, with the exception of the contraction frequency, were extracted from the FFT of the distance and strain signals; in particular, the SD was calculated applying Parseval's theorem. In order to improve their quality and strengthen their link with uterine motion, these features were extracted in the frequency band [$f_1 = 0.008$ - $f_2 = 0.066$ Hz] as used for ER metrics calculation. Estimation of f_c was obtained by a zero-crossing detector in time domain.

5.4.3 Statistical analysis

Statistical analysis was performed to identify significant differences between menses, LF, EL, and LL phases based on the extracted distance and strain features. According to Shapiro-Wilk test²⁶, all data were not Gaussian distributed ($p < 0.05$). Therefore, the four phases were compared for each adopted feature by Kruskal-Wallis test²⁷ to establish the significance level (p value) of the median differences. Dunn-Sidak Post-Hoc test²⁸ was then performed as multi-comparison test between the four groups. For all the analyses, the confidence level was set at 0.05.

5.5 RESULTS

5.5.1 Ex-vivo optimization

Figure 5.7 shows the relation ER vs. singular values, derived from Equation 2 based on the *ex-vivo* experiment. The ER metric was optimized considering thresholds from 0.4 to 0.8 (namely 0.4, 0.5, 0.6, 0.7 and 0.8) highlighted in grey colour as shown in Figure 5.7. For each threshold, singular values were selected consecutively resulting in a choice of eight subsequent singular values.

After SVD filtering, the image sequences presented a speckle size of 1.03 mm^2 , calculated as the full-width halfmaximum of the autocorrelation function¹⁴. The block size for SAD was determined as twice the new speckle size, resulting in $4.12 \times 4.12 \text{ mm}^2$.

Down-sampling after SVD filtering revealed $\Delta t = 15$ frames to produce the best tracking results in terms of r and MSE with respect to the reference markers. These results ($r = 0.84 \pm 0.15$ and $\text{MSE} = 0.29 \pm 0.24$) improved those obtained in Sammali et al.¹² without SVD filtering and down-sampling ($r = 0.66 \pm 0.38$ and $\text{MSE} = 0.34 \pm 0.30$).

Table 5.1 reports the agreement between the two search methods, FGS and DS. Only insignificant differences were revealed by our performance measures r and MSE, showing the DS method to preserve similar tracking accuracy while improving the computational efficiency by over 300%. Therefore, a DS was integrated and used in the block-matching algorithm for patient data analysis.

Table 5.1 Comparison between full search and diamond search method after SVD filtering for $\Delta t = 15$ frames. These results of the two adopted metrics, r and MSE, are reported in terms of mean \pm standard deviation. Their performance difference is expressed in percentage.

Metrics	FGS	DS	Difference %
r	0,843 \pm 0,154	0,841 \pm 0,155	0,200 \pm 0,006
MSE	0,298 \pm 0,246	0,301 \pm 0,244	1 \pm 0,002

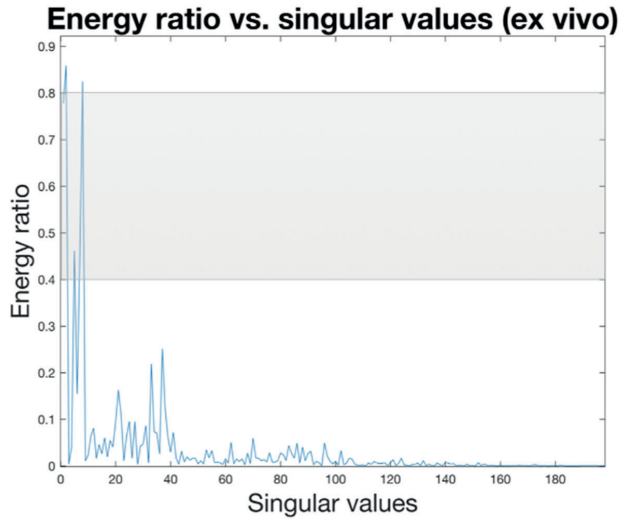


Figure 5.7: *Ex-vivo* energy ratio (ER) calculated per each singular value according to (Equation 2) in the frequency band [0.04 - 0.06 Hz]. The range of the ER thresholds here tested is highlighted in grey. Consecutive singular values are selected for each threshold resulting in the choice of eight singular values.

5.5.2 In-vivo validation

The parameters for SVD filtering and tracking optimized *ex vivo* were translated to the *in-vivo* analysis. An example of ER plot for each selected phase is shown in Figure 5.8. For the *in-vivo* analysis, we considered an ER threshold equal to 0.5, selecting only the singular values representing over 50% of the total energy. The reconstructed US image sequences were based on subsequent singular values in the range $[1, n]$ above 0.5; moreover, the 2nd singular value, which consistently reflected probe motion by the operator, was always discarded. The value of n varied among patients and phases; in particular, the highest averaged value for n , 26.37 ± 4.59 , was selected in the LF phases, following 25.88 ± 3.40 in the EL phases, 25.25 ± 4.33 in the LL phases, and finally, 24.50 ± 7.34 in the menses phases.

The four sites manually selected on each US image for each woman and phase were tracked over time with frame interval $\Delta t = 15$ and applying median filtering. An example of the derived

distance and strain signals relative to the LF phase of one of the included women are shown in Figure 5.9. The features extracted from the measured distance and strain signals were used to discriminate between the four selected phases of the menstrual cycle. Figure 5.10 shows the box plots representing the statistical analysis of the data that provided significant difference between different phases; in particular, the frequency-related features, f_c and MDF extracted from the distance signal along the longitudinal direction provided significant difference between LF and LL phase, and between menses and LF phase, respectively.

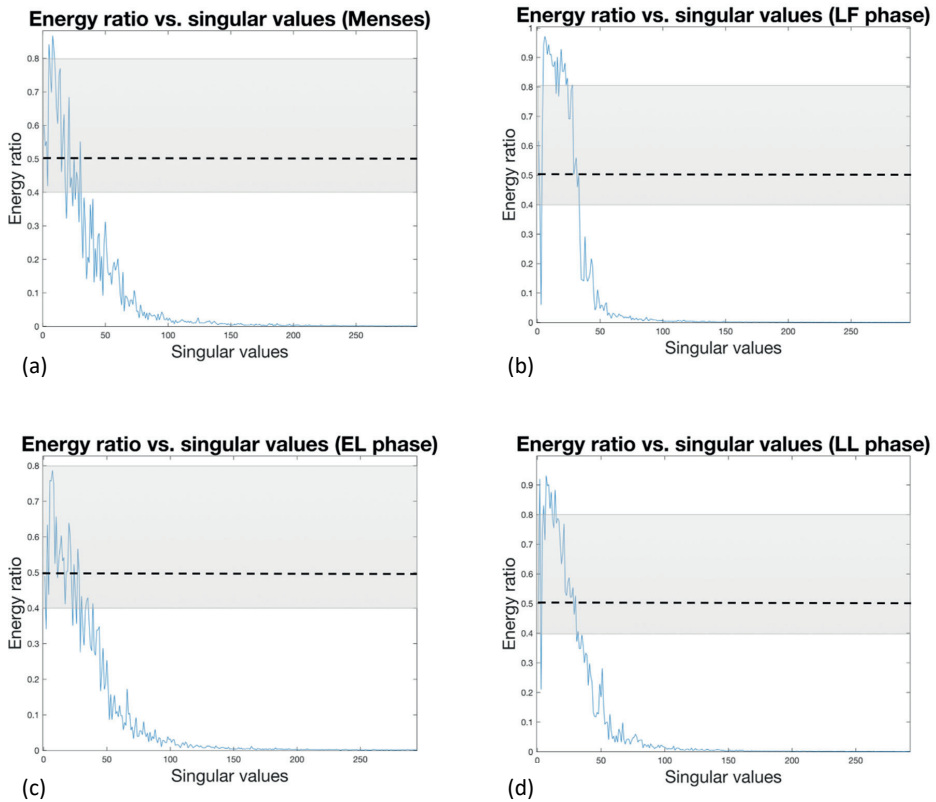


Figure 5.8: Example of energy ratio vs. singular values for the menses (a), LF (b), EL (c), and LL (d) phases in one of the included patients. The energy ratio threshold employed *in vivo* is indicated with the black dashed line.

5.6 DISCUSSION

The characterization of uterine motion outside pregnancy represents a relevant aspect in natural as well as assisted reproduction. Uterine contractions play an important role for the

success of conception⁹. Quantitative assessment of uterine motion outside pregnancy may open up new possibilities for clinical studies aimed at understanding differences in uterine tissue motion and strain reflecting different conditions and functions. Unfortunately, the lack of a quantitative method hampers our understandings of uterine motion and contractility.

This study presents a dedicated approach for quantification of uterine motion and strain by US speckle tracking. The performance of the proposed method is improved by SVD filtering, discarding singular values that are uncorrelated with uterine motion. Median and mean filtering are also introduced to improve the tracking robustness and accuracy of the method. Moreover, a DS is evaluated to improve the computational time. The proposed method is first tested and optimized *ex vivo*, by means of our recently developed experimental set-up based on a human *ex-vivo* uterus, and then translated to *in-vivo* patient-data analysis.

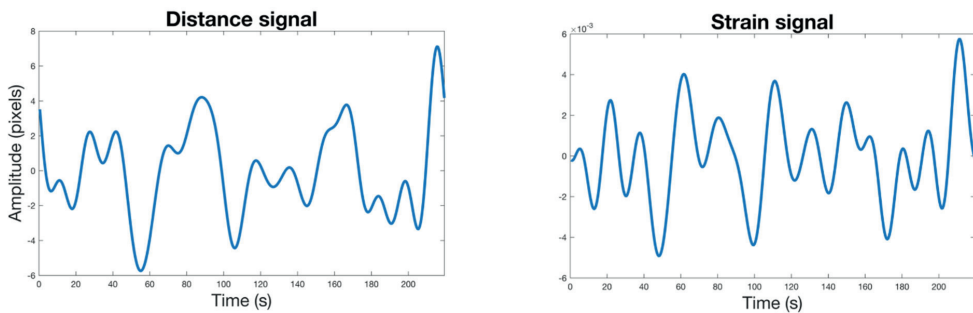


Figure 5.9: Example of distance (a) and strain (b) signal calculated longitudinally from P1 in the LF phase of one of the included woman using frame interval $\Delta t = 15$ frames and median filtering.

Ex vivo, SVD filtering improves the performance of the speckle tracking technique by optimizing the correlation and squared error with our *ex-vivo* reference. This is the result of an enhancement of uterine motion with respect to other components in the signal. SAD block matching algorithm is accelerated by using a DS strategy reducing the computational time to less than 1/3. Several ER thresholds were tested in combination with different frame intervals Δt . Figure 5.7 shows a clear separation between singular values with high and low ER; accordingly, a range of 8 subsequent singular values was selected to reconstruct the US video loop. Generally, below the considered thresholds, singular values can be discarded. In this specific case, discarding singular values below each threshold would have produced the selection of a discontinuous sequence of singular values. Discontinuity in the choice of singular values introduces image artefacts in the reconstructed US loop. Therefore, to overcome this phenomenon, singular values were selected consecutively for each threshold resulting in a choice of 8 subsequent singular values. The improved tracking according to the defined objective metrics supports the proposed ER criterion for SVD filtering. However, alternative options should also be tested and evaluated in future research. Besides the amplitude spectrum of $V(t)$, its phase components can also carry relevant information for singular value selection. After optimization, the proposed dedicated approach outperformed the standard method used in chapter 6¹², showing the best performance for $\Delta t = 15$ frames. Use of a fast DS for block-

matching does not result in deterioration of the tracking quality, as confirmed by the comparable performance with FGS obtained for r and MSE metrics. Therefore, the DS method was adopted for the *in-vivo* block-matching analysis in patients.

In vivo, uterine motion and strain were assessed along the transversal and longitudinal direction by the tracking method optimized *ex vivo*. SVD filtering was applied *in vivo* with an ER threshold of 0.5. This resulted in different singular values for the different phases, with the highest number in the LF phase and the lowest in the menses phase. Although 0.5 seems a reasonable threshold, confirmed by our *ex-vivo* results, future research with a larger dataset should evaluate the effect of different thresholds on the ability to provide accurate assessment of uterine motion.

Based on our *ex-vivo* results, the adopted frame interval, Δt , was 15 frames. However, smaller Δt can also be considered in future studies in order to account for a possibly larger bandwidth compared to that resulting from the sinusoidal motion in the *ex-vivo* set-up.

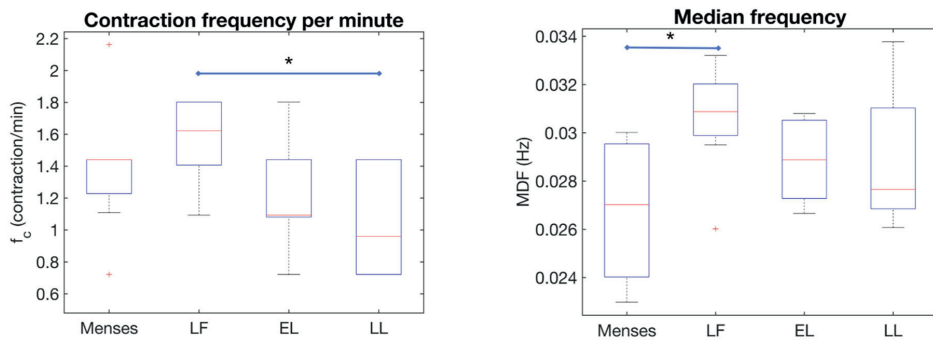


Figure 5.10: Box plots describing the statistical results for f_c (a) and MDF (b) features extracted from the distance signal along the longitudinal direction. The middle red line represents the median of the analysed data while the red crosses (+) represent the outliers. The asterisk (*) indicates a significant difference ($p < 0.05$).

On the measured strain and distance signals, a number of features were extracted to test the ability to distinguish between the menses, LF, EL, and LL phase, where the uterus seems to behave differently, ranging from an active to a quiet state. Our statistical analysis reveals a significant difference ($p < 0.05$) between menses and LF phase, when the MDF is extracted from the distance signal in the longitudinal direction, and between LF and LL phase, when f_c is extracted from the distance signal in the longitudinal direction. These significant results are obtained when median filtering is included in the block-matching algorithm together with the DS. Differently from standard FGS, the DS is not constrained in a predefined search area and the presence of outliers can be severe. Median filtering mitigates the effect of outliers more efficiently than mean filtering, which is especially relevant in combination with a DS without predefined search area.

The number of contractions per minute, f_c , extracted from the distance signal in the longitudinal direction, reveals the LF phase to be the most active phase (1.57 ± 0.27), following

the EL (1.20 ± 0.31), menses (1.38 ± 0.40) and LL (1.05 ± 0.34) phase. The resulting trend is in line with the literature⁴, showing the LF and LL phase as the most active and the most quiet, respectively. Instead, the average number of detected contractions is different than that reported in the literature, with an underestimation in the LF and EL phases and an overestimation in the menses and LL phases. In the literature, f_c is merely based on visual inspection, making no distinction between the different layers of the myometrium muscle and counting a global number of contractions. In this study, we focussed specifically on the subendometrial layer, where the tracking was performed. During the LL phase, the results in Bulletti et al.⁴ suggest the f_c to be equal to 0.8 ± 0.3 contractions/min, while we detected 1.05 ± 0.34 contractions/min. Being the most quiet phase, a possible reason might reside in the low amplitude of LL contractions, which are too small to be visualized and may lead to miscounting by visual inspection.

The MDF extracted from the distance signal in the longitudinal direction revealed the most active phase to be the LF phase, confirming the literature⁴; differently, the most quiet phase was represented by the menses phase. A possible explanation may relate to the special behaviour of menses contractions, when the uterine muscle manifests labour-like activity alternated to quiescent periods of inactivity^{4,29–31}; all the activity concerns mainly the outer two-third layer of the myometrium while the inner one-third or subendometrial layer, the region investigated in this study, remains mostly quiet³². During the other phases, LF, EL, and LL, a wavelike, peristaltic activity of the uterine muscle is reported^{30,33}.

Interesting results to elucidate on the spatial distribution of the uterine activity have also been obtained by electrohysterography (EHG)³⁴, revealing higher uterine activity during the menses phase. Being more sensitive to the outer layers of the myometrium muscle, this EHG study suggests a higher activity of these layers during the menses phase. Combined with our US results (MDF feature) from the subendometrial layer, these EHG results seem to confirm the different activity of inner and outer myometrial layers during this phase.

The finding obtained by the MDF features is also confirmed by the number of selected singular values based on the ER metrics. The singular values refer to the temporal dynamics of the temporal-variation signal $V(t)$; during the LF phase, the uterus seems to show more activity and more singular values are selected for representing that particular uterine state; on the contrary, during menses fewer singular values are selected for representing the quiet state. As a result, data from different women and phases are processed with different SVD filters, retaining a different number of singular values.

SVD filtering could affect the spatiotemporal representation of the signals influencing the speckle size; based on our results, we can observe that less singular values results in larger speckle size, which decreases as more singular values are used to reconstruct the image. Eventually, the speckle size converges to the original one, when all singular values are retained. Obviously, the speckle size can become smaller than the original one when the first singular values are excluded, enhancing higher frequency components that are mostly related to noise. Dedicated work to identify the relationship between the number of singular values selected and the speckle size should be carried out in the future.

The frequency band used in this study was based on the contraction frequencies obtained by Bulletti et al.⁴ for each phase by visual inspection. Based on our results, future studies should investigate different frequency bands, also depending on the tracked myometrial layers. In fact, based on the introduction of novel quantitative tools, the general terminology referring to uterine activity should be made more specific, referring to spectral and amplitude features in relation to local motion and strain, also accounting for their spatial distribution. The presented work represents a first preliminary step in this direction, showing already the ability to distinguish between different phases in the menstrual cycle. The clinical translation of the proposed method requires however more extensive validation and optimization *in vivo*, possibly also in the context of fertilization procedures. This can also spur additional insight expanding our knowledge on UP and its role in conception and fertilization.

5.7 CONCLUSIONS

Characterizing the uterine motion outside pregnancy is rather complicated due to several technical and clinical challenges, such as complex and irregular patterns, complex multilayer uterine structure and speckle distribution, as well as limited and slow motion of the uterus compared to neighbouring organs. Against these challenging aspects, a dedicated speckle-tracking approach based SAD block matching is proposed for quantification of uterine motion. The method is accelerated by DS and improved by SVD and median filtering.

The proposed method was first optimized *ex vivo* by a dedicated experimental set-up and then successfully validated *in vivo* on nine healthy women. The obtained promising results suggest SVD filtering to produce effective enhancement of the uterine motion. Block-matching by SAD including DS and median filtering provided accurate estimation of motion and strain in the longitudinal direction; especially the frequency related motion features, MDF and f_c , showed significant differences between menses and LF phase as well as between LF and LL phase.

These promising results motivate towards future work aiming at quantifying and characterizing uterine contractions outside pregnancy. Further extensive validation is required to optimize the method with a larger dataset, as well as to assess its clinical value in the context of fertilization procedures.

Several innovative solutions proposed in this study, such as ER-based SVD filtering, median filtering, and DS, could also be adjusted and reused in different clinical applications. Moreover, despite our choice for grey-level video loops, facilitating the clinical translation of the method, application to US RF (radio frequency) signals can also be envisaged to improve the method accuracy.

5.8 ACKNOWLEDGEMENTS

We acknowledge the Dutch TTW HTSM-13901 grant along with the financial contribution from Ferring and Samsung companies.

BIBLIOGRAPHY

1. Iljand, M. M., Evers, J. L., Dunselman, G. A. & Hoogland, H. J. Subendometrial contractions in the nonpregnant uterus: an ultrasound study. *Eur.J.Obstet.Gynecol.Reprod.Biol.* **70**, 23–24 (1996).
2. de Ziegler, D., Bulletti, C., Fanchin, R., Epiney, M. & Brioschi, P. A. Contractility of the nonpregnant uterus: the follicular phase. *Ann.N.Y.Acad.Sci.* **943**, 172–184 (2001).
3. Sebag-Peyrelevade, S. & Fanchin, R. Uterine Contractility and Embryo Transfer. in *Human Embryo Transfer* 61–68 (Springer, 2015). doi:10.1007/978-81-322-1115-0_8
4. Bulletti, C. *et al.* Uterine contractility during the menstrual cycle. *Hum. Reprod.* **15**, 81–89 (2000).
5. Fanchin, R. *et al.* Uterine contractions at the time of embryo transfer alter pregnancy rates after in-vitro fertilization. *Hum.Reprod.* **13**, 1968–1974 (1998).
6. Martinez-Gaudio, M., Yoshida, T. & Bengtsson, L. P. Propagated and nonpropagated myometrial contractions in normal menstrual cycles. *Am.J.Obstet.Gynecol.* **115**, 107–111 (1973).
7. Kunz, G. & Leyendecker, G. Uterine peristaltic activity during the menstrual cycle: characterization, regulation, function and dysfunction. *Reprod.Biomed.Online.* **4 Suppl 3**, 5–9 (2002).
8. Jayaprakasan, K. & Panchal, S. *Ultrasound in Subfertility: Routine Applications and Diagnostic Challenges.* (Jaypee Brothers, 2014).
9. Bulletti, C. & de Ziegler, D. Uterine contractility and embryo implantation. *Curr. Opin. Obstet. Gynecol.* **18**, 473–484 (2006).
10. Wagner, R. F., Insana, M. F. & Brown, D. G. Unified approach to the detection and classification of speckle texture in diagnostic ultrasound. *Opt. Eng.* **25**, 738–742 (1986).
11. Burckhardt, C., Schadt, M. & Helfrich, W. Holographic Recording with an Electrooptic Liquid Crystal Cell. *Appl. Opt.* **10**, 2196 (1971).
12. Sammali, F. *et al.* Experimental setup for objective evaluation of uterine motion analysis by ultrasound speckle tracking. *Biomed. Phys. Eng. Express* **4**, 035012 (2018).
13. Kuenen, M. P. J., Saidov, T. A., Wijkstra, H. & Mischi, M. Contrast-ultrasound dispersion imaging for prostate cancer localization. *Ultrasound Med. Biol.* **39**, 4268–4271 (2014).
14. Wagner, R. F., Smith, S. W., Sandrik, J. M. & Lopez, H. Statistics of Speckle in Ultrasound B-Scans. *IEEE Trans. Sonics Ultrason.* **30**, 156–163 (1983).
15. Guo, W., Wang, Y. & Yu, J. A Sidelobe Suppressing Beamformer for Coherent Plane Wave Compounding. *Appl. Sci.* **6**, 359 (2016).
16. Mauldin, F. W., Lin, D. & Hossack, J. A. The Singular Value Filter : A General Filter Design Strategy for PCA-Based Signal Separation in Medical Ultrasound Imaging. *IEEE Trans. Med. Imaging* **30**, 1951–1964 (2011).
17. Sadek, R. A. SVD Based Image Processing Applications: State of The Art, Contributions and Research Challenges. *Int. J. Adv. Comput. Sci. Appl.* **3**, (2012).
18. Liu, X., Wen, Z. & Zhang, Y. Limited Memory Block Krylov Subspace Optimization for Computing Dominant Singular Value Decompositions. *SIAM J. Sci. Comput.* **35**, A1641–A1668 (2013).
19. Demené, C. *et al.* Spatiotemporal Clutter Filtering of Ultrafast Ultrasound Data Highly Increases Doppler and fUltrasound Sensitivity. *IEEE Trans. Med. Imaging* **34**, 2271–2285 (2015).
20. Iljand, M. M., Evers, J. L. H. & Hoogland, H. J. Velocity of endometrial wavelike activity in spontaneous cycles. *Fertil. Steril.* **68**, 72–75 (1997).
21. Barjatya, A. Block matching algorithms for motion estimation. *IEEE Trans. Evol. Comput.* **8**, 225–239 (2004).
22. Zhu Shan & Kai-Kuang, M. A New Diamond Search Algorithm for Fast Block-Matching Motion Estimation. *Ieee Trans. Image Process.* **9**, 287–290 (2000).
23. Huang, S. W. *et al.* Analysis of correlation coefficient filtering in elasticity imaging. *IEEE Trans.*

- Ultrason. Ferroelectr. Freq. Control* **55**, 2426–2441 (2008).
24. Rabotti, C. *et al.* Relationship between electrohysterogram and internal uterine pressure: A preliminary study. in *Annual International Conference of the IEEE Engineering in Medicine and Biology - Proceedings* **1**, 1661–1664 (2006).
 25. Rabotti, C. & Mischi, M. Propagation of electrical activity in uterine muscle during pregnancy: A review. *Acta Physiol.* **213**, 406–416 (2015).
 26. Shapiro, S. S. & Wilk, M. B. An analysis of variance test for normality (complete samples). *Biometrika* **52**, 591–611 (1965).
 27. Breslow, N. A generalized test for comparing of censorship to unequal patterns subject. *Biometrika* **57**, 579–594 (1970).
 28. García, S. & Fernández, A. Advanced nonparametric tests for multiple comparisons in the design of experiments in computational ... *Inf. Sci. (Ny)*. **180**, 2044–2064 (2017).
 29. Moawad, A. H. & Bengtsson, L. P. In vivo studies of the motility patterns of the nonpregnant human uterus. I. The normal menstrual cycle. *Am. J. Obstet. Gynecol.* **98**, 1057–1064 (1967).
 30. van Gestel, I., IJland, M. M., Hoogland, H. J. & Evers, J. L. Endometrial wave-like activity in the non-pregnant uterus. *Hum.Reprod.Update.* **9**, 131–138 (2003).
 31. Hendricks, C. H. Inherent motility patterns and response characteristics of the nonpregnant human uterus. *Am. J. Obstet. Gynecol.* **96**, 824–841 (1966).
 32. Kuijsters, N. P. M. *et al.* Uterine peristalsis and fertility: current knowledge and future perspectives: a review and meta-analysis. *Reprod. Biomed. Online* **35**, 50–71 (2017).
 33. Hendricks, C. H. A New Technique for the Study of Motility in the Non-Pregnant Human Uterus. *BJOG An Int. J. Obstet. Gynaecol.* **71**, 712–716 (1964).
 34. Sammalı, F., Kuijsters, N. P. M., Schoot, B. C., Mischi, M. & Rabotti, C. Feasibility of Transabdominal Electrohysterography for Analysis of Uterine Activity in Nonpregnant Women. *Reprod. Sci.* 193371911876870 (2018). doi:10.1177/1933719118768700

6

BLIND SOURCE SEPARATION FOR CLUTTER AND NOISE SUPPRESSION IN ULTRASOUND IMAGING: CRITICAL REVIEW

Abstract: *Blind Source Separation (BSS) refers to a number of signal processing techniques that decompose a signal into several “source” signals. In recent years, BSS is increasingly employed for the suppression of clutter and noise in ultrasonic imaging. In particular, its ability to separate sources based on measures of independence rather than their temporal or spatial frequency content, makes BSS a powerful filtering tool for data in which the desired and undesired signals overlap in the spectral domain. The purpose of this work was to critically review existing BSS methods and their potential in ultrasound imaging. Furthermore, we tested and compared the effectiveness of these techniques in the field of ultrasound super-resolution, contrast quantification, and speckle tracking. For all applications, this was done in silico, in vitro, and in vivo. We found that the critical step in BSS filtering is the identification of components containing the desired signal and we highlighted the value of a priori domain knowledge to define effective criteria for signal component selection.*

From: R. R. Wildeboer, **F. Sammali**, R.J.G. van Sloun, Y. Huang, P. Chen, M. Bruce, C. Rabotti, S. Shulepov, G. Salomon, B.C. Schoot, H. Wijkstra, and M. Misch. **“Blind Source Separation for Clutter and Noise Suppression in Ultrasound Imaging: Critical Review for Different Applications”**. *Submitted to IEEE Transactions on Ultrasonics, Ferroelectrics, and Frequency Control*, 2019.

6.1 INTRODUCTION

In recent years, increasingly advanced algorithms have been developed to analyse ultrasonic (US) acquisitions; from the generation of super-resolution images revealing vascular structures beyond the diffraction limit^{1,2} to the distinct extraction of time-intensity curves in the cardiac system or well-perfused organs^{3,4} up to dedicated speckle-tracking algorithms to estimate strain^{5,6} in e.g. the heart, arteries, and uterus. The gravity of data preprocessing should not be overlooked when appreciating the impressive results obtained by these methods. Especially in clinical application, US data are often obscured by prevalent clutter sources, artefacts can arise due to patient or operator motion, and noise levels may well exceed those in laboratory conditions. Therefore, robust filtering is needed to separate the desired signal(s) from the undesired signals prior to further analysis.

Traditionally, clutter and noise suppression in US recordings is performed with temporal filters (e.g., for clutter removal⁷) and spatial filters (e.g., for de-speckling^{8,9}). Infinite and finite impulse response filters (IIR, FIR) as well as regression filters have been widely applied for this purpose.^{7,10–12} These filters rely on the assumption that the temporal or spatial frequency content of clutter, noise, and the signal of interest are distinctly different. This assumption is not always valid; there is thus a real risk of losing useful information or failing to remove signals that affect the performance of the algorithms used for e.g. super-resolution and speckle tracking.

In this respect, blind source separation (BSS) techniques have been receiving more and more attention. Unlike the aforementioned filters, BSS techniques decompose data into underlying “sources”, or *components*. Components corresponding to clutter or noise sources are subsequently discarded. Especially in blood flow imaging^{10,12–14} and, more recently, ultrasound super-resolution imaging,^{15–17} BSS is increasingly applied. The identification of the clutter and signal components has been intensively studied. Although thresholds might be heuristically or empirically established, signal content can vary from application to application, between different acquisitions, or even within the same acquisition over time. Many authors therefore coin the need for generalisable, adaptive filtering.^{10,13}

The purpose of this work was to critically review, evaluate, and compare several existing BSS methods as well as a wide range of (recently proposed as well as novel) adaptive criteria for clutter and noise suppression in US imaging. To this end, we tailored the BSS filtering to three fields of interest: (A) super-resolution by US localisation microscopy; (B) contrast-enhanced US quantification by time-intensity curve analysis, and (C) US speckle tracking. As BSS in Doppler imaging has been most studied, we refer to some excellent papers on this subject for a treatise on effective BSS implementation in blood flow imaging.^{10,12–14}

Albeit the three included applications are ultrasound-based, very different features in the US videos are regarded as undesired. For example, whereas speckles are considered noise in contrast ultrasound, they are essential to speckle tracking. However, as these application fields are very broad, we only refer to the key articles of each application and focus more in-depth on the implementation of adaptive BSS filtering. This way, we provide the reader with

guidelines for custom BSS filter design in ultrasound imaging.

This chapter is organised as follows. In Section 6.2, the theoretical framework of BSS is introduced and discussed. Section 6.3 elaborates on the use of BSS for the adaptive filtering of ultrasound data. Together these sections provide a general framework for the different strategies and implementations of dedicated US filtering that will be discussed and tested for the three different US applications. This is described in Section 6.4. Finally, the results are discussed in Section 6.5 and conclusions are drawn in Section 6.6.

6.2 THEORETICAL FRAMEWORK AND (BLIND) SOURCE SEPARATION METHODS

6.2.1 Fundamentals of (blind) source separation

Irrespective of the US imaging technique used, relevant information is to some extent distorted or obscured by undesired signals.^{18–20} In this work, we strive to specifically separate the desired signal from noise (i.e., random distortions of the signal; e.g., electronic noise), clutter (i.e., undesired, deterministic sources from the measurement space; e.g., tissue movement and multiplicative (speckle) noise), and artefacts (i.e., signal distortions caused by the operator, patient, or external structures; e.g., motion artefacts and shadowing).

As we are interested in dynamic US acquisitions throughout this paper, we will refer to our observed signal using the Casorati matrix \mathbf{X} of size $N_s \times N_t$, with all our spatial dimensions condensed in the rows (i.e., $N_s = N_x \cdot N_y$) and our temporal dimension distributed over the columns. \mathbf{X} will be a mix of all above-mentioned sources. For BSS, we assume this mixing process occurs through linear combination,

$$\mathbf{X} = \mathbf{X}_{signal} + \mathbf{X}_{noise} + \mathbf{X}_{clutter} + \mathbf{X}_{artefact} . \quad (6.1)$$

When filtering, we aim to maximise our signal-to-noise ratio (SNR) by removing the undesired sources mixed into our observed image \mathbf{X} . This procedure is often based on signal decomposition or basis transformation, that is, the mapping of the signal onto new bases that will enable discrimination and identification of the sources that make up the signal. When appropriate bases are found, a filtered output image is readily generated by transforming only a (weighted) subset of distinct signal components back to the image space.

Traditionally, *a priori* knowledge of the signal and undesired sources is used to determine the basis onto which \mathbf{X} will be projected. A widely used example of such a strategy is frequency filtering, where the sampled signals are transformed to the frequency domain through Discrete Fourier Transformation (DFT). When the spectral characteristics of the desired signal or, alternatively, of the undesired signals (e.g., high-frequency noise or interference by the power mains) are known, a filtered image can be reconstructed by disregarding specific frequency components. Spatial filters (e.g., smoothing) work essentially in a similar fashion, filtering out undesired spatial frequencies. In many applications, however, desired and undesired signals may be present in the same (spatial) frequency bands, rendering the DFT strategy insufficient.^{7,10,12,21} The same holds for other non-blind transformations, such as the discrete wavelet transformation often used in de-speckling strategies.⁸

Another approach would be to determine the basis transformation *adaptively*, that is, depending on the signal statistics themselves. As we do not need prior information on the sources underlying our observations or how the mixture is formed, we refer to this strategy as *blind source separation* (BSS).^{19,22} Filtering is then a three-step process, consisting of (1) finding the bases that provide the best separation of sources; (2) identifying the components that should subsequently be (partially) removed from the signal; (3) mapping the remaining signal back to its original domain.²¹ In this section, the first and last step will be discussed; the second step will be treated in Section 6.3.

6.2.2 Discrete Fourier analysis

DFT is perhaps the most common form of non-blind source separation, where \mathbf{X} is decomposed into several frequency bands (in this case, these are the “sources”). In matrix form, the inverse DFT reads

$$\mathbf{X}^T = \mathbf{W}_{\text{DFT}}^{-1} \mathbf{Y}^T, \quad (6.2)$$

where \mathbf{Y} is a complex $N_s \times N_t$ matrix containing the magnitude and phase of every frequency component in each pixel and \mathbf{W}_{DFT} is the $N_t \times N_t$ DFT matrix,²³

$$\mathbf{W}_{\text{DFT}} = \begin{bmatrix} 1 & 1 & \dots & 1 \\ 1 & e^{-j2\pi/N_t} & \dots & e^{-j2\pi(N_t-1)/N_t} \\ 1 & e^{-j4\pi/N_t} & \dots & e^{-j4\pi(N_t-1)/N_t} \\ \vdots & \vdots & \ddots & \vdots \\ 1 & e^{-j2\pi(N_t-1)/N_t} & \dots & e^{-j2\pi(N_t-1)^2/N_t} \end{bmatrix}. \quad (6.3)$$

No information is lost during the procedure and the image can be fully restored through its inverse transformation. We refer to this as lossless. For comparison with BSS methods, we show that the representation of an individual frequency component k can be isolated through multiplication of the k^{th} column of matrix \mathbf{Y} and the k^{th} column of the inverse DFT matrix,

$$\mathbf{X}_k^T = \mathbf{w}_{\text{DFT},k}^{-1} \mathbf{y}_k^T. \quad (6.4)$$

6.2.3 Singular value decomposition

As said, in contrast to DFT where the bases are defined *a priori*, BSS infers them from the signal itself. One of the most frequently used BSS techniques is singular value decomposition (SVD), a generalisation of eigendecomposition that decomposes any matrix \mathbf{X} as²⁴

$$\mathbf{X} = \mathbf{U} \mathbf{\Sigma} \mathbf{V}^T. \quad (6.5)$$

Here, \mathbf{U} is an $N_s \times N_s$ unitary matrix (i.e., orthogonal for real-valued inputs), $\mathbf{\Sigma}$ is a $N_s \times N_t$ pseudo-diagonal matrix containing the singular values σ as diagonal elements, conventionally

in descending order, and \mathbf{V} is an $N_t \times N_t$ unitary matrix. The columns in \mathbf{V} can be viewed to contain the singular vectors carrying the temporal information corresponding to spatial information in the column vectors of \mathbf{U} . Accordingly, we have separated $k = \min(N_s, N_t)$ sources that can be retrieved through

$$\mathbf{X}_k = \sigma_k \mathbf{u}_k \mathbf{v}_k^T. \quad (6.6)$$

Statistically, we have now decomposed our data into orthogonal subspaces. The vectors \mathbf{u}_k in \mathbf{U} and \mathbf{v}_k in \mathbf{V} correspond to the eigenvalues of the autocovariance matrix of \mathbf{X} ,²⁵ and therefore intrinsically provide a basis with maximum covariance. In fact, according to the Eckart-Young theorem,²⁶ a partial SVD provides the lowest rank approximation of \mathbf{X} of all low-rank matrices and therefore, by definition, equals or outperforms DFT in effectively decomposing \mathbf{X} .^{10,27} This can be related to the minimisation of the nuclear norm, that is, the l_1 -norm of its eigenvalues. Although $\mathbf{\Sigma}$ is unique, its singular vectors are not.

Furthermore, whereas SVD and DFT (see Equation 6.2) both create an orthonormal temporal basis (i.e., \mathbf{W}_{DFT} and \mathbf{V}^T respectively), the spatial vectors in \mathbf{Y} are not by definition orthogonal as is $\mathbf{U}\mathbf{\Sigma}$. Interestingly, Demené *et al.* showed that for their US data the high singular vectors were associated with low-frequency and low singular vectors with high-frequency temporal signals.¹⁰ This is a consequence of the small (tissue-related) movements being more spatiotemporally coherent in blood flow imaging rather than a general rule, however, similar behaviour can be observed in many ultrasonic applications. On the other hand, for example, Sammali *et al.* found the frequency of periodic uterine contractions (and its harmonics) in the first few singular components as these make up the most dominant spatiotemporally coherent signals.²⁸

6.2.4 Principal component analysis

SVD methods are often presented in the framework of principal component analysis (PCA), a widely used method for dimensionality reduction, decomposing an image into a new orthogonal representation that retains maximum covariance. There are several ways to perform PCA,²⁹ but the simplest might be an eigendecomposition of the autocovariance matrix,

$$\mathbf{C} = (\mathbf{X} - \bar{\mathbf{X}})^T (\mathbf{X} - \bar{\mathbf{X}}). \quad (6.7)$$

In this work, we will refer to PCA only if the orthogonal axes are also maximally *decorrelated*. When each column in \mathbf{X} is centred (i.e., has a mean of zero) and standardised (i.e., has a standard deviation of 1), the autocovariance matrix translates into the autocorrelation matrix. As such, PCA is also referred to as the Karhunen-Loève transform.^{11,30} Decorrelation can now be performed through eigendecomposition of the (square and symmetric) autocorrelation matrix,

$$\mathbf{R} = \mathbf{X}^T \mathbf{X} = \mathbf{V} \mathbf{\Lambda} \mathbf{V}^T, \quad (6.8)$$

where, similar to SVD, $\mathbf{\Lambda}$ contains the eigenvalues λ in descending order along the diagonal and the matrix \mathbf{V} contains the temporal eigenvectors as columns, that is, the principal components. In fact, SVD can be exploited to perform PCA without having to perform eigendecomposition. Since \mathbf{V} and \mathbf{U} are unitary matrices,

$$\mathbf{R} = \mathbf{X}^T \mathbf{X} = \mathbf{V} \mathbf{\Sigma}^T \mathbf{U}^T \mathbf{U} \mathbf{\Sigma} \mathbf{V}^T = \mathbf{V} \mathbf{\Sigma}^2 \mathbf{V}^T. \quad (6.9)$$

Accordingly, the eigenvalues of the autocorrelation matrix are related to the singular values through

$$\lambda_k = \sigma_k^2. \quad (6.10)$$

Following Equation 6.5, the spatial distribution of the principal components can be retrieved through $\mathbf{U} = \mathbf{X} \mathbf{V} \mathbf{\Sigma}^{-1}$. Therefore, after centerisation and standardisation, one can perform ordinary SVD and retrieve the individual principal components through Equation 6.6. Subsequently, these components form the original image when multiplied with the former standard deviations and added to the mean that was retracted previously.

6.2.5 Independent component analysis

In the thus far described BSS techniques, the desired and undesired signals are assumed to principally end up in distinct subspaces. Independence between the components is promoted by requiring them to be orthogonal and of maximum autocovariance. However, orthogonality does not necessarily indicate that the components are mutually independent and orthogonal axes might therefore not fully separate the different sources.¹¹

As opposed to eigendecomposition-related techniques, independent component analyses (ICA) decompose signals by assuming linear independence between the sources mixed into the observed signal.³¹ Often, ICA techniques iteratively maximise the non-Gaussianity of N_s sources. This originates from the underlying concept that, as the Central Limit Theorem states that the sum of independent random variables grows towards a Gaussian distribution, independent sources can be identified by their deviation from this Gaussianity.

There is a wide range of possible cost functions ensuring non-Gaussianity, of which kurtosis, (neg)entropy and mutual information are most employed.^{32,33} The kurtosis is easily implementable but often more sensitive to outliers. Negentropy, on the other hand, is a more robust and statistically elegant estimator of non-Gaussianity, but computationally difficult to implement as it depends on e.g. sample counting or kernel-density estimation.³² Therefore the negentropy is often approximated rather than fully calculated. For both cost functions, the data needs to be centred and standardised prior to analysis. Often the data are also whitened,³⁴ so that signal components are uncorrelated like in PCA and the ICA problem is simplified. For uncorrelated, unit-variance data, the negentropy and mutual information differ only by a

constant.³²

For ICA with N_n sources, it is assumed that components in an $N_n \times N_s$ source matrix \mathbf{S} are linearly mixed into the observed signal by an $N_t \times N_n$ mixing matrix \mathbf{W}_{ICA} following

$$\mathbf{X}^T = \mathbf{W}_{\text{ICA}}\mathbf{S} + \mathbf{N}^T, \quad (6.11)$$

where \mathbf{N} is the residual noise matrix, resulting from ICA not being lossless. In this formulation, the temporal independence between the bases vectors is promoted; likewise, a transposed Casorati matrix formulation of the ICA procedure would yield spatial independence.³⁵ Choosing the number of independent sources N_n is not a trivial problem; it might be determined in an iterative fashion,³⁶ by data-reduction through e.g. SVD prior to analysis,³⁵ or using information theoretic criteria (see Section 6.3.1).³⁷

Once the number of sources is established, the unknown matrices \mathbf{W}_{ICA} and \mathbf{S} can be approximated for instance using the often used fastICA fixed-point iteration algorithm proposed by Hyvärinen.³⁸ Other methods include the Joint Approximate Diagonalisation Eigenmatrices (JADE)^{39,40} and Information-Maximisation (InfoMax) algo-rithms.⁴¹ Finally, in line with the other methods, also ICA allows the extraction of individual components by multiplication of the k^{th} column of matrix \mathbf{W}_{ICA} and the k^{th} row of matrix \mathbf{S} ,

$$\mathbf{X}_k^T = \mathbf{w}_{\text{ICA},k}\mathbf{s}_k. \quad (6.12)$$

The order of the independent sources in \mathbf{S} depends on the initialisation of the iterative procedure. However, the sources can readily be arranged in descending order of the discrete-time signal energy (i.e., $E_k = \mathbf{s}_k^T\mathbf{s}_k$), provided that the corresponding columns in \mathbf{W}_{ICA} all have the same energy.³² In contrast to PCA and SVD, the ICA-decomposed subspaces are not necessarily orthogonal.

When the desired and undesired sources are indeed independent, ICA generally achieves more accurate separation.⁴² This is likely the case for additive noise and some distinct sources of clutter and artefacts. However, some other noise sources can be very much interdependent with the desired signal: for example multiplicative noise or the relation between blood flow and wall motion.¹¹ Moreover, though \mathbf{W}_{ICA} is assumed stationary in this ICA approach, the mixing may be considerably time variant (i.e., nonstationary).⁴³

6.2.6 Nonnegative matrix factorisation

Another BSS approach is nonnegative matrix factorisation (NMF). This method does not impose independence, orthogonality or maximum covariance, but aims to decompose the observations \mathbf{X} into a nonnegative $N_s \times N_n$ basis matrix \mathbf{W}_{NMF} and an $N_t \times N_n$ nonnegative encoding matrix \mathbf{H} given a certain cost function,^{44,45}

Table 6.1: Details of (blind) source separation methods for ultrasonic application.

Method	Name	Blindness	Preprocessing	Cost function	Properties	Invertibility
DFT	Discrete Fourier Transform	<i>a priori</i>	-	-	orthogonal	lossless
SVD	Singular Value Decomposition	blind	-	autocovariance	orthogonal	lossless
PCA	Principal Component Analysis	blind	centred / standardised	autocorrelation	orthogonal	lossless
ICA	Independent Component Analysis	blind	centred / standardised	kurtosis	-	lossy
NMF	Nonnegative Matrix Factorisation	blind	-	root-mean-square residual	-	lossy

$$\mathbf{X} = \mathbf{W}_{\text{NMF}}\mathbf{H} + \mathbf{N} \quad (6.13)$$

Because also NMF is lossy, Equation 6.13 contains a residual noise matrix \mathbf{N} . Similar to the other methods, individual components can be retrieved by multiplication of the k^{th} column and k^{th} row of \mathbf{W}_{NMF} and \mathbf{H} :

$$\mathbf{X}_k = \mathbf{w}_{\text{NMF},k}\mathbf{h}_k \quad (6.14)$$

An advantage of NMF is that the nonnegativity constraint leads to more physically intuitive bases than, for instance, ICA and PCA.⁴⁴ Even though ultrasound images can-not contain negative values, the bases found by the latter two methods usually have abundant negative values that cancel out when linearly combined to form the original image. In contrast, being nonnegative by definition, the NMF-bases in \mathbf{W}_{NMF} generally have more physical correspondence to the sources underlying \mathbf{X} .⁴⁵

6.3 ADAPTIVE FILTERING

Now we turn to examining how BSS filtering strategies (as summarised in Table 6.1) can be tailored to an ultrasonic application. An essential step is the identification of the signal components. There are three approaches to select the appropriate subset of desired components: empirically per acquisition or application^{e.g. 16,46–51} experimentally optimised per acquisition,^{e.g. 10,17} or adaptively based on the characteristics of the components.^{e.g. 12–14,21,28,52–55}

For the first two methods, respectively, a specific subset of components is defined manually or by experimentally maximising specific quality measures such as the contrast-to-noise ratio

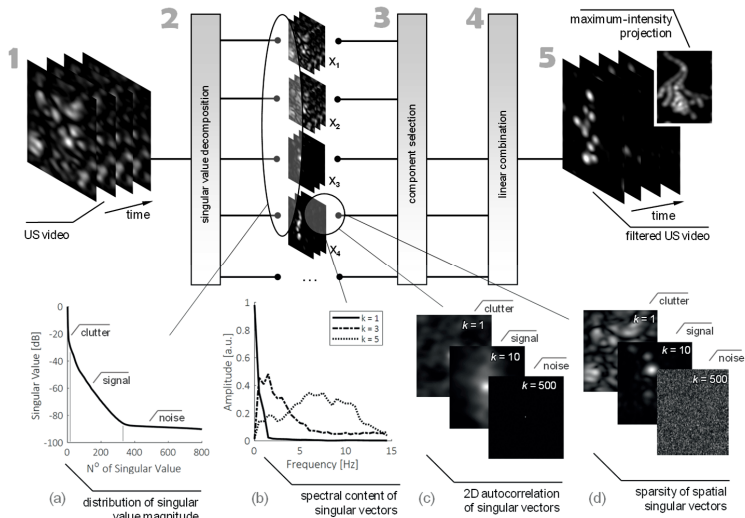


Figure 6.1: Schematic representation of a BSS filtering strategy for super-resolution imaging, depicting (1) the original data, (2) SVD, (3) component selection, (4) linear combination of the remaining components, and (5) the filtered data. Component selection might be based on (a) the distribution of the singular vectors, (b) the spectral content of the temporal singular vectors, (c) the autocorrelation within the spatial singular vectors, or (d) a sparsity model of the spatial components.

(CNR). The adaptive approach is generally more robust and generalisable, since it does not rely on qualitative assessment of decomposition characteristics, which may differ considerably across acquisitions. Several adaptive criteria for component selection have been proposed in recent years. Traditionally, information theoretic criteria have been used for dimensionality reduction and thus for pruning the noise components from the signal. As these criteria are not able to identify the undesired but deterministic clutter signals, also approaches based on e.g.

each component's spectral content, spatial similarity, eigen- or singular value distribution have been considered (see Figure 6.1 for a schematic representation of the filtering paradigm and Table 6.2 for an overview of approaches).

6.3.1 Information theory

An advantage of information theoretic criteria for component selection is in that they do not rely on user-set thresholds; we consider only the components that are theoretically necessary to carry the information of our image and, consequently, regard the other components as noise. The optimal number of components arises as a trade-off between an as large as possible descriptive power (i.e., high log-likelihood) and an as low as possible model complexity (i.e., low number of components). There are several ways to weight this trade-off, of which the Minimum

Description Length (MDL)⁵⁶ and Akaike's Information Criterion (AIC)⁵⁷ are the most common, that is,^{37,58}

$$E_{MDL}(k) = -L(k) + \frac{1}{2}(k(2N_k - k))\log(N_t), \quad (6.15)$$

$$E_{AIC}(k) = -2L(k) + 2(k(2N_k - k)), \quad (6.16)$$

where N_k is the number of components and $L(k)$ is the log-likelihood function. For SVD and PCA, Wax and Kailath⁵⁸ formulated a description of the log-likelihood based on the eigenvalues,

$$L(k) = \log \left[\frac{\prod_{i=k+1}^{N_k} \lambda_i^{1/(N_k-k)}}{\frac{1}{N_k - k} \sum_{i=k+1}^{N_k} \lambda_i} \right]^{(N_k-k)N_t}. \quad (6.17)$$

To apply information theoretic filtering, we include only the first k components, where k minimises either $E_{MDL}(k)$ or $E_{AIC}(k)$, a method that has been proven useful for subspace selection in e.g. contrast-ultrasound velocity imaging.⁵⁹ For ICA and NMF, on the other hand, the number of sources (i.e., components) is predefined. It has been proposed to use the MDL and AIC criteria to determine the number of (independent) sources that have to be assumed for the best description of the data.³⁷

6.3.2 Noise modelling

Instead of selecting the components that contain signal, we could also identify those that contain noise. Again, for ICA and NMF, the number of sources should be chosen such that noise-containing components are avoided. For SVD and PCA, however, a majority of the components will predominately consist of noise. As described by Marčenko and Pastur,⁶⁰ a random matrix will have a set of eigenvalues that log-linearly decreases in value. This fact can be exploited by identifying the component number after which the eigenvalues start decreasing linearly in the log-domain.¹⁴

In a more pragmatic implementation of this principle, Yu and Lovstakken²¹ describe noise removal from Doppler acquisitions by excluding components with an eigenvalue that is too similar to the previous one ($\lambda_k/\lambda_{k-1} \approx 1$). Alternatively, one could also exclude those components of which the eigenvalues only explain the remaining amount of variance (i.e., restricting the cumulative percentage variance, CPV),^{13,52} or those of which the eigenvalue is below the average eigenvalue.⁵² Finally, examining the spatiotemporal entropy of each component, one can appreciate that signal and noise components usually occupy a low-entropy and a high-entropy domain, respectively. Gaussian noise exhibits maximum entropy.⁶¹

6.3.3 Signal energy

Unfortunately, the two aforementioned approaches are only designed to separate (white) noise from deterministic signals. To remove clutter signals from a recording, we should take a closer look at our component characteristics. In fact, closely related to the previous approach, one could assume that clutter, signal, and noise differ in their contribution to the signal energy. In flow imaging, for example, the strongest signals are usually associated with clutter and the lowest with noise.^{10,13,47}

For ICA and NMF, each component's signal energy could be considered. In SVD and PCA, the removal of the strongest components is easiest by examining the eigenvalues and (partially) rejecting those above a certain cut-off ($\lambda_k > \lambda_c$).^{12,21} Another approach is to examine the slope of the singular value distribution and defining different regimes that are associated with clutter, signal, and noise.¹³ Here, the "turning points" in the singular curve defined by local minima in the curvature radius mark the transition between regimes.

6.3.4 Spectral content

Another way to separate clutter and noise from the desired signal, is by investigating each component's spectral content. This can be done by requiring the selected components to have at least a certain fraction of their spectral density within a pre-set frequency band. This approach differs from the DFT approach in that not all frequency components outside the desired band are filtered out, but only those that are not in some way related to the desired sources.

Table 6.2: Filtering approaches for BSS component selection.

Method	Criterion	Domain Knowledge*	Super-resolution	Speckle Tracking	TIC Modelling
Empirical	Arbitrary Subset of Components ^{16,46-48,50,51}				
Experimental	Maximum CNR ^{10,17,62}				
Information Theory	*Minimum Description Length	N/A	-	-	-
	*Akaike's Information Criterion	N/A	-	-	-
Noise Modelling	*Marčenko-Pastur Noise ¹⁴	N/A	-	-	-
	*Singular Curve Slope ²¹	$[\sigma_{k+1}/\sigma_k]_c$	>0.99	>0.99	>0.99
	*Cumulative Percent Variance ¹³	$\text{Var}(\mathbf{X}_k)_c$	>99/9%	>90%	>20%
	*Average Eigenvalue ⁵²	N/A	-	-	-
	*Spatiotemporal Entropy	N/A	-	-	-
Component Energy	*Singular Value Magnitude ^{12,21,55}	$\sigma_c; \lambda_c$	1	$\sim 10^{10}; 10^7$	-
	*Relative Singular Magnitude ¹³	σ_c [dB]	>-20 dB	>-55 dB (h) >-100 dB (u)	>-20 dB
	*Singular Curve Turning Point ¹³	N/A	-	-	-

Spectral Content	Spectral Power Density ^{13,21,28}	f_c	>10 Hz	0.5-1.5 Hz (h) 0.04-0.06 Hz (u)	<0.15 Hz
			Spatial Coherence	2D FWHM-radius _c	<0.13-mm
	Spatial Frequency Spectrum	ξ_c	>3.3 mm ⁻¹	<0.1 mm ⁻¹ (h) <0.5 mm ⁻¹ (u)	<0.75 mm ⁻¹
	Spatial Similarity Matrix ^{13,53,54}	N/A	-	-	-
Model Fitting	Goodness-of-fit	model; ϵ_c	sparsity	periodicity	LDRW

* = SVD, PCA only; [*]_c = cut-off value; h = heart; u = uterus.

For example, Sannali *et al.* determined a band of singular components for speckle tracking of uterine motion, based on the component's spectral energy within the clinically relevant bandwidth of uterine contractions,²⁸ and Yu and Lovstakken reported on removing components with a mean Doppler value in a certain clutter frequency band.²¹ Alternatively, Wu *et al.* enhanced motion artefacts prior to motion compensation by iteratively determining the weights for every PCA component so that the full-image energy content within a predefined frequency band was maximised with respect to the total.⁶³

6.3.5 Spatial coherence

In a similar approach, one could look at the spatial content of each component. As all spatial dimensions are condensed in the Casorati matrix, the spatial image of each component first has to be reconstructed. Subsequently, for example, the spatial frequencies present in each spatial vector reflect the size of the structures that are visualised and could therefore be used to select smaller-scale structures such as individual bubbles in super-resolution imaging. 2D spatial autocorrelation quantified by e.g. the 2D full width half maximum may represent a more robust measure for spatial coherence; white noise would have the shape of a delta function, whereas highly coherent effects such as shadowing might have a very broad profile. Alternatively, there has been looked at the spatial similarity between the different spatial singular vectors.^{13,53,54} Specific blocks of high spatial similarity were found to be related to clutter, signal, and noise, and the boundaries of the signal block were adaptively estimated.

6.3.6 Model fitting

Finally, one could also only select those components of which the temporal or spatial vectors have expected shapes. For instance, when filtering out the bolus dynamics from a contrast video, only the components that have a bolus-like shape are usable. Analogously, super-resolution components should exhibit sparsity and for speckle tracking in cardiac or uterine movies a certain degree of periodicity can be assumed. Components with a significantly different behaviour are likely to contain clutter or noise. It should be noted however that, in particular for SVD and PCA, only the combination of certain components might make up a meaningful source signal.

6.4 APPLICATION OF BSS FILTERING IN ULTRASOUND IMAGING

To evaluate the described adaptive BSS framework, we applied this type of filtering in three different US applications: (A) US localisation microscopy, (B) time-intensity curve modelling, and (C) US speckle tracking. Since for each application different source signals are considered desired and undesired, we briefly introduce each application and its dedicated BSS filtering. To compare the results to nonfiltered or conventionally filtered data, we also introduce an objective performance measure for verification both *in silico* and *in vitro*. Finally, we also apply BSS filtering to an *in-vivo* example of each application. For reference, the adopted application-specific thresholds are listed in Table 6.2.

6.4.1 Ultrasound localisation microscopy

Super-resolution microvascular imaging by ultrasound localisation microscopy (ULM) is a relatively recent development within the field of US, primarily inspired by advances in optical super-resolution.⁶⁴ It exploits the known backscattering nature of ultrasound contrast agents (UCAs), which are microbubbles with a size comparable to blood vessels, to track and visualise their position with a higher precision than the resolution of the imaging system.² This way, super-resolved images can be generated that reveal vascular structures beyond the diffraction limit.

Accurate, uncorrupted detection of isolated UCA signals is vital to this technique. Its fidelity is therefore largely affected by noise, clutter, and movement. Even if contrast-specific imaging is used,⁶⁵ signals arising from tissue are still present. To cope with this problem, SVD-filtering is already widely applied for this purpose, aimed at removing the spatiotemporally highly coherent clutter components below a certain singular value cut-off that is pre-set,^{15,16,48} or adaptively determined to optimise tissue-vessel contrast.^{14,17} However, there might still be (higher-singular-order) components that only carry noise.^{13,14} Isolation of the UCA signals is therefore often two-fold: (1) separation of microbubbles and tissue and (2) removal of electronic and speckle noise.

In our BSS framework, we therefore assess a combination of component selection methods. First, for the lossless methods only, we remove the noise using information theoretic criteria or noise modelling. Subsequently, we examine either the spatiotemporal spectral content, spatial coherence, energy, or sparsity of each component. As the tissue moves slowly compared to blood and is spatially much more coherent,^{10,13,47} we favour high-frequency and spatially low-coherent components. Component sparsity is quantified by the normalised kurtosis of the spatial vector

$$\hat{k}_4 = n \frac{\sum_{k=1}^n Q_k^4}{\left(\sum_{k=1}^n Q_k^2\right)^2}, \quad (6.18)$$

with Q being the quantisation levels and n the number of elements.⁶⁶ Moreover, two “turning points” have to be identified to separate the three regimes.

In this work, we implemented a basic US localisation microscopy approach. Single UCA centroids were localised in the beamformed image assuming a Gaussian-shaped point spread function, similar to Errico *et al.*¹ BSS was applied to the RF data for all methods except NMF, as the nonnegative nature of backscatter intensity can only be exploited after envelope detection. Subsequently, the super-resolution performance was quantified by the localisation F_1 -score, which reads

$$F_1 = \frac{2TL}{2TL + 2FL + ML}, \quad (6.19)$$

in which, for each pixel, TL accounts for a true, FL for a false, and ML for a missed localisation. The F_1 -score is hence a reflection of the trade-off between wrong and missed localisations.

6.4.1.1 *In-silico* verification

Ultrasonic imaging of microbubbles travelling through a (micro)vascular network was simulated by propagating 26 microbubbles with random backscatter coefficients along digitally generated trajectories at ~ 2 mm/s (comparable to 5th generation microvasculature),⁶⁷ in a similar approach as Van Sloun *et al.*¹⁵ Subsequently, we mimicked the tissue signal by adding 500 scatterers of random backscatter intensities that were on average 1/3 lower than that of the microbubbles. These tissue scatterers moved together following a random walk at a speed of approximately 0.2 mm/s. Image formation was then simulated through the 7 MHz-modulated point spread function (PSF): a 2D Gaussian with standard deviation 0.14-mm and 0.16-mm in axial and lateral direction, respectively. The simulation resulted in a 2-s contrast-enhanced US (CEUS) video, with a pixel spacing of 0.03×0.03 mm and a frame rate of 400 Hz.

We found that especially the SVD-based approach in combination with spectral, turning-point, and sparsity-based criteria yielded the best F_1 scores of 0.76, 0.73, and 0.72, respectively. A spectral threshold of $f > 10$ Hz (roughly resembling the PSF travelling at 2 mm/s) and a sparsity threshold of $\hat{k}_4 > 8$ (corresponding roughly to half the \hat{k}_4 of 13 PSFs in an empty measurement domain) were adopted. For comparison, the nonfiltered and DFT-filtered image yielded scores of 0.19 and 0.50, respectively. Although the noise threshold did not significantly affect the performance, appropriate thresholds allowed substantial reduction in the number of components to be included. ICA and NMF had difficulty in representing the sparse source signals, but could identify the clutter. Subsequently, subtracting the clutter sources from the original video led to an appreciable F_1 -score of 0.76. We refer to Figure 6.2-1 for an illustration of the filtering performance.

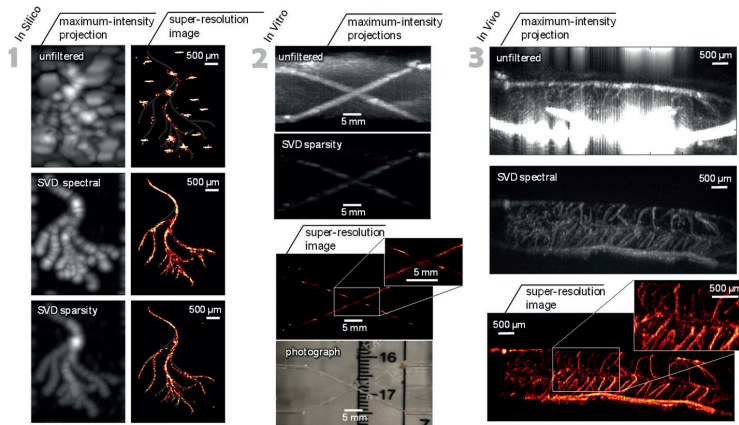


Figure 6.2: (1) *In-silico* verification of BSS for super-resolution imaging, depicting maximum intensity projections and super-resolution images overlaying the artificial vascular phantom. (2) Super-resolution image of a phantom with two diagonal vessels, compared with a photographic ground truth. (3) Super-resolution image of a rat's spinal vasculature after SVD-spectrally-filtered data preprocessing.

6.4.1.2 *In-vitro* verification

We evaluated both spectral and sparsity-based BSS filtering on an *in-vitro* phantom consisting of two 300- μm channels crossing each other in a slab of polyacrylamide. The phantom was infused with a 1/500 dilution of ~ 1 mL SonoVue[®] UCA (Bracco, Milan, Italy) and imaged with a Vantage ultrasound system (Verasonics, Seattle, WA), equipped with a 3.5-MHz L11-4V probe, at a frame rate of 100 Hz, a resolution of 5 mm, and a reconstructed pixel spacing of 0.15×0.15 mm. In Figure 6.2-2, it can be appreciated how the filtering effectively removes the background clutter. Using a photograph of the phantom as reference, an F_1 -score of 0.67, 0.71, and 0.72 was maintained for the spectral, turning-point, and sparsity-criteria in the *in-vitro* situation. In contrast to the simulations, the choice of noise criterion was more critical to ensure a high super-resolution performance. Especially the noise modelling strategies (i.e., Marčenko-Pastur) proved useful, the information theoretic criteria being too strict due to the dominance of clutter. The ICA approach failed to remove the clutter.

6.4.1.3 *In-vivo* verification

To assess the performance of the BSS techniques *in vivo*, we filtered a high frame-rate CEUS acquisition of a rat spinal cord. For this, a Sprague-Dawley rat (Harlan Labs, Indianapolis, IN, USA) was imaged at the University of Washington.⁶⁸ The study was approved by the Institutional Animal Care and Use Committee and all appropriate guidelines were followed. The spinal cord was exposed by laminectomy. After tail-vein infusion of 0.15 mL of Definity[®] (Lantheus, N. Billerica, MA), 400-Hz CEUS was performed with the Vantage scanner (Verasonics, Seattle, WA) equipped with a 15-MHz transducer. A power-modulation scheme was adopted for contrast enhancement.⁶⁹ The video consists of 720 frames and has a pixel spacing of 0.03×0.03 mm; the super-resolved image has a 10- μm pixel spacing.

The spectral and sparsity threshold were adjusted to $f > 50$ Hz and a sparsity threshold of $\hat{\kappa}_4 > 25$ to fit the *in-vivo* acquisition. In absence of a ground truth, we can only qualitatively compare the images (see Figure 6.3-3). Whereas the sparsity-based and turning-point approaches could not remove all artefacts, the spectral approach was robust for *in-vivo* use.

6.4.2 Contrast-ultrasound time-intensity curve analysis

The intravascular nature of UCAs does not only allow CEUS imaging to visualise vascularity, but it can also be used for quantification of blood flow and perfusion. Over the years, several methods have been developed to extract meaningful features from the evolution of contrast intensity over time, referred to as time-intensity curves (TICs).⁷⁰ For example, extracted parameters were shown to correlate with tumour presence or progression (after treatment) in e.g. liver, thyroid, breast, kidney, and prostate.^{71,72} In addition, CEUS quantification has been shown useful to estimate e.g. pulmonary blood volume.^{73,74} Quantification of CEUS can be performed either using a bolus injection⁴ or a continuous infusion combined with a disruption-replenishment technique.⁷⁵

In the remainder of this section, we will focus on filtering CEUS videos for lesion localisation in the prostate using a bolus injection. However, the implementation can readily be extrapolated to perfusion quantification in other organs. More specifically, BSS was employed to retrieve the TIC wash-in time (WIT), a heuristic parameter often used to assess tissue perfusion.⁷⁰ The performance was quantified by both the coefficient of determination (R^2) reflecting the goodness-of-fit of the TIC by the physics-driven local density random walk (LDRW) model^{4,76} and the relative error in the WIT estimation (ΔWIT) at each pixel. As the influx of UCAs is the dominant signal in these CEUS videos, all single-threshold techniques were implemented such that the high-frequency, low-coherence, and noise-containing components are removed.

6.4.2.1 *In-silico* verification

2D CEUS imaging of the prostate was simulated using a $\sim 4 \times 4$ -cm 2D phantom image containing two lesions. For each pixel (~ 0.5 mm, reflecting the resolution of a iU22 commercial scanner (Philips, Bothell, USA) at ~ 4 cm)⁷⁷ TICs were simulated using the LDRW model and parameters typically encountered in malignant lesions (i.e., $\kappa = 1 \pm 0.1 \text{ s}^{-1}$ and $2 \pm 0.1 \text{ s}^{-1}$; $\mu = 25 \pm 1 \text{ s}$ and $15 \pm 0.1 \text{ s}$) and benign tissue (i.e., $\kappa = 0.5 \pm 0.1 \text{ s}^{-1}$; $\mu = 30 \pm 0.1 \text{ s}$).⁷⁶ The resulting videos were subsequently degraded by multiplicative noise, a scanner-specific point spread function modelled by a Gaussian spatial smoothing filter ($\sigma_x = 1$ mm), a sinusoidal 1-mm motion artefact resembling a breathing frequency of 0.2 Hz,⁷⁸ random-walk displacement representing manual probe handling, and Gaussian-distributed electronic noise (SNR of ~ 4 dB compared to mean signal).

All BSS methods and component selection criteria were evaluated for this simulation. In general, the relevant TIC dynamics were captured in the first few components of each BSS technique (see Figure 6.3-1). Although many selection criteria yielded a similar performance, spectral thresholding of PCA and ICA were generally superior in terms of median goodness-of-fit (both $R^2 > 0.99$), and error in parameter estimation, $\Delta\text{WIT} = 5\%$ and 5.1% , respectively. The unfiltered, 0.15-Hz DFT, and 0.5-mm spatially smoothed images yielded performances of $R^2 =$

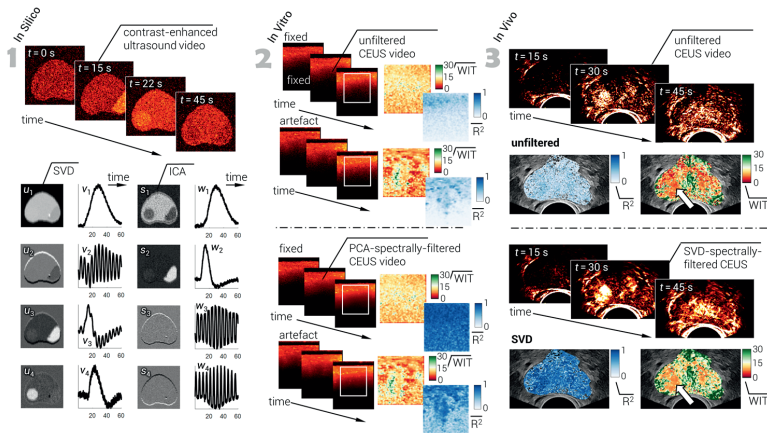


Figure 6.3: (1) First four component vectors after SVD and ICA of an *in-silico* transrectal CEUS video of the prostate with two, early-enhancing regions. (2) TIC modelling results of the contrast bolus infused into a sponge phantom, with and without a deliberate artefact. (3) Unfiltered and SVD-spectrally-filtered *in-vivo* CEUS video with the corresponding R^2 and WIT maps; a prostate cancer lesion was found at the location of the arrow.

0.14, 0.94, and 0.71 and Δ WIT = 12.2%, 12.1%, and 5.5%, respectively.

6.4.2.2 *In-vitro* verification

In-vitro testing comprised a sponge encapsulated in gelatin that was perfused with a bolus of 1-mL SonoVue® (Bracco, Milan, Italy) UCA dilution in 10~mL saline and imaged in contrast-mode with the Vantage ultrasound system (Verasonics, Seattle, WA), using a 3.5-MHz L11-4V transducer, at a frame rate of 50 Hz and pixel spacing of 0.18×0.18 mm. Recordings were performed with the probe fixed to the set-up, with the probe subjected to controlled motion, and with the probe undergoing irregular hand-held movements. After filtering, the TICs were measured at each pixel, linearised, and fitted by the LDRW model. The unfiltered and 0.5-mm spatially smoothed data could be fitted with an R^2 of 0.17 and 0.66 in the fixed scenario, and 0.14 and 0.44 in the worst-case scenario, respectively. Both spectrally filtered PCA and ICA were able to generate data with R^2 -scores of 0.87 and 0.83 in the fixed, and 0.54 and 0.62 in the worst-case scenario. The WIT estimates were similar over all methods.

6.4.2.3 *In-vivo* verification

In a prospective 48-patient trial at the Martini Clinic (University Hospital, Hamburg-Eppendorf, Germany), patients with biopsy-proven prostate cancer underwent three CEUS recordings with an Aixplorer® ultrasound scanner (SuperSonic Imagine, Aix-en-Provence, France) equipped with a 3.2-MHz SE12-3 probe at a frame rate of 27 Hz. After radical prostatectomy, prostate histopathology was matched to the CEUS images by assigning benign and malignant regions of interest. By extracting the pixelwise WIT in those regions, we evaluated this metric's diagnostic

potential in terms of the area under the Receiver Operating Characteristics curve (ROC-AUC).

By appending the preprocessing with a spectral-threshold-based SVD, we found an improvement in tumour classification compared to the conventionally filtered recordings, increasing the ROC-AUC from 0.66 to 0.68 for prostate cancer. The goodness-of-fit (R^2) improved only slightly from 0.68 ± 0.07 to 0.69 ± 0.12 , but we observed a substantial decrease in the number of TICs that could not be fitted by the LDRW model (from 23% to 14%). Hence, the use of BSS substantially improved the parametric maps, also increasing the classification performance. Figure 6.3-3 shows an example of filtered images.

6.4.3 Ultrasound speckle tracking

US speckle tracking imaging allows quantitative evaluation of global and regional tissue motion. A speckle is commonly defined as a typical spatial distribution of greylevel values in US B-mode images caused by constructive and destructive interference of reflections from individual tissue scatterers, forming a unique and deterministic pattern. Speckle tracking techniques track the speckle pattern during subsequent frames allowing for motion and strain imaging analysis. Speckle tracking by US imaging is an active field of research that has already been translated into several applications; in particular, for cardiovascular⁷⁹ and muscular⁸⁰ investigations, vector Doppler imaging,⁸¹⁻⁸³ and, recently, for the assessment of uterine motion outside pregnancy.²⁸

US loops recorded e.g. in the heart, skeletal muscle, and uterus comprise slow and fast tissue movement, respiratory motion, stationary tissue clutter, shadowing, and other artefacts. For this work, we studied the effect of BSS filtering prior to US speckle tracking in an *in-silico* cardiac image sequence, an *ex-vivo* uterine motion acquisition, and an *in-vivo* uterine recording. Similar to TIC modelling, the desired signal is generally the most prominent signal in this application and thus the first few BSS components were selected for the single-threshold methods. Furthermore, as we apply speckle tracking to periodic movements, we adopted periodicity as an additional criterion for component selection. For this criterion, we compute the normalised temporal autocorrelation of each component and only include those with a sufficiently high autocorrelation peak (i.e., >0.6) aside from the one at zero-lag.

To objectively assess the tracking quality in terms of agreement with the reference motion before and after BSS filtering, the Pearson correlation coefficient (Pearson r) and Mean Squared Error (MSE) were employed as metrics.

6.4.3.1 *In-silico* verification

To study the effect of BSS filtering on speckle tracking echocardiography, a synthetic 2D cardiac US acquisition was simulated and tracked over several cardiac cycles. The video was generated using a 3D finite-element model of the human living heart that follows cardiac excitation and contraction based on a two-field finite-element formulation of coupled electrical and mechanical fields.⁸⁴ The finite-element nodes moving with the mechanical deformation of the heart served as US scatterers. A 2D four-chamber view by a phased-array transducer was created by 3D modelling 161 scan lines positioned every 0.6° in a coronal plane. For each line,

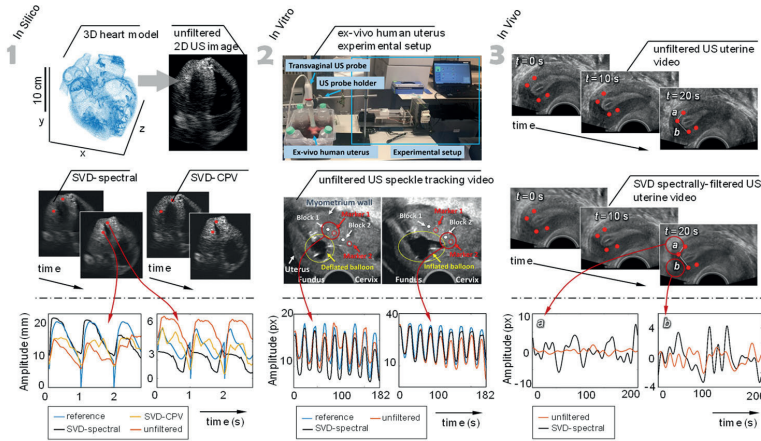


Figure 6.4: (1) 3D finite-element model of a human heart and the corresponding 2D US simulation that was SVD-spectrally- and CPV-filtered prior to speckle tracking. (2) Experimental set-up inducing controlled, rhythmic motion during 2D US imaging of an *ex-vivo* uterus; the blocks' position during deflation and inflation used for speckle tracking are indicated in the unfiltered uterine images. (3) Unfiltered and SVD-spectrally-filtered US uterine video used for the comparison of motion tracking along the (a) longitudinal and (b) transversal direction.

all scatterer contributions were simulated by a convolution between the scatterer location and the location-dependent PSF. This PSF was approximated by assuming a Fraunhofer pressure field modulated by a four-cycle 2.5-MHz cosine function in the propagation direction. In order to reduce the side lobes of the rectangular transducer, Hamming apodisation was adopted.⁸⁵ Prior to generating a 54-Hz multicycle US heart video through demodulation of the scanlines, clutter and Gaussian noise were introduced in the RF data. A resulting 2D US image of the heart is shown in Figure 6.4-1.

On the 2D US synthetic heart image, speckles associated with tissue deformation of the left ventricle (LV) can be identified and tracked by calculating frame to frame changes. Out-of-plane motion occurs due to rotation and motion of the heart into the chest cavity, and may cause the disappearance of the speckles over a few frames.⁸⁶ In this work, a pyramidal Lucas-Kanade optical flow method was implemented for the tracking, as this method provides sufficient tracking accuracy for large and fast motion.⁸⁷ Two blocks were manually selected in the LV wall (Figure 6.4-1) and tracked over time during three cardiac cycles of the video, both before and after BSS filtering. The estimated motion of the tracked blocks, calculated as the absolute motion (i.e., Euclidean distance from the initial position), was compared with the absolute motion of the corresponding scatterer in the 3D finite-element model.

All BSS methods and component selection criteria were evaluated for this *in-silico* verification (Figure 6.4-1). Only four selection criteria yielded an improved performance compared to unfiltered US image sequences. Among these four criteria, the CPV of SVD-filtered data revealed to be generally superior in terms of correlation coefficient (Pearson $r = 0.71 \pm 0.07$) while [0.5 Hz – 0.15 Hz]-spectral thresholding of the SVD was superior in terms of MSE (MSE = $0.00048 \pm 0.00032 \text{ mm}^2$). Speckle tracking on the unfiltered US image sequences yielded

performances of Pearson $r = 0.64 \pm 0.06$ and MSE = $0.13 \pm 0.11 \text{ mm}^2$, respectively.

6.4.3.2 *In-vitro* verification

The use of BSS filtering in speckle tracking *in vitro* and *in vivo* is evaluated in US imaging of the uterus. Similar to the heart, uterine US loops not only capture the uterine motion (i.e., uterine peristalsis), but also fast motion of neighbouring organs, respiration, and probe motion. First, all BSS methods and component selection criteria were evaluated in an *ex-vivo* human uterus, removed by laparoscopic hysterectomy, undergoing controlled and rhythmic motion to establish a reference for the assessment of speckle tracking performance. The US acquisitions were performed at the Catharina Hospital (Eindhoven, The Netherlands). The patient signed an informed consent; all the acquired US postsurgical loops were exempt from relevant ethical committee approval.

The controlled motion was generated by a dedicated experimental set-up described by Sammalı *et al.*,⁸⁸ a sinusoidal displacement of a syringe piston was generated by an electromagnetic actuator injecting saline water through a balloon catheter inserted into the uterine cavity. Rhythmic inflation and deflation of the uterine cavity was generated with a period of 20 s corresponding to a frequency of 0.05 Hz, representing the averages during the most active phase of the menstrual cycle.⁸⁹ Reference for the uterine motion was realised by inserting two needles in the myometrial wall.

Four-minute US recording were performed immediately after surgical removal of the uterus with an US scanner WS80A (Samsung Medison, Seoul, South Korea) equipped with a transvaginal V5-9 probe imaging at 5.6-MHz central frequency. The employed frame rate was 30 Hz, amply sufficient to meet the Nyquist condition given the limited bandwidth of the uterine motion.⁹⁰ A block-matching speckle tracking technique was applied based on 12 blocks that were manually positioned around each needle marker, as described by Sammalı *et al.*⁸⁸

In general, the relevant uterine dynamics were captured in the first few components of each BSS technique. Many selection criteria yielded comparable speckle tracking performances in terms of Pearson r between the average of the 12 blocks and the needle marker, but spectral thresholding of SVD performed best both in Pearson r (0.84 ± 0.15) and MSE ($0.29 \pm 0.24 \text{ mm}^2$), outperforming speckle tracking of the unfiltered data (Pearson $r = 0.66 \pm 0.38$; MSE = $0.34 \pm 0.30 \text{ mm}^2$). As uterine dynamics are slower than the heart contractions, a frequency interval $f_c = [0.04 \text{ Hz} - 0.06 \text{ Hz}]$ was used.

6.4.3.3 *In-vivo* verification

For the ethical-committee-approved study described by Sammalı *et al.*,²⁸ several healthy women underwent four-minute US recordings during four selected phases of the natural menstrual cycle, suggested to indicate variations in uterine contractility.⁹¹ The US scanner and settings were the same as in the *in-vitro* acquisitions and four blocks were manually defined along the myometrial wall in the fundus area, which is considered to be the most contractile part of the uterus. These four sites were then tracked over time by a dedicated US speckle tracking algorithm²⁸ and the Euclidean distances between longitudinal and transversal pairs, as

shown in Figure 6.4-3, served as a measure of absolute motion.

For this work, we evaluated spectral thresholding of SVD adjusting the frequency interval to $f_c = [0.008 \text{ Hz} - 0.066 \text{ Hz}]$ to cover the entire motion range of the different menstrual cycle phases. We extracted the median frequency (MF) from both filtered and unfiltered distance signal as representative of uterine motion frequency for the given example in Figure 6.4-3. The filtered signal presented MF = 0.0360 Hz while the unfiltered signal yielded MF = 0.0176 Hz, indicating that the BBS-filtering produces better estimates when values reported in the literature for the specific menstrual phase are considered as ground truth (0.035-0.055 Hz).⁹⁰ Indeed, as can be appreciated in Figure 6.4-3, larger uterine motions can be tracked, which may lead to a more robust estimate of the MF.

6.5 DISCUSSION

In this work, we reviewed and compared several BSS approaches for noise and clutter suppression in US recordings. As the nature of a desired signal differs among applications, it is important to tailor a filtering approach to the acquisition at hand using specific domain knowledge. Furthermore, although the decompositions comprising BSS are intrinsically adaptive, the retrieval of the signal subspace is often performed manually. Adaptive strategies to identify the components that make up the desired signal are far from established; therefore, we also focussed on several adaptive criteria for component (i.e., “source”) rejection. After all, even though it is possible that the qualitatively best-looking images are formed using a heuristic or empirical rather than an adaptive approach, especially when optimising CNR, such a strategy has limited generalisability and reproducibility. Clutter source dominance as well as noise levels can substantially change from acquisition to acquisition. Whereas Demené *et al.* found that the cut-off value is not critical,¹⁰ we have observed substantial differences in the applications investigated. A similar experience is reported by Baranger *et al.*¹³

For the discussed applications, well-tailored BSS filtering outperformed the more traditional filtering techniques. The reason for this is that BSS exploits the statistical independence or orthogonality of the image “sources”; therefore, it is less affected by overlap of clutter and noise in the spatial or temporal (frequency) domain. Over all US applications considered, SVD in combination with spectral thresholding performed best. This way, effectively, also the known temporal characteristics of the desired sources were exploited; non-noise high-frequency components revealed UCA signals in ULM, the low-frequency components harboured the TIC information, and a well-chosen frequency passband allowed for the separation of cardiac and uterine motion from uncorrelated sources and noise contamination in US speckle tracking. Of all BSS techniques examined, SVD best isolated the temporal components for this purpose.

Furthermore, whereas ICA and NMF show benefit for TIC modelling, they under-perform for super-resolution. This is the result of the linear mixing matrix not being able to represent a source translation over time. We believe that for blood flow imaging, where clutter is abundant but blood vessels are less sparsely infused, also ICA and NMF could be considered. Also in US speckle tracking, NMF underperformed compared to the other BSS methods, possibly because periodic motion is best approximated by allowing negative values. This effect can be

appreciated within the first few components of the *in-silico* TIC modelling validation, where the simulated breathing frequency is clearly visible.

A drawback of BSS techniques is in that they generally require substantially more computational power and time compared to conventional filters, in particular when dealing with the vast amount of data obtained in ultrafast imaging and long-running acquisitions. As all spatial dimensions are collected as rows in the Casorati matrix, filtering can easily be extended to volumetric videos. In fact, as discussed by Demené *et al.*,¹⁰ the availability of a larger spatial support might even lead to an improved BSS performance.

Although beyond the scope of this article, there are methods available to speed up processing without compromising the accuracy or effectiveness of the decomposition itself; for example, randomised SVD⁴⁶ or a blockwise method as proposed by Song *et al.*¹⁴ The latter method even allows for a more accurate clutter and noise rejection, as it can adapt to spatial variations in SNR and resolution. Alternatively, one could think of an approach in which frequency requirements are adjusted during the recording, for example, having a different frequency threshold for different phases of the cardiac cycle.¹⁰ In one such approach,⁵¹ the ideal clutter cut-off was manually initialised for the first 60 frames, and then adaptively retained by tracking the evolution of singular values for each consecutive 60-frame SVD as the coronary ultrafast Doppler video progressed.

Even more promising are approaches that circumvent filter cut-off values by integrating filtering in the BSS algorithm. For example, in a low-rank plus sparse methodology known as robust PCA,⁹² implemented in MRI^{93,94} and more recently in ultrasound,^{95,96} sparse and low-rank (highly coherent) elements are separated in an alternating two-step fashion. This way, remaining overlap between signal and clutter in the SVD components is even further minimised. Separation of sparse and low-rank matrices is also studied for Sparse Signal Separation.⁹⁷⁻⁹⁹ Moreover, deep learning could be utilised to speed up the recovery of sparse sources.¹⁵

It remains to be investigated, whether a gradual rather than a hard threshold can improve BSS filtering by avoiding block artefacts as mentioned by Mauldin Jr *et al.*¹² Furthermore, although most authors use a cut-off value and some observe artefacts caused by partial removal of a complementary subset of components,²⁸ the inclusion of only consecutive singular components is not strictly required. As shown in Figure 6.3-1, a single component could represent an artefact whereas the surrounding components carry the desired signal. This is however dependent on the application and should be studied in more detail.

6.6 CONCLUSION

BSS filtering is increasingly applied to US acquisitions and exhibits great potential for effective noise and clutter suppression. However, as BSS as well as subspace selection have to be tailored to an application, the choice and dedicated design of such a filter is of vital importance. Here, we have determined the best domain-knowledge-based, adaptive approaches for BSS filtering in several US applications.

6.7 ACKNOWLEDGMENTS

This research was conducted in the framework of the IMPULS2 program within the Eindhoven University in collaboration with Philips. This study was also funded by an unrestricted grant from the Dutch Cancer Society (#UVA2013-5941), and a Starting Grant from the European Research Council (#280209). We acknowledge also the Dutch TTW HTSM-13901 grant along with the (financial) contribution from Ferring, SuperSonic Imagine, and Samsung companies.

BIBLIOGRAPHY

1. Errico, C., J. Pierre, S. Pezet, Y. Desailly, Z. Lenkei, O. Couture, and M. Tanter. Ultrafast ultrasound localization microscopy for deep super-resolution vascular imaging. *Nature* 527:499, 2015.
2. Couture, O., V. Hingot, B. Heiles, P. Muleki-Seya, and M. Tanter. Ultrasound Localization Microscopy and Super-Resolution: A State of the Art. *IEEE Trans. Ultrason. Ferroelectr. Freq. Control* 65:1304–1320, 2018.
3. Heidenreich, P. A., J. G. Wiencek, J. G. Zaroff, S. Aronson, L. J. Segil, P. V Harper, and S. B. Feinstein. In Vitro Calculation of Flow by Use of Contrast Ultrasonography. *J. Am. Soc. Echocardiogr.* 6:51–61, 1993.
4. Strouthos, C., M. Lampaskis, V. Sboros, A. McNeilly, and M. Averkiou. Indicator dilution models for the quantification of microvascular blood flow with bolus administration of ultrasound contrast agents. *Ultrason. Ferroelectr. Freq. Control. IEEE Trans.* 57:1296–1310, 2010.
5. Jasaityte, R., B. Heyde, and J. D’hooge. Current State of Three-Dimensional Myocardial Strain Estimation Using Echocardiography. *J. Am. Soc. Echocardiogr.* 26:15–28, 2013.
6. Collier, P., D. Phelan, and A. Klein. A Test in Context: Myocardial Strain Measured by Speckle-Tracking Echocardiography. *J. Am. Coll. Cardiol.* 69:1043 LP-1056, 2017.
7. Bjaerum, S., H. Torp, and K. Kristoffersen. Clutter filter design for ultrasound color flow imaging. *IEEE Trans. Ultrason. Ferroelectr. Freq. Control* 49:204–216, 2002.
8. Joel, T., and R. Sivakumar. An extensive review on Despeckling of medical ultrasound images using various transformation techniques. *Appl. Acoust.* 138:18–27, 2018.
9. Calópe, P. B., F. N. S. Medeiros, R. C. P. Marques, and R. C. S. Costa. A Comparison of Filters for Ultrasound Images. *Telecommun. Netw.* 1035–1040, 2004.
10. Demené, C., T. Deffieux, M. Pernot, B. F. Osmanski, V. Biran, J. L. Gennisson, L. A. Sieu, A. Bergel, S. Franqui, J. M. Correas, I. Cohen, O. Baud, and M. Tanter. Spatiotemporal Clutter Filtering of Ultrafast Ultrasound Data Highly Increases Doppler and fUltrasound Sensitivity. *IEEE Trans. Med. Imaging* 34:2271–2285, 2015.
11. Gallippi, C. M., K. R. Nightingale, and G. E. Trahey. BSS-based filtering of physiological and ARFI-induced tissue and blood motion. *Ultrasound Med. Biol.* 29:1583–1592, 2003.
12. Mauldin, F. W., D. Lin, and J. A. Hossack. The singular value filter: a general filter design strategy for PCA-based signal separation in medical ultrasound imaging. *IEEE Trans. Med. Imaging* 30:1951–1964, 2011.
13. Baranger, J., B. Arnal, F. Perren, O. Baud, M. Tanter, and C. Demené. Adaptive Spatiotemporal SVD Clutter Filtering for Ultrafast Doppler Imaging Using Similarity of Spatial Singular Vectors. *IEEE Trans. Med. Imaging* 37:1574–1586, 2018.
14. Song, P., A. Manduca, J. D. Trzasko, and S. Chen. Ultrasound Small Vessel Imaging With Block-Wise Adaptive Local Clutter Filtering. *IEEE Trans. Med. Imaging* 36:251–262, 2017.
15. van Sloun, R. J. G., O. Solomon, M. Bruce, Z. Z. Khaing, H. Wijkstra, Y. C. Eldar, and M. Misch. Super-resolution Ultrasound Localization Microscopy through Deep Learning. *arXiv Prepr. arXiv1804.07661*, 2018.
16. Lin, F., J. K. Tsuruta, J. D. Rojas, and P. A. Dayton. Optimizing Sensitivity of Ultrasound Contrast-Enhanced Super-Resolution Imaging by Tailoring Size Distribution of Microbubble Contrast Agent. *Ultrasound Med. Biol.* 43:2488–2493, 2017.
17. Ghosh, D., F. Xiong, S. R. Sirsi, P. W. Shaul, R. F. Mattrey, and K. Hoyt. Toward optimization of in vivo super-resolution ultrasound imaging using size-selected microbubble contrast agents. *Med. Phys.* 44:6304–6313, 2017.
18. Breyer, B., T. Viculin, and B. Vojnović. Noise in ultrasonic imaging. *Ultrasonics* 18:81–84, 1980.
19. Gallippi, C. M., and G. E. Trahey. Adaptive Clutter Filtering via Blind Source Separation for Two-Dimensional Ultrasonic Blood Velocity Measurement. *Ultrason. Imaging* 24:193–214, 2002.
20. Mateo, J. L., and A. Fernández-Caballero. Finding out general tendencies in speckle noise reduction in ultrasound images. *Expert Syst. Appl.* 36:7786–7797, 2009.

21. Yu, A. C. H., and L. Lovstakken. Eigen-based clutter filter design for ultrasound color flow imaging: a review. *IEEE Trans. Ultrason. Ferroelectr. Freq. Control* 57:1096–1111, 2010.
22. Cardoso, J.-F. Blind signal separation: statistical principles. *Proc. IEEE* 86:2009–2025, 1998.
23. Rao, K. R., and P. C. Yip. The transform and data compression handbook. CRC press, 2000.
24. Moon, T. K., and W. C. Stirling. Mathematical Methods and Algorithms for Signal Processing. New York, NY: Prentice Hall, Inc., 2000.
25. Golub, G. H., and C. Reinsch. Singular value decomposition and least squares solutions. *Numer. Math.* 14:403–420, 1970.
26. Eckart, C., and G. Young. The approximation of one matrix by another of lower rank. *Psychometrika* 1:211–218, 1936.
27. Martin, C. D., and M. A. Porter. The extraordinary SVD. *Am. Math. Mon.* 119:838–851, 2012.
28. Sammali, F., C. Blank, Y. Huang, N. Kuijsters, C. Rabotti, B. C. Schoot, and M. Mischi. Dedicated ultrasound speckle tracking for quantitative analysis of uterine motion outside pregnancy. *IEEE Trans. Ultrason. Ferroelectr. Freq. Control* 66:581–590, 2018.
29. Miranda, A. A., Y.-A. Le Borgne, and G. Bontempi. New Routes from Minimal Approximation Error to Principal Components. *Neural Process. Lett.* 27:197–207, 2008.
30. Gerbrands, J. J. On the relationships between SVD, KLT and PCA. *Pattern Recognit.* 14:375–381, 1981.
31. Comon, P. Independent component analysis, a new concept? *Signal Processing* 36:287–314, 1994.
32. Hyvärinen, A., and E. Oja. Independent component analysis: algorithms and applications. *Neural Networks* 13:411–430, 2000.
33. Amari, S., A. Cichocki, and H. H. Yang. A new learning algorithm for blind signal separation. *Adv. Neural Inf. Process. Syst.* 757–763, 1996.
34. Bell, A. J., and T. J. Sejnowski. The “independent components” of natural scenes are edge filters. *Vision Res.* 37:3327–3338, 1997.
35. Bai, P., H. Shen, X. Huang, and Y. Truong. A supervised singular value decomposition for independent component analysis of fMRI. *Stat. Sin.* 1233–1252, 2008.
36. Jouan-Rimbaud Bouveresse, D., A. Moya-González, F. Ammari, and D. N. Rutledge. Two novel methods for the determination of the number of components in independent components analysis models. *Chemom. Intell. Lab. Syst.* 112:24–32, 2012.
37. Li, Y., T. Adalı, and V. D. Calhoun. Estimating the number of independent components for functional magnetic resonance imaging data. *Hum. Brain Mapp.* 28:1251–1266, 2007.
38. Hyvarinen, A. Fast and robust fixed-point algorithms for independent component analysis. *IEEE Trans. Neural Networks* 10:626–634, 1999.
39. Rutledge, D. N., and D. J.-R. Bouveresse. Independent components analysis with the JADE algorithm. *TrAC Trends Anal. Chem.* 50:22–32, 2013.
40. Cardoso, J. F., and A. Souloumiac. Blind beamforming for non-Gaussian signals. *IEE Proc. F - Radar Signal Process.* 140:362–370, 1993.
41. Bell, A. J., and T. J. Sejnowski. An information-maximization approach to blind separation and blind deconvolution. *Neural Comput.* 7:1129–1159, 1995.
42. Stone, J. V. Independent component analysis: an introduction. *Trends Cogn. Sci.* 6:59–64, 2002.
43. Lee, T.-W., M. Girolami, and T. J. Sejnowski. Independent component analysis using an extended infomax algorithm for mixed subgaussian and supergaussian sources. *Neural Comput.* 11:417–441, 1999.
44. Lee, D. D., and H. S. Seung. Learning the parts of objects by non-negative matrix factorization. *Nature* 401:788, 1999.
45. Berry, M. W., M. Browne, A. N. Langville, V. P. Pauca, and R. J. Plemmons. Algorithms and applications for approximate nonnegative matrix factorization. *Comput. Stat. Data Anal.* 52:155–173, 2007.
46. Song, P., J. D. Trzasko, A. Manduca, B. Qiang, R. Kadirvel, D. F. Kallmes, and S. Chen. Accelerated Singular Value-Based Ultrasound Blood Flow Clutter Filtering With Randomized Singular Value

- Decomposition and Randomized Spatial Downsampling. *IEEE Trans. Ultrason. Ferroelectr. Freq. Control* 64:706–716, 2017.
47. Desailly, Y., A.-M. Tissier, J.-M. Correas, F. Wintzenrieth, M. Tanter, and O. Couture. Contrast enhanced ultrasound by real-time spatiotemporal filtering of ultrafast images. *Phys. Med. Biol.* 62:31, 2016.
 48. Sloun, R. J. G. van, O. Solomon, Y. C. Eldar, H. Wijkstra, and M. Mischi. Sparsity-driven super-resolution in clinical contrast-enhanced ultrasound. *Proc. IEEE Int. Ultrason. Symp.* 1–4, 2017.
 49. Lediju, M. A., M. J. Pihl, S. J. Hsu, J. J. Dahl, C. M. Gallippi, and G. E. Trahey. A motion-based approach to abdominal clutter reduction. *IEEE Trans. Ultrason. Ferroelectr. Freq. Control* 56:2437–2449, 2009.
 50. van der Ven, M., J. J. Luime, L. L. van der Velden, J. G. Bosch, J. M. W. Hazes, and H. J. Vos. High-Frame-Rate Power Doppler Ultrasound Is More Sensitive than Conventional Power Doppler in Detecting Rheumatic Vascularisation. *Ultrasound Med. Biol.* 43:1868–1879, 2017.
 51. Maresca, D., M. Correia, M. Tanter, B. Ghaleh, and M. Pernot. Adaptive Spatiotemporal Filtering for Coronary Ultrafast Doppler Angiography. *IEEE Trans. Ultrason. Ferroelectr. Freq. Control* 65:2201–2204, 2018.
 52. Valle, S., W. Li, and S. J. Qin. Selection of the number of principal components: the variance of the reconstruction error criterion with a comparison to other methods. *Ind. Eng. Chem. Res.* 38:4389–4401, 1999.
 53. Ikeda, H., R. Nagaoka, M. Lafond, S. Yoshizawa, R. Iwasaki, M. Maeda, S. Umemura, and Y. Saijo. Singular value decomposition of received ultrasound signal to separate tissue, blood flow, and cavitation signals. *Jpn. J. Appl. Phys.* 57:07LF04, 2018.
 54. Arnal, B., J. Baranger, C. Demene, M. Tanter, and M. Pernot. In vivo real-time cavitation imaging in moving organs. *Phys. Med. Biol.* 62:843, 2017.
 55. Kruse, D. E., and K. W. Ferrara. A new high resolution color flow system using an eigendecomposition-based adaptive filter for clutter rejection. *IEEE Trans. Ultrason. Ferroelectr. Freq. Control* 49:1739–1754, 2002.
 56. Rissanen, J. Modeling by shortest data description. *Automatica* 14:465–471, 1978.
 57. Akaike, H. A new look at the statistical model identification. *IEEE Trans. Automat. Contr.* 19:716–723, 1974.
 58. Wax, M., and T. Kailath. Detection of signals by information theoretic criteria. *IEEE Trans. Acoust.* 33:387–392, 1985.
 59. van Sloun, R. J. G., L. Demi, A. W. Postema, J. J. de la Rosette, H. Wijkstra, and M. Mischi. Ultrasound-contrast-agent dispersion and velocity imaging for prostate cancer localization. *Med. Image Anal.* 35:610–619, 2017.
 60. Marčenko, V. A., and L. A. Pastur. Distribution of eigenvalues for some sets of random matrices. *Math. USSR-Sbornik* 1:457, 1967.
 61. Shannon, C. E. A mathematical theory of communication. *Bell Syst. Tech. J.* 27:379–423, 1948.
 62. Kim, M., C. K. Abbey, J. Hedhli, L. W. Dobrucki, and M. F. Insana. Expanding Acquisition and Clutter Filter Dimensions for Improved Perfusion Sensitivity. *IEEE Trans. Ultrason. Ferroelectr. Freq. Control* 64:1429–1438, 2017.
 63. Wu, K., X. Zhang, G. Chen, F. Weng, and M. Ding. Respiratory motion compensation algorithm of ultrasound hepatic perfusion data acquired in free-breathing. *Proc. SPIE - MIPPR 2013 Parallel Process. Images Optim. Med. Imaging Process.* 8920:892001, 2013.
 64. Betzig, E., G. H. Patterson, R. Sougrat, O. W. Lindwasser, S. Olenych, J. S. Bonifacino, M. W. Davidson, J. Lippincott-Schwartz, and H. F. Hess. Imaging Intracellular Fluorescent Proteins at Nanometer Resolution. *Science* 313:1642–1645, 2006.
 65. Viessmann, O. M., R. J. Eckersley, K. Christensen-Jeffries, M. X. Tang, and C. Dunsby. Acoustic super-resolution with ultrasound and microbubbles. *Phys. Med. Biol.* 58:6447, 2013.
 66. Hurley, N., and S. Rickard. Comparing measures of sparsity. *IEEE Trans. Inf. Theory* 55:4723–4741, 2009.
 67. Pries, A. R., T. W. Secomb, P. Gaehtgens, and J. F. Gross. Blood flow in microvascular networks.

- Experiments and simulation. *Circ. Res.* 67:826–834, 1990.
68. Khaing, Z. Z., L. N. Cates, D. M. DeWees, A. Hannah, P. Mourad, M. Bruce, and C. P. Hofstetter. Contrast-enhanced ultrasound to visualize hemodynamic changes after rodent spinal cord injury. *J. Neurosurg. Spine* 29:306–313, 2018.
 69. Tremblay-Darveau, C., R. Williams, L. Milot, M. Bruce, and P. N. Burns. Combined perfusion and doppler imaging using plane-wave nonlinear detection and microbubble contrast agents. *IEEE Trans. Ultrason. Ferroelectr. Freq. Control* 61:1988–2000, 2014.
 70. Dietrich, C. F., M. A. Averkiou, J.-M. Correas, N. Lassau, E. Leen, and F. Piscaglia. An EFSUMB introduction into Dynamic Contrast-Enhanced Ultrasound (DCE-US) for quantification of tumour perfusion. *Ultraschall der Medizin-European J. Ultrasound* 33:344–351, 2012.
 71. Claudon, M., C. F. Dietrich, B. I. Choi, D. O. Cosgrove, M. Kudo, C. P. Nolsøe, F. Piscaglia, S. R. Wilson, R. G. Barr, M. C. Chammas, N. G. Chaubal, M.-H. Chen, D. A. Clevert, J. M. Correas, H. Ding, F. Forsberg, J. B. Fowlkes, R. N. Gibson, B. B. Goldberg, N. Lassau, E. L. S. Leen, R. F. Mattrey, F. Moriyasu, L. Solbiati, H.-P. Weskott, and H.-X. Xu. Guidelines and Good Clinical Practice Recommendations for Contrast Enhanced Ultrasound (CEUS) in the Liver – Update 2012: A WFUMB-EFSUMB Initiative in Cooperation with Representatives of AFSUMB, AIUM, ASUM, FLAUS and ICUS. *Ultrasound Med. Biol.* 39:187–210, 2013.
 72. Fröhlich, E., R. Muller, X.-W. Cui, D. Schreiber-Dietrich, and C. F. Dietrich. Dynamic Contrast-Enhanced Ultrasound for Quantification of Tissue Perfusion. *J. Ultrasound Med.* 34:179–196, 2015.
 73. Herold, I. H. F., M. A. Soliman Hamad, H. C. van Assen, R. A. Bouwman, H. H. M. Korsten, and M. Mischi. Pulmonary blood volume measured by contrast enhanced ultrasound: a comparison with transpulmonary thermodilution. *BJA Br. J. Anaesth.* 115:53–60, 2015.
 74. Mischi, M., T. A. Kalker, and E. H. Korsten. Contrast echocardiography for pulmonary blood volume quantification. *IEEE Trans. Ultrason. Ferroelectr. Freq. Control* 51:1137–1147, 2004.
 75. Quaia, E. Assessment of tissue perfusion by contrast-enhanced ultrasound. *Eur. Radiol.* 21:604–615, 2011.
 76. Kuenen, M. P. J., M. Mischi, and H. Wijkstra. Contrast-ultrasound diffusion imaging for localization of prostate cancer. *IEEE Trans Med Imaging* 30:1493, 2011.
 77. Kuenen, M. P. J., T. A. Saidov, H. Wijkstra, and M. Mischi. Contrast-Ultrasound Dispersion Imaging for Prostate Cancer Localization by Improved Spatiotemporal Similarity Analysis. *Ultrasound Med. Biol.* 39:1631–1641, 2013.
 78. Dinkel, J., C. Thieke, C. Plathow, P. Zamecnik, H. Prüm, P. E. Huber, H.-U. Kauczor, H.-P. Schlemmer, and C. M. Zechmann. Respiratory-Induced Prostate Motion. *Strahlentherapie und Onkol.* 187:426–432, 2011.
 79. Lopata, R. G. P., M. M. Nillesen, C. N. Verrijp, S. K. Singh, M. M. Y. Lammens, J. A. W. M. van der Laak, H. B. van Wetten, J. M. Thijssen, L. Kapusta, and C. L. de Korte. Cardiac biplane strain imaging: initial in vivo experience. *Phys. Med. Biol.* 55:963–979, 2010.
 80. Kawagishi, T. Speckle Tracking for Assessment of Cardiac Motion and Dyssynchrony. *Echocardiography* 25:1167–1171, 2008.
 81. Bohs, L. N., B. J. Geiman, M. E. Anderson, S. C. Gebhart, and G. E. Trahey. Speckle tracking for multi-dimensional flow estimation. *Ultrasonics* 38:369–375, 2000.
 82. Udesen, J., F. Gran, K. L. Hansen, J. A. Jensen, C. Thomsen, and M. B. Nielsen. High frame-rate blood vector velocity imaging using plane waves: Simulations and preliminary experiments. *IEEE Trans. Ultrason. Ferroelectr. Freq. Control* 55:1729–1743, 2008.
 83. Lenge, M., A. Ramalli, E. Boni, H. Liebgott, C. Cachard, and P. Tortoli. High-frame-rate 2-D vector blood flow imaging in the frequency domain. *IEEE Trans. Ultrason. Ferroelectr. Freq. Control* 61:1504–1514, 2014.
 84. Baillargeon, B., N. Rebelo, D. D. Fox, R. L. Taylor, and E. Kuhl. The living heart project: a robust and integrative simulator for human heart function. *Eur. J. Mech.* 48:38–47, 2014.
 85. Weisstein, E. W. Apodization Function. , 2019.at
<<http://mathworld.wolfram.com/ApodizationFunction.html>>

86. Goffinet, C., and J.-L. Vanoverschelde. Speckle tracking echocardiography. *Eur. Cardiovasc. Dis.* 3:1–3, 2007.
87. Bouguet, J.-Y. Pyramidal implementation of the affine lucas kanade feature tracker description of the algorithm. *Intel Corp.* 5:4, 2001.
88. Sammali, F., C. Blank, L. Xu, Y. Huang, N. P. M. Kuijsters, B. C. Schoot, and M. Misch. Experimental setup for objective evaluation of uterine motion analysis by ultrasound speckle tracking. *Biomed. Phys. Eng. Express* 4:35012, 2018.
89. Ziegler, D., C. Bulletti, R. Fanchin, M. Epiney, and P. BRIOSCHI. Contractility of the nonpregnant uterus. *Ann. N. Y. Acad. Sci.* 943:172–184, 2001.
90. Bulletti, C., D. de Ziegler, V. Polli, L. Diotallevi, E. Del Ferro, and C. Flamigni. Uterine contractility during the menstrual cycle. *Hum. Reprod.* 15:81–89, 2000.
91. Ijland, M. M., J. L. H. Evers, G. A. J. Dunselman, and H. J. Hoogland. Subendometrial contractions in the nonpregnant uterus: an ultrasound study. *Eur. J. Obstet. Gynecol. Reprod. Biol.* 70:23–24, 1996.
92. Candès, E. J., X. Li, Y. Ma, and J. Wright. Robust principal component analysis? *J. ACM* 58:11, 2011.
93. Otazo, R., E. Candès, and D. K. Sodickson. Low-rank plus sparse matrix decomposition for accelerated dynamic MRI with separation of background and dynamic components. *Magn. Reson. Med.* 73:1125–1136, 2015.
94. Bouwmans, T., S. Javed, H. Zhang, Z. Lin, and R. Otazo. On the Applications of Robust PCA in Image and Video Processing. *Proc. IEEE* 106:1427–1457, 2018.
95. Bayat, M., and M. Fatemi. Concurrent Clutter and Noise Suppression via Low Rank Plus Sparse Optimization for Non-Contrast Ultrasound Flow Doppler Processing in Microvasculature. *Proc. IEEE Int. Conf. Acoust. Speech Signal Process.* 1080–1084, 2018.
96. Solomon, O., R. Cohen, Y. Zhang, Y. Yang, H. Qiong, J. Luo, R. J. G. van Sloun, and Y. C. Eldar. Deep Unfolded Robust PCA with Application to Clutter Suppression in Ultrasound. *arXiv Prepr. arXiv1811.08252*, 2018.
97. Turek, J. S., M. Elad, and I. Yavneh. Clutter Mitigation in Echocardiography Using Sparse Signal Separation. *Int. J. Biomed. Imaging* 2015:958963, 2015.
98. Zibulevsky, M., and B. A. Pearlmutter. Blind source separation by sparse decomposition in a signal dictionary. *Neural Comput.* 13:863–882, 2001.
99. Li, P., X. Yang, D. Zhang, and Z. Bian. Adaptive clutter filtering based on sparse component analysis in ultrasound color flow imaging. *IEEE Trans. Ultrason. Ferroelectr. Freq. Control* 55:1582–1596, 2008.

Part III

Assessment of uterine activity for predicting
successful embryo implantation

7

ASSESSMENT OF UTERINE CONTRACTILITY DURING IN-VITRO FERTILIZATION BY QUANTITATIVE ULTRASOUND IMAGING

Abstract: About 10% of women have difficulty to get pregnant. In-vitro fertilization (IVF), often involving intracytoplasmatic sperm injection (ICSI), represents the most advanced treatment for infertile or sub-fertile women; however, failure rates remain over 70%. There is evidence that implantation failure may be caused by altered uterine activity. In this study, we assess the uterine contraction characteristics by quantitative ultrasound imaging during IVF treatment. Sixteen women undergoing IVF/ICSI with a fresh single embryo transfer were measured by two-dimensional transvaginal ultrasound in 3 phases of the treatment: follicle stimulation (FS), one hour before embryo transfer (ET1), and five to seven days after ET (ET5-7). Uterine motion analysis was implemented by a dedicated speckle tracking algorithm; frequency- and amplitude-related features were extracted from the derived signals to characterize the uterine contractions in relation to ongoing implantation (positive human chorionic gonadotropin after six weeks) as well to ongoing pregnancy (positive heart rate after 11 weeks). The relationship with clinical features, as well as uterine contractions patterns in healthy women, was also investigated. Overall, uterine activity in terms of frequency and amplitude significantly decreased along the phases of the IVF/ICSI treatment showing FS as the most active phase followed by ET1 and ET5-7. When comparing the two groups, women with ongoing implantation/pregnancy showed overall significantly higher uterine contraction frequency compared to those with no ongoing implantation/pregnancy in all the measured phases. On the other hand, uterine contraction amplitude was lower in women with ongoing implantation/pregnancy compared to those with no ongoing implantation/pregnancy, but statistical significance was only achieved in ET5-7. These results suggest that, especially in ET1, uterine activity with higher frequency and lower amplitude may favor embryo implantation. These promising results motivate towards an extended validation in the context of in-vitro fertilization procedures

From: C. Blank, F. Sammali, N. P. M Kuijsters, Y. Huang, C. Rabotti, P. de Sutter, M. Mischi, B.C. Schoot. **"Assessment of uterine contractility during in-vitro fertilization by quantitative ultrasound imaging"**. Submitted to *Fertility and Sterility Journal*.

7.1 INTRODUCTION

The prevalence of infertility is estimated to be around 9 % worldwide for women aged 20-44 years old¹. In the past decades, the number of in-vitro fertilization (IVF) treatments increased considerably. However, despite considerable efforts to improve the success of ART, the overall effectiveness remains below 40% per treatment cycle, even for IVF or intracytoplasmic sperm injection (ICSI) with blastocyst transfer, which is the most advanced technique to date². In up to 20% of the subfertile couples, no explanation can be found for unsuccessful IVF/ICSI¹. Within this group, a possible explanation could be implantation failure due to increased uterine contractions, especially during and after embryo transfer (ET), expelling the transferred embryo outside the uterine cavity^{3-6,6-8}. Furthermore, dysfunctional uterine contraction activity has previously been reported as a possible cofactor influencing the outcome of fertility treatment^{5,9}.

It is known that during the natural menstrual cycle, the uterine contraction pattern will change under the influence of estradiol and progesterone¹⁰. Extensive research has focused on the clinical relevance of these contractions and opportunities to influence them with medication or surgery. Different methods such as hysterosalpingoscintigraphy, visual qualitative inspection by two- (2D) and three-dimensional (3D) ultrasound (US) and intrauterine pressure measurements have been used to assess uterine activity. Unfortunately, these methods are not suitable for objective, non-invasive or reliable assessment of uterine activity in the non-pregnant uterus, especially during IVF treatment¹⁰.

Ultrasound imaging represents a non-invasive option that is perfectly suited to investigate the uterine mechanical function in the context of IVF treatment. However, only qualitative evaluation of movement has been performed, evidencing variations during the menstrual cycle¹¹ and the important role of peristaltic movements on IVF performance⁸. The operator-dependency of qualitative ultrasound analysis complicates its adoption for follow-up and comparative studies¹², therefore hampering the establishment of ultrasound imaging for monitoring the uterine function in relation to IVF. As a result, current knowledge on uterine movements remains limited.

A recent study on healthy women (HW) with regular cycles¹⁵ proposed a non-invasive novel method based on US strain imaging to quantitatively assess and characterize uterine contractility in terms of amplitude and frequency of the uterine activity¹³.

It is evident that the possibility of an objective and noninvasive assessment of the uterine contraction characteristics during the IVF cycle is an essential step to improve our understanding of the impact of contractions on IVF failure, possibly leading to improved IVF success rates. Therefore, the aim of this study is to evaluate the use and clinical value of this novel, non-invasive method, based on quantitative US imaging, for the characterization of uterine contractions in terms of amplitude and frequency during the IVF cycle, especially in relation to implantation success and failure.

7.2 MATERIAL AND METHODS

7.2.1 Patient selection

All women undergoing oocyte retrieval for IVF or ICSI between January 1, 2017 and July 31, 2018 at the department of Reproductive Medicine of Ghent University Hospital, Belgium, were recruited as potential study patients. Transfer with more than one embryo per transfer, uterine

anomalies or pathologies, previous caesarean section, mental disability or/and significant language barrier were the exclusion criteria adopted in this study.

Data of 29 patients that met all inclusion criteria and were planned for an IVF treatment with a fresh SET were included in the dataset. Only 16 patients completed the three measurements and were included in the final analysis. The main reasons for patient the drop-out were cancellation of the fresh SET (Escape intra-uterine insemination due to less follicles: n=4; no embryos available after laboratory phase: n=3; double embryo transfer: n=1; freeze all embryos in the context of ovarian hyper stimulation syndrome: n=2) and withdraw of the patient (n=3). Indication for IVF/ICSI treatment were male subfertility (50%), tubal pathology (12.5%), unexplained subfertility (18.8%) or hormonal disorders (18.8%).

7.2.2 IVF procedures

In our study population, two protocols for pituitary down-regulation were used. Using the agonist protocol (considered as standard treatment), patients started with a pre-treatment for at least 14 days with ethinylestradiol50/levonorgestrel150 (M50) (Microgynon '50'; Bayer Pharma AG, Berlin, Germany). After discontinuation of M50 (day 0 of the cycle), down-regulation followed using a daily dose of 0.1 mg gonadotropin-releasing hormone agonist (GnRH-a) Triptorelin (Decapeptyl®; Ferring, Hoofddorp, The Netherlands) for 7 days. In the antagonist group, gonadotropins were started on day three of the natural cycle and 0.25 mg Cetorelix (Cetrotide®, Merck Serono, Geneva, Switzerland) was injected subcutaneously as a daily dose from cycle day six until the day of oocyte maturation triggering. Controlled ovarian hyperstimulation was achieved using a daily doses between 112.5 IU and 300 IU of recombinant follicle stimulating hormone (Bemfola®; Finox biotech AG, Balzers, Liechtenstein) or human menopausal gonadotropin (Menopur®; Ferring, Hoofddorp, The Netherlands) depending on age, anti-Mullerian hormone¹⁴ and previous response, starting from day three.

Oocytes were retrieved 34-36 hours after a 5000-IU human chorionic gonadotropin (hCG) injection (Pregnyl; MSD Oss, the Netherlands). Oocytes were inseminated with spermatozoa (IVF: 19%) or injected with a spermcell (ICSI: 81 %) between two and four hours after aspiration.

Embryos were cultured individually in pre-equilibrated Cleavage media (Sydney IVF Cleavage Medium®, Cook, USA) and were transferred to blastocyst media (Sydney IVF Blastocyst Medium®, Cook, USA) in a 5% O₂, 6% CO₂ and 89% N₂ incubator at 37°C.

ET was performed five days after oocyte retrieval. In all cases, the best quality embryo, based on the Alpha scoring system¹⁵ was transferred. Women were treated with intravaginal progesterone (Utrogestan Besins Healthcare, Brussels, Belgium) starting on the day of hCG-injection to support the luteal phase. An hCG test was performed sixteen days after ET.

7.2.3 Data collection

Patients underwent three 2D transvaginal US measurements of four-minutes during three different moments of the IVF/ICSI treatment. The first measurement was planned during the follicle stimulation (FS) phase (at least one follicle >16 mm), the second measurement one hour before the embryo transfer (ET1) and the last measurement five to seven days after the embryo transfer (ET5-7). US acquisitions were performed using the WS80A US scanner (Samsung-Medison) with a transvaginal V5-9 probe. All recordings were performed at 5.6-MHz central frequency and 30 frames/s. The recorded B-mode data were then exported to AVI (Audio Video

Interleave) format for the analysis, implemented in Matlab® (MathWorks, Natick, USA).

7.2.4 Uterine contractility assessment: quantitative ultrasound imaging

The uterine contractility in stimulated menstrual cycles was assessed using US motion tracking. US motion tracking was implemented by dedicated speckle-tracking based on block matching as proposed by Sammali et al.,¹³. The method employs a number of advanced technical solutions to improve accuracy and reliability¹³. In particular, uterine motion is enhanced by applying Singular Value Decomposition (SVD) filtering to the US image sequences after speckle regularization and prior to speckle tracking analysis. The obtained results demonstrated the ability of the proposed SVD filtering to separate uterine motion from uncorrelated signals deriving from multiple sources, such as fast motion elicited by surrounding organs, respiratory motion, US probe motion and stationary tissue clutter, which affect speckle tracking performance. The obtained promising results motivated us to use SVD in the context of IVF. To this end, SVD was applied to the acquired US image sequences for enhancing the uterine motion recordings in stimulated cycles. The latter was enhanced by selecting relevant components, according an energy metric proposed in¹³, in the frequency interval [$f_1 = 0.0083 - f_2 = 0.0833$ HZ], chosen to reflect the uterine motion bandwidth during the IVF cycle according to Fanchin et al.³. The obtained SVD spectral filtered US image sequences were then used for motion analysis by speckle tracking. Block matching, consisting of selecting a block in the target frame and searching for the optimal match in the following frame, was accelerated by implementation of a Diamond search method based on a predefined search patterns. A block similarity measure, represented by the sum of absolute differences (SAD), was employed to determine the optimal match. Details on the developed algorithm can be found in¹³.

Four blocks were manually defined along the myometrial wall in the fundus area, known to be the most contractile part¹⁶. In particular, the sites were positioned in the subendometrial layer of the myometrium as shown in Figure 7.1, being the muscle involved in the contractions. The four blocks were coupled in pairs, and distance and strain signals were derived between each pair along the longitudinal (LD) and transversal (TD) direction as indicated in Figure 7.1. Euclidean distance was adopted to derive the distance between each pair resulting in an absolute motion. The strain was defined as the relative variation of the distance between the tracked blocks as

$$\epsilon = \frac{d(j)-d(j-1)}{d(j-1)}, \quad (7.1)$$

where $d(j)$ and $d(j-1)$ indicate the distance between the tracked blocks at the current frame (j) and previous frame ($j-1$), respectively.

As shown in¹³, amplitude-related features such as standard deviation (SD) and unnormalized first statistical moment (UFM), and frequency-related features such as mean frequency (MF in Hz) and median frequency (MDF in Hz), allowed for a good understanding of the uterine contractility throughout the natural menstrual cycle. To this end, these specific features were also considered in this study in order to obtain a good understanding of the uterine contractility during the IVF cycle. To this end, the contraction frequency (f_c), expressed in contractions per minutes based on a zero crossing estimator, was also evaluated. After normalization, SD and UFM were combined as an overall amplitude/strength indication of the uterine contractions while, MF, MDF, and f_c were combined as an overall frequency indication of those uterine contractions. All features were normalized based on their maximum value to combine the

results of the distance and strain signals in both longitudinal and transversal directions. This was performed per each patient and phase. Technical details about features extraction as well as preprocessing analysis can be found in Sammali et al.¹³.

7.2.5 Outcome

The main outcome measures were frequency and amplitude of the uterine contractions during an IVF/ICSI cycle; as well as correlation of uterine contractions with ongoing implantation (OI) and ongoing pregnancy (OP) after a fresh SET transfer. OI/OP were defined as a positive hCG test at gestational age of at least six weeks (OI) or detectable heart rate at a gestational age of at least 11 weeks (OP).

Furthermore, the outcome measures of the uterine contraction were correlated with clinical features such as hormone levels, follicle stimulation doses and number of days and thickness of endometrial layer (TED).

Finally, data of the IVF patients were compared with previously obtained and published data of HW (details are described in Sammali *et al.*¹³). Similar data acquisitions were performed (during different four phases of menstrual cycle: menses, late follicular phase (LF), early luteal phase (EL), and late luteal phase (LL)) as in the IVF group.

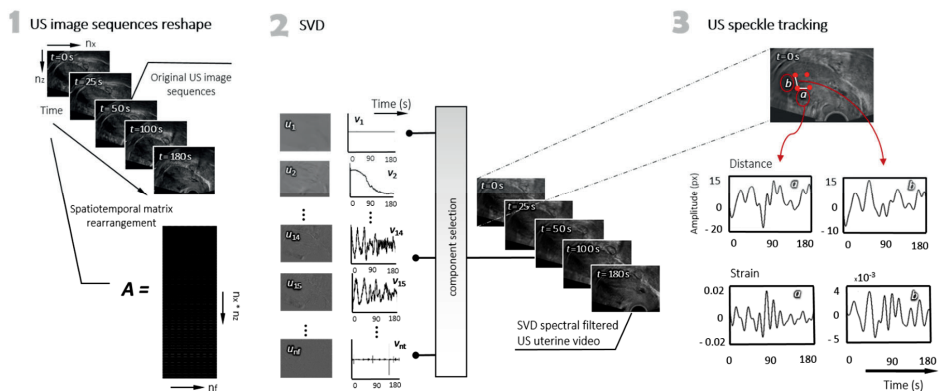


Figure 7.1: (1) The uterine US image sequences are reshaped into the 2D Casorati matrix A representing a new spatiotemporal representation; all pixels at each time instant are arranged in each column of A . (2) The Casorati matrix A is decomposed by SVD into individual spatiotemporal matrices, U and V . By selecting the first n couples of singular vectors, artifacts and high-frequency noise can be rejected and a good US uterine image can be obtained. (3) Example of distance and strain signals derived along the longitudinal a) and transversal b) direction by US speckle tracking after SVD filtering, for 3-min recordings.

7.2.6 Database and statistical analysis

Relevant data, including maternal information, clinical diagnosis, IVF protocol and response, laboratory information on embryo morphology, hormone levels, treatment outcomes of all IVF cycles as well as features of the quantitative ultrasound imaging (frequency and amplitude) were collected and recorded in Research Manager.

Statistical analysis was performed using SPSS software version 25 and Matlab 2017a. Categorical variables were analyzed by Pearson's chi-square test or in case more than 20% of the cells have expected frequencies less than five a Fisher's exact test was used. A Student's t-test (in case of Gaussian distribution) or Mann-Whitney U-test (in case of non-Gaussian

distribution) were used for continuous variables. In order to obtain a global characterization of the uterine contractility during the three investigated phases of the IVF cycle in terms of contraction amplitude and frequency, frequency (MF, MDF, f_c) and amplitude (SD, UFM) features were combined into two separate groups and evaluated during the three phases. Prior to their combination, the values of the extracted features were normalized relative to their maximum value per patient and phase.

A p-value <0.05 was considered statistically significant. Correlation analysis was based on Pearson's and Spearman's correlation coefficient and was considered statistically significant with a p-value of <0.01.

7.2.7 Ethical approval

All patients gave informed consent and the Regional Ethics Review Board of the Ghent University hospital approved the study (UH Ghent reference: 2017/0758-Belgian registration number: B670201732669).

7.3 RESULTS

7.3.1 General characteristics

The overall OP rate for fresh SET with a day-5 embryo was 43.8%, while 56.3% of all patients had a positive hCG test at gestational age of six weeks (OI). One patient had a biochemical pregnancy and another patient an ectopic implantation.

As shown in Table Ia, no significant difference between the groups with or without OP were observed in the baseline characteristics, including maternal age (Overall: 32.1 ± 4.7 , OP: 29.9 ± 3.9 vs no OP: 33.9 ± 4.6), body mass index (Overall: 25.9 ± 4.7 , OP 25.7 ± 4.0 vs no OP 26.0 ± 5.4), previous gravidity (Overall: 1 (0-6), OP 1 (0-2) vs no OP 1 (0-6)), parity (Overall: 0 (0-1), OP 0 (0-1) vs no OP: 0 (0-1)), early miscarriage (Overall: 0.5 (0-6), OP 0 (0-2) vs no OP 1 (0-6)), indication (tubal pathology (12.5%), male subfertility (50%), hormonal disorder (18.8%), repeated miscarriage (6.3%) or unexplained subfertility (25%)) for IVF/ICSI treatment, duration of subfertility (Overall: 50 ± 437 months, OP 35 ± 36 months vs no OP 61 ± 35 months) or previous failed IVF/ICSI cycles (Overall: 2.0 ± 1.7 , OP 1.3 ± 1.4 vs no OP 2.6 ± 1.7). Only estradiol levels during the FS as well 5-7 days after ET were significant different between patients with or without OP (FS: OP: 842 pmol/L (210-1450 pmol/L) vs no OP: 1240 pmol/L (1030-2630 pmol/L) p = 0.039; ET5-7: OP 25 pmol/L (25-44) vs no OP: 326 pmol/L (70-486 pmol/L) p = 0.001) (Table Ib).

Controlled ovarian stimulation was performed using a mean dose of $2777 \text{ IU} \pm 980 \text{ IU}$ recombinant follicle stimulating hormone or human menopausal gonadotropin. Mean number of mature oocytes retrieved and available embryos were 10.7 ± 5.7 and 2.8 ± 2.0 , respectively. According the ESHRE/Alpha guidelines, most of the replaced embryos were score as good or even excellent quality (n=12) (Table Ic). No significant difference in embryo quality was observed between the pregnant women and non-pregnant women (Table Ic).

Table Ia. Characteristics of the clinical variables

	Overall	OP	No OP	p-value
Maternal age (y)*	32.1 ± 4.7	29.9 ± 3.9	33.9 ± 4.6	0.087
BMI (kg/m²)*	25.9 ± 4.7	25.7 ± 4.0	26.0 ± 5.4	0.909
Gravidity**	1 (0-6)	1 (0-2)	1 (0-6)	0.866
Parity**	0 (0-1)	0 (0-1)	0 (0-1)	0.390
Previous miscarriages**	0.5 (0-6)	0 (0-2)	1 (0-6)	0.565
Length of natural cycle in days**	27 (0-31)	28 (0-31)	26 (0-30)	0.484
Length of natural cycle in days**	31 0 (0-60)	31 (0-45)	30 (0-60)	0.557
Indication for IVF/ICSI*** ^				0.509
Tubal pathology	2 (12.5%)	1 (50.0)	1 (50.0%)	
Unexplained subfertility	4 (25.0%)	3 (75.0%)	1 25.0%)	
Male subfertility	8 (50.0%)	3 (37.5%)	5 (62.5%)	
Hormonal disorders	3 (18.8%)	1 (33.3%)	2 (66.7%)	
Repeated miscarriage	1 (6.3%)	0 (0.0%)	1 (100.0%)	
Number of previous failed IVF/ICSI cycles*	2.0 ± 1.7	1.3 ± 1.4	2.6 ± 1.7	0.137
Duration of subfertility in months *	50 ± 37	35 ± 36	61 ± 35	0.166
Days of stimulation*	13 ± 2.4	13 ± 2.4	12 ± 2.3	0.283
Total gonadotropin or FSH dose (IU)*	2777 ± 978	2770 ± 767	2783 ± 1163	0.979
Fertilization method				0.375
IVF	3 (18.8%)	2 (66.7%)	1 (33.3%)	
ICSI	13 (81.2%)	5 (38.5%)	8 (61.5%)	
Number of oocytes*	10.7 ± 5.7	12.1 ± 5.3	9.6 ± 6.0	0.388
Number of available embryos*	2.8 ± 2.0	2.9 ± 1.7	2.7 ± 1.0	0.861
Values are presented as number, mean ± SD*, median (range)**, or number (percentage)***				

Table Ib. Characteristics of the blood levels

	Overall	OP	No OP	p-value
Basal Blood levels				
TSH (mU/L)*	1.5 ± 0.6	1.5 ± 0.6	1.5 ± 0.7	0.935
AMH (µg/L)*	2.7 ± 1.8	3.7 ± 1.4	2 0 ± 1.8	0.056
Estradiol (ng/L) **				
During measurement follicle stimulation phase (FS)	1115 (210-2630)	1240 (1030-2630)	842 (210-1450)	0.039
During measurement 5-7 after embryo transfer (ET5-7)	153 (25-486)	326 (70-486)	25 (25-44)	0.001

Progesterone (ng/L) **				
During measurement follicle stimulation phase (FS)	0.3 (0.15-1.23)	0.3 (0.15-0.75)	0.31 (0.15-1.23)	0.595
During measurement 5-7 after embryo transfer (ET5-7)	15 (8-71)	16 (13-37)	13 (8-71)	0.088
Values are presented as mean \pm SD* or median (range)**				

Table 1c. Characteristics of the embryos

	Overall	OP	No OP	p-value
Embryo Quality				0.182
Excellent: 4/5AA, 4/5AB	2 (12.5%)	2 (100.0%)	0 (0.0%)	
Good: 3AA, 3AB, 3/4/5BA, 3/4/5BB, 3/4/5AC, 3/4/5BC, 3/4/5CA, 3/4/5CB, 4/5CC	10 (62.5%)	3 (30.0%)	7 (70.0%)	
Moderate: 3CC, Blast 1, Blast 2	4 (25.0%)	2 (50.0%)	2 (50.0%)	
Poor: All other embryos	0 (0.0%)	0 (0.0%)	0 (0.0%)	
Values are presented as number (percentage)				

7.3.2 Uterine contractility patterns during all phases of IVF treatment

Overall significantly higher uterine-contraction frequency-features (based on the combination of f_c , MDF and MF) as well as amplitude-features (based on the combination of amplitude (SD) and energy (UFM)) were observed during the FS in comparison to ET1 and ET5-7 (Figure 7.2). When comparing the uterine activity in terms of frequency and amplitude for the OP and no OP, Figure 7.3 shows significantly lower uterine activity for the OP group in the FS in terms of frequency features, also paralleled by lower amplitude features, but not significantly lower compared to the no OP group. Instead, during the ET1 and ET5-7 the OP group showed significantly higher frequency features, paralleled by lower amplitude features. However, amplitude features were not significantly lower for the ET1 compared to the no OP group. Individual significant features based on distance and strain signals in LD or TD were f_c during ET1 and MF and MDF during ET5-7. None of the amplitude features showed individually significant results. One hour before ET (ET1), f_c (UC/min) of patients with OI (based on DS) as well OP (based on DS) was significantly higher than in patients with no OI or OP (OI: 1.35 ± 0.44 UC/min vs no OI: 0.91 ± 0.19 UC/min, $p = 0.028$; OP: 1.45 ± 0.42 UC/min vs no OP: 0.93 ± 0.22 UC/min, $p = 0.006$) (both in LD). During the measurement at ET5-7, the median and mean frequency was significantly higher in patients with OI or OP (median frequency (strain signal): OI: 0.050 Hz \pm 0.005 vs no OI: 0.045 Hz \pm 0.004 , $p = 0.040$; OP: 0.050 Hz \pm 0.004 vs no OP: 0.045 Hz \pm 0.005 , $p = 0.027$; mean frequency (DS): OP: 0.035 ± 0.001 vs no OP: 0.032 Hz \pm 0.003 , $p = 0.032$). (all in TD).

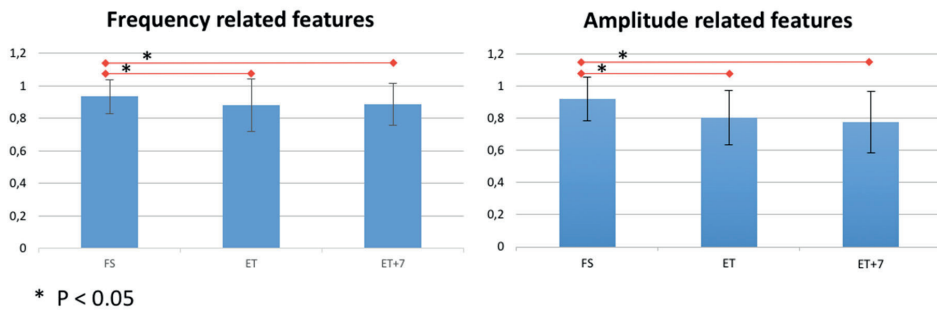


Figure 7.2: Mean and SD of all uterine contraction related features during each phase (follicle stimulation phase (FS), one our before embryo transfer (ET1) and 5-7 days after ET (ET5-7)). All features are normalized to combine the results of both directions and on distance as well strain signals. The frequency results are based on the contractions frequency per minute, mean frequency (Hz) and median frequency (Hz).

7.3.3 Correlation between uterine contraction features and clinical variables

A. Hormone levels

Progesterone levels:

In general, higher or lower progesterone levels were not significantly correlated with the implantation and pregnancy outcome. On the other hand, during the FS, the UFM amplitude feature of the uterine contractions showed a negative correlation with progesterone levels during the same phase ($r = -0.621$, $p = 0.010$) (based on distance signal in TD).

Estradiol levels:

Significant higher levels of estradiol during the FS, as well the ET5-7, were associated with a higher ongoing pregnancy rate (FS: $p = 0.039$; ET5-7: $p = 0.001$). A positive correlation between estradiol levels during the FS and f_c during ET1 was observed ($r = 0.693$, $p = 0.003$) (based on distance signal in LD).

B. Stimulation related features

The stimulation doses as well the stimulation days were not significantly correlated with any of the uterine contraction features.

C. Thickness of endometrium layer

During the FSP, both amplitude features (SD and UFM) showed a positive correlation with the thickness of the endometrium during the measurement ET1 (for UFM: $r = 0.717$, $p = 0.002$; for SD: $r = 0.700$ – $p = 0.003$) (both based on distance signal in TD).

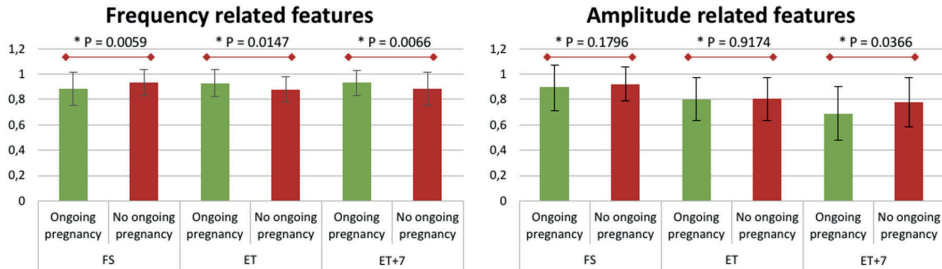


Figure 7.3: Comparison of mean and SD of all uterine contraction related features during each phase (follicle stimulation phase (FS), one our before embryo transfer (ET1) and 5-7 days after ET (ET5-7)) in patients with OP and no OP. All features are normalized respect to their maximum value to combine the results of both directions and on distance as well strain signals. The frequency results are based on the contractions frequency per minute, mean frequency, and median frequency, while the amplitude results are based on standard deviation and unnormalized first moment.

7.3.4 Correlation between phases in IVF patients and phases of the natural menstrual cycle in healthy women

All features which showed significant differences between pregnant women after IVF treatment and non- pregnant women after IVF treatment were selected. These features were compared with the values of the same features in the different phases of the natural menstrual cycle of HW as previously investigated¹³. In particular, if a feature showed significant difference between OP and no OP during ET1, this was compared with the LF and EL phases in a natural cycle. Similarly, the ET5-7 phase was compared with the LL phase, in case significant features between no OP and OP were present.

The comparison of features between ET1 and LF/EL showed a significant difference for f_c between the non-pregnant IVF women in comparison with the HW during the LFP/EL (IVF-no OP group: 0.93 ± 0.22 UC/min vs HW-LF: 1.57 ± 0.27 UC/min / HW-EL: 1.22 ± 0.33 UC/min, $p < 0.001$ / $p = 0.046$), while for the pregnant IVF women, f_c was comparable with that of HW (IVF-OP: 1.45 ± 0.42 UC/min vs HW-LF: $1. \pm 0.27$ 57 UC/min / HW-EL: 1.22 ± 0.33 UC/min, $p = 0.526$ / $p = 0.247$) (based on distance signal in LD).

Comparing significant features (MDF and MF) based on OP outcome of the ET5-7 with the LL of HW, MDF was significantly different between HW and IVF patients (pregnant and non-pregnant) (IVF-no OP: 0.045 ± 0.005 Hz, IVF-OP: 0.050 ± 0.004 Hz vs HW: 0.041 ± 0.004 Hz, $p = 0.049$ / $p = 0.001$). MF showed a significant difference between the IVF pregnant group and HW during the LL (IVF-OP: 0.035 ± 0.001 Hz, HW: 0.029 ± 0.003 Hz, $p = 0.001$), whereas this difference was not significant between the non-pregnant IVF group and the HW (IVF-no OP: 0.032 ± 0.003 Hz, HW: 0.029 ± 0.003 Hz, $p = 0.071$) (based on distance signal in in TD).

7.4 DISCUSSION

It has been reported that uterine contractions may play an important role for the success of conception¹⁷. Assessing objectively and noninvasively uterine contraction characteristics during the IVF cycle seems an essential step to understand the impact of contractions on IVF failure and potentially boost IVF success rates by introducing specific uterine motion modulators.

In this study, we measured and characterized uterine contractions during IVF treatment based on quantitative US imaging. We assessed the relationship between uterine contraction patterns during IVF, characterized by the extracted frequency- and amplitude-related features, and implantation and pregnancy rates. The relationship with clinical features, as well as uterine contractions patterns in HW, was also investigated.

The observed reduction in uterine contraction frequency (measured as UC/min) between FS and ET1 is comparable with previous studies^{3, 18}. Overall the contraction frequencies observed in our study are lower compared to other studies^{3, 18, 19}. As explained by Sammali et al.¹³, f_c in literature is mostly based on visual inspection, providing a global assessment without distinction between the different layers of the uterus. In this study, the subendometrial layer was specifically considered for speckle tracking. Contrary to previous published studies^{9, 19}, we observed a significantly higher number of contractions during ET1 (f_c) in patients with OI or/and OP (ET1: OI: $p = 0.028$, OP: $p = 0.006$). An explanation may be found in the comparison with HW. The f_c of pregnant IVF women during ET1 was comparable to the f_c of HW during LF and EL, whereby uterine contractions play a key physiological role aimed at favoring conception.

On the contrary, non-pregnant IVF women showed significantly lower f_c in the same phases (LF: $p < 0.001$ and EL: $p = 0.046$). Although Zhu et al.⁹ observed a lower uterine f_c in pregnant IVF women in ET1, women with f_c in the range 1.1-2.0 UC/min had the highest clinical pregnancy rate (63.55%); this range is comparable with our results (f_c OP: 1.45 ± 0.42 UC/min (pregnant women)).

In general, the results in figure 7.3 suggest that immediately before embryo transfer (ET1), the combination of higher frequency and lower amplitude in the uterine activity may contribute to successful embryo implantation. It would in fact be reasonable to think that the embryo, once inserted into the uterine cavity, needs help (moderate uterine contractions) for positioning and implantation; on the other hand, these contractions should not be strong (higher amplitude) as they could expel the embryo out of the uterine cavity.

During the ET5-7 measurement, the uterine frequency features were significantly higher in patients with OI or OP, whereas the amplitude features were significantly lower in patients with OI or OP. These findings might be explained by the fact that moderate uterine contractions prevent the embryo for being expelled during this implantation phase. However, since contraction directions were not taken into account in this study, we can only speculate about to the expulsion of the embryo.

On the one hand, the obtained results can find a physiological explanation, as previously described. On the other hand, the negative correlation between frequency and amplitude features may also result by the effect of noise on the frequency estimator. At low contraction amplitudes, approaching the noise floor, the estimated frequency characteristics may be dominated by the noise frequency spectrum, resulting in higher values. In future studies, the frequency spectra of noise and estimated signals (motion and strain signals) should be investigated in order to confirm the hypothesized physiological rationale explaining our measurement results.

Positive correlation between estradiol levels during the FS and f_c during ET1 was observed and it resulted to be in line with previous studies and the suggestion that the increase of f_c is caused by estradiol secretion by the growing dominant follicle^{10, 21-23}. In general, estradiol levels during FS as well during ET5-7 were significantly higher in patients with OP compared to no OP, which also might explain the higher f_c in the pregnant group during the ET5-7. Progesterone levels during FS showed a negative correlation with the amplitude (UFM) of the uterine contractions, which is also in agreement of existing literature²⁴.

Thickness of the endometrial layer (TED) was positively correlated with both amplitude features (SD and UFM) during the measurement ET1. No significant differences between the pregnant and non-pregnant women were observed, but a TED < 5 mm is suggestive for lower implantation changes in agreement with previous published studies²⁵.

In conclusion, in our study women with successful implantation and OP have a higher contraction frequency during ET1 (f_c) and during ET5-7 (MDF, MF). This may find explanation in the similarity of the measured OP values with those measured in HW. Indeed, previous studies suggest the presence of an optimal range of contraction frequencies, which is associated with successful embryo implantation and OP. At lower and higher contraction frequencies, IVF is less likely to succeed. To expand our evidence and knowledge on uterine contractions during IVF, and their relation with successful treatment, research in this field should be extended and evaluate additional relevant features related e.g. to contraction velocity and direction. Their combination and predictive value could also be investigated in a probabilistic framework by machine learning techniques. To this end, more extensive datasets are required.

7.5 AUTHOR'S ROLES

M. S. and B. S. planned and implemented the study. C. B. collected the data and performed all ultrasound recordings. F. S. implemented the signal analysis algorithms. C. B. and F. S. did the statistical analyses. C. B. wrote the first draft of the manuscript. All authors participated to the discussion of the findings and revised the manuscript.

7.6 FUNDING

This study was funded by the Dutch Technology Foundation TTW (Utrecht, The Netherlands), applied science division of NWO (The *Netherlands* Organization for *Scientific* Research), and the Technology Program of the Ministry of Economic Affairs, grant no. 13901.

BIBLIOGRAPHY

1. ESHRE. ART fact Sheet. 2016; Available from: <https://www.eshre.eu/~media/sitecore-files/Guidelines/ART-fact-sheet-2016.pdf?la=en>
2. Blake DA, Farquhar CM, Johnson N, Proctor M. Cleavage stage versus blastocyst stage embryo transfer in assisted conception. *Cochrane database Syst Rev* 2007;(4):CD002118.
3. Fanchin R, Ayoubi JM, Righini C, Olivennes F, Schonauer LM, Frydman R. Uterine contractility decreases at the time of blastocyst transfers. *Hum Reprod* 2001;16(6):1115–9.
4. Fanchin R, Ayoubi JM. Uterine dynamics: impact on the human reproduction process. *Reprod Biomed Online* 2009;18 Suppl 2:57–62.
5. Fanchin R, Righini C, Ayoubi JM, Olivennes F, de Ziegler D, Frydman R. Uterine contractions at the time of embryo transfer: a hindrance to implantation? *Contracept Fertil Sex* 1998;26(7–8):498–505.
6. Lesny P, Killick SR, Tetlow RL, Manton DJ, Robinson J, Maguiness SD. Ultrasound evaluation of the uterine zonal anatomy during in-vitro fertilization and embryo transfer. *Hum Reprod* 1999;14(6):1593–8.
7. Pusey J, Kelly WA, Bradshaw JM, Porter DG. Myometrial activity and the distribution of blastocysts in the uterus of the rat: interference by relaxin. *Biol Reprod* 1980;23(2):394–7.
8. Ijland MM, Hoogland HJ, Dunselman GA, Lo CR, Evers JL. Endometrial wave direction switch and the outcome of in vitro fertilization. *Fertil Steril* 1999;71(3):476–81.
9. Zhu L, Che HS, Xiao L, Li YP. Uterine peristalsis before embryo transfer affects the chance of clinical pregnancy in fresh and frozen-thawed embryo transfer cycles. *Hum Reprod* 2014;29(6):1238–43.
10. Kuijsters NPM, Methorst WG, Kortenhorst MSQ, Rabotti C, Mischi M, Schoot BC. Uterine peristalsis and fertility: current knowledge and future perspectives: a review and meta-analysis. *Reprod Biomed Online* 2017;35(1):50–71.
11. Bulletti C, de Ziegler D, Polli V, Diotallevi L, Del Ferro E, Flamigni C. Uterine contractility during the menstrual cycle. *Hum Reprod* 2000;15 Suppl 1:81–9.
12. Finberg HJ. Whither (wither?) the ultrasound specialist? *J. Ultrasound Med.* 2004;23(12):1543–7.
13. Sammali F, Kuijsters NPM, Huang Y, Blank C, Rabotti C, Schoot BC, et al. Dedicated ultrasound speckle tracking for quantitative analysis of uterine motion outside pregnancy. *IEEE Trans Ultrason Ferroelectr Freq Control* 2018;PP(c):1.
14. La Marca A, Sunkara SK. Individualization of controlled ovarian stimulation in IVF using ovarian reserve markers: from theory to practice. *Hum Reprod Update* 2014;20(1):124–40.
15. Alpha, ESHRE. The Istanbul consensus workshop on embryo assessment: proceedings of an expert meeting. *Hum Reprod* 2011;26(6):1270–83.
16. Ijland MM, Evers JLH. Subendometrial contractions in the nonpregnant uterus: an ultrasound study. *Eur J Obstet Gynecol Reprod Biol* 1996;70(1):23–4.
17. Bulletti C, de Ziegler D. Uterine contractility and embryo implantation. *Curr Opin Obstet Gynecol* 2006;18(4):473–84.
18. Ayoubi JM, Epiney M, Brioschi PA, Fanchin R, Chardonnens D, De Ziegler D. Comparison of changes in uterine contraction frequency after ovulation in the menstrual cycle and in in vitro fertilization cycles. *Fertil Steril* 2003;79(5):1101–5.
19. Fanchin R, Righini C, Olivennes F, Taylor S, de Ziegler D, Frydman R. Uterine contractions at the time of embryo transfer alter pregnancy rates after in-vitro fertilization. *Hum Reprod* 1998;13(7):1968–74.
20. Sammali F, Kuijsters NPM, Huang Y, Blank C, Rabotti C, Schoot BC, et al. Dedicated ultrasound speckle tracking for quantitative analysis of uterine motion outside pregnancy. *IEEE Trans Ultrason Ferroelectr Freq Control* 2018;PP(c):1.
21. Bulletti C, De ZD, Polli V, Diotallevi L, Del FE, Flamigni C, et al. Uterine contractility during the

- menstrual cycle. *Hum Reprod* 2000;15(SUPPL. 1):81–9.
22. IJland MM, Volovics L, Evers JLH, Hoogland HJ, Dunselman GAJ, Volovics L, et al. Relation between endometrial wavelike activity and fecundability in spontaneous cycles. *FertilSteril* 1997;67(3):492–6.
 23. Kunz G, Noe M, Herbertz M, Leyendecker G. Uterine peristalsis during the follicular phase of the menstrual cycle: effects of oestrogen, antiestrogen and oxytocin. 1998.
 24. Fanchin R, M Ayoubi J, Olivennes F, Righini C, de Ziegler D, Frydman R. Hormonal influence on the uterine contractility during ovarian stimulation. 2000.
 25. De Ziegler D, Fanchin R, De Moustier B, Bulletti C. The hormonal control of endometrial receptivity: Estrogen (E2) and progesterone. *J Reprod Immunol* 1998;39(1–2):149–66.

8

MULTI-MODAL UTERINE-ACTIVITY MEASUREMENTS FOR PREDICTION OF EMBRYO IMPLANTATION BY MACHINE LEARNING

Abstract: *In-vitro fertilization (IVF) is the most advanced treatment for infertility problems; however, its failure rate is still above 70% and the exact causes are often unknown. There is increasing evidence of involvement of uterine contractions in IVF failure especially during and after embryo transfer. In this paper, we propose a method to predict the success of embryo implantation based on features extracted from electrohysterography (EHG) and B-mode transvaginal ultrasound (TVUS) recordings. Sixteen women undergoing IVF treatment were measured during follicular stimulation (FS) phase, one hour before embryo transfer (ET1), and five to seven days after ET (ET5-7). After correlation filtering, multiple features were selected by forward feature selection and optimally combined by different machine learning methods, including support vector machine (SVM), K-nearest neighbors (KNN), and Gaussian mixture model (GMM). Hyper-parameter optimization and validation of each model were performed in a nested cross validation loop. Using Leave-one-out approach on our database, the highest overall accuracy (93.8%) was achieved by SVM and KNN in both FS and ET1 phase. Contraction frequency, standard deviation and unnormalized first statistical moment, obtained from EHG and TVUS analysis, were optimum features common to the SVM and KNN classifiers. These features may contribute to produce the best prediction for successful embryo implantation improving the IVF procedure. Yet, a larger dataset is required for improved training of the considered classifiers.*

From: **F. Sammali**, C. Blank, T. G. F. Bakkes, Y. Huang, C. Rabotti, B.C. Schoot, M. Mischi, **“Multi-modal uterine-activity measurements for prediction of embryo implantation by machine learning”**. Submitted to *IEEE Journal of Biomedical and Health Informatics*, 2019.

8.1 INTRODUCTION

In developed countries, infertility represents a serious problem for 20% of couples¹. Due to the trend to postpone childbirth, the rate of these couples is rapidly increasing. Against this problem, advanced in-vitro fertilization (IVF) technologies are developing. It is estimated that in Europe IVF represents the only reproduction option for over 2.5 million couples². In spite of major efforts to improve IVF, its success rate remains below 30%³. As a result, many couples undergo repeated IVF treatments with the hope of a successful fertilization.

There is increasing evidence of major involvement of uterine contraction in IVF failure⁴⁻⁷ especially during and after embryo transfer (ET), when the embryo may need some quiescence to implant in the uterine cavity.

Uterine contractions are believed to represent an important determinant of uterine receptivity, both in IVF and natural menstrual cycle. It is established that uterine receptivity is a key factor during the so-called implantation window, a short period in which the embryo approaches the endometrium in order to implant⁸. This embryo-maternal dialogue is crucial for the establishment of a healthy pregnancy. The uterine receptivity is therefore of major importance to the success of IVF. Specific and precise pharmacological intervention on uterine contractions is feasible and can potentially improve embryo implantation success after ET⁹⁻¹¹. Unfortunately, the role of uterine contractions in IVF failure is not yet understood and the value of pharmacological treatments acting on contractions within IVF treatment remains to be established.

Understanding the role of uterine contractions in influencing uterine receptivity, especially in relation to embryo implantation success, has always been complicated. The lack of quantitative measurement tools has represented a major obstacle for a complete characterization of the uterine activity outside pregnancy. The latter represents an essential step towards improved embryo implantation both in IVF and natural menstrual cycle. Especially in IVF, a better understanding of the role of uterine contractions may lead to the definition of new strategies for tailoring specific IVF protocols and pharmacological treatments. It is therefore evident that objective reproducible quantitative assessment of uterine contractions is essential.

In previous studies, we have proposed new methods to quantitatively and non-invasively measure the electrical and mechanical activity in human non-pregnant uteri by electrohysterography (EHG)¹² and transvaginal ultrasound (TVUS) motion analysis¹³. EHG is a monitoring technique which measures the electrical activity that triggers and drives the mechanical contraction of the uterine muscle^{12, 14}; TVUS speckle tracking assesses the mechanical behavior of these contractions by tracking locally a specific area of the uterine muscle¹³.

A set of amplitude-, frequency-, and energy-related features provided a good understanding of the uterine activity in natural menstrual cycle and showed the ability to discriminate the active and quiescent state of the uterus.

On the one hand, the obtained results were promising and confirmed the physiological role of uterine activity to enhance the reproductive process, e.g., active uterine state in the follicular phase and quiescent uterine state in the luteal phase of the menstrual cycle.

On the other hand, these studies demonstrated the feasibility of the proposed methods outside pregnancy and motivated us towards the assessment of their clinical value in the context of IVF, especially in relation to ET for improving embryo implantation prediction.

Machine-learning approaches are increasingly applied to automatically find patterns within data, which enables doctors and healthcare professionals to improve clinical decision making¹⁵. Supervised machine learning algorithms are most commonly used to develop models based on labelled data.

In this study, we aim at investigating the use of probabilistic classification of the uterine activity by machine learning to improve the success rate of IVF, especially in relation to ET. In particular, we aim at providing those features or their combination (amplitude-, frequency-, and energy-related features) that are necessary to classify uterine contraction characteristics as either favorable or adverse to embryo implantation during ET. In case of unfavorable uterine activity, classification would permit proper decision making. In fact, ET could either be delayed to later cycles or uterine contraction characteristics could be modulated by specific treatment for favoring embryo implantation^{11, 16}.

To achieve this goal, enabled by the implemented EHG and TVUS speckle tracking methods, the uterine activity is measured and characterized during stimulated cycles by extracting the same frequency-, amplitude-, and energy- related features as in natural menstrual cycle. The electromechanical uterine activity is first simultaneously recorded by EHG and B-mode TVUS in patients undergoing IVF treatment. In particular, the patients are measured during three phases, i.e, follicular stimulation (FS), one hour before ET (ET1), and five to seven days after ET (ET5-7).

Based on IVF outcome, patients are divided in successful and unsuccessful pregnancy groups where successful pregnancy is defined as a positive fetal heart rate at the moment of a gestational age of at least 11 weeks, known as “vital pregnancy”.

The EHG and TVUS motion and strain features are then extracted from the recorded signals following the same protocol as in Sammali et al.^{12, 13}.

Prior to machine learning, an additional method for EHG and TVUS feature extraction is here proposed that is based on singular value decomposition (SVD) of the acquired EHG and TVUS measurements. The same EHG and TVUS features were extracted directly from the temporal variation signal obtained after dedicated SVD filtering. This SVD approach provides a global estimate of the uterine activity that is different from standard EHG and TVUS analysis.

First, correlation filtering is performed on the all features extracted by the proposed methods in order to reduce redundancy in the data. The resulted feature pool is hence composed by relevant features able to possibly classify uterine activity characteristics as either favorable or adverse to embryo implantation during ET. A forward feature selection procedure is then

carried out on the feature pool to search the optimum feature set that performs best in differentiating successful and unsuccessful pregnancy.

This is performed separately for the three different measurements, in order to appreciate variations in the predictability.

The classifiers used in this study are the support vector machine (SVM), K-nearest neighbors (KNN) and Gaussian mixture model (GMM). Hyper-parameter optimization is performed in a nested cross validation, in the interest of reducing over-fitting by leave-one-out cross-validation.

8.2 METHOD

8.2.1 Patients and IVF protocol

We prospectively studied 29 consecutive ovarian stimulation cycles for IVF- ET undertaken in 29 infertile women. Women with uterine anomalies or pathologies, caesarean section experience, mental disability and/or significant language barrier were not enrolled in this study. Clinical indications for IVF- ET were male subfertility (50%), tubal pathology (12.5%), unexplained subfertility (18.8%) or hormonal disorders (18.8%). Prior to IVF treatment, all patients signed an informed consent and this study received approval by the relevant medical ethical committee. The enrolled patients controlled ovarian hyperstimulation using a recombinant follicle stimulating hormone (Bemfola[®]; Finox biotech AG, Balzers, Liechtenstein) or human menopausal gonadotropin (Menopur[®]; Ferring, Hoofddorp, The Netherlands) after pituitary down-regulation with a gonadotropin-releasing hormone agonist (GnRH-a) (Decapeptyl[®]; Ferring, Hoofddorp, The Netherlands) or gonadotropins (Cetrotide[®], Merck Serono, Geneva, Switzerland).

Oocytes were retrieved 34-36 hours after the hormone injection and inseminated with spermatozoa in order to obtain embryos. Five days after oocyte retrieval, the best quality embryos based on the Alpha score system¹⁷ were selected and transferred. Prior to ET, patients were treated with intravaginal progesterone tablet (Utrogestan Besins Healthcare, Brussels, Belgium) to support the luteal phase of the uterus which is thought to facilitate embryo implantation.

After excluding 13 patients due to cancellation of fresh single-embryo transfer or patient withdrawing, a total of 16 patients underwent ET and were thus analyzed in this study. Further, TVUS examination of the patients was performed in order to monitor the success of earlier ET. Seven patients presented successful pregnancy defined as positive fetal heart rate at gestational age of at least 11 weeks.

8.2.2 Multi-modal data acquisition

All measurements were performed at the Reproductive Medicine department of Ghent University Hospital, (Belgium).

During standard recording sessions, 4-min TVUS scans and EHG recordings were simultaneously performed three times during three specific phases of the IVF treatment: during follicle

stimulation (FS) where at least one follicle was larger than 16 mm, one hour before ET (ET1) and five to seven days after ET (ET5-7). An US scanner WS80A (Samsung Medison, Seoul, South Korea) equipped with a transvaginal V5-9 probe was employed for the TVUS scans acquired at a 5.6 MHz central frequency and 30 frames/s (sampling frequency f_s (US), amply sufficient to meet Nyquist condition given the limited bandwidth of uterine motion ($f < 0.066$ Hz)¹⁸.

After skin preparation for contact impedance reduction, EHG was recorded by placing on the abdomen, immediately above the pubic zone, a flexible electrode grid. The latter was correctly placed by guidance of TVUS in order to maximize alignment with the uterus. A Refa multichannel amplifier (TMSI International, Enschede, the Netherlands) for electrophysiological signal acquisitions was employed for recording and digitizing the EHG at a sampling frequency of 1024 Hz (f_s (EHG)).

8.2.3 Multi-modal feature extraction

A set of amplitude-, frequency-, and energy-related features were extracted from the recorded signals by the adopted methods. In the following section, we describe the feature extraction by performing the EHG signal analysis described in Sammali at al.¹², TVUS speckle tracking analysis described in Sammali at al.¹³ and a novel SVD approach that is here proposed.

The adopted multi-modal feature extraction approach is schematically described in Figure 8.1.

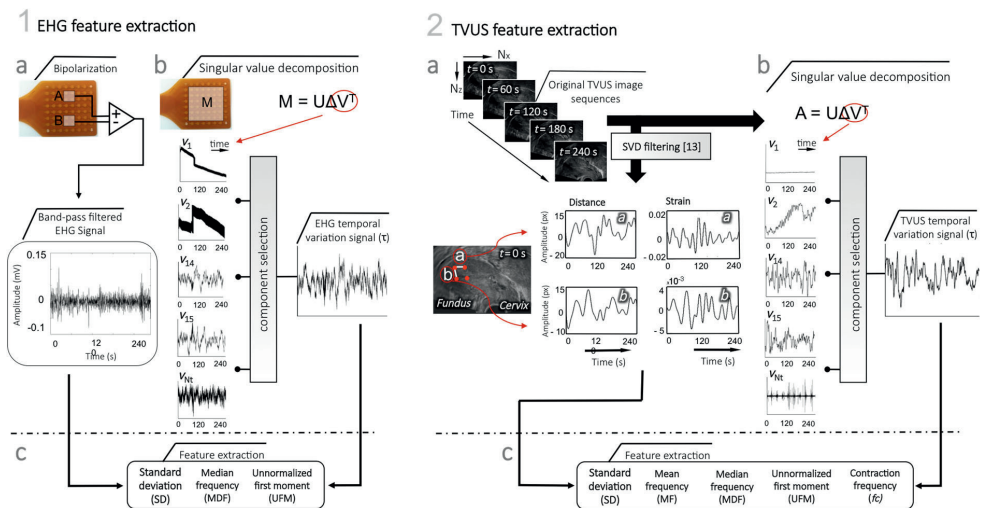


Figure 8.1 (1-a) Feature extraction by EHG: (a) the EHG filtered signal is obtained after bipolarization; (1-b) The EHG temporal variation signal (τ) is obtained as a weighted sum operation after decomposing the EHG matrix by singular value decomposition (SVD). After retrieving k sources by a dedicated SVD filtering, the singular vectors \vec{v}_k carrying the temporal information are multiplied by their weight factors (retrieved singular values) λ_k , and the results are added together to obtain the output EHG temporal variation signal. (1-c) Amplitude-, frequency-, and energy-related features extracted from both filtered and temporal variation EHG signal. (2-a) Feature extraction by TVUS speckle tracking: the unfiltered TVUS video is SVD spectrally filtered for the estimation of motion tracking (distance and strain signals) along the (a) longitudinal

and (b) transversal direction. (2-b) The TVUS temporal variation signal (τ) is obtained as a weighted sum operation after retrieving k sources through a dedicated SVD filtering. The singular vectors \vec{r}_i carrying the temporal information are multiplied by their weight factors (retrieved singular values) λ_k , and the results are added together to obtain the output TVUS temporal variation signal. (1-c) Amplitude-, frequency-, and energy-related features extracted from distance and strain signals along the longitudinal (a) and transversal (b) direction, as well as from the TVUS temporal variation signal. For both EHG and TVUS motion analysis, dedicated SVD filtering is performed according to Sammali et. al.¹³.

8.2.3.1 Feature extraction by EHG

For each recording session, three features were extracted from the single-channel EHG signal. As in previous study¹², we focused on single-channel analysis to qualitatively evaluate contraction timing and strength in stimulated cycles; therefore, high-spatial resolution was not required.

Details on EHG signal analysis are described in Sammali et al.¹². Briefly, the EHG signal quality was improved by averaging neighboring electrodes (sensing surfaces A and B indicated in Figure 8.1 (1-a)) and simulating a larger sensing surface^{19, 20}. The choice of surfaces A and B was supported by the fact that larger interelectrode distances are more suited than a high-density grid for investigation of electrophysiological signals of the non-pregnant uterus originated deeper in the body and far from the electrode^{19, 20}. Furthermore, a better signal-to-noise ratio is provided by vertical derivations that are aligned to the middle line of the muscle and expected to be closer to uterus. A single bipolar signal was derived by subtracting the two surface areas A and B, improving the signal quality by reduction of common-mode noise^{21, 22}.

The bipolar EHG signal was then preprocessed by a 4th order, band-pass Butterworth filter with lower and upper cut-off frequencies equal to 0.3 and 5 Hz, respectively. In the uterus, only frequencies below 5 Hz are expected¹⁴, but the frequencies below 0.3 Hz can be affected by motion artifacts due to e.g. respiration^{23, 24}.

Standard deviation (SD), median frequency (MDF), and unnormalized first statistical moment (UFM) were the features extracted from the filtered EHG signal.

8.2.3.2 Feature extraction by TVUS speckle tracking

For each recording session, five features were extracted from the distance and strain signals derived along the longitudinal and transversal direction in stimulated cycles.

Details on TVUS distance and strain signal analysis are described in Sammali et al.¹³; here we briefly report the procedure of motion analysis and feature extraction delving into the novel SVD spatiotemporal filtering which will be discussed in the next section.

Motion tracking was implemented by a dedicated speckle tracking algorithm. First, dedicated SVD filtering was introduced to enhance uterine motion suppressing uncorrelated signals that affect speckle tracking performance. The TVUS image sequences, represented as 3D matrices of dimensions $N_x \times N_z \times N_t$, were reshaped into a new spatiotemporal representation (Casorati matrix) which was decomposed by SVD in a new spatial singular vector basis U and a new temporal singular vector basis V as:

$$A = U\Delta V^T. \quad (8.1)$$

Here, A represents the Casorati matrix with dimensions $N_x N_z \times N_t$, U is a $N_x N_z \times N_x N_z$ squared matrix (i.e., orthogonal for real-value inputs), V is a $N_t \times N_t$ squared matrix, and Δ is a $N_x N_z \times N_t$ diagonal matrix containing non-negative real numbers known as singular values λ on the diagonal. These values are conventionally in descending order. N_t and $N_x N_z$ are the number of video frames and image pixels, respectively. The columns of V are the right-singular vectors of A carrying the temporal information corresponding to spatial information in the columns of U which are the left-singular vectors of A .

For each temporal signal $V_i(t)$, where i indicates the number of the singular values, two energies were obtained by integration of the power spectrum over the entire frequency band [$f_0 = 0$ Hz – $f_{s(\text{US})/2} = 15$ Hz] and over the interval [$f_1 = 0.0083$ Hz – $f_2 = 0.083$ Hz], which was chosen to reflect the uterine bandwidth in the IVF cycles according to⁵.

The adopted energy metrics was then defined as

$$ER_i = \frac{\sum_{f=f_1}^{f_s} |X_i(f)|^2}{\sum_{f=0}^{f_s/2} |X_i(f)|^2}, \quad (8.2)$$

where, f_s is the TVUS frame rate ($f_{s(\text{TVUS})}$), $X_i(f)$ represents the Fast-Fourier Transform (FFT) of each $V_i(t)$. As a result, the ER_i represents the amount of uterine dynamics for each singular value i compared to the full signal. Only a range of subsequent singular values representing over 50% of the total energy was selected to enhance the uterine motion in the TVUS video while suppressing undesired components. Accordingly, we have separated $\tilde{i} = \min(N_x N_z, N_t)$ sources that can be retrieved through

$$A_i = \lambda_i U_i V_i^T(t). \quad (8.3)$$

After SVD filtering, the speckle was regularized by Wiener deconvolution filtering and speckle tracking was implemented for tracking over time four defined blocks manually selected on the subendometrial layer (junctional zone), known to be the most contractile part of the uterus²⁵. The match between corresponding blocks in consecutive frames was determined by the minimum of the sum of absolute differences (SAD). The block size for SAD was adaptively determined as twice the speckle size calculated after SVD filtering for each patient and phase. The block matching was then accelerated by a diamond search (DS) strategy, maintaining similar tracking accuracy as the typical full-grid search (FGS) method with the benefit of a reduced computational time. Median filtering on the displacement of neighboring blocks (matching coordinates) was also introduced to improve the tracking robustness and accuracy of the method. The defined four blocks were coupled in pairs in order to estimate distance and strain signals along the longitudinal and transversal direction (Figure 8.1 (2-a)). The longitudinal direction was defined to be in line with back and forward motion between the cervix and fundus, while the transversal direction was the motion perpendicular to that.

The distance, d , and strain, ϵ , were calculated between each pair. In particular, d was defined as the Euclidean distance between each pair of sites in a 2-D space, resulting in an absolute

motion estimate. The strain, ϵ , was defined as the relative variation of d between the tracked sites.

Standard deviation (SD), mean frequency (MF), median frequency (MDF), contraction frequency (f_c), and unnormalized first moment (UFM) were the features extracted from the distance and strain signals along the two directions. All features, with the exception of (f_c), were extracted from the FFT of the recorded signals; in particular, the SD was calculated by applying Parseval's theorem. Moreover, the features were extracted in the frequency band [$f_1 = 0.0083$ Hz – $f_2 = 0.083$ Hz] to improve their quality and strengthen their link with the uterine motion in a stimulated cycle⁵. The same frequency band was used for the ER metrics calculation. A zero-crossing detector was employed in the time domain for the estimation of f_c in terms of number of contractions per minute.

8.2.3.3 Feature extraction by SVD

Both for EHG and TVUS analysis, features were extracted from the temporal variation matrix V after SVD. The latter was performed on the 6×6 matrix (36 channels in total) of the EHG electrode grid as well as on the TVUS image sequences reshaped into a new spatiotemporal representation (Casorati matrix). The external square of the EHG electrode grid containing 28 external channels are excluded due to the risk of poor contact between skin and sensor, which may occur at the edges. The input matrices were then decomposed into a new spatial singular vector basis U and a new temporal singular vector basis V according to (8.4).

For EHG (Figure 8.1 (1-b)), high-frequency noise and dynamics were described in the first singular values and vectors and the uterine activity appeared to be described by those close to the last singular values and vectors. On the contrary, for TVUS (Figure 8.1 (2-b)), stationary tissue and clutter were described by the first singular values and vectors while high-frequency noise was described by the last singular values and vectors. Slow uterine motion was expected to be described by the singular values and vectors close to the first ones.

By selecting a proper range of singular values according to the ER metric in (8.2), we separated $k = \min(N_x N_z, N_t)$ sources and the temporal variation signal, τ , was retrieved through a weighted sum operation as

$$\tau = \frac{1}{k} \sum_{k=1}^{k-1} \lambda_k V_k^T. \quad (8.4)$$

In this operation, the singular vectors \vec{v}_k carrying the temporal information, were multiplied by their weight factors (retrieved singular values) λ_k , and the results, represented by N weighted temporal vector, were added together to obtain the output temporal variation signal τ for both EHG and TVUS recordings.

The EHG and TVUS temporal variation signals representing the electrical and mechanical uterine activity are shown in Figure 8.1 (1-b) and Figure 8.1 (2-b), respectively.

For EHG analysis, the ER metric was obtained by integration of the power spectrum over the entire frequency band [$f_0 = 0$ Hz – $f_s(\text{EHG})/2 = 512$ Hz] and over the interval [$f_1 = 0.3$ – $f_2 = 5$ Hz] which was here chosen to reflect the EHG signal according to¹⁴.

All EHG and TVUS features were extracted from the FFT of the temporal variation signal following the same procedure described in Sections 8.2.2.1 and 8.2.2.2.

In particular, EHG features were extracted in the frequency interval [$f_3 = 0 \text{ Hz} - f_4 = 5 \text{ Hz}$] based on the frequency content observed on the FFT of the time averaged signal; in fact, most of the information appeared to be characterized by very low-frequency content.

In this way, a global assessment of the electromechanical uterine activity in time was obtained by reconstructing time signals that reflected the expected uterine activity in the IVF cycle.

8.2.4 Machine learning framework

Three machine-learning models were implemented to classify successful and unsuccessful embryo implantation using both EHG and TVUS features.

For each machine-learning model, feature selection was carried out to identify the optimum feature set using forward feature selection with a leave-one-out approach. The proposed classifiers were tested and trained in a nested cross validation (CV) loop, in the interest of reducing over-fitting.

In particular, as shown in Figure 8.2, our adopted strategy consisted of first performing forward-feature selection, then tuning the hyper-parameters of the classifiers in an inner CV loop and, finally, validating the output model on new data in an outer CV loop.

8.2.4.1 Feature selection

Feature selection is an important step in machine learning and it has several advantages such as, enabling the machine learning algorithm to train faster, reducing the complexity of the model and making it easier to interpret, improving the model accuracy if the right subset of features is chosen, and reducing over-fitting.

Several methodologies and techniques can be employed to define a subset of the feature space and help the model performing better and efficiently. In this study, correlation filtering was first performed to reduce redundancy in the data by measuring the relevance of the features based on their correlation with the class labels²⁶.

All features were ranked based on the obtained Pearson's correlation coefficient and the top 10 features were selected and used as the best subset of features.

When the feature vector has multiple dimensions, less significant features might contribute as well to increase the performance of the classifier when combined with other features. A wrapper method based on forward feature selection²⁷ was employed to search the optimum feature set that performs best in classifying successful and unsuccessful pregnancies.

Briefly, the whole machine learning process started by loading one feature at the time. The feature giving the best performance was chosen first; additional features were, then, added incrementally. At each step, the combination of features that gave the largest improvement was chosen.

The forward feature selection process stopped when the addition of a new feature did not improve the performance of the model.

The scale of the features in the dataset varied greatly; discriminative machine learning techniques depend on the distance of observations, and this can produce a bias²⁸; therefore, prior to feature selection, the data were normalized to zero mean and unit variance.

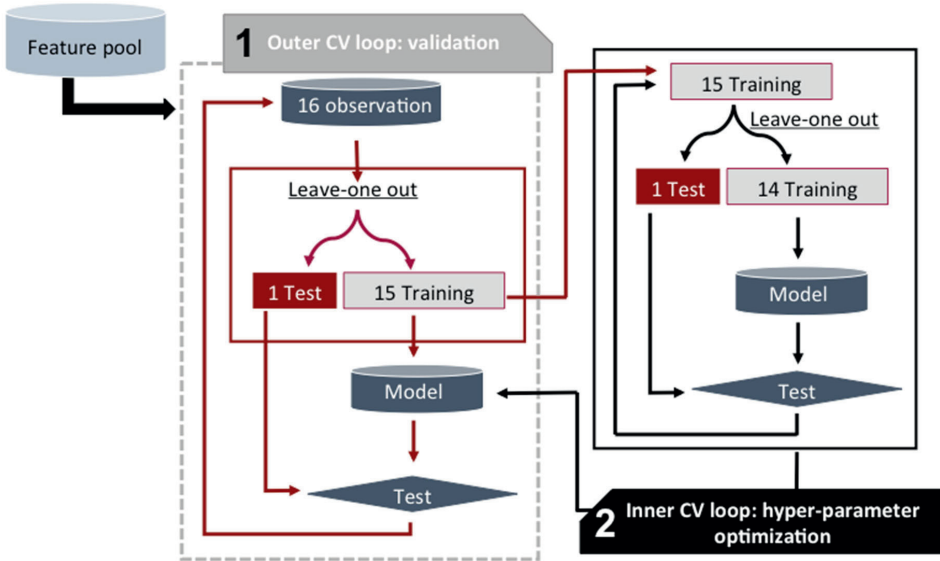


Figure 8.2: Overview of the machine-learning framework with nested cross validation. The entire nested cross validation loop starts after selecting a feature pool by correlation filtering. (1) The outer loop is used to validate the model selected by the inner CV loop (2). The original dataset (16 observations) is divided in training set (15 observations) and test set (1 observation) by performing the leave-one-out method. (2) The inner CV loop is used for tuning the hyper-parameters of the classifier. Here, the training set (15 observations), generated by the outer loop, is further divided in training set (14 observations) and test set (1 observation) in a Leave-one-out fashion.

8.2.4.2 Nested cross validation

Generally, model selection with CV uses the same data to optimize the model parameters and evaluate the model performance. The resulting information may thus ‘leak’ into the model overfitting the data. The entity of this effect is mainly dependent on the size of the dataset and stability of the model²⁹.

To avoid this problem, we employed nested CV, often used to train models in which hyper-parameters also need optimization that adequately uses a series of train/validation/test set splits.

The nested CV consisted of an inner CV loop nested in an outer CV loop. After performing correlation filtering to obtain a feature pool aiming at helping the model to make better prediction, first an inner CV loop Figure 8.2-2 was used to tune the hyper-parameters of the

classifier. Second, an outer CV loop (Figure 8.2-1) was used to validate the model selected by the inner CV loop on new data.

The adopted approach consisted of splitting the set of n observation (16 patients) into a training and test set by using leave-one-out approach. In this way, the training set contained all but one observation while the test set contained only that one observation (Figure 8.2-1). For each training set, the inner CV loop was used for tuning the hyper-parameters of the model containing the first feature that was loaded. Here, the training set was split again into a training set (14 observations) and test set (1 observation) by leave-one-out. The model was trained with each hyper-parameter on the training set and evaluated on the test set, keeping track of the performance metrics. This process was repeated as many times as the length of the training set (15 observations) for each hyper-parameter. The hyper-parameters that showed the highest performance on the test set were then chosen to be the optimal ones.

The outer CV loop (Figure 8.2-1) was then used to validate the model with the loaded feature and the best hyper-parameters selected in the training set (inner loop). The whole process was repeated 16 times such that each observation is used in the test set one time. Finally, the score for the 16 observations was saved and the highest score was chosen. Once all 16 observations are tested, performance metrics are used for assessing the prediction performance of the full machine-learning models and the feature selection.

Then, additional features were added incrementally and the nested CV loop was again performed. Repeating the strategy described above, the combination of features that gave the most improvement was chosen.

Based on the test set in the outer CV loop, a confusion matrix was obtained that describes the complete performance of the machine learning models³⁰. From this confusion matrix, accuracy, sensitivity, and specificity were derived for evaluating the performance of different feature combinations together with best hyper-parameters for the three adopted classifiers.

The method used for optimizing the hyper-parameters was based on a full search where all possible combinations of values are tested together with the loaded features. For each feature and/or combination of features loaded into the model, hyper-parameter optimization was performed. Accuracy was also here adopted as performance metrics for choosing the best hyper-parameters in the inner CV loop.

8.2.4.3 Classifier

Three machine-learning models were employed to classify successful and unsuccessful pregnancy groups using the extracted EHG and TVUS features. The machine learning models are briefly introduced as follows.

- a) **Support vector machine:** A Support Vector Machine (SVM) is a discriminative classifier formally defined by a separating hyperplane. SVM maps the input vector into a feature space of higher dimensionality and identifies the hyper-plane that separates the observations into two classes³¹. The marginal distance between the decision hyper-

plane and the instances that are closest to the boundary between the two classes was maximized.

In a real-life scenario, the data are not always linearly separable; therefore, a kernel trick can be applied for mapping the data to a higher dimension in order to achieve more effective data separation²⁸. In this study, the radial based function (rbf) was chosen as a kernel trick.

The optimization of the parameter setting was carried out in the inner CV loop for each feature combination. The optimization was achieved by a full grid search using exponentially growing sequences which have been shown to give the best results for optimizing SVM hyper-parameters³².

The ranges adopted in this study for hyper-parameter optimization by grid search are $\{10^{-6}, 10^{-5}, \dots, 10^5, 10^6\}$ for the cost and $\{2^{-6}, 2^{-5}, \dots, 2^5, 2^6\}$ for the kernel scale.

The optimum hyper-parameter was then chosen based on the best performance score given by the accuracy metrics.

- b) **K-nearest neighbors:** K-nearest neighbors (KNN) is a simple classifier that can be used to classify multiple classes. KNN assumes similarity of observations in close proximity. In other words, an observation is classified by a majority vote of its neighbors, with the observation being assigned to the class most common among its K nearest neighbors measured by a similarity measure which was here chosen to be the Euclidean distance. The range adopted in this study for optimizing K was $\{1, 3, 5, 7, 9\}$. K was chosen to be odd number preventing the occurrence of a tie; moreover, it was limited to nine because higher K values did not increase the classifier performance. The best K was selected based on the accuracy metric.
- c) **Gaussian mixture model:** A Gaussian mixture model is a probabilistic model that assumes all the observations to be generated from a mixture of a finite number of Gaussian distributions with unknown parameters. The Gaussian distributions were estimated using an iterative Expectation-Maximization algorithm which is based on computing the probability that an observation belongs to a distribution for all observations. From these posterior probabilities, mean and variance were computed by maximum-likelihood. The classes were separately modeled using a mixture of Gaussian distributions which were set to either one or two per class and subject to optimization. The class with the highest probability was selected by the classifier.

8.2.5 Statistical analysis

Statistical analysis was performed to identify significant differences between the successful and unsuccessful pregnancy groups based on the extracted features by EHG and TVUS methods. Shapiro-Wilk test³³ was employed to assess data Gaussianity. Two-tailed Student's test was performed for comparing the two groups for each adopted feature in case of Gaussian distribution ($p > 0.05$), while Wilcoxon-signed rank test³⁴ was performed to establish the significance level (p value) of the median differences for each adopted features in case of data not Gaussian distributed ($p < 0.05$). For all the analyses, the confidence level α was set at 0.05.

8.3 RESULTS

8.3.1 Statistical analysis of EHG and TVUS feature pool

The feature pool obtained after correlation filtering are reported in Table 8.1 per each measurement phase together with their values and the statistical results.

In particular, all EHG features were not Gaussian distributed ($p < 0.05$) according to the Shapiro-Wilk test. Therefore, successful and unsuccessful pregnancy groups were compared for each adopted EHG feature by Wilcoxon-signed rank test to establish the significance level (p value) of the median differences. All the adopted EHG features did not significantly differ and their p values are reported together with their median and interquartile range (IQR) values.

According to the Shapiro-Wilk test, all TVUS features were instead Gaussian distributed ($p > 0.05$). Therefore, two-tailed Student's t-test was performed for comparing successful and unsuccessful pregnancy groups for each adopted TVUS features. The significance of feature differences able to separate successful and unsuccessful pregnancy groups for features extracted by speckle tracking and SVD methods, respectively, are reported in Table 8.1 together with their mean and standard deviation (SD) values.

8.3.1 Classification results

Table 8.2, Table 8.3, and Table 8.4 report the performance of different feature combinations in terms of accuracy, sensitivity, and specificity using the three adopted classifiers. The performance is reported per each measurement phase. The best performance of each machine learning method using its own optimum feature set is highlighted in each table in light red color.

8.4 DISCUSSION

In this study, we assessed the clinical value of our proposed methods for uterine activity analysis in the context of IVF procedure and we explored classification pregnancy success initiated by IVF using frequency-, amplitude-, and energy-related features extracted from EHG and TVUS motion signals. A crucial task for pregnancy prediction is identifying effective feature combinations able to distinguish successful and unsuccessful pregnancy groups. To this end, multiple features were combined to serve as input for the proposed machine-learning models, and forward-feature selection was employed to find the optimum feature set. Three classifiers were employed and compared on the same database. Hyper-parameter optimization was performed in a nested-cross validation loop.

When an individual feature was used, f_c (DL) (contraction frequency extracted from the distance along the longitudinal direction by TVUS speckle tracking) provided the best accuracy performance on SVM (81.3%), KNN (87.5%), and GMM (81.3%) during ET1 phase, e.g., one hour before embryo transfer. Moreover, this feature showed already significant separation ($p < 0.05$) between successful and unsuccessful pregnancy outside a machine-learning framework, as also shown in Table 8.1.

According to Tables 8.2 and 8.3, individual frequency features such as MF (DT) and MDF (DT) also provided a good performance on SVM (87.5%) in the FS phase, and on KNN (81.35%) in the

ET5-7 phase, respectively. These results indicate that frequency-related features can distinguish between successful and unsuccessful pregnancies in a machine-learning framework. However, these two features did not significantly separate the two group outside the machine-learning framework (Table 8.1). Further in the selection procedure, different features were added into each optimum feature set leading to an improved classification performance.

Besides the best individual features f_c (DL), MF (DT), and MDF (DT), there are common features selected by the three machine-learning models in the three measurement phases. In particular,

Table 8.1: Feature pool selected after correlation filtering per each measurement phase. The values are given in terms of mean \pm SD of the successful (SP) and unsuccessful pregnancy (FP) group together with the p values obtained from two-tailed Student's t-test for Gaussian distributed data. In case of non Gaussian distributed data, the values are reported in terms of median and interquartile range (IQR) together with the p values obtained from Wilcoxon-signed rank test.

MEASUREMENT PHASE: FS (Follicle stimulation)				
Feature	Method	SP	FP	p value
F _{1 FS} : MDF (DT) [Hz]	TVUS speckle tracking	0,030 \pm 0,003	0,034 \pm 0,003	0,041*
F _{2 FS} : f_c (DL) [UC/min]	TVUS speckle tracking	1,154 \pm 0,252	1,500 \pm 0,003	0,103
F _{3 FS} : MF [Hz]	TVUS - SVD	1,043 \pm 0,003	0,040 \pm 0,003	0,021*
F _{4 FS} : MDF [Hz]	TVUS - SVD	0,046 \pm 0,006	0,041 \pm 0,006	0,031*
F _{5 FS} : f_c (SL) [UC/min]	TVUS speckle tracking	2,907 \pm 0,230	3,030 \pm 0,006	0,271
F _{6 FS} : f_c (DT) [UC/min]	TVUS speckle tracking	1,253 \pm 0,414	1,455 \pm 0,006	0,282
F _{7 FS} : MF (DT) [Hz]	TVUS speckle tracking	0,033 \pm 0,001	0,034 \pm 0,002	0,336
F _{8 FS} : MF (DL) [Hz]	TVUS speckle tracking	0,034 \pm 0,002	0,035 \pm 0,002	0,384
F _{9 FS} : f_c [UC/min]	TVUS - SVD	2,754 \pm 0,255	2,532 \pm 0,602	0,048*
F _{10 FS} : MDF [Hz]	EHG	0,477 (IQR: 0,338)	0,605 (IQR: 0,588)	0,812
MEASUREMENT PHASE: ET1 (one hour before embryo transfer)				
Feature	Method	SP	FP	p value
F _{1 ET1} : f_c (DL) [UC/min]	TVUS speckle tracking	1,452 \pm 0,388	0,930 \pm 0,301	0,006*
F _{2 ET1} : MDF (SL) [Hz]	TVUS speckle tracking	0,048 \pm 0,002	0,050 \pm 0,002	0,171
F _{3 ET1} : UFM [mV Hz ^{3/2}]	EHG - SVD	0,8x10 ⁸ (IQR: 5,2x10 ⁸)	1,2x10 ⁸ (IQR: 1,7x10 ⁸)	0,937
F _{4 ET1} : SD [mV]	EHG - SVD	0,88 (IQR: 0,08x10 ⁻²)	1,07 (IQR: 0,02x10 ⁻²)	0,938
F _{5 ET1} : f_c (DT) [UC/min]	TVUS speckle tracking	1,508 \pm 0,600	1,241 \pm 0,290	0,289
F _{6 ET1} : f_c (ST) [UC/min]	TVUS speckle tracking	3,214 \pm 0,536	2,870 \pm 0,632	0,298
F _{7 ET1} : MF (DT) [Hz]	TVUS speckle tracking	0,035 \pm 0,003	0,033 \pm 0,003	0,313
F _{8 ET1} : SD (DT) [pix]	TVUS speckle tracking	1,054 \pm 0,540	0,836 \pm 0,303	0,355
F _{9 ET1} : MF (ST) [Hz]	TVUS speckle tracking	0,048 \pm 0,004	0,047 \pm 0,003	0,453
F _{10 ET1} : MDF (ST) [Hz]	TVUS speckle tracking	0,051 \pm 0,005	0,050 \pm 0,004	0,459
MEASUREMENT PHASE: ET5-7 (five to seven after embryo transfer)				
Feature	Method	SP	FP	p value
F _{1 ET5-7} : MDF (ST) [Hz]	TVUS speckle tracking	0,050 \pm 0,003	0,045 \pm 0,004	0,042*
F _{2 ET5-7} : MF (DT) [Hz]	TVUS speckle tracking	0,035 \pm 0,001	0,032 \pm 0,003	0,032*
F _{3 ET5-7} : MDF (DT) [Hz]	TVUS speckle tracking	0,032 \pm 0,001	0,028 \pm 0,004	0,098
F _{4 ET5-7} : f_c (DT) [UC/min]	TVUS speckle tracking	1,466 \pm 0,441	1,099 \pm 0,420	0,135
F _{5 ET5-7} : f_c [UC/min]	TVUS - SVD	2,320 \pm 0,416	1,999 \pm 0,365	0,225
F _{6 ET5-7} : f_c (SL) [UC/min]	TVUS speckle tracking	2,882 \pm 0,350	3,207 \pm 0,437	0,155
F _{7 ET5-7} : MDF [Hz]	EHG	0,576 (IQR: 0,170)	0,653 (IQR: 0,231)	0,218

$F_{8\text{ ETS-7}}$: MF (ST) [Hz]	TVUS speckle tracking	0,046 ± 0,002	0,045 ± 0,003	0,246
$F_{9\text{ ETS-7}}$: SD [mV]	EHG - SVD	0,398 (IQR: 0,730)	1,664 (IQR: 4,797)	0,578
$F_{10\text{ ETS-7}}$: MDF (SL) [Hz]	TVUS speckle tracking	0,047 ± 0,002	0,046 ± 0,002	0,505

* = $p < 0,05$ according to the two-tailed Student's t-test; (DL) and (DT): feature extracted from the distance signal along the longitudinal and transversal direction, respectively; (SL) and (ST): feature extracted from the strain signal along the longitudinal and transversal direction, respectively.

during the ET1 phase, UFM, SD, and f_c (DT) features are included together with the strongest feature f_c (DL) in the optimum feature set for both SVM and KNN classifiers; the same classifiers included features MDF (DT) and f_c (SL) in their optimum feature set in the ET5-7 phase.

Table 8.2: Performance of different feature combinations using the Support Vector Machine in the three considered measurement phases. The optimum feature set is highlighted in red.

MEASUREMENT PHASE: FS (Follicle stimulation)				
Iteration	Feature	Accuracy (%)	Sensitivity (%)	Specificity (%)
1	{ $F_{7\text{ FS}}$ }	87,5 %	71,4 %	100 %
2	{ $F_{7\text{ FS}}$, $F_{4\text{ FS}}$ }	75,0 %	85,7 %	66,7 %
3	{ $F_{7\text{ FS}}$, $F_{4\text{ FS}}$, $F_{1\text{ FS}}$ }	87,5 %	71,4 %	100 %
4	{ $F_{7\text{ FS}}$, $F_{4\text{ FS}}$, $F_{1\text{ FS}}$, $F_{9\text{ FS}}$ }	93,8 %	100 %	88,9 %
5	{ $F_{7\text{ FS}}$, $F_{4\text{ FS}}$, $F_{1\text{ FS}}$, $F_{9\text{ FS}}$, $F_{2\text{ FS}}$ }	68,8 %	71,4 %	66,7 %
MEASUREMENT PHASE: ET1 (one hour before embryo transfer)				
Iteration	Feature	Accuracy (%)	Sensitivity (%)	Specificity (%)
1	{ $F_{1\text{ ET1}}$ }	81,3 %	57,1 %	100 %
2	{ $F_{1\text{ ET1}}$, $F_{3\text{ ET1}}$ }	93,8 %	85,7 %	100 %
3	{ $F_{1\text{ ET1}}$, $F_{3\text{ ET1}}$, $F_{4\text{ ET1}}$ }	93,8 %	85,7 %	100 %
4	{ $F_{1\text{ ET1}}$, $F_{3\text{ ET1}}$, $F_{4\text{ ET1}}$, $F_{5\text{ ET1}}$ }	93,8 %	100 %	88,9 %
5	{ $F_{1\text{ ET1}}$, $F_{3\text{ ET1}}$, $F_{4\text{ ET1}}$, $F_{5\text{ ET1}}$, $F_{7\text{ ET1}}$ }	87,5 %	71,4 %	100 %
MEASUREMENT PHASE: ETS-7 (five to seven days after embryo transfer)				
Iteration	Feature	Accuracy (%)	Sensitivity (%)	Specificity (%)
1	{ $F_{3\text{ ETS-7}}$ }	68,8 %	42,9 %	88,9 %
2	{ $F_{3\text{ ETS-7}}$, $F_{6\text{ ETS-7}}$ }	75,0 %	71,4 %	77,8 %
3	{ $F_{3\text{ ETS-7}}$, $F_{6\text{ ETS-7}}$, $F_{1\text{ ETS-7}}$ }	75,0 %	71,4 %	77,8 %
4	{ $F_{3\text{ ETS-7}}$, $F_{6\text{ ETS-7}}$, $F_{1\text{ ETS-7}}$, $F_{5\text{ ETS-7}}$ }	75,0 %	57,1 %	88,9 %
5	{ $F_{3\text{ ETS-7}}$, $F_{6\text{ ETS-7}}$, $F_{1\text{ ETS-7}}$, $F_{5\text{ ETS-7}}$, $F_{2\text{ ETS-7}}$ }	81,3 %	71,4 %	88,9 %
6	{ $F_{3\text{ ETS-7}}$, $F_{6\text{ ETS-7}}$, $F_{1\text{ ETS-7}}$, $F_{5\text{ ETS-7}}$, $F_{2\text{ ETS-7}}$, $F_{9\text{ ETS-7}}$ }	87,5 %	71,4 %	100 %
7	{ $F_{3\text{ ETS-7}}$, $F_{6\text{ ETS-7}}$, $F_{1\text{ ETS-7}}$, $F_{5\text{ ETS-7}}$, $F_{2\text{ ETS-7}}$, $F_{9\text{ ETS-7}}$, $F_{4\text{ ETS-7}}$ }	75,0 %	57,1 %	88,9 %

These results indicate that the distinguishing ability of these features is independent of the adopted machine-learning models. On the other hand, the three classifiers ended up with different optimum feature sets, suggesting that the optimum feature set is dependent on the classifier; hence, in order to achieve the best classification performance, the feature selection procedure should be carried out separately for each machine-learning model.

In general, SVM and KNN classifiers achieved better accuracy performance than GMM using their own optimum feature sets. In particular, SVM and KNN achieved the highest accuracy performance (93.8%) in the FS and ET1 phases, although the optimum feature sets were different. Lower accuracy performance (87.5%) was achieved in the ET5-7 phase.

A general observation concerns the type of features that are included in each optimum feature set. According to our results, in the FS phase both SVM and KNN classifiers included only frequency-related feature in their optimum feature sets while in the ET1 phase they included the combination of frequency-, amplitude, and energy-related features. In particular, in the FS phase, the successful pregnancy group presented overall lower values of the frequency

Table 8.3: Performance of different feature combinations using the K-Nearest neighbors in the three considered measurement phases. The optimum feature set is highlighted in red.

MEASUREMENT PHASE: FS (Follicle stimulation)				
Iteration	Feature	Accuracy (%)	Sensitivity (%)	Specificity (%)
1	{F _{1 FS} }	75,0 %	57,2 %	88,9 %
2	{F _{1 FS} , F _{2 FS} }	81,3 %	71,4 %	88,9 %
3	{F _{1 FS} , F _{2 FS} , F _{4 FS} }	87,5 %	71,4 %	88,9 %
4	{F _{1 FS} , F _{2 FS} , F _{4 FS} , F _{10 FS} }	93,8 %	100 %	88,9 %
5	{F _{1 FS} , F _{2 FS} , F _{4 FS} , F _{10 FS} , F _{3 FS} }	87,5 %	100 %	77,8 %
MEASUREMENT PHASE: ET1 (one hour before embryo transfer)				
Iteration	Feature	Accuracy (%)	Sensitivity (%)	Specificity (%)
1	{F _{1 ET1} }	81,3 %	57,1 %	100 %
2	{F _{1 ET1} , F _{5 ET1} }	93,8 %	85,7 %	100 %
3	{F _{1 ET1} , F _{5 ET1} , F _{4 ET1} }	93,8 %	85,7 %	100 %
4	{F _{1 ET1} , F _{5 ET1} , F _{4 ET1} , F _{8 ET1} }	93,8 %	100 %	88,9 %
5	{F _{1 ET1} , F _{5 ET1} , F _{4 ET1} , F _{8 ET1} , F _{3 ET1} }	93,8 %	85,7 %	100 %
6	{F _{1 ET1} , F _{5 ET1} , F _{4 ET1} , F _{8 ET1} , F _{3 ET1} , F _{2 ET1} }	87,5 %	85,7 %	88,9 %
MEASUREMENT PHASE: ET5-7 (five to seven days after embryo transfer)				
Iteration	Feature	Accuracy (%)	Sensitivity (%)	Specificity (%)
1	{F _{3 ET5-7} }	81,3 %	74,1 %	88,9 %
2	{F _{3 ET5-7} , F _{6 ET5-7} }	87,5 %	71,4 %	100 %
3	{F _{3 ET5-7} , F _{6 ET5-7} , F _{8 ET5-7} }	87,5 %	71,4 %	100 %
4	{F _{3 ET5-7} , F _{6 ET5-7} , F _{8 ET5-7} , F _{2 ET5-7} }	75,0 %	71,4 %	77,8 %

Table IV: Performance of different feature combinations using the Gaussian Mixture Model in the three considered measurement phases. The optimum feature set is highlighted in red.

MEASUREMENT PHASE: FS (Follicle stimulation)				
Iteration	Feature	Accuracy (%)	Sensitivity (%)	Specificity (%)
1	{F _{6 FS} }	75,0 %	57,1 %	88,9 %
2	{F _{6 FS} , F _{9 FS} }	56,3 %	42,9 %	66,7 %
MEASUREMENT PHASE: ET1 (one hour before embryo transfer)				
Iteration	Feature	Accuracy (%)	Sensitivity (%)	Specificity (%)
1	{F _{1 ET1} }	81,3 %	71,4 %	88,9 %
2	{F _{1 ET1} , F _{3 ET1} }	87,5 %	87,5 %	88,9 %

3	{ $F_{1\text{ET1}}$, $F_{3\text{ET1}}$, $F_{10\text{ET1}}$ }	81,3 %	85,7 %	77,8 %
MEASUREMENT PHASE: ETS-7 (five to seven days after embryo transfer)				
Iteration	Feature	Accuracy (%)	Sensitivity (%)	Specificity (%)
1	{ $F_{7\text{ETS-7}}$ }	75,0 %	100 %	55,6 %
2	{ $F_{7\text{ETS-7}}$, $F_{8\text{ETS-7}}$ }	75,0 %	85,7 %	77,8 %
3	{ $F_{7\text{ETS-7}}$, $F_{8\text{ETS-7}}$, $F_{4\text{ETS-7}}$ }	75,0 %	85,7 %	66,7 %
4	{ $F_{7\text{ETS-7}}$, $F_{8\text{ETS-7}}$, $F_{4\text{ETS-7}}$, $F_{5\text{ETS-7}}$ }	62,5 %	57,1 %	66,7 %

features compared to the unsuccessful pregnancy group. This finding may be related to the uterine reaction to hormone injection for follicle stimulation. According to the mean values in Table I, the unsuccessful group presented an excessive response to the treatment showing higher uterine activity. Noteworthy, in this study some of the indications for IVF treatment comprise endometriosis and hormonal disorders. It is known that in the presence of moderate endometriosis the uterine activity is higher compared to healthy conditions or mild endometriosis^{35, 36} and it might become even higher under hyperstimulation during the IVF cycle. Unfortunately, very little is known about the effect of hormone administration during IVF on uterine activity and, therefore, on the receptiveness of the uterus.

Regarding the ET phase, the successful pregnancy group presented overall higher values of the frequency features and lower values of the energy and amplitude features compared to the unsuccessful pregnancy group. This result suggests that the combination of higher frequency with lower energy and amplitude in the uterine activity, observed one hour before ET, might favour embryo implantation and, thus, successful IVF treatment. It would be reasonable to think that the embryo, once inserted into the uterine cavity, needs contractions in order to bind to the uterine wall and implant. On the other hand, these contractions should not be strong in terms of amplitude and energy as they could cause the expulsion of the embryo out of the uterine cavity.

The inclusion of frequency-, energy-, and amplitude-related features in the optimum feature sets of the SVM and KNN classifiers may also suggest that a complete characterization of the uterine activity is needed for prediction of IVF success.

An interesting result concerns the strongest single feature f_c (DL); the obtained mean values are comparable to what is reported in Zhu et al.³⁷ where the highest pregnancy rate (63.55%) was observed in women with f_c in the range 1.1- 2.0 UC/min while women with $f_c \leq 1.0$ UC/min presented reduced pregnancy rate (58.97%), which became even lower (6.25% and 0.00%) for $f_c > 3.1$ UC/min. In our study, we could not observe f_c higher than 2.0 UC/min for the unsuccessful pregnancy group; a possible reason may reside in our small dataset to the large dataset (292 women) included in Zhu et al.³⁷. Also Woolcott et al.³⁸ reported that improved IVF outcome was obtained when uterine activity was present just before the ET in comparison with cases in which it was absent.

Based on the optimum feature set of each classifier, mostly consisting of frequency features, the characterization of the uterine activity in terms of frequency is dependent on the classifier; it is therefore difficult to generalize on the uterine activity-characteristics required for prediction of successful pregnancy.

In general, the obtained predictions of embryo implantation during the ET5-7 phase was poor. Unfortunately, there is no literature on uterine activity in relation to IVF outcome during this phase; based on our results, we can only speculate about the fact that the embryo is expected to be already implanted at this stage of the IVF cycle; therefore, the uterine contractions might no longer hinder the embryo nesting process in the uterine wall.

The uterine activity is a complex phenomenon involving either the outer or inner muscle layers with generalized and local consequences. Therefore, in this study, we combined EHG and B-mode TVUS motion analysis for a complete assessment of electromechanical uterine activity. In particular, we assessed local uterine activity by tracking specific areas of the subendometrial layer as well as global uterine activity by EHG analysis, being more sensitive to the outer muscle layer, and by deriving the temporal variation signals after SVD decomposition of both EHG and TVUS recordings.

The proposed approach based on SVD only shows promise. This is also confirmed by the number of features included in the optimum feature set of each classifier in the three measurement phases. In particular, the features F2 and F4 (median and contraction frequency extracted from the TVUS temporal variation signal) significantly ($p < 0.05$) separated successful and unsuccessful pregnancy group in the FS phase outside the machine-learning framework.

The frequency band used in this study for calculating the energy ratio metric for singular value selection both in EHG and B-mode TVUS recordings was based on the contraction frequency observed in^{5, 14}. Future studies with larger datasets should also investigate different frequency bands based on our results.

Besides frequency-, energy-, and amplitude-related features, uterine activity patterns appear to be a promising feature of uterine receptivity, at least in natural menstrual cycles^{39, 40}. In IVF cycles, specific wave-like activity patterns are associated to the occurrence of pregnancy^{39, 41}. Therefore, the estimation of additional features representative of the spatiotemporal uterine activity patterns, such as propagation direction and velocity, could add relevant information to our machine-learning framework for the predictability of a successful embryo implantation.

In the future, optimization of IVF treatment protocols based on patient characteristics could also be carried out by e.g. personalizing the dose of medications administrated during the IVF treatment before ET to modulate uterine activity for approaching optimal range. For example, in the presence of unfavorable uterine activity, classification would permit proper decision making, either delaying ET to later natural cycles by freezing the embryos or modulating uterine activity by specific and precise pharmacological intervention, e.g. oxytocin antagonists, such as Atosiban, Nolasiban, and Barusiban, for favoring embryo implantation⁹⁻¹¹.

As improvement to the classifier it might be interesting to look at other feature reduction techniques like backwards feature selection or a feature filter based on mutual information. These techniques can help reduce overfitting during the optimization process⁴². If a larger dataset becomes available in the future other cross validation methods, like K-fold cross validation, can be tested besides the leave one-out method. This type of cross validation methods are expected to produce less variance in the performance metrics⁴².

The presented work represents a first step toward better embryo implantation prediction, showing already the ability to classify successful and unsuccessful pregnancy when measuring the uterine activity one hour before ET. The clinical value of our proposed method requires however extensive validation *in vivo* during the IVF cycle; this can spur additional insight expanding our knowledge on the electromechanical uterine activity and its role in conception and fertilization.

8.5 CONCLUSION

Understanding the role of uterine activity in influencing uterine receptivity, especially during ET, has always been limited by the lack of quantitative measurement tools. The possibility to objectively and noninvasively measure and classify uterine activity outside pregnancy represents a fundamental step towards improved embryo implantation and thus IVF treatment.

In this study, probabilistic classification of the electromechanical uterine activity, as either favorable or adverse to ET, was investigated by machine learning.

Enabled by the adopted multi-modal EHG and TVUS acquisitions of the uterine activity, frequency-, amplitude-, and energy-related features were extracted from the recorded signals and optimally combined by three machine-learning models; a forward-feature selection procedure was employed to find the optimum feature set in each of the three measurement phases.

Our classification results reveal that among the three considered classifiers, the SVM and KNN produced higher accuracy. In particular, the highest accuracy (93.8%) was obtained when measuring during the follicle stimulation and one hour before ET; in fact predicting before the ET has more impact on clinical practice. Lower accuracy (87.5%) was instead achieved when measuring five to seven days after ET.

Frequency-, energy-, and amplitude-related features such as f_c , UFM and SD, respectively, obtained from TVUS motion and EHG analysis, were included by SVM and KNN in their optimum feature sets; this suggests that the ability of these features to separate successful and unsuccessful pregnancy is independent of classifiers. These features may contribute to produce the best prediction of embryo implantation improving the IVF procedure. Yet, a larger dataset is required for improved training of the considered classifiers.

BIBLIOGRAPHY

1. G. F. Whitman-Elia and E. G. Baxley, "A primary care approach to the infertile couple. The Journal of the American Board of Family Practice, vol. 14, no. 1, pp. 33–45, 2001.
2. E. C. W. Group et al., Social determinants of human reproduction, "Human Reproduction, vol. 16, no. 7, pp. 1518–1526, 2001.
3. A. Nyboe Andersen, V. Goossens, A. Ferraretti, S. Bhattacharya, R. Felberbaum, J. de Mouzon, K. Nygren. The European IVF-monitoring (EIM) Consortium, and E. (ESHRE), Assisted reproductive technology in Europe, 2004 :results generated from European registers by ESHRE, Human Reproduction, vol. 23, no.4, pp. 756–771, 2008. [Online]. Available: <http://dx.doi.org/10.1093/humrep/den014>.
4. R. Fanchin and J.M.Ayoubi, Uterine dynamics: impact on the human reproduction process, Reproductive BioMedicineOnline, vol. 18, pp. S57 – S62, 2009. [Online]. Available:<http://www.sciencedirect.com/science/article/pii/S1472648310604506>
5. R. Fanchin, C. Righini, F. Olivennes, S. Taylor, D. de Ziegler, and R. Frydman, Uterine contractions at the time of embryo transfer alter pregnancy rates after in-vitro fertilization, vol. 13, pp. 1968–74, 081998.
6. P. Lesny, S. Killick, J. Robinson, G. Raven, and S. Maguiness, Junctional zone contractions and embryo transfer: is it safe to use atenaculum?, Human reproduction, vol. 14, no. 9, pp. 2367–2370, 1999.
7. M. M. IJland, H. J. Hoogland, G. A. Dunselman, C. R. Lo, and J. L.Evers, "Endometrial wave direction switch and the outcome of in vitro fertilization, Fertility and sterility, vol. 71, no. 3, pp. 476–481, 1999.
8. A. Heger, M. Sator, and D. Pietrowski, Endometrial receptivity and its predictive value for ivf/icsi-outcome, Geburtshilfe und Frauen-heilkunde, vol. 72, no. 08, pp. 710–715, 2012.
9. P. Pierzynski, T. M. Reinheimer, and W. Kuczynski, "Oxytocin antagonists may improve infertility treatment, Fertility and sterility, vol. 88, no. 1, pp. 213–e19, 2007.
10. P. Pierzynski, "Oxytocin and vasopressin v1a receptors as new therapeutic targets in assisted reproduction, Reproductive biomedicine online, vol. 22, no. 1, pp. 9–16, 2011.
11. O. Moraloglu, E. Tonguc, T. Var, T. Zeyrek, and S. Batioglu, "Treatment with oxytocin antagonists before embryo transfer may increase implantation rates after ivf, Reproductive biomedicine online, vol. 21, no. 3, pp. 338–343, 2010.
12. F. Sammal, N. P. M. Kuijsters, B. C. Schoot, M. Mischi, and C. Rabotti, Feasibility of transabdominal electrohysterography for analysis of uterine activity in nonpregnant women, Reproductive Sciences, p.1933719118768700, 2018.
13. F. Sammal, N. P. Kuijsters, Y. Huang, C. Blank, C. Rabotti, B. C. Schoot, and M. Mischi, "Dedicated ultrasound speckle tracking for quantitative analysis of uterine motion outside pregnancy, IEEE transactions on ultrasonics, ferroelectrics, and frequency control, vol. 66, no. 3, pp.581–590, 2019.
14. D. Devedeux, C. Marque, S. Mansour, G. Germain, and J. Duch^ene, Uterine electromyography: a critical review, American journal of obstetrics and gynecology, vol. 169, no. 6, pp. 1636–1653, 1993.
15. C. Gui and V. Chan, Machine learning in medicine, University of Western Ontario Medical Journal, vol. 86, no. 2, pp. 76–78, 2017.
16. "OxytocinReceptorAntagonists,AtosibanandNolasiban,InhibitProstaglandinF2 α -inducedContractionsandInflammatoryResponsesinHumanMyometrium,"ScientificReports,vol. 9,no.1,p.5792,dec2019.[Online].Available:<http://www.ncbi.nlm.nih.gov/pubmed/30962532>htt

- [p://www.pubmedcentral.nih.gov/articlerender.fcgi?artid=PMC6453954](http://www.pubmedcentral.nih.gov/articlerender.fcgi?artid=PMC6453954)<http://www.nature.com/articles/s41598-019-42181-2>.
17. C. Blank, R. R. Wildeboer, I. DeCroo, K. Tilleman, B. Weyers, P. de Sutter, M. Mischi, and B. C. Schoot, "Prediction of implantation after blastocyst transfer in in vitro fertilization: a machine-learning perspective, *Fertility and sterility*, vol. 111, no. 2, pp. 318–326, 2019.
 18. C. Bulletti, D. de Ziegler, V. Polli, L. Diotallevi, E. D. Ferro, and C. Flamigni, Uterine contractility during the menstrual cycle, *Human reproduction*, vol. 15, no. suppl1, pp. 81–89, 2000.
 19. M. J. Rooijackers, S. Song, C. Rabotti, S. G. Oei, J. W. Bergmans, E. Cantatore, and M. Mischi, Influence of electrode placement on signal quality for ambulatory pregnancy monitoring, *Computational and mathematical methods in medicine*, vol. 2014, 2014.
 20. C. Rabotti and M. Mischi, Propagation of electrical activity in uterine muscle during pregnancy: a review, *Acta Physiologica*, vol. 213, no. 2, pp. 406–416, 2015.
 21. L. Xu, C. Rabotti, and M. Mischi, "Novel vibration-exercise instrument with dedicated adaptive filtering for electromyographic investigation of neuromuscular activation," *IEEE Transactions on Neural Systems and Rehabilitation Engineering*, vol. 21, no. 2, pp. 275–282, 2013.
 22. —, "Analysis of vibration exercise at varying frequencies by different fatigue estimators," *IEEE Transactions on Neural Systems and Rehabilitation Engineering*, vol. 24, no. 12, pp. 1284–1293, 2016.
 23. W. L. Maner, R. E. Garfield, H. Maul, G. Olson, and G. Saade, Predicting term and preterm delivery with transabdominal uterine electromyography, *Obstetrics & Gynecology*, vol. 101, no. 6, pp. 1254–1260, 2003.
 24. C. Buhimschi, M. B. Boyle, and R. E. Garfield, Electrical activity of the human uterus during pregnancy as recorded from the abdominal surface, *Obstetrics & Gynecology*, vol. 90, no. 1, pp. 102–111, 1997.
 25. M. M. Ijland and J. L. H. Evers, Subendometrial contractions in the nonpregnant uterus: an ultrasound study, *European Journal of Obstetrics & Gynecology and reproductive Biology*, vol. 70, no. 1, pp. 23–24, 1996.
 26. L. Yu and H. Liu, "Feature selection for high-dimensional data: A fast correlation-based filter solution," in *Proceedings, Twentieth International Conference on Machine Learning*, T. Fawcett and N. Mishra, Eds., vol. 2, 2003, pp. 856–863.
 27. A. Marcano-Cedeño, J. Quintanilla-Dominguez, M. Cortina-Januchs, and D. Andina, Feature selection using sequential forward selection and classification applying artificial metaplasticity neural network, in *IECON 2010-36th annual conference on IEEE industrial electronics society*. IEEE, 2010, pp. 2845–2850.
 28. J. Grus, *Data Science from Scratch: First Principles with Python*, 1st ed. O'Reilly Media, Inc., 2015.
 29. G. C. Cawley and N. L. C. Talbot, On over-fitting in model selection and subsequent selection bias in performance evaluation, *Journal of Machine Learning Research*, vol. 11, pp. 2079–2107, 2010.
 30. A. Tripathy, A. Agrawal, and S. K. Rath, Classification of sentimental reviews using machine learning techniques, *Procedia Computer Science*, vol. 57, pp. 821–829, 2015.
 31. K. Kourou, T. P. Exarchos, K. P. Exarchos, M. V. Karamouzis, and D. I. Fotiadis, Machine learning applications in cancer prognosis and prediction, *Computational and structural biotechnology journal*, vol. 13, pp. 8–17, 2015.
 32. C. W. Hsu, C. C. Chang, and C. J. Lin, A practical guide to support vector classification, Department of Computer Science, National Taiwan University, Tech. Rep., 2003. [Online]. Available: <http://www.csie.ntu.edu.tw/~cjlin/papers.html>.

33. S. S. Shapiro and M. B. Wilk, "An analysis of variance test for normality (complete samples), *Biometrika*, vol. 52, no. 3/4, pp. 591–611, 1965.
34. R. Woolson, Wilcoxon signed-rank test, *Wiley encyclopedia of clinical trials*, pp. 1–3, 2007.
35. C. Bulletti, D. De Ziegler, V. Polli, E. Del Ferro, S. Palini, and C. Flamigni, Characteristics of uterine contractility during menses in women with mild to moderate endometriosis, *Fertility and sterility*, vol. 77, no. 6, pp. 1156–1161, 2002.
36. N. P. M. Kuijsters, W. G. Methorst, M. S. Q. Kortenhorst, C. Rabotti, M. Mischi, and B. C. Schoot, "Uterine peristalsis and fertility: current knowledge and future perspectives: a review and meta-analysis," *Reproductive biomedicine online*, vol. 35, no. 1, pp. 50–71, 2017.
37. L. Zhu, H. Che, L. Xiao, and Y. Li, "Uterine peristalsis before embryo transfer affects the chance of clinical pregnancy in fresh and frozen-thawed embryo transfer cycles," *Human Reproduction*, vol. 29, no. 6, pp. 1238–1243, 2014.
38. R. Woolcott and J. Stanger, "Potentially important variables identified by transvaginal ultrasound-guided embryo transfer." *Human reproduction* (Oxford, England), vol. 12, no. 5, pp. 963–966, 1997.
39. M. M. Ijland, J. L. Evers, G. A. Dunselman, L. Volovics, and H. J. Hoogland, "Relation between endometrial wavelike activity and fecundability in spontaneous cycles," *Fertility and sterility*, vol. 67, no. 3, pp. 492–496, 1997.
40. Y. Huang, F. Sammal, C. Blank, N. Kuijsters, C. Rabotti, B. Schoot, and M. Mischi, "Quantitative Ultrasound Imaging and Characterization of Uterine Peristaltic Waves," in 2018 IEEE International Ultrasonics Symposium (IUS). IEEE, oct 2018, pp. 1–4. [Online]. Available: <https://ieeexplore.ieee.org/document/8580218/>.
41. M. M. Ijland, J. L. Evers, G. A. Dunselman, C. van Katwijk, C. R. Lo, and H. J. Hoogland, "Endometrial wavelike movements during the menstrual cycle," *Fertility and sterility*, vol. 65, no. 4, pp. 746–749, 1996.
42. James, G., Witten, D., Hastie, T., & Tibshirani, R. (2013). *An introduction to statistical learning* (Vol. 112, p. 18). New York: Springer.

Epilogue

9

DISCUSSION AND FUTURE PERSPECTIVES

This final chapter provides a critical discussion and conclusion of the research conducted in this thesis, along with future perspectives.

In this work, new methods have been proposed to quantitatively and non-invasively measure the electromechanical uterine activity both in natural and stimulated cycles, especially in relation to embryo transfer. To this end, transabdominal EHG and TVUS motion analysis have been investigated. Frequency-, amplitude-, and energy-related features have been extracted from the measured signals with the help of a dedicated signal processing strategies. The extracted features have been further assessed, as either favorable or adverse to embryo implantation, through probabilistic classification by machine learning. In the following sections the resulting observations, contributions and main limitations of the adopted strategies are discussed separately for each method. Finally, general conclusions are drawn and some future perspectives are given.

9.1 Part I: Electrohysterography in the non-pregnant uterus

9.1a Propagation of spontaneous biopotentials in the *ex-vivo* human uterus (Chapter 2)

In **Chapter 2**, the electrophysiology underlying the uterine contractions was studied in *ex-vivo* human uteri. By performing multichannel EHG measurements directly on a resected uteri, without any connection to the human body as well as without electrical or hormonal stimulus, the presence of spontaneous electrical activity was investigated and its propagation characterized. The main objective of this study was to evaluate the ability of the uterus to produce biopotentials autonomously, as well as to investigate the presence of particular areas where the contractions originate.

Main observations and contributions

- Spontaneous biopotentials can be measured and characterized in an unstimulated *ex-vivo* human uterus by performing EHG measurements. This finding is supported by two observations: EHG signals with significantly higher average amplitude (root mean squared values) than control showing decay over time, and the presence of propagation both internally and externally.
- Among the five measured uteri, four showed erratic propagation while only one showed plane-wave propagation. This uterus showing plane wave, belonged to a patient who was operated while menstruating. Notwithstanding the limited number of included uteri, this finding, which may be a coincidence, is in line with existing theories comparing menstruation to labour^{2, 15, 77, 81, 98}. In fact, during labor biopotentials are more coordinated and characterized by recognizable directions¹⁹. Moreover, based on physiological changes that occur during menstruation, which resemble pregnancy, labour has been actually considered as just delayed menstruation²⁰. Therefore, the observed difference in the propagation patterns between the menstruating uterus and the other uteri might be ascribed to electrophysiological changes comparable to those observed during the evolution from pregnancy to labor.

- No specific pace-making area has been found in the myometrial tissue. This finding, which is in line with other studies carried on during pregnancy and in animals²¹⁻²⁵, suggests the presence of many pace-making areas throughout the uterus. Therefore, the initiation and propagation of electrical activity in the uterus, unlike the heart, appears to be a complex mechanism²⁶ suggesting that every myocyte has pace-making capabilities.
- Unfortunately, internal measurements performed by the intrauterine array did not show a pattern in the direction and velocity of the measured biopotentials as compared to external measurements. The observed disagreement might be explained by the architecture of the uterus itself. In this regard, substantiated theory states that the inner layer of the myometrium and endometrium form a functional unit with a different embryological origin compared to outer myometrial layers²⁷. Along the side of this theory, the inner and outer uterine layers could exhibit different propagation patterns, which would explain the discrepancy between the two measurements.

Challenges and limitations

- The major limitation of this study relates to the small group size of 5 uteri, which cannot be representative of the various uterine behaviors observed in women during the different phases of the menstrual cycle; therefore, the characterization of the electrophysiological uterine activity results difficult, especially because the results refer to pathological conditions, such as adenomyosis and leiomyoma. Moreover, one uterus was menstruating and, by nature, this myometrial tissue behaves differently compared to not menstruating uteri²⁸. Including more *ex-vivo* uteri that could be grouped based on pathology and phase of the menstrual cycle could significantly improve the scientific contribution of the study.
- Simultaneous electrical and mechanical recordings could support a deeper understanding of the uterine physiology *ex vivo*. In this study, the presence of the high-density grid covering most of the myometrial wall and the intrauterine array inserted into the uterine cavity, hampered the possibility to perform simultaneous US measurements. However, in similar conditions, no movement could be observed by US in *ex-vivo* uteri. This is possibly due to the lack of muscle perfusion, limiting the metabolic possibilities and energy levels to produce actual muscle contraction.
- The comparison between external and internal measurements has been complicated by the different material, geometry and size of the adopted sensors. Moreover, while the high-density grid was well attached to the myometrial wall, the position of the intrauterine array was not well identified after its insertion into the cavity. Therefore, some of the electrodes on the internal array could have had poor electrode-tissue contact which might also explain the lower average root mean squared (RMS) amplitude compared to the one measured with the external grid.

9.1b Feasibility of transabdominal electrohysterography for analysis of uterine activity in non-pregnant women (Chapter 2)

Based on **Chapter 2**, transabdominal EHG has proven valuable to characterize noninvasively electrical uterine activity, but results of this technique in non-pregnant women are scarce. Therefore, in **Chapter 3**, the feasibility of EHG was investigated in healthy non-pregnant women to differentiate uterine activity throughout the menstrual cycle. In fact, due to the lack of a golden standard for assessment of electrical uterine activity outside pregnancy, the validation approach relied on different motion patterns reported for the uterus at different phases of the menstrual cycle^{4,9,17}.

Main observations and contributions

- With respect to alternative invasive methods, such as IUP, HSSG, and qualitative US measurements, transabdominal EHG measurements allowed for the first time the recording of biopotentials underlying the physiological process of uterine muscle contractions across the menstrual cycle in non-pregnant human uteri.
- Literature has indicated that uterine activity in the healthy uterus fluctuates across the menstrual cycle reaching an active state in the follicular phase and becoming progressively more quiet during the luteal phase. Moreover, a wave-like, peristaltic activity has been observed during most of the menstrual cycle as opposed to menses and parturition when cramping-like contractions dominate¹⁻⁶. The obtained results have shown consistent, significant differences, especially when using the UFM indicator, between menses phase and all the other phases, possibly due to the cramping-like contractions. The fact the women can feel cramps and pain during menstruation represents an additional evidence of these cramping-like contractions characterized, according to our results, by higher energy and amplitude compared to the other phases.
- All the extracted features have shown a decreasing trend in their values along the menstrual cycle from menses to luteal phase. Although the measured decrease was not significant, it may reflect a progressively more quiet state of the uterus along the menstrual cycle that is in line with the uterine function of promoting embryo implantation by increased receptivity. These findings are in contrast to previous TVUS and IUP measurement results, which have reported a progressive increase of the uterine activity in terms of frequency and intensity in the follicular phase followed by a decrease in the luteal phase^{7,8,3}. Moreover, when the uterus manifests labour-like contractions (during menses), the activity concerns mainly the outer two-third layer of the myometrium, while in the inner one-third layer (subendometrial layer) remains mostly quiet⁹.
- With the help of a multichannel grid we have demonstrated the feasibility of multichannel EHG recordings, paving the way to possible future studies aimed at assessing contraction direction and velocity.

- The obtained promising results motivate towards the employment of EHG measurement as a method to improve understanding and management of uterine dysfunction related to abnormal contractions, such as infertility, endometriosis, and dysmenorrhea.

Challenges and limitations

- The validation of the results presented in this work is hampered by the lack of a golden standard for quantification of uterine contractions in a non-pregnant human uterus. The results of this study have been indirectly validated based on physiological observations, which rely on the different contraction patterns reported for the uterus at different phase of the menstrual cycle.
- The difference between the results obtained in this study and those reported from previous studies based on TVUS and IUP measurements may be ascribed to the different nature of the measurement approaches (electrical vs. mechanical); therefore, their direct comparison is not straightforward due to the underlying physiological mechanisms, which remains still unknown.
- While the electrical activity of the uterus is better characterized during pregnancy^{10, 11, 53, 54}, there is no standard technique for recording electrical data on the small contractions that occur outside pregnancy¹². An EHG measurement system typically consists of a set of electrodes placed on the abdominal skin. In the studies available up until now, mostly during pregnancy, a wide range of electrode types, number of electrodes, and electrode positions have been used to measure electrical uterine activity^{12, 51, 55}, and no analyses have been performed to determine the optimal configurations. In this study, the choice of a multichannel-electrode grid may provide sufficient spatial resolution for analysis of EHG propagation properties in future work^{13, 14}. Yet, broader coverage of the abdominal surface may be useful for further improved recording and assessment of uterine activity.

9.2 Part II: Quantitative sonography in the non-pregnant uterus

9.2a Experimental setup for objective evaluation of uterine motion analysis by ultrasound speckle tracking (Chapter 4)

In **Chapter 4**, we presented an experimental setup based on a human *ex-vivo* uterus able to generate controlled uterine motion aiming at assessing the accuracy of motion tracking techniques and obtaining clear indications on the optimal imaging setting. Uterine motion was obtained by injecting saline through a balloon catheter inserted into the uterine cavity. This way, controlled, rhythmic uterine motion was generated by an electromagnetic actuator while maintaining the original speckle characteristics. The proposed setup was used for comparison of ultrasound speckle tracking methods. We used a two-step control approach which consisted of comparing first the motion of the needle markers, used to realize a clear reference for uterine motion tracking, with the driving sinusoidal signal of

the motor, and then comparing the tracked motion of surrounding uterine tissue with the motion of the corresponding needle markers.

Main observations and contributions

- The proposed experimental setup based on an *ex-vivo* uterus is able to generate controlled tissue motion, providing a realistic ground truth for objective evaluation of US speckle tracking methods.
- The motion of the needle markers, established by the proposed speckle tracking method, showed high agreement with the driving signal (correlation coefficient: $r = 0.909 \pm 0.054$; mean squared error: $MSE = 0.010 \pm 0.054$; Hausdorff distance: $H_d = 0.413 \pm 0.250$; normalized values expressed in terms of mean and standard deviation), revealing the ability of the needle markers to follow the well-controlled and rhythmic uterine motion generated by the experimental setup.
- The best agreement with the needle markers (the reference signals) was obtained by sum of absolute difference (SAD) tracking with a block size equal to twice the uterine speckle size ($3.448 \times 3.448 \text{ mm}^2$). This size was therefore used for tracking the uterine motion in natural (**Chapter 5**) as well as in stimulated (**Chapter 7 and 8**) menstrual cycles.
- Besides wave-like (sinusoidal) motion, with the proposed setup, different motion patterns can also be generated for testing and optimizing the speckle tracking in different conditions, such as in the presence of adenomyosis, or myomas; in this way, it could be possible to better characterize the influence of abnormal tissue on uterine motion.

Challenges and limitations

- Compared to real uterine motion, the developed setup has led to motion limitations. Uterine motion normally propagates as a peristaltic wave-like along the myometrium⁹. Such a wave cannot be reproduced by the developed setup. However, our main objective was to generate controlled tissue motion maintaining the original speckle characteristics for objective evaluation of speckle tracking performance.
- Imaging and localizing needle markers is no trivial task. Extensive research in US is focused on needle tracking⁵⁶⁻⁵⁸. In our setup, we have selected an insonation angle that produced sufficient backscatter. Yet, the use of inserted needles can also affect tissue motion. In future studies, different markers should be considered that facilitate the tracking while limiting the effects on tissue motion

9.2b Dedicated ultrasound speckle tracking for quantitative analysis of uterine motion outside pregnancy (Chapter 5)

In **Chapter 5**, we proposed a dedicated approach for uterine-motion quantification by TVUS. Motion tracking was implemented by speckle tracking integrating several novel aspects, such as SVD filtering for enhancing uterine motion over noise, clutter, and uncorrelated motion induced by neighbouring organs and probe movements; median filtering of the matching coordinates for improving the robustness to noise and speckle decorrelation; diamond search to reduce the computational search time. The proposed methods were first validated *ex vivo* and then used *in vivo*. Due to the lack of a golden standard for assessment of mechanical uterine activity outside pregnancy, the validation approach relied on different motion patterns reported for the uterus at different phases of the menstrual cycle.

Main observations and contributions

- *Ex vivo*, SVD filtering aimed at optimizing the correlation and squared error with the *ex vivo* reference improved the performance of speckle tracking. An energy ratio (ER) metric for uterine component selection was defined, successfully optimized *ex vivo*, and finally applied for *in-vivo* analysis.
- *Ex vivo*, when comparing with full grid search (FGS), our diamond search (DS) strategy did not result in a deterioration of tracking quality as confirmed by the comparable performance with FGS obtained for the r and MSE metrics, while achieving a threefold increase in the computational speed. This favours the real-time implementation of the method in clinical practice.
- *In vivo*, block matching by SAD, including DS strategy and median filtering, provided the best estimation of motion and strain along the longitudinal direction, which is aligned with back and forward uterine motion between cervix and fundus. Differently from standard FGS, DS is not constrained in a predefined search area and the presence of outliers can severely affect the performance of speckle tracking. In this study, median filtering mitigated the effect of outliers more efficiently than mean filtering, which was especially relevant in combination with a DS without a predefined search area.
- Among the extracted amplitude-, frequency-, and energy features, contraction frequency (f_c) and median frequency (MDF) most significantly differentiated between the most active and the quietest phase of the uterus.
- f_c was higher in the late follicular phase and lower in the late luteal phase. The resulting trend is completely in line with previous studies based on TVUS visual inspection and intrauterine pressure (IUP) measurements^{17, 4}. Instead, the estimated f_c (1.57 ± 0.27 UC/min) was comparable to that obtained by Kunz et al.²⁹. However, this f_c appeared to be in the lower limits of what has been described by the majority of US studies, according to which f_c usually ranges between 1 and 5 UC/min, but can even reach up to 10 UC/min⁴.

- During the late luteal phase, the results in Bulletti et al. obtained by visual inspection¹⁷ suggest f_c to be equal to 0.8 ± 0.3 UC/min while we detected 1.05 ± 0.34 UC/min. The difficulty of visualizing small contractions may lead to miss-counting by visual inspection, possibly explaining the difference in the estimated f_c .
- MDF confirmed the late follicular phase to be the most active as shown previously in the literature¹⁷, while revealing menses phase to be the quietest. The particular electrical behavior of menses phase already assessed **in Chapter 2 and 3** for the measurement of the electrical uterine activity, occurs in the mechanical activity of the uterus as well. As already explained, during menses the uterine muscle manifests labour-like activity alternating with quiescent periods of inactivity^{17, 2, 4, 6} and all the activity concerns mainly the outer two-third layer of the myometrium while the inner one-third remains mostly quiet⁹. In this study, the region investigated by speckle tracking was the subendometrium (inner one-third layer), possibly explaining the lower uterine activity detected during menses.
- The number of selected singular values based on the ER metric confirmed the finding obtained by the MDF feature. As the singular values relate to the temporal dynamics of the temporal variation signal $V(t)$, during the LF phase, the uterus seemed to show more activity and more singular values were selected for representing that particular uterine state; on the contrary, during menses fewer singular values were selected for representing the quiet uterine state.

Challenges and limitations

- The validation of the results presented in this work is hampered by the lack of a golden standard for quantification of uterine contractions in a non-pregnant human uterus. In this study, as in the EHG study (**Chapter 2**), TVUS speckle tracking results have been indirectly validated based on physiological observations which rely on the different contractility reported for the uterus at different phases of the menstrual cycle.
- The frequency band used for singular value selection when using the ER metric was based on the contraction frequencies obtained by Bulletti et al.¹⁷ during the natural menstrual cycle by visual inspection. Investigation of different frequency bands, also depending on the tracked myometrial layers, is needed for optimization of our methods.
- In this study, the analysis of the mechanical uterine motion was limited to the fundal area of the uterus, known to be the most contractile part of the uterus³⁰. However, whether this area can be representative of the contraction behavior of the whole organ is still unknown. Also unknown is the strain in other directions and, in particular, in different tissue layers.
- Although this study represents a first preliminary step for accurate assessment of the mechanical uterine activity, also accounting for its spatial distribution, its clinical translation requires more extensive validation and optimization *in vivo*.

- Due to the three-dimensional (3D) evolution of contractions in the uterus, for which origin and direction of propagation are time-varying and a priori unknown, and due to movement artifacts, introduced either by the operator or by surrounding tissues, the 2D ultrasound image sequences used for this study can be affected by out-of-plane movements. A method for uterine contraction analysis that is robust to this type of artifacts should rely on 3D US image sequences. To this end, dedicated algorithms should be developed for 3D analysis that are optimized for the generated 3D speckle patterns.

9.2c Blind source separation for clutter and noise suppression in ultrasound imaging: critical review for different applications (Chapter 6)

In **Chapter 6**, we described and tested the use of BSS filtering in US for several applications, including speckle tracking. The employment of BSS filtering was tested *in silico* (human heart model), *in vitro* (*ex-vivo* human uterus), and *in vivo* (uteri in healthy women).

Main observations and contributions

- Focusing on US speckle tracking, well-tailored BSS filtering outperformed the traditional filtering techniques. The main reason for this lies in the fact that BSS exploits the statistical independence or orthogonality of the spatiotemporal “sources” and, therefore, it is less affected by overlap of clutter and noise in the spatial or temporal (frequency) domain.
- Among all US approaches considered, SVD in combination with spectral thresholding performed the best. This result confirms our choice for the proposed ER metric (**Chapter 5**), based on a specific frequency band, for the separation of uterine motion from uncorrelated sources and noise contamination in US speckle tracking.
- Compared to other BSS methods, NMF underperformed in US speckle tracking, possibly because periodic motion, such as uterine motion, is best approximated when the singular values may also be negative.

Challenges and limitations

- As all spatial dimensions are collected in rows in the Casorati matrix, filtering can be easily extended to 3D acquisitions. In fact, the availability of a larger spatial support might lead to improved BSS performance⁶². However, BSS techniques generally require substantially more computational power and time compared to traditional filtering.
- An alternative approach to SVD filtering might be considered in which the frequency requirements are adjusted during the recording or depending on the context; for example, different frequency thresholds could be employed for different phases of the menstrual cycle, accounting for the different uterine behavior. In this study, a fixed frequency band was used to retain the relevant components reflecting uterine motion in the all considered phases of the menstrual cycle.

- It remains to be investigated whether soft (smooth) rather than hard thresholding can improve BSS filtering by avoiding block artifacts⁶³. In this study, especially for US speckle tracking, the inclusion of consecutive singular components was adopted to avoid artifacts introduced by the inclusion of sparse components. The effect of these artifacts, however, depends on the specific application and should be studied more in detail.

9.3 Part III: Assessment of uterine activity for predicting successful embryo implantation

9.3a Quantitative ultrasound imaging for assessment of uterine contractility during in-vitro fertilization (Chapter 7)

In **Chapter 7**, the proposed TVUS speckle tracking method, optimized *ex vivo* (**Chapters 4 and 5**) and validated in healthy women (**Chapter 5**), was employed to measure and characterize the mechanical uterine activity in women undergoing IVF treatment, especially in relation to embryo implantation success. Frequency-, amplitude-, and energy-related features were extracted from the measured signals following the same measurement protocol as in **Chapter 6**. The obtained uterine activity was compared to that obtained in a natural menstrual cycle (**Chapter 6**). Moreover, the relationship between the implantation/pregnancy outcome and the measured uterine activity was assessed in terms of frequency and amplitude of the contractions. The correlation with clinical variables, such as hormone levels, stimulation related features, and thickness of endometrium layer was also evaluated.

Main observations and contributions

- The overall uterine activity, in terms of frequency and amplitude shows a decrease in uterine activity along the three measurement phases for all patients; in particular, the follicle stimulation (FS) phase significantly differed ($p < 0.05$) from one hour before embryo transfer (ET1) and five to seven days after embryo transfer (ET5-7) phases. This result, which is in line with the literature^{31, 32}, indicates that patients respond well to the FS treatment showing higher uterine activity that decreases immediately before embryo transfer.
- When comparing patients with non ongoing and ongoing implantation (OI) as well as non ongoing and pregnancy (OP), the contraction frequency (f_c), extracted from the distance signal longitudinally, appeared to be the most powerful feature able to significantly separate ($p = 0.028$ for OI and $p = 0.006$ for OP) the groups immediately before ET (ET1). Patients with OI and OP presented an average number of f_c equal to 1.35 UC/min and 1.45 UC/min, respectively, while lower values, 0.91 UC/min and 0.93 UC/min, were obtained in patients with no OI and no OP, respectively. These values are comparable to those reported by Zhu et al.³³, where the highest pregnancy rate (63.55%) was achieved when women presented f_c in the range 1.1 -2.0 UC/min while women with $f_c \leq 1.0$ UC/min presented reduced pregnancy rate (58.97%). Also Woolcott et al.³⁴ reported that improved IVF outcome was obtained when uterine activity was present compared to cases in which it was absent.

- Immediately before ET, patients with OI and/or OP presented significantly higher ($p = 0.015$) uterine activity in terms of frequency compared to patient with no OI and/or no OP. Uterine activity in terms of amplitude was instead lower for patients with OI and/or OP, but not significantly lower. This finding may suggest that the combination of higher frequency and lower amplitude in the uterine activity may contribute to successful embryo implantation. It is in fact reasonable to think that the embryo, once inserted into the uterine cavity, needs help (moderate uterine contractions) to bind to the uterine wall and implant; on the other hand, these contractions should not be strong (higher amplitude) as they could expel the embryo from the uterine cavity.
- No correlation was found between implantation/pregnancy outcome and the clinical variables, such as hormone levels, stimulation related features, thickness of endometrium layer and embryo quality. This evidences the potential of the proposed TVUS speckle tracking method in characterizing uterine activity for successful embryo implantation.
- Uterine activity in terms of amplitude and frequency in the OI and/or OP groups was comparable with that of healthy women while it was higher for the non OI and/or OP groups.

Challenges and limitations

- The clinical value of our proposed method requires extensive validation *in vivo* during the IVF cycle; this can spur additional insight expanding our knowledge on the uterine motion and its role in conception and fertilization.
- The obtained f_c appeared to be in the lower limit of that reported in other studies⁶⁵⁻⁶⁷ which are based on visual inspection counting a global number of contractions without distinguishing between the different uterine layers. In this study, we focused specifically on the subendometrial layer, where the tracking is performed.
- The negative correlation between frequency and amplitude features may also be ascribed to the effect of noise on the frequency estimator. At low contraction amplitudes, approaching the noise floor, the estimated frequency characteristics may be dominated by the noise frequency spectrum, resulting in higher values. In future studies, the frequency spectra of noise and estimated signals (motion and strain signals) should be investigated in order to confirm the hypothesized physiological rationale explaining our measurement results.

9.3b Multi-modal uterine-activity measurements for prediction of embryo implantation by machine learning (Chapter 8)

In **Chapter 8**, we proposed a method to predict the success of embryo implantation based on features extracted from EHG and TVUS measurements. To this end, probabilistic classification of the uterine activity, as either favorable or adverse to embryo transfer (ET), was investigated using machine learning.

Main observations and contributions

- The best prediction accuracy (93.8%) was achieved by the support vector machine (SVM) and K-nearest neighbours (KNN) classifiers when measuring during follicle stimulation (FS) and one hour before ET (ET1); in fact, predicting before ET has more impact on clinical practice as, in case of unfavorable uterine activity, ET could either be delayed to later cycles freezing the embryos or uterine contractions characteristics could be modulated by specific treatment for favoring embryo implantation^{35, 36}. Lower prediction accuracy (75%, 87.5%, and 75%) was instead achieved by the Gaussian mixture model (GMM) classifier when measuring during FS, ET1, and five to seven days after ET (ET5-7), respectively. This finding may suggest that our data cannot be well represented as a Gaussian distribution.
- The contraction frequency (f_c), extracted longitudinally from the distance signal when employing TVUS speckle tracking, provided the best prediction accuracy on SVM (81.3%), KNN (87.5%), and GMM (81.3%) during the ET1 measurement phase when it was used as individual feature in the machine-learning framework.
- Frequency-, amplitude-, and energy-related features, such as f_c , SD, and UFM, respectively, obtained from TVUS motion and EHG analysis, were included by SVM and KNN in their optimum feature sets; this suggests that the ability of these features to separate successful and unsuccessful IVF treatment is independent of the employed classifiers. Moreover, these features may contribute to produce the best prediction of embryo implantation improving, therefore, IVF treatment.
- The predictive value of uterine activity was independent of embryo quality; this evidences the great potential of the proposed method.

Challenges and limitations

- The clinical value of our proposed method requires extensive validation *in vivo* during the IVF cycle; this can spur additional insight expanding our knowledge on the electromechanical uterine activity and its role in conception and fertilization.
- The lack of direction and velocity features hampered the full characterization of the electromechanical uterine activity. Therefore, the estimation of additional features representative of the spatiotemporal uterine activity patterns, such as propagation direction and velocity, could add relevant information to the proposed machine-learning framework for the predictability of a successful embryo implantation.
- A 3D multi-parametric strategy, which combines the estimated parameters by EHG and TVUS, may provide a further boost to the diagnostic performance in predicting successful embryo implantation.
- A larger dataset would allow the use of other cross validation techniques, such as k-fold cross validation. This type of technique is expected to produce less variance in the performance metrics⁴⁶.

9.4 General discussion and conclusions

Characterizing uterine activity outside pregnancy is of key importance to improve diagnosis as well as clinical decision-making in the context of *in-vitro* fertilization (IVF). Uterine receptivity is a determinant for successful conception. There is strong evidence of a major involvement of uterine contractions in IVF failure^{47, 31, 48, 1}. Precise pharmacological interventions on contractions are possible and can boost the success rate of IVF^{36, 49, 50}. Therefore, new advanced technology is strongly needed for quantification of uterine contractions aimed at understanding their role during IVF as well as in natural menstrual cycles. Up until now, the only options for quantification of uterine contractions have been either invasive, such as intrauterine pressure catheters, or indirect and requiring ionizing radiations, such as hysterosalpingoscintigraphy. The first one can interfere with the natural contractions due to irritation and reflex mechanisms, while the second one, because of the associated exposure to ionizing radiations, is unsuitable in the context of IVF. Being safe, widely available, and cost-effective, TVUS represents a valuable alternative for characterization of mechanical uterine contractions while transabdominal EHG has been proven to be a reliable and non-invasive measurement tool for characterizing the uterine electrical activity during pregnancy.

Our research produced novel methods for the assessment of different aspects of uterine activity outside pregnancy by EHG and TVUS measurements. These measurements are complicated by several technical and clinical challenges, such as poor EHG SNR due to the small size of the non-pregnant human uterus, complex and irregular contraction patterns, complex multilayer uterine structure, and limited and slow uterine motion compared to neighboring organs as well as the lack of a ground truth that hampers the optimization of the proposed methods. To deal with these challenges, we have proposed an approach that relies on the design of methods that are based on knowledge of the uterine structure, physiology, and electromechanical behavior outside pregnancy. Frequency-, amplitude-, and energy-related features were extracted from the derived signals and compared among the representative phases of the menstrual cycle for validation. Moreover, the results obtained by the two methods elucidated the complex uterine behavior outside pregnancy; in particular, by investigation of the spatial distribution of the uterine activity, we confirmed and evidenced the different activity of the inner and outer myometrial layers measured by EHG and TVUS speckle tracking, respectively.

Electrical uterine activity was measured by recording biopotentials using an electrode matrix placed over the lower abdomen, just above the pubic bone. In order to maximize the coverage of the uterus, the correct placement of the grid was guided by TVUS. A set of features was extracted by the single-channel EHG signal. Dedicated pre-filtering was performed on the acquired signal. Features were extracted following a 2-step approach. In step 1 different methods were used to provide a set of signals, referred as time-varying features. From these features, the frequency, amplitude, and energy global indicators were extracted in step 2 and compared among the representative phases of the menstrual cycle for validation.

Accurate estimation of features describing frequency, amplitude, and energy of the uterine contractions is essential to understand their role in IVF treatments, aimed at supporting with timing and pharmacological preparation of the embryo transfer into the uterine cavity. In fact, the key objective of the proposed methods is to distinguish between potentially successful and unsuccessful IVF attempts by features extracted from ultrasound and EHG data recorded

before and/or at the moment of embryo transfer.

Mechanical uterine activity was assessed by strain analysis performed by speckle tracking, which was implemented by block matching, accelerated by a diamond search. Singular value decomposition was used as a pre-processing step to enhance the motion patterns associated with the uterine activity while suppressing other components related to other organs or cardiac pulse waves. All the parameters of the tracking method were optimized by a dedicated *ex-vivo* experimental setup. The output produced by the implemented analysis consisted of several types of motion and strain that are relative to the uterine anatomy, showing longitudinal and transversal motion and strain. Frequency-, amplitude-, and energy-related features were extracted from the derived signals and compared among the representative phases of the menstrual cycle for validation.

We examined several dedicated BSS techniques as preprocessing step to improve US speckle tracking. The obtained results suggest SVD in combination with spectral-thresholding to provide a more accurate estimate of the uterine motion relative to the one where SVD is not applied, confirming our choice to use SVD based on the ER metric in human studies. The obtained promising results also motivated the employment of SVD filtering for providing a better estimate of the electrical uterine activity.

We also exploited the combination of the extracted features by machine learning to boost the accuracy of our prediction model by exploiting the complementarity of the estimated features, ranging from the frequency and amplitude of the mechanical contractions, up to the characterization of their electrical source. Our classification results show that a multi-parametric strategy, which combines the estimated parameters, is feasible and establishes an improved prediction of ET success.

9.5 Future perspectives

The proposed methods could represent a technical breakthrough, opening up new possibilities to improve IVF through an established link between uterine contractility, infertility conditions, and IVF failure. TVUS speckle tracking and EHG, as proposed in this thesis, have potential to provide automatic assessment of the electromechanical uterine activity, establishing a solid basis for future research.

EHG measurements have proven to be reliable for monitoring uterine contractions during labour^{11, 19, 37, 42, 43, 55} and real-time EHG technology is available for use in daily practice. Real-time EHG analysis outside pregnancy could also be implemented and integrated in a dedicated system for clinical use. Along this line, flexible, lightweight multichannel active electrode patches have been recently proposed that can record and amplify biopotential signals as well as allow analogue-to-digital conversion and serial wireless transmission to a base station^{38,64}. Being flexible and conformable to the shape of the muscle under investigation, such an electrode patch is potentially less sensitive to motion artifacts; moreover, it increases patient comfort during long-term electromyography (EMG) and EHG recordings relative to bulky EMG and EHG devices. Accordingly, such patches would provide an asset for user-friendly measurements in daily clinical practice. However, extensive validation in the context of EHG is needed, especially outside pregnancy when dealing with low amplitude signals. Yet, the interpretability of the recorded biopotentials at the abdominal surface outside pregnancy is still

difficult. In fact, the uterine contraction physiology is not fully understood despite the promising results obtained in this thesis. These issues complicate the development of such an EHG measurement system.

Future work could aim at improving the interpretability of the measured abdominal biopotentials determining, for example, the optimal inter-electrode distance in relation to the increased depth at which the uterus lies into the uterine cavity compared to pregnancy (Figure 9.1). Moreover, technical challenges need to be addressed, such as the interference of other biopotential signals, for instance from surrounding organs such as bladder and intestine, respiration and movement artefacts, and variation in skin impedance³⁹⁻⁴². In this respect, the adoption of SVD, as a pre-processing step for IVF data, already contributed to an enhancement of the signal components associated with the uterine electrical activity while suppressing other components related to other organs or the electrocardiogram signal. The frequency band used for selecting the relevant singular values was based on the EHG frequency content during pregnancy⁴³; therefore, future studies should investigate different frequency bands, also depending on the measured EHG signal reflecting the myometrial activity. Moreover, an *in-vivo* propagation analysis on a larger dataset will provide information about the direction of the UC, which may play an important role for the embryo transfer, possibly helping to further improve the IVF treatment^{44, 45, 1}. An important contribution for studying the conduction properties of EHG signals can be provided by modeling techniques. The biological tissues interposed between the electrical source at the myometrium and the recording site at the skin act as a volume conductor producing a spatial low-pass filtering effect⁵¹. In the future, the effect of the volume conductor can be formalized in the spatial frequency domain by a transfer function that accounts for the physical and geometrical properties of the biological tissues interposed between the source of the electrical current in the myometrium and the recording site on the skin.

Our proposed TVUS measurements have provided powerful features for prediction of IVF success. Together with a larger dataset, features describing the direction and velocity of the uterine contractions may be considered in the future to understand their role in IVF treatments, as specific wave-like activity patterns are associated to the occurrence of pregnancy^{44, 45, 1}; in order to achieve this, a grid of points covering the full subendometrial area should replace the few points used in this thesis. Moreover, given the complex contraction mechanism of the non-pregnant uterus, 3D analysis would be required to achieve a better understanding of the contraction pattern throughout the menstrual cycle as well as in the context of IVF. To this end, enabled by the method described in this thesis, additional analysis focusing on strain mapping and of feasibility of 3D analysis by speckle tracking has been recently carried out⁴⁵ in our lab. Several types of strain that are relative to the uterine anatomy, showing longitudinal, circular, and radial strain, along with non-directional area or volume strain were derived by speckle tracking. Additional spatiotemporal analysis in the frequency domain was used to produce global estimates of propagation of the uterine contraction waves⁴⁵. An example of the produced strain maps is shown in Figure 9.2. Preliminary analysis of uterine motion has also been implemented in 3D, but the results pertain to a very small dataset. An example of a full 3D map is shown in Figure 9.3. Extensive datasets both in 2D and 3D are however required to

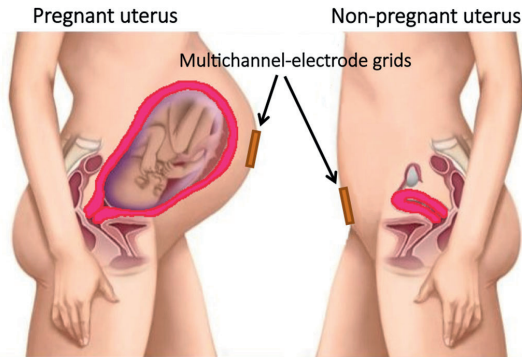


Figure 9.1: Anatomical difference between pregnant and non-pregnant human uterus.

produce additional clinical evidence and data for the optimization of the designed algorithms.

In general, the obtained promising results motivate reinforcing our clinical evidence and implementing minimal viable software that complies with medical requirements and can serve as a solid basis for a successful valorisation strategy. The method is currently implemented in a high-level programming language (Matlab), and is able to process 2D and 3D ultrasound acquisitions running on any desktop. The required input is a B-Mode ultrasound loop, which can be provided in DICOM or other video formats. As a result, the analysis can easily be performed on acquisitions made by any ultrasound scanner.

Next to the use of B-Mode images, which permits working with different scanners, speckle tracking can be performed directly on the radio-frequency (RF) signal (prior to demodulation), enabling high-resolution tracking which may be especially useful for tracking small uterine movements. Yet, similar to B-mode speckle tracking, this approach is also affected by the intrinsic anisotropy of ultrasound imaging, showing higher resolution in the axial direction. However, effective solutions to this limitation have been shown by compounding different ultrasound beam directions⁵⁰.

Incorporating the full set of transabdominal EHG and TVUS features, related to frequency, amplitude, energy, velocity and contraction direction into a clearly defined multi-parametric protocol is of great importance for the clinical implementation of these techniques. Future work should therefore include the development of a complete multi-parametric solution that suits the clinical workflow, and enables not only detection of the electromechanical uterine activity in terms of frequency, amplitude, and energy, but also in terms of velocity and direction.

Ultimately, the use of the proposed two methods (EHG and TVUS) should support decision making throughout the IVF cycle, possibly improving the success rate. Based on this work, TVUS motion analysis seems to provide the most suitable option for quantitative, non-invasive assessment of UCs in order to address IVF failure. This is also confirmed by the probabilistic classification analysis where a higher number of TVUS features are used by the classifiers compared to the EHG features. The lack of understanding about uterine contractility, in particular uncertainties on initiation, propagation, and relation to mechanical events, together with the low SNR due to the small size of the uterus, poses important challenges to the EHG

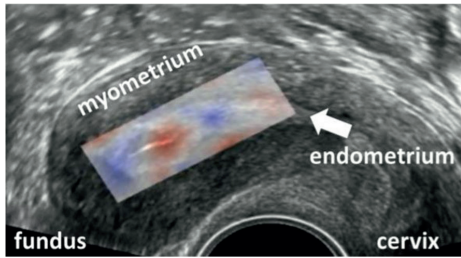


Figure 9.2: Example of uterine (area) strain map contraction (red) and relaxation (blue)⁴⁵.

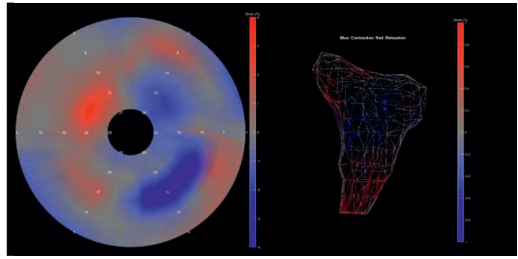


Figure 9.3: Examples of 3D representations of uterine contractions.

methodology. The uterine electrophysiology requires further investigation; in this respect, EHG analysis would certainly represent a valuable measurement tool, being non-invasive and suitable for long-term recordings. Mechanical uterine activity appears to be more understandable and interpretable by gynaecologists compared to the electrical activity, given the complex mechanisms underlying the uterine electrophysiology.

Another aspect which should not to be underestimated concerns the implementation of electromechanical measurements of the uterus by EHG and TVUS in the clinical workflow. While TVUS recordings are already part of clinical routine practice, EHG measurements are expected to require time for their clinical translation and acceptance. This is caused in part by a long learning curve, requiring good understanding of the analysis software and interpretation of complex biopotential plots.

On the other hand, while EHG measurements are suitable for long-term recordings, TVUS recordings are uncomfortable for both patient and for the sonographer, who needs to keep the probe in a fixed position for several minutes. In this study, we recorded the electromechanical uterine activity for 4 minutes, which is longer compared to standard/average US recordings in clinical practice. In this early stage of the research, longer measurements were necessary due to the uncertainties on UC characteristics and physiology. To reduce the patient discomfort due to the use of a TVUS probe, the possibility of decreasing the TVUS recording time to e.g. half time (2-min) should be considered and investigated in the future. Based on the available data, similar trends can already be detected by using half recording, even though the lower number of contractions (about two contractions in the late luteal phase) may limit the statistical significance of the observed differences.

Moreover, the use of a probe fix would seem a much more natural solution since the position of the non-pregnant uterus does not change over time.

The proposed methods can help clinicians make the crucial decision between performing the embryo transfer right away in a fresh cycle or freezing the embryo and postponing the embryo transfer to a more receptive moment. Nowadays, IVF embryo laboratories have knowledge and skills in freezing embryos such that the outcome is comparable or even superior with that obtained by fresh IVF transfers⁵⁹⁻⁶¹.

Next to adjusting the time of embryo transfer, modulation of the contraction characteristics by pharmacological compounds is an additional valuable option that can be pursued once uterine

contractions can objectively be characterized. This perspective can make the proposed methods attractive to pharmaceutical companies marketing compounds that modulate the uterine contractility (e.g., Atosiban, Nolasiban, and Barusiban). In the future, dedicated clinical trials can be designed with the aim of characterizing the effects of these pharmaceutical treatments and optimizing their use to improve IVF success.

More in general, quantitative analysis of electromechanical uterine activity can also serve as a valuable diagnostic tool for other common uterine pathologies, such as adenomyosis, myomas, menstrual pain and characterization of Cesarean scar niches.

BIBLIOGRAPHY

1. M. M., Evers, J. L., Dunselman, G. A., van Katwijk, C., Lo, C. R., & Hoogland, H. J. (1996). Endometrial wavelike movements during the menstrual cycle. *Fertility and sterility*, *65*(4), 746-749.
2. Hendricks, C. H. Inherent motility patterns and response characteristics of the nonpregnant human uterus. *Am. J. Obstet. Gynecol.* **96**, 824–841 (1966).
3. Bulletti, C. *et al.* Physiology: Electromechanical activities of human uteri during extra-corporeal perfusion with ovarian steroids. *Hum. Reprod.* **8**, 1558–1563 (1993).
4. van Gestel, I., IJland, M. M., Hoogland, H. J. & Evers, J. L. Endometrial wave-like activity in the non-pregnant uterus. *Hum.Reprod.Update.* **9**, 131–138 (2003).
5. Hendricks, C. H. A New Technique for the Study of Motility in the Non-Pregnant Human Uterus. *BJOG An Int. J. Obstet. Gynaecol.* **71**, 712–716 (1964).
6. Moawad, A. H. & Bengtsson, L. P. In vivo studies of the motility patterns of the nonpregnant human uterus. I. The normal menstrual cycle. *Am. J. Obstet. Gynecol.* **98**, 1057–1064 (1967).
7. IJland, M. M. *et al.* Endometrial wavelike movements during the menstrual cycle. *Fertil.Steril.* *65*, 746–749 (1996).
8. Lyons, E. A. *et al.* Characterization of subendometrial myometrial contractions throughout the menstrual cycle in normal fertile women. *Fertil. Steril.* **55**, 771–774 (1991).
9. Kuijsters, N. P. M. *et al.* Uterine peristalsis and fertility: current knowledge and future perspectives: a review and meta-analysis. *Reprod. Biomed. Online* **35**, 50–71 (2017).
10. Reinhard, J., Hayes-Gill, B. R., Schiermeier, S., Löser, H., Niedballa, L. M., Haarmann, E., ... & Louwen, F. (2011). Uterine activity monitoring during labour—a multi-centre, blinded two-way trial of external tocodynamometry against electrohysterography. *Zeitschrift für Geburtshilfe und Neonatologie*, *215*(05), 199-204.
11. Garcia-Casado, J., Ye-Lin, Y., Prats-Boluda, G., Mas-Cabo, J., Alberola-Rubio, J., & Perales, A. (2018). Electrohysterography in the diagnosis of preterm birth: a review. *Physiological Measurement*, *39*(2), 02TR01. <https://doi.org/10.1088/1361-6579/aaad56>
12. Soliman, A. M., Yang, H., Du, E. X., Kelley, C., & Winkel, C. (2016). The direct and indirect costs associated with endometriosis: a systematic literature review. *Human Reproduction*, *31*(4), 712-722.
13. Rabotti, C., Mischi, M., Oei, S. G., & Bergmans, J. W. (2010). Noninvasive estimation of the electrohysterographic action-potential conduction velocity. *IEEE Transactions on Biomedical Engineering*, *57*(9), 2178-2187.
14. Xu, L., Rabotti, C., & Mischi, M. (2016). Towards real-time estimation of muscle-fiber conduction velocity using delay-locked loop. *IEEE Transactions on Neural Systems and Rehabilitation Engineering*, *25*(9), 1453-1460.
15. Yoshida, T., & Hendricks, C. H. (1970). Resting pressure patterns in the nonpregnant human uterus. *American journal of obstetrics and gynecology*, *108*(3), 450-457.
16. Ziegler, D., Bulletti, C., Fanchin, R., Epiney, M., & BRIOSCHI, P. A. (2001). Contractility of the nonpregnant uterus. *Annals of the New York Academy of Sciences*, *943*(1), 172-184.
17. Bulletti, C. *et al.* Uterine contractility during the menstrual cycle. *Hum.Reprod.* **15 Suppl 1**, 81–89 (2000).
18. Lesny, P., & Killick, S. R. (2004). The junctional zone of the uterus and its contractions. *BJOG: An International Journal of Obstetrics & Gynaecology*, *111*(11), 1182-1189.
19. Mischi, M., Chen, C., Ignatenko, T., de Lau, H., Ding, B., Oei, S. G., & Rabotti, C. (2017). Dedicated entropy measures for early assessment of pregnancy progression from single-channel electrohysterography. *IEEE Transactions on Biomedical Engineering*, *65*(4), 875-884.
20. Pavlicev, M., & Norwitz, E. R. (2018). Human parturition: nothing more than a delayed menstruation. *Reproductive Sciences*, *25*(2), 166-173.

21. Harding, R. *et al.* Electromyographic activity of the nonpregnant and pregnant sheep uterus. *Am. J. Obstet. Gynecol.* **142**, 448–457 (1982).
22. Lammers, W. J. E. P. & Hamid, R. The initiation, continuation, and termination of spontaneous episodes of circus movements in the pregnant myometrium of the rat. *Am. J. Obstet. Gynecol.* **179**, 1515–1526 (1998).
23. Lammers, W. J. E. P. *et al.* Patterns of electrical propagation in the intact pregnant guinea pig uterus. *AJP Regul. Integr. Comp. Physiol.* **294**, R919–R928 (2008).
24. Lammers, W. J. E. P., Stephen, B., Al-Sultan, M. A., Subramanya, S. B. & Blanks, A. M. The location of pacemakers in the uteri of pregnant guinea pigs and rats. *Am. J. Physiol. Integr. Comp. Physiol.* **309**, R1439–R1446 (2015).
25. Parkington, H. C., Harding, R. & Sigger, J. N. Co-ordination of electrical activity in the myometrium of pregnant ewes. *J. Reprod. Fertil.* **82**, 697–705 (1988).
26. Singh, R., Xu, J., Garnier, N. G., Pumir, A. & Sinha, S. Self-organized transition to coherent activity in disordered media. *Phys. Rev. Lett.* **108**, 1–5 (2012).
27. Noe, M., Kunz, G., Herbertz, M., Mall, G. & Leyendecker, G. The cyclic pattern of the immunocytochemical expression of oestrogen and progesterone receptors in human myometrial and endometrial layers: characterization of the endometrial-subendometrial unit. *Hum.Reprod.* **14**, 190–197 (1999).
28. Saito, Y., Maki, M. & Sakamoto, H. Gap junction formation in the human uterine muscle cell of the corpus and cervix during the menstrual cycle and pregnancy. *Nippon Sanka Fujinka Gakkai zasshi* **39**, 135–140 (1987).
29. Kunz, G., Beil, D., Deininger, H., Wildt, L. & Leyendecker, G. The dynamics of rapid sperm transport through the female genital tract: evidence from vaginal sonography of uterine peristalsis and hysterosalpingoscintigraphy. *Hum.Reprod.* **11**, 627–632 (1996).
30. IJland, M. M., Evers, J. L., Dunselman, G. A. & Hoogland, H. J. Subendometrial contractions in the nonpregnant uterus: an ultrasound study.
31. Fanchin, R. *et al.* Uterine contractions at the time of embryo transfer alter pregnancy rates after in-vitro fertilization. *Hum.Reprod.* **13**, 1968–1974 (1998).
32. Bulletti, C. & de Ziegler, D. Uterine contractility and embryo implantation. *Curr. Opin. Obstet. Gynecol.* **18**, 473–484 (2006).
33. Zhu, L., Che, H. S., Xiao, L., & Li, Y. P. (2014). Uterine peristalsis before embryo transfer affects the chance of clinical pregnancy in fresh and frozen-thawed embryo transfer cycles. *Human Reproduction*, 29(6), 1238-1243.
34. Woolcott, R., & Stanger, J. (1997). Potentially important variables identified by transvaginal ultrasound-guided embryo transfer. *Human reproduction (Oxford, England)*, 12(5), 963-966.
35. Kim, S. H., Riaposova, L., Ahmed, H., Pohl, O., Chollet, A., Gotteland, J. P., ... & Terzidou, V. (2019). Oxytocin Receptor Antagonists, Atosiban and Nolasiban, Inhibit Prostaglandin F_{2α}-induced Contractions and Inflammatory Responses in Human Myometrium. *Scientific reports*, 9(1), 5792.
36. Moraloglu, O., Tonguc, E., Var, T., Zeyrek, T., & Batioglu, S. (2010). Treatment with oxytocin antagonists before embryo transfer may increase implantation rates after IVF. *Reproductive biomedicine online*, 21(3), 338-343.
37. Rabotti, C., Oei, S. G., van't Hooft, J., & Misch, M. (2011). Electrohysterographic propagation velocity for preterm delivery prediction. *American Journal of Obstetrics & Gynecology*, 205(6), e9-e10.
38. Garripoli, C., Abdinia, S., van der Steen, J. L. J., Gelinck, G. H., & Cantatore, E. (2018). A Fully Integrated 11.2-mm 2 a-IGZO EMG Front-End Circuit on Flexible Substrate Achieving Up to 41-dB SNR and 29-M Ω Input Impedance. *IEEE Solid-State Circuits Letters*, 1(6), 142-145.
39. Devedeux D, Marque C, Mansour S, Germain G, Duchene J. Uterine electromyography: a critical review. *Am J Obstet Gynecol* 1993;169:1636-53.

40. Ye-Lin Y, Garcia-Casado J, Prats-Boluda G, Alberola-Rubio J, Perales A. Automatic identification of motion artifacts in EHG recording for robust analysis of uterine contractions. *Comput Math Methods Med* 2014;2014:470786.
41. Tam HW, Webster JG. Minimizing electrode motion artifact by skin abrasion. *IEEE Trans Biomed Eng* 1977;24:134-9.
42. de Lau H, Rabotti C, Haazen N, Oei SG, Mischi M. Towards improving uterine electrical activity modeling and electrohysterography: ultrasonic quantification of uterine movements during labor. *Acta Obstet Gynecol Scand* 2013;92:1323-6.
43. Devedeux, D., Marque, C., Mansour, S., Germain, G., & Duchêne, J. (1993). Uterine electromyography: a critical review. *American journal of obstetrics and gynecology*, 169(6), 1636-1653.
44. Ijland, M. M., Evers, J. L., Dunselman, G. A., Volovics, L., & Hoogland, H. J. (1997). Relation between endometrial wavelike activity and fecundability in spontaneous cycles. *Fertility and sterility*, 67(3), 492-496.
45. Huang, Y., Sammal, F., Blank, C., Kuijsters, N., Rabotti, C., Schoot, B. C., & Mischi, M. (2018, October). Quantitative Ultrasound Imaging and Characterization of Uterine Peristaltic Waves. In *2018 IEEE International Ultrasonics Symposium (IUS)*(pp. 1-4). IEEE.
46. James, G., Witten, D., Hastie, T., & Tibshirani, R. (2013). *An introduction to statistical learning* (Vol. 112, p. 18). New York: springer.
47. Fanchin, R., & Ayoubi, J. M. (2009). Uterine dynamics: impact on the human reproduction process. *Reproductive biomedicine online*, 18, S57-S62.
48. Lesny, P., Killick, S. R., Robinson, J., Raven, G., & Maguiness, S. D. (1999). Junctional zone contractions and embryo transfer: is it safe to use a tenaculum?. *Human reproduction*, 14(9), 2367-2370.
49. Pierzynski, P., Reinheimer, T. M., & Kuczynski, W. (2007). Oxytocin antagonists may improve infertility treatment. *Fertility and sterility*, 88(1), 213-e19.
50. Hansen, H.H.G., R.G.P. Lopata, and C.L. de Korte, Noninvasive carotid strain imaging using angular compounding at large beam steered angles: validation in vessel phantoms IEEE Transactions on Medical Imaging, 2009. 28(6): p. 872-880.
51. Rabotti, C., Mischi, M., Beulen, L., Oei, G., & Bergmans, J. W. (2009). Modeling and identification of the electrohysterographic volume conductor by high-density electrodes. *IEEE Transactions on Biomedical Engineering*, 57(3), 519-527.
52. Ye-Lin, Y., Alberola-Rubio, J., Prats-boluda, G., Perales, A., Desantes, D., & Garcia-Casado, J. (2015). Feasibility and Analysis of Bipolar Concentric Recording of Electrohysterogram with Flexible Active Electrode. *Annals of Biomedical Engineering*, 43(4), 968–976.
53. Alberola-Rubio, J., Garcia-Casado, J., Prats-Boluda, G., Ye-Lin, Y., Desantes, D., Valero, J., & Perales, A. (2017). Prediction of labor onset type: Spontaneous vs induced; role of electrohysterography?. *Computer methods and programs in biomedicine*, 144, 127-133.
54. Rabotti, C., Mischi, M., van Laar, J. O., Oei, G. S., & Bergmans, J. W. (2008). Estimation of internal uterine pressure by joint amplitude and frequency analysis of electrohysterographic signals. *Physiological Measurement*, 29(7), 829.
55. Rabotti, C., & Mischi, M. (2015). Propagation of electrical activity in uterine muscle during pregnancy: a review. *Acta Physiologica*, 213(2), 406-416.
56. Neubach, Z., & Shoham, M. (2009). Ultrasound-guided robot for flexible needle steering. *IEEE Transactions on Biomedical Engineering*, 57(4), 799-805.
57. Vrooijink, G. J., Abayazid, M., & Misra, S. (2013, May). Real-time three-dimensional flexible needle tracking using two-dimensional ultrasound. In *2013 IEEE International Conference on Robotics and Automation* (pp. 1688-1693). IEEE.
58. Lee, S. S. M., Lewis, G. S. & Piazza, S. J. An algorithm for automated analysis of ultrasound images to measure tendon excursion in vivo. *J. Appl. Biomech.* **24**, 75–82 (2008).

59. Roque, M., Lattes, K., Serra, S., Sola, I., Geber, S., Carreras, R., & Checa, M. A. (2013). Fresh embryo transfer versus frozen embryo transfer in in vitro fertilization cycles: a systematic review and meta-analysis. *Fertility and sterility*, *99*(1), 156-162.
60. Evans, J., Hannan, N. J., Edgell, T. A., Vollenhoven, B. J., Lutjen, P. J., Osianlis, T., ... & Rombauts, L. J. (2014). Fresh versus frozen embryo transfer: backing clinical decisions with scientific and clinical evidence. *Human reproduction update*, *20*(6), 808-821.
61. Wong, K. M., van Wely, M., Mol, F., Repping, S., & Mastenbroek, S. (2017). Fresh versus frozen embryo transfers in assisted reproduction. *Cochrane Database of Systematic Reviews*, (3).
62. Demené, C., Deffieux, T., Pernot, M., Osmanski, B. F., Biran, V., Gennisson, J. L., ... & Cohen, I. (2015). Spatiotemporal clutter filtering of ultrafast ultrasound data highly increases Doppler and fUltrasound sensitivity. *IEEE transactions on medical imaging*, *34*(11), 2271-2285.
63. Mauldin, F. W., Lin, D., & Hossack, J. A. (2011). The singular value filter: A general filter design strategy for PCA-based signal separation in medical ultrasound imaging. *IEEE transactions on medical imaging*, *30*(11), 1951-1964.
64. Fuketa, H., Yoshioka, K., Shinozuka, Y., Ishida, K., Yokota, T., Matsuhisa, N., ... & Someya, T. (2014). 1 μ s Thickness Ultra-Flexible and High Electrode-Density Surface Electromyogram Measurement Sheet With 2 V Organic Transistors for Prosthetic Hand Control. *IEEE transactions on biomedical circuits and systems*, *8*(6), 824-833.
65. Fanchin R, Ayoubi JM, Righini C, Olivennes F, Schonauer LM, Frydman R. Uterine contractility decreases at the time of blastocyst transfers. *Hum Reprod* 2001;*16*(6):1115–9.
66. Ayoubi JM, Epiney M, Brioschi PA, Fanchin R, Chardonnens D, De Ziegler D. Comparison of changes in uterine contraction frequency after ovulation in the menstrual cycle and in in vitro fertilization cycles. *Fertil Steril* 2003;*79*(5):1101–5.
67. Fanchin R, Righini C, Olivennes F, Taylor S, de Ziegler D, Frydman R. Uterine contractions at the time of embryo transfer alter pregnancy rates after in-vitro fertilization. *Hum Reprod* 1998;*13*(7):1968–74.

ACKNOWLEDGMENTS

Undertaking this PhD study has been a truly life-changing experience for me and it would not have been possible without the support and guidance that I received from many people.

Firstly, I would like to express my sincere gratitude to my first promotor **prof. dr. ir. Jan Bergmans** for his support to my PhD study, for his immense knowledge and insightful comments, but also for his questions and observations during our project meetings, which incited me to widen my research from various perspectives. He contributed to several meetings that helped to shape this project and he was always willing to support me with my most complex issues, both professional and personal.

I am deeply thankful to my second promotor **prof. dr. Dick Schoot**, who provided me the opportunity to experience a patient-friendly hospital environment, and who gave access to the operating rooms and hospital facilities for conducting the measurements and collecting data. Without his vision and precious support it would not be possible to conduct this research. With him I experienced for the first time the OR practice assisting to a laparoscopic hysterectomy accompanied with a clear explanation of the full procedure. Beyond being my second promotor, prof. Schoot is a professional gynecologist with deep human understanding of patient problems and psychology, and I am extremely happy that he was the one giving birth to my baby. Life can be downright difficult at times and, getting through the tough times in life, these memories look like a fairytale. I will be always grateful for his professional and human support, essential to overcome all the difficult time and grief encountered in this last period of my life.

I will forever be thankful to my supervisor, **dr.ir. Chiara Rabotti**. Chiara has been helpful in providing advice many times during my graduation project, PDEng and PhD studies. She was and remains my best role model for a scientist, mentor, and teacher. I still think fondly of my time as an undergraduate student under her supervision, despite my initial language- and content-related difficulties she has always been patient and she always believed in me and motivated me to keep going. Chiara was the reason why I decided to pursue my PhD study. Her enthusiasm and love for teaching was contagious. Her guidance helped me across the entire period of my research and writing of my PDEng and PhD theses. But Chiara has been not only a great advisor and mentor for my research work and career, but also a friend. I like to thank her for helping in whatever way she could during my challenging personal period, for all the fun we have had during conferences, for the long conversations regarding children, food and sport.

Committee members: I would like to extend my gratitude to my PhD thesis committee, **dr. ir. J. G. Casado**, **prof. dr. ir. C. L. de Korte**, **prof. dr. J. Huirne**, **prof. dr.ir. Z. Del Prete**, and **prof. dr.ir. E. Cantatore**, for having accepted to be part of my committee and for having agreed to the

pursuit of the public defense of my PhD thesis. I am very glad to have had such a prestigious committee.

A very special and heartfelt thank you to my respected graduation mentor, **prof. dr. ir. Zaccaria Del Prete (Rino)**; without him I would never have even started this experience in the Netherlands carrying out my master thesis project but most of all I would never have known the man of my life, Massimo.

Rino, I still remember the day of my exam on “Mechanical measurements” before leaving to Eindhoven; I was supposed to be examined by one of your assistants but you immediately stopped him saying: “I am going to examine Federica because I would like to understand her intentions, whether she goes to Eindhoven for having fun or for studying seriously”. Well, it was a tough exam ended with a top score that allowed you to give me the green light to go on. I was supposed to spend 6 months in Eindhoven but I have never come back. I also remember my first poster presentation at the IEEE-EMBC conference in Milan during which you often came to bring me snacks and drinks. I was very tense and nervous and I really appreciated the way you took care of me in that circumstance. I am also very grateful to you for having accepted to be part of my PhD committee because with you my research journey has begun and with you it should reach this major milestone. You are simply a great professor and sensible person.

This PhD was part of two projects: “Characterization of uterine activity for improved assisted reproductive technology” and “Quantitative ultrasound imaging of the uterus for improved reproductive technology - QUIET”, supported by NWO. I would like to thank all the members of the user committee, **Jan Peusher (TMSI)**, **Vim van de Vooren (Samsung)**, **Marcel van Duin (Ferrings)**, **Steven Weyers**, **Frank Vandekerckhove**, and **Sara Somers (Ghent University Hospital)**, for their valuable feedbacks and inputs during our regular meetings.

These acknowledgments would not be complete without mentioning my research lab colleagues. In particular, I like to thank my fellow labmates, **Nineke** and **Celine**, for the stimulating discussions, for the sleepless nights spent working together before deadlines, and for all the fun we have had in the last years. You have been essential for the achievement of this thesis. All the experimental data of this thesis have been recorded both at the Catharina hospital in Eindhoven by Nienke and at the university hospital in Ghent by Celine. Dear ladies, I am very grateful and I feel indebted to you two for having struggled to find patients, written METC protocols, attached an infinite number of electrodes, made transvaginal ultrasound scans without moving your hands, and coped with our bulky devices. I really do not know how I could have done without you! With you, I had for the first time the opportunity to see and hold in my hands a real *ex-vivo* uterus as well as performing exciting but stressful measurements in the hospital. Ladies, you are not only invaluable research colleagues but also very good friends; you have shown me great affection, spiritual support, especially during my tough moments where you have never left me alone. A heartfelt thanks!

I also had the fortune to work with great engineers/friends whom I wish to thank for their important contribution to this thesis; in particular, I like to thank **Lin Xu**, **Rogier Wildeboer**, **Yizhou Huang** and **Tom Bakkes**. I would also like to thank other master students for their

contribution to this PhD work, **Xin Ye** and **Rudy de Roon**, as well as to my PDEng project, **Angelinda** and **Marinella Maragno**.

Many thanks to all the SPS group. To the staff members, **Marieke, Carla, Anja,** and **Judith** who dealt with the administrative mess that I created and with the virus I managed to get, infecting the entire TU/e campus, to the other valued colleagues in the SPS group (to name a few) **Rik, Elisabetta, Eleonora, Francesca, Luuk, Bas, Eleni, Beatrijs, Myrthe, Gabriele, Marina, Lieke, Anouk, Libertario, Salvatore, Guy, Aline, Michiel, Stefan.** To the officemates I had in the last years, **Simona, Nienke, Celine, Linda, Yizhou, Rogier, Ruud, Peiran, Anastasia, Paul, Maretha,** I would like to express my gratitude for their help, companionship, and inspiring discussions! I cannot forget my colleague and friend **Simona**; I had the pleasure to enjoy her company also away from the office. Simona, thanks for the nice evenings based on good food, friends and music, for the authentic Sicilian “arancine” and “sbriciolona” you made for me, for other Sicilian products I could taste and for the funny experience of Ramen-homemade I had; but most of all, thank you for the affection you have shown me in this last period for me very difficult. True friends are present in moments of difficulty, they do not abandon you and I will always thank you for this.

I could never forget to thank **Rian van Gaalen**, whose door has always been open to answer questions and help me with any problem I had during my PDEng. Rian, you are the most generous and kind person I have ever met. Thanks to your big heart, you facilitated the creation of a warm, friendly and personal PDEng research environment, the so called “PDEng big family”. Within this family, I like to thank in particular a few friends: **Chara, Lena, Kambiz, Juan Alfaro, Nenad, Nick, Antoine, Jao, Patrick, Alex, Ya, Jing, Weilu, Kirill, Maria, Garbi, Monica, Dimitris, Kevin,** and **Ilker.**

My joy knows no bounds in expressing my sincere and heartfelt gratitude to all my friends.

Besides my colleagues, there are a number of people I cannot forget, because they made my life in Eindhoven wonderful, even when my research was getting me through tough moments, and contributed to make my last years memorable. For this, many thanks to **Guim, Medhi, Koen, Rosa** and **Marlon**, but in particular to my favorite Italian flat mates and best friends **Veronica** (my paranymph) and **Lucone.** Veronica, you have been essential for me! Together we enjoyed the little simple things of life; you are a special friend, the one you can talk to with open heart because you understand everything about me, even my silences! You have been the sister I have never had.

Sincere thanks to the two super-moms **Klaudia** and **Jorinde** for the time spent and the fun we had together with our little boys: the 3 musketeers! With you, I experience the beauty to be a “desperate house-mom” rather than a “desperated housewife”. I wish myself to spend more time with you from now on.

Furthermore, I would like to express my gratitude to my friends **Cristina** (my paranymp), **Elisabetta** (my Dutch classmate also) and **Eleonora**. What really matters is not how much time we spent together but how we spent it and how we connected; sometimes people are beautiful not by appearance, not by what they say, but simply by what they are and you are beautiful as you are. True friendship is what is given to a friend in the time of need, with no pretensions, no ambiguity and falsehood. I am very proud and glad to have received your precious friendship, especially in the last period of my life.

Non potrei mai dimenticare di ringraziare le mie amiche di una vita, **Elisa, Ilaria, Sabrina ed Agostina** (autrice della cover di questa tesi). Un amico lontano e' a volte piu' vicino di qualcuno a portata di mano. Voi, anche da lontano, siete riuscite a non farmi mancare il vostro affetto e supporto; nessun luogo per noi e' lontano, nessuna distanza materiale puo' separarci, se desideri essere accanto a qualcuno che ami ci sei e basta! Noi, nonostante tutto, ci siamo. Non vedo l'ora di passare del tempo insieme come ai vecchi tempi!

Un infinito ed incommensurabile grazie ai miei genitori **Rossana e Stefano** ed ai miei fratelli **Emanuele ed Angelo**, grazie ai quali sono quella che sono. Un grazie speciale alla mia seconda mamma, **Stefania**. Grazie a tutti voi per aver sempre creduto in me e per avermi sempre incoraggiata a seguire i miei sogni. La vita ci ha allontanati ma e' l'amore, quello vero, a tenerci uniti.

Un grazie di cuore va anche ai miei zii **Sandro, Silvana e Fulvio**, ai miei cugini **Michela e Davide**, alla mia mitica, invincibile ed indistruttibile **nonna Lulli**, ai miei altri nonni diventati stelle, **i due Angeli e Marisa** che hanno sempre vegliato su di me, alla mia famiglia tutta, alle mie due cognate **Martina e Veronica** ed a mio suocero **Mauro** per il suo infinito affetto.

I would like to address my thanks to **Susan**, for her understanding, for her friendship, and for her important help during the most difficult periods. Together, we have helped each other to create a peaceful and happy family. I will always thank you for giving me the chance to take care of the sweetest Mara.

Michael and Mara: it is with the heart full of joy and the pride of a mother that I thank you for making my life so special.

Michael, with your 2 and a half years you have been able to give me and to show me so much love despite the difficulties and the hard moments that life has placed me. You have been and you continue to be my cure for everything. *“Sara` difficile lasciarti al mondo e tenere un pezzetto per me e nel bel mezzo del tuo girotondo non poterti proteggere. Sara` difficile ma sara` fin troppo semplice mentre tu ti giri e continui a sorridere”*. Mom loves you!

My lovely Maya, it was May when I found out to be pregnant. I immediately started loving you but a cruel destiny has taken you away from me. You were beautiful, I will always remember your little hands and feet, your sweet mouth and nose and your beautiful eyes. It has been hard

to conclude this thesis, the pain was immense but I would like to thank you for giving me the possibility to have been your mom, even if for five months only; you have been with me during the most stressful moments: submitting papers, writing introduction, discussion and conclusions, and integrating comments. Together we could make it and I will always be grateful to you for not having abandoned me before. Despite everything, I needed your support because it took courage to love during those days, to look for beauty even in sad things. If I had another life, another existence, I would come looking for you because I can not get enough. To feel a little safe with this heart in revolt, I would look at you every day again like it was the first time. My heart seems like a battlefield where there is silence but, luckily, I will always have you!

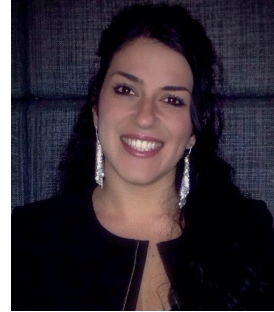
Last but not the least, an eternal thanks to **the men I love the most**. This thesis could have never been done without the fundamental contribution of **prof.dr.ir. Massimo Mischi**. I will forever be thankful to you for your precious ideas, enthusiasm, and support. Massimo, you are an example of humility, loyalty, passion and dedication. The message you convey to the students is extraordinary. Not always a successful man can also be a man of value; You are! You taught me a lot and you keep doing it; for me it is an honor to have had you as a professional guide during my studies, but above all, it is an honor to have you as a life partner. Life brought us tears down, but it didn't succeed in canceling our smiles. Life has robbed us of many hopes, but it has not taken away our dreams. Life has thrown us down so many times, but we never gave up. Together we had the courage and strength to get up and move forward. You gave me the strength to go on and I will forever be grateful to you but most of all, I will never stop thanking you for giving me the most precious gift of life: Michael. ***"Io e te, come nelle favole"***!

-Fede

CURRICULUM VITAE

Federica Sammali was born on March 5th, 1986 in Genoa, Italy. She grew up in Rome, Italy, where she received her high school diploma in 2005.

After high school, she started her studies in Biomedical Engineering at the University of Rome “La Sapienza”, Rome, Italy. In 2012, she was awarded with a scholarship to carry out her master thesis at the Eindhoven University of Technology within the Biomedical Diagnostics (BM/d) lab of Signal Processing Systems (SPS) group. During her graduation project, she worked on measurements and analysis of electrophysiological responses to vibrating loads. To this end, the H-reflex was stimulated by trans-cutaneous electrical nerve stimulation and measured by electromyography. In 2013, she received her M.Sc. degree with specialization in Biomechanical Engineering.



After completing her master studies, she conducted a PDEng traineeship at the Eindhoven University of Technology within the BM/d lab of the SPS group. Her work focused on the analysis of the uterine electrical activity outside pregnancy by electrohysterography.

In November 2015, she started a PhD project at the BM/d lab on measurement of the uterine activity of the non-pregnant human uterus for improving *in-vitro* fertilization treatment, with special emphasis on uterine contraction and strain quantification by electrohysterography and ultrasound speckle tracking, respectively.

Since May 2019, she is a post-doctoral fellow at the TU/e within the Eindhoven MedTech Innovation Center (e/MTIC) partnership that combines an academic partner (TU/e), 3 semi-academic hospitals (Catahrina Hospital, Maxima Medical Center, Kempenhaeghe). Her research interests include meditech solutions for earlier detection of cardiovascular disease (MEDICAID).

LIST OF AUTHOR'S PUBLICATIONS

(journals and symposia proceeding)

Journal papers

2019-

- [JP1] Dedicated Ultrasound Speckle tracking for Quantitative Analysis of Uterine Motion outside pregnancy.
F. Sammali, N. P. M. Kuijsters, Y. Huang, C. Blank, C. Rabotti, B. C. Schoot, and M. Mischi.
IEEE Transaction on Ultrasonics, Ferroelectrics, and Frequency Control, vol. 66, no. 3, pp. 581-590, 2019.
- [JP2] Visual inspection of transvaginal ultrasound videos to characterize uterine peristalsis: an inter-observer agreement study.
N. P. M. Kuijsters, **F. Sammali**, C. Rabotti, M. Mischi, and B. C. Schoot.
Journal of Ultrasound, pp. 1-8, 2019
- [JP3] Blind Source Separation for Clutter and Noise Filtering of Ultrasound Imaging.
R. R. Wildeboer, **F. Sammali**, R. J. G. van Sloun, C. Rabotti, H. Wijkstra, and M. Mischi.
Submitted to *IEEE Transaction on Ultrasonics, Ferroelectrics, and Frequency Control*.
- [JP9] Propagation of spontaneous electrical activity in the ex-vivo human uterus.
N. P. M. Kuijsters, **F. Sammali**, X. Ye, C. Blank, L. Xu, M. Mischi, B. C. Schoot, and C. Rabotti.
Submitted to *Nature Scientific Reports*.
- [JP4] Multi-modal uterine-activity measurements for prediction of embryo implantation by machine learning.
F. Sammali, C. Blank, T. H. G. F. Bakkes, C. Rabotti, B. C. Schoot, and M. Mischi.
Submitted to *IEEE Journal of Biomedical and Health Informatics*.
- [JP5] Quantitative ultrasound imaging for assessment of uterine contractility during in-vitro fertilization.
C. Blank, **F. Sammali**, N. P. M. Kuijsters, C. Rabotti, M. Mischi, P. de Sutter, and B. C. Schoot.
Submitted to *Fertility and Sterility Journal*.

2018-

- [JP6] Effect of vibration-induced fatigue on the H-reflex.
F. Sammali, L. Xu, C. Rabotti, M. Cardinale, Y. Xu, J.P. van Dijk, M.J. Zwarts, Z. Del Prete, and M. Mischi.
Journal of Electromyography and Kinesiology, vol. 39, pp. 134-141, 2018.
- [JP7] Feasibility of transabdominal electrohysterography for analysis of uterine activity in nonpregnant women.
F. Sammali, N. P. M. Kuijsters, B. C. Schoot, M. Mischi, and C. Rabotti.
Reproductive Science, vol. 25, no. 7, pp. 1124-1133, 2018.

- [JP8] Experimental setup for objective evaluation of the uterine motion analysis by ultrasound speckle tracking.
F. Sammali, C. Blank, L. Xu, Y. Huang, B. C. Schoot, and M. Mischi.
Biomedical Physics & Engineering express, vol. 4, no. 3, p. 035012, 2018.

International conferences

2019-

- [IC1] Prediction of embryo implantation by machine learning based on ultrasound motion analysis.
F. Sammali, C. Blank, T. Bakkes, C. Rabotti, B. C. Schoot, and M. Mischi.
IEEE International Ultrasonics Symposium (IUS),
Glasgow (Scotland), Oct 6-9, 2019. Oral presentation.
- [IC2] Prediction of embryo implantation by machine learning based on multi-modal uterine acquisitions.
F. Sammali, C. Blank, T. Bakkes, C. Rabotti, B. C. Schoot, and M. Mischi.
Engineering in Medicine and Biology Conference (EMBC),
Berlin (Germany), July 23-27, 2019. Poster presentation.

2018-

- [IC3] Quantitative analysis of uterine motion outside pregnancy by dedicated ultrasound speckle tracking.
F. Sammali, N. P. M. Kuijsters, Y. Huang, C. Blank, C. Rabotti, B. C. Schoot, and M. Mischi.
IEEE International Ultrasonics Symposium (IUS),
Kobe (Japan), Oct 22-25, 2018. Poster presentation.
- [IC4] Quantitative ultrasound imaging and characterization of uterine peristaltic waves.
Y. Huang, **F. Sammali**, C. Blank, N. P. M. Kuijsters, C. Rabotti, B. C. Schoot, and M. Mischi.
IEEE International Ultrasonics Symposium (IUS),
Kobe (Japan), Oct 22-25, 2018. Oral presentation.
- [IC5] Ultrasound-based strain mapping for contraction frequency in the non-pregnant uterus.
C. Blank, Y. Huang, N. P. M. Kuijsters, **F. Sammali**, B. C. Schoot, and M. Mischi.
28th World Congress on Ultrasound in Obstetrics and Gynecology,
Singapore, Oct 20- 24, 2018. Oral presentation.
- [IC6] Experimental setup for objective evaluation of ultrasound speckle tracking in the human uterus.
F. Sammali, C. Blank, L. Xu, Y. Huang, B. C. Schoot, and M. Mischi.
XXII Congress of the International Society of Electrophysiology and Kinesiology (ISEK),
Dublin (Ireland), June 29- July 2, 2018. Oral presentation.
- [IC7] Ultrasound-based strain mapping for quantitative characterization of uterine activity outside pregnancy.
Y. Huang, C. Blank, **F. Sammali**, N. P. M. Kuijsters, M. Mischi, and B. C. Schoot.
XXII Congress of the International Society of Electrophysiology and Kinesiology (ISEK),
Dublin (Ireland), June 29- July 2, 2018. Poster presentation.

- [IC8] Quantitative motion analysis of the uterus by optical flow and two-dimensional strain mapping. Y. Huang, **F. Sammali**, N. P. M. Kuijsters, B. C. Schoot, and M. Mischi. *13th Annual IEEE International Symposium on Medical Measurement & Applications (MeMeA)*, Rome (Italy), June 11-13, 2018. Oral presentation.

2017-

- [IC9] Ex-vivo phantom for evaluation of ultrasound speckle tracking in the uterus. **F. Sammali**, C. Blank, L. Xu, B.C. Schoot, and M. Mischi. *IEEE International Ultrasonics Symposium (IUS)*, Washington (USA), Sep 6-9, 2017. Poster presentation.
- [IC10] Objective assessment of uterine peristalsis outside pregnancy by high-order texture analysis of ultrasound images. C. Caresio, C. Blank, N. P. M. Kuijsters, **F. Sammali**, M. Mischi, F. Molinari, and B. C. Schoot. *27th World Congress on Ultrasound in Obstetrics and Gynecology*, Vienna (Austria), Sep 16-19, 2017. Poster presentation.
- [IC11] Ultrasound-based strain mapping for quantitative characterization of uterine activity outside pregnancy. Y. Huang, C. Blank, **F. Sammali**, N. P. M. Kuijsters, M. Mischi, and B. C. Schoot. *27th World Congress on Ultrasound in Obstetrics and Gynecology*, Vienna (Austria), Sep 16-19, 2017. Poster presentation.

2016-

- [IC12] Feasibility of quantitative uterine motion analysis by ultrasound speckle tracking outside pregnancy. **F. Sammali**, N.P.M. Kuijsters, C. Rabotti, B.C. Schoot, and M. Mischi. *XXI Congress of the International Society of Electrophysiology and Kinesiology (ISEK)*, Chicago (USA), Jul 5-8, 2016. Oral presentation.
- [IC13] Feasibility of uterine electromyography outside pregnancy. C. Rabotti, **F. Sammali**, N.P.M. Kuijsters, B. C. Schoot, and M. Mischi. *XXI Congress of the International Society of Electrophysiology and Kinesiology (ISEK)*, Chicago (USA), July 5-8, 2016. Oral presentation.

2015-

- [IC14] Feasibility of uterine speckle tracking for improved embryo implantation. M. Mischi, N.P.M. Kuijsters, **F. Sammali**, and C. Rabotti. *IEEE International Ultrasonics Symposium (IUS)*, Taipei (Taiwan), Oct 21-24, 2015. Oral presentation.
- [IC15] Automatic Contraction Detection During the Menstrual Cycle By Electrohysterography. N.P.M. Kuijsters, C. Rabotti, **F. Sammali**, M. Mischi, and B.C. Schoot. *24th Annual Congress of the European Society for Gynaecology Endoscopy (ESGE)*, Syma-Budapest (Hungary), Oct 7-10, 2015. Oral presentation.

[IC16] Analysis of uterine activity in Nonpregnant Women by Electrohysterography: A Feasibility Study.
C. Rabotti, **F. Sammali**, N.P.M. Kuijsters, M.S.Q. Kortenhorst, B. C. Schoot, and M. Mischi.
IEEE Engineering in Medicine and Biology Society (EMBC),
Milan (Italy), Aug 25-29, 2015. Poster presentation.

[IC17] Effect of Fatigue Induced by Vibration Exercise on the H-Reflex.
F. Sammali, L. Xu, C. Rabotti, J.P. van Dijk, M.J. Zwarts, Z. Del Prete, and M. Mischi.
IEEE Engineering in Medicine and Biology Society (EMBC),
Milan (Italy), Aug 25-29, 2015. Poster presentation.

2014-

[IC18] H-reflex in vibration exercise.
F. Sammali, L. Xu, C. Rabotti, J.P. van Dijk, M.J. Zwarts, Z. Del Prete, and M. Mischi.
XX Congress of the International Society of Electrophysiology and Kinesiology (ISEK),
Rome (Italy), Jul 15-18, 2014. Oral presentation.

2011-

[IC19] Numerical Evaluation of the Electric Field Induced in a Cubic Phantom by Different Antennas at 2.45 GHz.
A. Paffi, E. Liberti, **F. Sammali**, R. Stefanelli, D. Trincherio, and F. Apollonio.
International symposium on Electromagnetics in Advanced Applications (ICEAA),
Turin (Italy), Sept 12-16, 2011. Poster presentation.

Regional conferences

2019-

[RC1] Quantitative ultrasound imaging and characterization of uterine peristaltic waves.
Y. Huang, **F. Sammali**, C. Blank, N.P.M. Kuijsters, C. Rabotti, B.C. Schoot, and M. Mischi.
7th Dutch Bio-Medical Engineering Conference,
Egmond aan Zee (The Netherlands), Jan 24-25, 2019. Oral presentation.

2017-

[RC2] Experimental setup for objective evaluation of ultrasound speckle tracking in the uterus.
F. Sammali, C. Blank, L. Xu, Y. Huang, B.C. Schoot, and M. Mischi.
IEEE-EMBS Benelux Chapter,
Brussels (Belgium), Nov 30, 2017. Oral presentation.

2016-

[RC3] Quantitative analysis of uterine contractions in non-pregnant uteri using Speckle Tracking.
N.P.M. Kuijsters, **F. Sammali**, C. Rabotti, B.C. Schoot, and M. Mischi.
14th Belgian Day on Biomedical Engineering,
Brussels (Belgium), March 4, 2016. Poster presentation.

2015-

- [RC4] Analysis of the uterine electrical activity outside pregnancy.
F. Sammali, N.P.M. Kuijsters, C. Rabotti, B.C. Schoot, and M. Mischi.
IEEE-EMBS Benelux Chapter,
Liege (Belgium), Nov 26, 2015. Oral presentation.

2013-

- [RC5] Neuromuscular reflex in vibration exercise.
F. Sammali, L. Xu, C. Rabotti, J.P. van Dijk, M.J. Zwarts, Z. Del Prete, and M. Mischi.
12th Belgian Day on Biomedical Engineering: Joint Meeting with IEEE-EMBS Benelux Chapter,
Brussels (Belgium), Dec 5-6, 2013. Poster presentation.

